REPORT

January 26, 2007
EWI Project No. 47447GTH
Final Report

Strain-Based Design: Strain Concentration at Girth Welds

Submitted to:

MMS and PRCI

EWI

MATERIALS JOINING TECHNOLOGY

Final Report

Project No. 47447GTH

on

Strain-Based Design: Strain Concentration at Girth Welds

to

MMS and PRCI

January 26, 2007

William Mohr
EWI
1250 Arthur E. Adams Drive
Columbus, OH 43221

Disclaimers

This report is furnished to Pipeline Research Council International, Inc. (PRCI) under the terms of PRCI contract PR-185-04506, between PRCI and Edison Welding Institute (EWI). The contents of this report are published as received from EWI. The opinions, findings, and conclusions expressed in the report are those of the authors and not necessarily those of PRCI, its member companies, or their representatives. Publication and dissemination of this report by PRCI should not be considered an endorsement by PRCI of EWI, or the accuracy or validity of any opinions, findings, or conclusions expressed herein.

In publishing this report, PRCI and EWI make no warranty or representation, expressed or implied, with respect to the accuracy, completeness, usefulness, or fitness for purpose of the information contained herein, or that the use of any information, method, process, or apparatus disclosed in this report may not infringe on privately owned rights. PRCI and EWI assume no liability with respect to the use of, or for damages resulting from the use of, any information, method, process, or apparatus disclosed in this report.

This report has been reviewed by the Minerals Management Service and approved for publication. Approval does not signify that the contents necessarily reflect the views and policies of the Service, nor does mention of trade names or commercial products constitute endorsement or recommendation for use.

This study was funded by the Minerals Management Service, U.S. Department of the Interior, Washington, D.C., under Contract Number 1435-01-02-CT-85093.

Contents

Page

Disclaimers i

Executive Summary xii

Acronyms xiii

1.0 Introduction 1

2.0 Objectives 1

3.0 Summary of Previous Program on Strain-Based Design Guidance 2

4.0 Softening of Girth Weld HAZs 2
4.1 Literature Survey 3
4.1.1 HAZ Softening – General Metallurgy 3
4.1.2 HAZ Softening – Base Metal Chemistries 4
4.1.3 HAZ Softening – Weld Procedure Effects 5
4.1.4 HAZ – Testing 6
4.1.5 Testing Results 7
4.1.5.1 Specifics for X-70 and Lower Strength 7
4.1.5.2 Specifics for X-80 8
4.1.5.3 Specifics for X-100 and Higher Strength 9
4.2 Testing of Softened Region Extent in X-100 Plate Using Hardness 12
4.2.1 X-100 HAZ Softening – Hardness Results 12
4.2.2 Interpretation of HAZ Hardness Traverses in X-100 Plate Welds 13
4.3 Testing of Softened Region Properties Using X-100 Pipe as Base Metal 14
4.3.1 Weld 1 15
4.3.2 Weld 2a – Dual Torch 16
4.3.3 Weld 2b – Tandem 18
4.4 Summary 19

5.0 Loading Mode Effects on Strain Concentration at Girth Welds 19
5.1 Finite-Element Models 20
5.2 Conclusions 21

6.0 Strain Concentrations at Girth Welds 21
6.1 Effect of Softened HAZ Width on 10-mm (0.39-in.)-Thick Pipe 21
6.2 Effect of Weld Metal Strength on 10-mm (0.39-in.)-Thick Pipe 23
6.3 Effect of Pipe Thickness 23
6.4 Effect of Lower Internal Pressure 24
6.5 Strains in the HAZ 25
6.6 Strains in the Weld Metal 26
6.7 Peak Strain Concentrations 26

Contents (Continued)

Page

7.0 Strain Concentrations at Girth Welds Using Finer-Grained Material Models 27
7.1 Model Assumptions 28
7.1.1 Material Stress-Strain Properties 28
7.2 Effects of Pressure and 4% Axial Strain 29
7.3 Constraint as a Function of Internal Pressure 31
7.3.1 Constraint Descriptions 31
7.3.2 Hoop Stress 32
7.3.3 Ductile Failure Parameters 33
7.4 Effect of Weld Misalignment Due to Ovality 34
7.4.1 Ovality for X-100 Pipe 34
7.4.2 Ovality for X-65 Pipe 36
7.4.3 Estimating Effects of Ovality 36

8.0 Strain Concentrations in Specific X-65 Pipes 37

9.0 An Estimating Tool for Full-Thickness Shear Bands 39
9.1 An Estimating Tool That Includes Root Flaws 41

10.0 Constraint Effects of Pressure and Axial Loading 42
10.1 Constraint Effects on Previous Fracture Measurements 42
10.2 Constraint Parameters 43
10.3 Elastic Model Results 44
10.4 Plastic Model Results 45
10.4.1 J-Q Calculations 47
10.5 Conclusions 48

11.0 ECA Methods for Strain-Based Design of Girth Welds 48
11.1 Basic Methods 49
11.2 Inputs to the Assessment 49
11.2.1 Toughness 49
11.2.2 Flaw Size, Position, and Type 50
11.2.3 Strength 50
11.3 Failure Assessment Diagram (FAD) Choice 51
11.3.1 Non-FAD Methods 52
11.4 Applied Strains 52
11.4.1 Variation of Strength and Thus Strain with Position 53
11.4.2 Welding Residual Stress or Strain 53
11.4.3 Geometrical Strain Concentration 54
11.4.4 Applied Stress 55
11.5 Effect of Internal Pressure 55
11.6 Additional Behavior – Crack Growth into Different Material 55
11.7 Additional Behavior – Cyclic Loading 55

Contents (Continued)

Page

12.0 Comparisons to Installed Capacity in High-Strength Steel Pipelines 56

13.0 Path Forward 56
13.1 Institutional Hurdles 57
13.2 Technical Hurdles 58

14. 0 Conclusions 59

15. 0 References 60

Appendix A - Guidance Document on Strain-Based Design

Tables

Table 1. Laing et al.[14] Vickers 10 kg Hardness Data for 1980s and 1990s Vintage X-80 64

Table 2. Summary of Welding Procedures 64

Table 3. Summary of HV 1-kg Hardness Data Compiled from Hardness Traverses in the Weld Metal and HAZ on X-100 Plate 65

Table 4. Hammond et al.[19] Hardness (HV 10 kg) Results for X-100 Welds 66

Table 5. Summary of Welding Procedures 67

Table 6. Summary of HV 1-kg Hardness Data Compiled from Hardness Traverses in the Weld Metal and HAZ on X-100 Plate 67

Table 7 Base Pipe Tensile Testing Results Adjacent to Weld W1 68

Table 9. Microtensile Testing Results for Weld W1 69

Table 10. Base Metal Chemistry for Pipe Adjacent to Welds 2a and 2b 69

Table 11. Base Metal Tensile Testing Results for Welds 2a and 2b as Provided by Supplier Company 70

Table 12. Weld Metal Tensile Testing Results for Weld 2a as Provided by Supplier Company 70

Table 13. Weld Metal Stub Tensile Data for Weld 2a 71

Table 14. Microtensile Testing Results for Weld W2a 71

Contents (Continued)

Page

Table 15. Weld Metal Tensile Testing Results for Weld W2b as Provided by Supplier Company 72

Table 16. Weld Metal Stub Tensile Data for Weld W2b 72

Table 17. Microtensile Testing Results for Weld W2b 73

Table 18. Peak HAZ Strain Observed at 3 mm (0.12 in.) from Root Under 4% Remote Loading 74

Table 19. HAZ Strain Concentration Observed at 3 mm (0.12 in.) from Root 74

Table 20. Peak Strain at Weld Centerline Observed Under 4% Remote Loading 75

Table 21. Peak Strain Concentration Observed at Weld Centerline 75

Table 22. Peak Strain Observed Under 4% Remote Loading 76

Table 23. X-100 Finer-Grained Model Results for Local Strain at 3 mm from Root 76

Table 24. X-100 Finer-Grained Model Results for Peak Local Strain at Weld Centerline 76

Table 25. X-100 Finer-Grained Model Results for Local Strain at 3 mm (0.12 in.) from the Root with 1.5-mm (0.06-mm) High-Low 77

Table 26. X-100 Finer-Grained Model Results for Peak Local Strain at Weld Centerline with 1.5-mm (0.06-in.) High-Low 77

Table 27. X-100 Finer-Grained Model Results for Local Strain Concentrations at 3 mm (0.12 in.) from the Root Due to 1.5-mm (0.06-in.) High-Low 77

Table 28. X-100 Finer-Grained Model Results for Local Strain Concentrations at 3 mm (0.12 in.) from the Root Due to Internal Pressure for the Case of 1.5-mm (0.06-in.) High-Low 78

Table 29. X-100 Finer-Grained Model Results for Local Strain at 3 mm (0.12 in.) from the Root with 0.75-mm (0.03-in.) High-Low 78

Table 30. X-100 Finer-Grained Model Results for Peak Local Strain at Weld Centerline with 0.75-mm (0.03-in.) High-Low 78

Table 31. X-65 Finer-Grained Model Results for Local Strain at 3 mm (0.12 in.) from the Root with 1.5-mm (0.06-in.) High-Low 79

Table 32. X-65 Finer-Grained Model Results for Peak Local Strain at Weld Centerline with 1.5-mm (0.06-in.) High-Low 79

Table 33. Examples of Pressurized Pipelines of X-80 and Higher Strength 80

Contents (Continued)

Page

Figure 1. HAZ Regions in a Multipass Weld 81

Figure 2. Example Regions in a Multipass Weld Where Structure is Affected by Multiple Heating Cycles 82

Figure 3. Widgery Hardness Conversion 83

Figure 4. Tokyo Gas Example of Softening Adjacent to Girth Weld in X-80 84

Figure 5. Procedure Description for W11 85

Figure 6. Extended Hardness Traverse for Weld W1 in X-100 Plate 86

Figure 7. Extended Hardness Traverses for Weld W3 in X-100 Plate 87

Figure 8. Extended Hardness Traverses for Weld W7 in X-100 Plate 88

Figure 9. Extended Hardness Traverses for Weld W8 in X-100 Plate 89

Figure 10. Extended Hardness Traverses for Weld W10 in X-100 Plate 90

Figure 11. Average Hardness Values by Position in HAZs of X-100 Plate for Welds W1, W3, W7, W8, and W10 91

Figure 12. Design of Stub Tensile Specimen 92

Figure 13. Examples of Microtensile Specimen Before and After Tensile Testing 93

Figure 14. Position of Microtensile Specimens 94

Figure 15. Cross Section of Weld W1 in 914-mm (36-in.)-Diameter Pipe 95

Figure 16. Base Metal Stress-Strain Properties for Pipe Adjacent to Weld W1 96

Figure 17. Stress-Strain Curves for Stub Tensile Specimens for Weld W1 97

Figure 18. Microtensile Test Results for Weld W1 98

Figure 19. Hardness Matrix for Girth Weld W1 99

Figure 20. Cross Section of Dual Torch Weld W2a 100

Figure 21. Base Metal Tensile Test Results Adjacent to Weld W2a 101

Figure 22. Stub Tensile Results for Dual Torch Weld W2a 102

Figure 23. Microtensile Results for Dual Torch Weld W2a 103

Figure 24. Hardness Map for Dual Torch Weld W2a 104

Contents (Continued)

Page

Figure 25. Cross Section of Tandem Weld W2b 105

Figure 26. Base Metal Tensile Test Results Adjacent to Tandem Weld W2b 106

Figure 27. Stub Tensile Results for Tandem Weld W2b 107

Figure 28. Microtensile Results for Tandem Weld W2b 108

Figure 29. Hardness Map for Tandem Weld W2b 109

Figure 30. Drawing, 2D, and 3D Mesh for Finite-Element Modeling Assessment with Weld on Right 110

Figure 31. Stress-Strain Curves for Assessment of Loading Type Effect 111

Figure 32. Strain Distribution Under Tension Loading to 6% Remote Strain 112

Figure 33. Strain Distribution Under Bending Loading to 6% Remote Strain 113

Figure 34. Strain Distribution Under Combination Loading to 6% Remote Strain 114

Figure 35. Local Strain Distribution at Weld Under Tension Loading 115

Figure 36. Local Strain Distribution at Tension Side of Weld Under Bending Loading 116

Figure 37. Local Strain Distribution at Peak Tension Side of Weld Under Combination Loading 117

Figure 38. Two-Dimensional Model With Softened Zone Width About 2 mm (0.08 in.) 118

Figure 39. Two-Dimensional Model With Softened Zone Width About 3 mm (0.12 in.) 118

Figure 40. Two-Dimensional Model With Softened Zone Width About 4 mm (0.16 in.) 119

Figure 41. Two-Dimensional Model With Softened Zone Width About 7.5 mm (0.30 in.) 119

Figure 42. Stress-Strain Curves for Three-Material Model 120

Figure 43. von Mises Stress for Axial Strain of 4% and No Internal Pressure 121

Figure 44. Axial Strain for Remote Axial Strain of 4% and No Internal Pressure 122

Figure 45. Equivalent Plastic Strain for 4% Remote Strain and No Internal Pressure 123

Figure 46. von Mises Stress for 4% Remote Axial Strain and 6.43-MPa (933-psi) Internal Pressure 124

Contents (Continued)

Page

Figure 47. Axial Strain for 4% Remote Axial Strain and 6.43-MPa (933-psi) Internal Pressure 125

Figure 48. Equivalent Plastic Strain for 4% Axial Remote Strain and 6.43-MPa (933-psi) Internal Pressure 126

Figure 49. von Mises Stress for 4% Axial Strain and 6.43-MPa (933-psi) Internal Pressure, Weaker Weld Metal 127

Figure 50. Axial Strain for 4% Remote Strain and 6.43-MPa (933-psi) Internal Pressure, Weaker Weld Metal 128

Figure 51. Plastic Equivalent Strain for 4% Remote Strain and 6.43-MPa (933-psi) Internal Pressure, Weaker Weld Metal 129

Figure 52. HAZ Models for 20-mm (0.79 in.)-Thick Pipe 130

Figure 53. von Mises Stresses for 4% Remote Strain and 12.86-MPa (1866-psi) Internal Pressure, 20-mm (0.79-in.) Pipe 131

Figure 54. Axial Strains for 4% Remote Strain and 12.86-MPa (1866-psi) Internal Pressure, 20-mm (0.79-in.) Pipe. 132

Figure 55. Equivalent Plastic Strains for 4% Remote Strain and 12.86-MPa (1866-psi) Internal Pressure, 20-mm (0.79-in.) Pipe 133

Figure 56. von Mises Stresses for 4% Remote Strain and 3.125-MPa (453-psi) Internal Pressure, 10-mm (0.39-in) Pipe 134

Figure 57. Axial Strains for 4% Remote Strain and 3.125-MPa (453-psi) Internal Pressure, 10-mm (0.39-in.) Pipe 135

Figure 58. Equivalent Plastic Strains for 4% Remote Strain and 3.125-MPa (453-psi) Internal Pressure, 10-mm (0.39-in.) Pipe 136

Figure 59. von Mises Stresses for 4% Remote Strain and 3.125-MPa (453-psi) Internal Pressure, Weaker Weld Metal 137

Figure 60. Axial Strains for 4% Remote Strain and 3.125-MPa (453-psi) Internal Pressure, Weaker Weld Metal 138

Figure 61. Equivalent Plastic Strains for 4% Remote Strain and 3.125-MPa (453-psi) Internal Pressure, Weaker Weld Metal 139

Figure 62. von Mises Stress for 4% Axial Strain and 6.43-MPa (933-psi) Internal Pressure, 20-mm (0.79-in.) Pipe 140

Contents (Continued)

Page

Figure 63. Axial Strain for 4% Remote Strain and 6.43-MPa (933-psi) Internal Pressure, 20-mm (0.79-in.) Pipe 141

Figure 64. Equivalent Plastic Strain for 4% Remote Strain and 6.43-MPa (933-psi) Internal Pressure, 20-mm (0.79-in.) Pipe 142

Figure 65. Material Regions in the Pipe Model Used With the Finer-Grained Material Model 143

Figure 66. Ramberg-Osgood Stress-Strain Curves Fitted to Microtensile Data from Weld W1 144

Figure 67. Stress-Strain Curves Used for Finer-Grained Model 145

Figure 68. True-Stress/True-Strain Curves for the Materials in X-100 Model 146

Figure 69. Axial Strain for Isotropic Case with 4% Remote Strain 147

Figure 70. Axial Strain for Orthotropic Case with 4% Remote Strain 148

Figure 71. Axial Strain for Base Metal Orthotropic Case with 4% Remote Strain 149

Figure 72. Hoop Stress in MPa for Isotropic Case with 4% Remote Strain 150

Figure 73. Hoop Stress in MPa for Orthotropic Case with 4% Remote Strain 151

Figure 74. Hoop Stress in MPa for Base Metal Orthotropic Case with 4% Remote Strain 152

Figure 75. Stress Triaxiality Map for Isotropic Case with 4% Remote Strain 153

Figure 76. Stress Triaxiality Map for Base Metal Orthotropic Case with 4% Remote Strain 154

Figure 77. Levels of High-Low Misalignment Modeled in this Project 155

Figure 78. Model Configuration for Examination of High-Low at 1.5-mm (0.06-in.) Maximum High-Low 156

Figure 79. Axial Strain Around Girth Weld at 1.5-mm (0.06-in.) Maximum High-Low (Base Metal Orthotropic Case) 157

Figure 80. Model Configuration for Examination of High-Low at 0.75-mm (0.03-in.) Maximum High-Low 158

Figure 81. Axial Strain Around Girth Weld at 0.75-mm (0.03-in.) Maximum High-Low for X-100 (Base Metal Orthotropic Case) 159

Contents (Continued)

Page

Figure 82. Stress-Strain Curves for X-65 Material Derived from Kim et al.[8] Microtensile Tests 160

Figure 83. Axial Strain Around Area of Peak Misalignment of 1.5 mm (0.06 in.) in X-65 Girth Weld Region 161

Figure 84. Model Configuration for Models of X-65 Pipes 162

Figure 85. True-Stress/True-Strain Curves for X-65 Pipe Materials and Welds Areas 163

Figure 86. Axial Strain Distributions for Girth Welds in X-65 164

Figure 87. Axial Strain Distributions for Overmatched Welds in X-65 Pipes 165

Figure 88. Axial Strain Distributions for X-65 Pipes with Lower Yield-to-Tensile 166

Figure 89. Schematic of Weld Showing 45-Degree Shear Band Positions 167

Figure 90. Diagram of Cases Where Full-Thickness Shear Bands in HAZ can be Expected 168

Figure 91. Diagram of Cases Where Full Thickness Shear Bands in Weak Material can be Expected at Undermatched Girth Welds 169

Figure 92. Schematic of Weld with Root Flaw Showing Shear Band Positions 170

Figure 93. Diagram of Cases where Shear Bands from a 3-mm (0.12-in.)-Deep Root Flaw can be Expected 171

Figure 94. Diagram of Cases where Shear Bands in Weak Material can be Expected from a 3-mm (0.12-in.)-Deep Root Flaw in an Undermatched Weld 172

Figure 95. Hydrostatic Stress Distribution Around Crack Tip with Specific Values 173

Figure 96. Geometry for Model of Cracked Cylinder 174

Figure 97. Elastic Results for J vs. Normalized T-Stress 175

Figure 98. Stress Strain Curve for Plastic Constraint Models 176

Figure 99. Hydrostatic Stress in MPa Around Crack Tip for Axial Strain of 0.1% 177

Figure 100. Hydrostatic Stress in MPa Around Crack Tip for Pressure with Ends Held Fixed 177

Figure 101. Hydrostatic Stress in MPa Around Crack Tip for Axial Strain Followed by Pressure 178

Contents (Continued)

Page

Figure 102. Hydrostatic Stress in MPa Around Crack Tip for Pressure Followed by Axial Strain....178

Figure 103. J Progression as Either Internal Pressure of 0.1% Remote Strain is Applied First Followed by the Other....179

Figure 104. J Progression as Either Internal Pressure or 4% Remote Strain is Applied First Followed by the Other....180

Figure 105. Axial Stress in MPa for Axial Strain to 4%....181

Figure 106. Hydrostatic Stress in MPa for Axial Strain to 4%....182

Figure 107. Axial Stress in MPa for Pressure and 4% Axial Strain....183

Figure 108. Hydrostatic Stress in MPa for Pressure and Axial Strain....184

Figure 109. Finite-Element Model of Crack Tip in Infinite Body for Q Calculation....185

Figure 110. J and Q as a Function of Applied Strain for Pressure and No Pressure Cases....185

Figure 111. Q as a Function of J for Pressure and No Pressure Cases....186

Figure 112. J and Q_h as a Function of Applied Strain for Pressure and No Pressure Cases....187

Figure 113. Q_h as a Function of J for Pressure and No Pressure Cases....188

Figure 114. J and Q for Double Size Model....189

Figure 115. J and Q_h for Double Size Model....190

Strain-Based Design: Strain Concentration at Girth Welds

Executive Summary

This program aimed to improve guidelines for strain-based design of pipelines by studying cases with combinations of internal pressure and axial plastic strain in tension. Softened heat-affected zone (HAZ) regions have been observed to concentrate strain, particularly under internal pressure.

HAZ softening has been observed for welds on X-70 and X-80 steels. Cases with little or no softening have also been observed for other welds in these same grades. This project extended these findings to X-100 steels, with cases of obvious softening and little or no softening observed. Higher heat inputs and larger weld volumes per pass associated with submerged arc welding (SAW) as compared to gas metal arc welding (GMAW) have been correlated with greater softening in each of these pipe grades.

Finite-element modeling of girth welds was used to learn the relative effects of overall loading mode, HAZ thickness, weld metal strength, and pipe wall thickness. While strain may be severely concentrated in some cases, most cases did not show large increases in strain in the HAZ even with 10% lower tensile properties in the HAZ than in the base metal. The cases of severe strain concentration showed shear bands forming at 45 degrees to the radial direction along the internal weld toe and extending in regions of lower mechanical strength than the base metal. These bands may go away from the weld centerline or toward the weld centerline so that they cross in the weld metal.

Models more representative of real welds in X-100 and in X-65 did not show high strain concentrations. These models included stress-strain relations and HAZ widths based on local mechanical testing. Some checks of strain concentration with high-low misalignment were also made using these material models.

Internal pressure in the pipe tends to increase the applied J or crack-tip opening displacement (CTOD) for a crack in a zone with plastic axial strain compared to cases without internal pressure. It was found that this increase is not correlated to an increase in constraint. If constraint is high, as in standard fracture toughness specimens, deformation tends to be localized around the crack tip. For lower constraint cases, the deformation is less localized, perhaps with more deformation of a nearby free surface.

Acronyms

Coarse-grained HAZ	CGHAZ
Crack-tip-opening displacement	CTOD
Digital image correlation	DIC
Engineering-critical assessment	ECA
Failure assessment diagram	FAD
Fusion line	FL
Gas metal arc welding	GMAW
Grain-refined HAZ	GRHAZ
Heat-affected zone (HAZ)	HAZ
Inter-critically reheated HAZ	ICHAZ
Shielded arc welding	SAW
Single-edge notched tension	SENT
Standard Minimum Yield Strength	SMYS
Stress concentration factor	SCF
Sub-critically reheated HAZ	SCHAZ
Weld center line	WCL

1.0 Introduction

Strain-based design is used for many situations for pipelines where the loadings from forces other than the internal pressure can be the largest generators of stress and strain in the pipe wall. Such loadings can be generated by soil subsidence, frost heave, thermal expansion and contraction, landslides, pipe reeling, pipe laying, and several other types of environmental loading. Designing based on strain for these cases has an advantage over designing based on stress because these loadings tend to apply a given displacement rather than a given force to the pipe.

Standards are much better developed for stress-based design than for strain-based design. While several standards are available that have some coverage of strain-based design, there is a tendency to cover only limited types of loading, as in API RP 1111 for offshore pipe laying.

This program has been designed to provide information to improve the general guidance particularly for pipelines with axial tensile loadings in combination with internal pressure.

2.0 Objectives

Provide improved guidance on strain-based design of pipelines related to the tensile strain capacity of girth welded areas.

Provide methods of assessing regions of lower strength in the heat-affected zone (HAZ) of pipeline girth welds.

The original objectives for this program were reconfigured in consultation with the sponsors and industry representatives. The original objectives were as follows:

“The major objective of the proposed project is to develop design and assessment guidelines for pipelines that may experience high strains in service. The guidelines will include:

- Recommended pipeline material specifications to minimize strain localization (soft HAZ)
- Recommended welding specifications to minimize strain localization at pipeline girth welds
- Recommended engineering critical assessment (ECA) and validation test methods to verify pipeline performance.”

These original objectives were modified based on findings within the project that other methods than material specification limits or welding procedure designation could be used to minimize strain concentration. The ECA objective was modified based on the need for a more extensive testing program to achieve this goal than could be contained in this program and other currently active programs on modeling and testing for strain-based ECA.

3.0 Summary of Previous Program on Strain-Based Design Guidance

During the previous program funded by the Minerals Management Service and the Department of Transportation Office of Pipeline Safety, Mohr[1] reviewed the available information on strain-based design of pipelines and used that information to create a summary guidance document.

Two areas were the focus of additional reviews. The first was the supporting data for the allowable compressive strains as they accounted for pipe size, girth welding, and internal and external pressure. These were found to provide good support to the standard provisions, which could be improved by some relatively minor modifications related to pressure effects. The second was the combination of tension strains, internal pressure, and regions of lower strength. These combinations were observed in a limited number of finite-element models to give high local strains in the region of lower strength.

The finding of a pressure effect on local strain concentration was sufficiently unexpected that additional modeling and a model test on girth-welded aluminum tubes were conducted. Each of these confirmed that strain concentrations were higher in the cases with internal pressure, although the overall failure strain in the aluminum tube test was not found to be a strong function of pressure.

The guidance document produced at the end of this previous project left the question of the assessment of tensile strain capacity with limited guidance. It was recognized that regions of lower strength around girth welds were possible and the concentrations of strain in these regions could be made more severe with internal pressure. However, the definition of cases where these behaviors would affect the overall strain capacity was not complete.

4.0 Softening of Girth Weld HAZs

A survey of the literature on the formation of softened regions in the HAZ of steel pipeline girth welds was performed, extended with two experimental studies. The first study used hardness measurements on existing weld cross sections from simulated girth welds in X-100 plate

sections. The second study used small-scale tensile specimens and hardness measurements to determine the local mechanical properties of regions of the HAZ of girth welds in X-100 pipe.

4.1 Literature Survey

This literature survey is focused on the softening potential of regions of the HAZ. Much of the existing literature describes efforts to avoid excessive hardening of the HAZ or efforts to design in additional HAZ toughness. These areas are not addressed in any detail here.

4.1.1 HAZ Softening – General Metallurgy

HAZs have been one of the main areas of testing for new welding procedures and for new pipeline steels, particularly for the high-strength grades now coming into use, X-80, X-100, and on to X-120. In these regions the original chemistry of the base pipe is retained, but the heating from welding modifies the microstructure and the properties that are dependent on microstructure. HAZ testing has also been an important component of testing of more common pipe grades and their welding procedures, although the testing has primarily been focused on areas of hardening rather than softening and HAZ toughness.

The HAZ must also be considered as a group of regions, because the heating history will be different depending on the distance of a particular location from each weld pass. Welds, because they have been heated to steel melting over a local area, generally cool more quickly than a large piece of steel heated to the same temperature. For a single weld pass, we can simply compare the transformation temperatures with the temperatures reached at the location of interest. Close to the weld, the microstructure is transformed to austenite and the austenite grains can grow during the time the welding heat is applied. Thus, a region adjacent to the fusion line, the coarse-grained HAZ (CGHAZ) is expected to have larger grains than other areas of the HAZ. The next zone further out has grains that have transformed to austenite and then re-transformed on cooling with only a small amount of grain growth. This is the grain-refined HAZ (GRHAZ). Slightly further from the weld, only part of the structure transforms to austenite during the heating. This area is in the inter-critical temperature range. Thus, the area of the inter-critically reheated HAZ (ICHAZ) will have grain sizes mostly controlled by the previous structure of the steel, but will have some transformed components. Beyond the ICHAZ, the steel has not reached the temperature where the austenite transformation begins. This sub-critically reheated HAZ (SCHAZ) has little visible sign of heating, although some effects can be observed on the microscopic constituents of the structure. These regions are shown in Figure 1.

When multiple weld passes are used, some regions can have more than one pass close enough to heat the location to the critical temperature for austenite transformation. Particular microstructures can be formed, for instance, by the combination of region in the CGHAZ of the first pass that is in the ICHAZ of the second pass. These regions are shown in Figure 2.

As pipeline steels are designed for higher and higher yield strength, strengthening methods are applied that may not be tolerant of the heating in the HAZ. For instance, precipitates may be used to pin grain boundaries and dislocations. Both of these actions prevent deformation and thus increase yield strength. These precipitates will be most effective at a particular size. The heating from welding can change the size of the precipitates so that they no longer function to give improved strength. Another method to achieve higher base metal strength is creating small or oriented grains. This is obviously disrupted in the CGHAZ and ICHAZ.

4.1.2 HAZ Softening – Base Metal Chemistries

The base metals of high-strength pipes can be more or less sensitive to HAZ softening based upon the chemistry chosen. This section aims to provide some guidance on the types of chemistries that are more or less sensitive to HAZ softening.

In general, the higher the target strength of the base metal, the higher is the chance that the HAZ will be relatively softened. In simple terms, as more and more mechanisms are used to strengthen the pipe body, some of these are likely to be disrupted by the welding heat without other corresponding increases in strength from changes of the microstructures.

Strengthening mechanisms that rely on high dislocation density or on small grain size can be particularly affected by the heat of welding. Strengthening mechanisms that rely on solid-solution alloying elements and phases stable at the temperatures induced by welding will be much less affected.

Toughness control for the HAZ has been an important issue for pipe makers. This has led to microalloying additions specific to affecting the HAZ microstructure. A particular focus of effort has been the CGHAZ, where limits on the grain growth and the adding of nucleation sites for ferrite are desired. Microalloying with Ti has been used, so that oxide, nitride, carbide, or combination precipitates can be used to both limit grain size of austenite and have many locations for nucleation of new phases on cooling. Other alloying elements such as Mg have been used to further reduce the final grain size in the CGHAZ.

A steel design has been proposed by Hukla et al.[2] for X-80 that explicitly considered softening of the HAZ as an effect to be minimized. They specifically wished to avoid excessive softening during the high heat input joining by flash butt welding. The steel design limited carbon to lower values than usual for this grade (~0.03%) while increasing Nb (~0.07-0.10%) and Mn (1.5-2.0%) in combination with tight controls on N and Ti so that TiN would form with little remaining free nitrogen.

A quite different approach to alloy design was described by Lillig et al.[3], whose primary goal was to achieve desired properties, particularly lower yield-to-tensile ratio, in the pipe material in the longitudinal direction after the pipe coating process. They recommended higher stop temperatures for accelerated cooling, in combination with restrictions on amounts of Mo, Cr, Nb, V, Ti, and Cu. The leaner chemistry was designed to provide a ferrite phase with low supersaturation of carbon in addition to the harder second phase, primarily bainite. To achieve the desired grade level, slightly higher levels of carbon and Mn were suggested. They noted that lower welding heat input may be desirable for reducing HAZ softening.

4.1.3 HAZ Softening – Weld Procedure Effects

The weld only communicates a heating cycle to the HAZ. The part of the cycle as the heat increases is not understood to have a large effect upon the HAZ, but two parameters related to cooling, the peak temperature and the cooling rate from 800 to 500°C, are widely recognized as important parameters.

The welding procedure can affect the peak temperature and the cooling rate independently based on changes in heat input and travel speed.

Welding practices designed to limit the size of the visible HAZ can also be used to limit the affected volume of HAZ and the amount of any softening. These practices include minimizing pre-heat and inter-pass temperatures, choosing a smooth bevel, making fewer beads per layer, limiting the individual pass thickness, and choosing low heat input procedures.

Multipass welds tend to have the tempering effects of the subsequent adjacent weld passes add up for HAZ areas. Much less tempering can occur at the cap where the HAZ may not be re-heated after it reaches its peak temperature. The result is that the root side HAZ strength and hardness are lower than in the HAZ at the cap, even at the same distance from the fusion line. This general tempering effect can also widen the soft zone at the root side compared to the cap side.

A limited number of comparisons of multiple welding procedures on the same base pipe material have been published that discuss HAZ softening. Kim et al.[4] examined welding of X-80 at two heat input levels, 1.12-kJ/mm (28.4-kJ/in) and 2.7-kJ/mm (69-kJ/in), with HAZ softening only observed at the higher heat input. Johnson [5] examined several procedures on X-100 plate with 15 procedures to model girth welding procedures. The welding procedures are described in Table 2. The welding procedure was more complicated for Weld W11. The procedure record sheet for that weld is shown in Figure 5. Higher heat input welding was generally correlated with lower minimum HAZ hardness, such as when W4 and W6 have softer areas than W5 and the SMA weld has among the lowest minimum HAZ hardness. The greater variability of the HV 1 kg measurements compared to HV 10 kg measurements used by other investigators may be playing a role in the complexity of finding trends within this data set related to preheat or travel speed.

4.1.4 HAZ – Testing

The thin regions of the HAZ make determination of the mechanical properties specific to the HAZ problematic. This section discusses the different methods of determination of mechanical properties.

The primary method of demonstrating the range of mechanical properties through the HAZ is by hardness testing of weld cross sections. Microhardness measurement allows a parameter related to strength to be determined at many locations within the HAZ. Softening or hardening of areas in the HAZ is often judged only on microhardness values. Vickers microhardness tests can be performed with several different loading forces, such as 0.1, 0.5, 1, and 10 kgf (0.22, 1.1, 2.2, and 22 lbf). For a larger load a larger volume of material is tested. This tends to average over the microstructure under an individual indent and reduce the variability of the reported hardness between indents. Smaller loads are used during traverses or maps to better understand local variability of hardness without having adjacent indentations interact.

The hardness change is correlated with changes in the strength, but the hardness is more strongly related to the tensile strength than to the yield strength. Figure 3 shows a correlation developed for weld metal and published by D. J. Widgery.[6] This indicates a rough estimate that each 10 HV 10 points that the hardness goes down correlates to about 22 MPa (3.2 ksi) of reduction in yield and tensile strength. Statistical correlation bands are not available in the original publication.

Transverse tensile tests can give some indication of the strength of the HAZ, but the support of adjacent stronger zones can change the results drastically, even moving the failure away from

an area of the HAZ with lower tensile strength than adjacent areas. This is still true of transverse tensile tests where the reduced section region is limited to HAZ material. Adeeb et al.[7] used a system that determined local strains on the surface of the HAZ by following changes in the painted external surface.

Sub-size longitudinal tensile tests can be used to give full stress-strain curves for the material in the HAZ. These tests must involve very small amounts of material if a narrow HAZ or a particular zone of the HAZ is the object of the testing. Kim et al.[8] have used 2-mm × 0.5-mm (0.08-in. × 0.02-in.) cross sections for their microtensile specimens.

Tensile tests of simulated HAZ material might also be used to determine the stress-strain curves. The Gleeble weld thermal simulator might be used to create microstructures that correspond to a particular thermal history.

4.1.5 Testing Results

4.1.5.1 Specifics for X-70 and Lower Strength

For low-strength pipes, the HAZ hardness usually increases compared to the base metal. In many cases efforts to limit this increase have been undertaken to help prevent local corrosion or corrosion cracking of the HAZ.

Studies of the distribution of hardness in the HAZ and the effects of welding procedures have been performed quite exhaustively by many researchers (see for instance Düren and Niederhoff).[9] These have most often been interested in surface hardness and peaks in hardness rather than softening. Baek et al.[10] discussed the HAZ hardness in 17.5-mm (0.69-in.) thick X-65 welded with a variety of processes. They primarily showed that the HAZ hardness did not exceed 248 HV. The results were also described with minimum values of HV in the HAZ at the same level as in the base metal.

Kim et al.[8] performed extensive characterization of the stress-strain curves of HAZ material in one X-65 girth weld. They used microtensile specimens (2-mm × 0.5-mm cross section) to measure stress-strain curves at a series of locations near mid-thickness. The pipe was 762-mm (30.0-in.) diameter 17.5-mm (0.69-in.) wall X-65 with a yield plateau to 2% plastic strain. A region of slightly lowered stress-strain curves was observed between 8 and 13 mm (0.31 and 0.51 in.) from the weld center. The difference in tensile strength was 30 MPa (4.4 ksi) from 500 MPa (72.5 ksi) in the softened region to 530 MPa (76.9 ksi) in the base metal. The difference in yield strength was smaller, less than 20 MPa (2.9 ksi), but the yield plateau was longer in the

HAZ, extending to 3.5% plastic strain. The overall strength of the base metal would be higher, since the pipe surfaces showed slightly higher strength than the mid-thickness. Hardness measurements taken nearby indicated a slight softening from 212 HV 0.5 to 202 HV 0.5. The region of lower hardness tended to be further from the fusion line by about 2 mm (0.08 in.) than the region of lower tensile strength. There was also slightly more variability in the hardness results than would appear to be indicated by the microtensile results. Some features observed on the microtensile tests such as the extended yield plateau may relate to the small sample size providing less property variation within the sample than would be found in a larger scale specimen.

Ishikawa et al.[11] observed some HAZ softening adjacent to double submerged arc welding (DSAW) seam welds in 29-mm (1.14-in.) thick X-70. The hoop direction strengths of the pipe material were given as 495 MPa (72.8 ksi) yield and 620 MPa (89.9 ksi) tensile. The average base metal hardness was given as 198 HV 10, while the average hardness in the GRHAZ and ICHAZ was 178 HV 10. They correlated this change to a drop in yield and ultimate strength of about 50 MPa (7.3 ksi) in 4-mm (0.16-in.) wide regions on either side of the seam weld. Their hardness plot indicated a shallow gradient in hardness at the outer edge of the HAZ, transitioning to the hardness of the remote base metal.

4.1.5.2 Specifics for X-80

Tokyo Gas[12] has reported the softening of the HAZ of an example X-80 girth weld. Hardness traverses were taken near the root and near the cap. They report a drop of about 30 HV 10 compared to the base metal over about 4 mm (0.16 in.) in the visible and SCHAZ. The hardness is slightly lower at the root and the HAZ is slightly wider, mostly due to the root bead size. The hardness results for these root and cap traverses are shown in Figure 4.

Ishikawa et al.[13] have reported the hardness distribution for an X-80 pipe with a relatively low ratio of yield-to-tensile strength (62%). Gas metal arc welding (GMAW) was used with heat input of 0.46 kJ/mm (11.7 kJ/in.) for the root pass and about 1 kJ/mm (25.4 kJ/in.) for the fill and cap passes. The weld metal was slightly overmatched compared to the X-80 pipe. The zone of softening in the HAZ was about 5-mm (0.2-in.) wide with a reduction compared to the base metal hardness (HV 10) of 18%. The HAZ was wider at the root than at mid-thickness or the cap. Minimal softening of the HAZ was observed at mid-thickness.

Laing et al.[14] reported very limited reductions in hardness in the HAZ for three different weld procedures applied to three different X-80 pipes: a Japanese pipe at 10.6-mm (0.42-in.) wall (Pipe A), a German pipe at 18.3-mm (0.72 in.) wall (Pipe B), and a Canadian spiral-welded pipe

at 12.1-mm (0.48-in.) thick (Pipe C). Table 1 shows the HV 10 hardness ranges recorded for the weld, HAZ, and base metal on polished cross-sections. Generally the ranges for the HAZ are not much below that for the base metal, although the base metal ranges are rather large (in one case greater than 40 HV 10). It may be that the base metal values include some measurements from the SCHAZ.

As part of the report of testing of ultra low-cycle fatigue testing of girth-welded X-80, Kawanishi et al.[15] described three welds that were made with differing HAZ hardness. One weld was described as having no softened region, one had a 6-mm-(0.24-in.)-wide softened region with a hardness drop of 30 HV, and one had a 10-mm-(0.39-in.)-wide softened region with a hardness drop of 50 HV.

Kim et al.[4] reported HAZ hardness traverses for both SAW and gas metal arc welding (GMAW) butt welds in plates that simulated long seam and girth welds in pipe. No HAZ softening was observed for the GMAW weld with 1.12-kJ/mm (28.4-kJ/in.) heat input, while some softening was observed on the two-pass SAW weld with heat input of 2.7-kJ/mm (69-kJ/in) per pass. The maximum softening of about 25 HV 10 kg was observed between 2 and 3 mm (0.08 and 0.12 in.) from the fusion line. The plate material was limited to 0.07%C with higher Mn (1.78%) and Mo (0.24%) than in some other versions of X-80.

Huang et al.[16] reported hardness at mid thickness for a SAW seam weld in X-80 plate. The X-80 plate was a low carbon material (0.04%). Hardness was reduced from the base metal average of 226 HV 10 to about 210 HV 10 in 3-mm (0.12-in.)-wide HAZ bands. The paper described procedures in 16-mm (0.63-in.) and 17.5-mm (0.69-in.) plate with 1.4 kJ/mm (36 kJ/in.) and 2.4 kJ/mm (61 kJ/in.) heat inputs, but the hardness traverse results are not matched to a particular procedure.

Hamad et al.[17] performed limited hardness checks on girth welds areas for SAW girth welds in X-80 pipe. The average hardness for 12 locations measured in the HAZ was 235 HV 10, slightly smaller than the average hardness in the base metal of 246 HV 10. The welds were four pass welds with about 1.55 kJ/mm (39.4 kJ/in.) per pass. The largest HAZ hardness values were observed adjacent to the cap passes.

4.1.5.3 Specifics for X-100 and Higher Strength

EWI[5] examined the hardness of HAZs for a variety of welding procedures for X-100 in a program for PRCI.

"Second Generation" X-100 base plate, from about the year 2000, was used for the experiments. The thickness of the base material supplied to EWI was 20 mm (0.79 in.). The bulk composition of the base metal is 0.058C-1.9Mn-0.15Ni-0.17Mo-0.24Cu with the addition of Ti. Unlike some X-80 steels that contain significant quantities of microalloying elements, the additions of Al (0.040 wt%), V (0.040 wt%), Ti (0.010 wt%), and Nb (0.030 wt%) were small.

The welding procedures are described in Table 2. The welding procedure was more complicated for Weld W11. The procedure record sheet for that weld is shown in Figure 5.

The hardness test results are summarized in Table 3. Microhardness traverses across the weld fusion line at the near surface location [0.75 mm (0.03 in.) below the surface], mid-thickness location, and in the weld root [0.75 mm (0.03 in.) above the bottom of the plate] were produced. The hardness of the ER120S-1 weld metal is consistent with the maximum hardness of martensite in steel with carbon content of 0.11 wt%, although the microstructure includes both martensite and ferrite. Slightly lower hardness is observed in the root and mid-thickness locations due to tempering of the weld metal during multipass welding. Hardness in the E100S-1, E110C-G, and E10018 weld metals also decreased in the mid-thickness and root locations. The maximum hardness measured in these weld metals was ~300-305 VHN and hardness decreased to ~260 VHN in the root and mid-thickness locations.

Consistent with the base metal carbon concentrations, peak hardness measured in the HAZ rarely exceeded 300 VHN. The average hardness of the as-received base metal was 275 VHN. Slight softening (minimum hardness between 218 to 240 VHN) in the SCHAZ regions was observed in all HAZs. The band of softening widened closer to the root to include the other zones of the HAZ. The SCHAZ is also wider at the root as more cycles of heating are applied close to that location. The full width of the band of softening in the SCHAZ was not measured, since the primary area of interest was the visible HAZ (CGHAZ and ICHAZ).

Additional testing was performed on some of these specimens to better characterize the extent of the softened zone. These results are discussed in Section 4.2 below.

Ishikawa et al.[13] have reported a hardness distribution for 15-mm-(0.59-in.)-thick X-100 pipe welded with the same procedure used for the X-80 pipe described above. The micrograph shows the weld deposit to be nearly as wide at the weld root as at the weld cap. The softening in the HAZ was observed over a 5-mm (0.2-in.) width with a peak reduction in hardness (HV 10 kg) of about 21%. The weld metal was also slightly lower in hardness than the base metal.

Sumitomo[18] has reported the hardness of the HAZ adjacent to long seams weld in X-100. The reduction of hardness for weld with 3.0-kJ/mm (76-kJ/in.) heat input in 19.1-mm-(0.75-in.)-thick X-100 was over about 5 mm (0.2 in.) from the fusion line with a reduction in hardness of magnitude of about 17%. Other tests showed reductions from 8 to 18%. The DSAW process used for the long seams can be viewed as an upper limit for heating of girth welds.

J. Hammond et al.[19] reported root and cap average hardnesses for HAZs in X-100 welded with several different procedures. These values are given in Table 4. All but three hardness traverses adjacent to base pipe show the average HAZ of the HAZ lower than the base metal. These both were at the cap side and showed 30 HV 10 or more difference between the HAZ average and the HAZ maximum hardness. The hardness reduction at the root was commonly around 10%, but both lower values of 5% and higher values of 17% were observed. Hardnesses were also taken at the area where the girth weld HAZ crosses the pipe longitudinal seam. These areas often had higher hardnesses than the base metal, apparently due to the greater alloy content of the seam weld material. J. Hammond and N. A. Millwood[20] have reported single values of HAZ hardness that are in excess of the adjacent base metal for GMAW joints in X-100 that was delivered in 1995. These results were probably taken in the visible HAZ.

Rajan and Hartman[21] observed some HAZ softening on hardness traverses of butt welds using experimental metal-cored welding consumables. The base metal was 19-mm (0.75-in.) thick X-100 pipe that had been flattened into plate form. Heat inputs were in the range of 0.7 to 0.8 kJ/mm (18 to 20 kJ/in). The pipe material had an average hardness of 280 HV 10, while the HAZs of three welds gave hardnesses between 260 HV 10 and 285 HV 10. All the HAZ hardnesses were measured within 3 mm (0.12 in.) of the fusion line near mid-thickness.

Adeeb et al.[7] used strain measurement during tensile testing to assess the HAZ softening of X-100 welds. The welds were made with mechanized GMAW on 14.3-mm (0.56-in.) wall thickness. The strain measurements using the digital image correlation (DIC) technique indicated softening in the HAZ. The DIC strain measurements indicated concentration of strain early in the test loading, both at yield strain and at 2% longitudinal strain. These were interpreted as a drop in yield strength in this area of about 10 MPa (1.45 ksi). Hardness traverses were performed both with HV 10 kg and HV 200 g near the cap and root and at the 1/3 and 2/3 through thickness positions. However, the spacing was about 12 mm (0.47 in.), too large to capture local variations in HAZ hardness.

It appears that soft zones in X-100 should be expected in the SCHAZ and that other zones of the weld HAZ, particularly away from the cap side may also be softened. The amount of

softening depends both on the base metal microalloying and the heating cycles applied by the welding. The width of the girth weld HAZ softened area may be as little as 1 mm (0.04 in.) at the cap, but values of 3 to 6 mm (0.12 to 0.24 in.) are more common. One reported value of 10 mm (0.39 in.) appears to be excessive.

4.2 Testing of Softened Region Extent in X-100 Plate Using Hardness

EWI has performed additional hardness testing on X-100 weld cross sections on welds previously tested at EWI. These welds, listed in Table 5, are some of the same welds that are listed in the literature survey in Table 2, listed with those weld numbers. The weld process parameters for determining comparative heat input are given. Hardness values previously reported are given in Table 6. The new hardness traverses were designed to examine the extent of the softened zone, the variability of hardness within this zone, and the transition from the softened region to the harder base metal.

As noted above, "Second Generation" X-100 base plate from about 2000 was used for the experiments. The thickness of the base material supplied to EWI was 20 mm (0.79 in.). The bulk composition of the base metal is 0.058C-1.9Mn-0.15Ni-0.17Mo-0.24Cu with the addition of Ti. Unlike some X-80 steels that contain significant quantities of microalloying elements, the additions of Al (0.040 wt%), V (0.040 wt%), Ti (0.010 wt%), and Nb (0.030 wt%) were small. Since it was plate that had not been formed into pipe, the yield and ultimate strengths measured by EWI were lower than those expected for X-100 pipe in the hoop direction. The values perpendicular to the rolling direction were 656 MPa (95.1 ksi) for the yield strength and 821 MPa (119.0 ksi) for the ultimate strength. The values parallel to the rolling direction were 628 MPa (91.1 ksi) for the yield strength and 794 MPa (115.2 ksi) for the ultimate strength.

4.2.1 X-100 HAZ Softening – Hardness Results

Hardness values (HV 1 kg) for the five welds in Table 6 were measured over the full width of the visible HAZ plus 3 mm (0.12 in.). For each weld, hardness traverse locations were chosen at mid-thickness, 0.75 mm (0.03 in.) below the cap, and 0.75 mm (0.03 in.) above the root. These results are shown in Figures 6 through 10. The zero position was the fusion line. In addition to hardness measurements every 0.25 mm (0.010 in.) in the region, some measurements were also taken in the weld metal.

The previous measurements for HAZ hardness given in Table 6 were concentrated in the visible HAZ. These results can be compared with the hardness traces in Figures 6 through 10.

The traces in Figures 6 through 10 show a general tendency to lower hardness near the root compared to near the cap, due to tempering of the HAZ associated with early passes by the later passes near the cap. Regions of higher hardness near the cap were observed in welds were observed at and adjacent to the fusion line.

Of these five welds, only one, W3, was welded with an ER120S-1 consumable. All the others used one of two ER100S-1 consumables. Thus the higher weld metal hardnesses in W3 can be explained by the higher strength consumable.

4.2.2 Interpretation of HAZ Hardness Traverses in X-100 Plate Welds

The hardness values measured in the HAZ show a softened region in both the visible HAZ and in the region just outside of the visible HAZ. Not all of the visible HAZ is softened. In particular, the portion of the visible HAZ closest to the cap side near the fusion line has higher hardness than the base metal.

The HAZ and base metal data for these five welds was averaged over the five welds for each position. This averaged hardness data is plotted in Figure 11.

The softened zone size was estimated from this plot as extending for 0.5 mm (0.02 in.) from the fusion line to 3.5 mm (0.14 in.) from the fusion line for both the root and mid-wall measurement. At the cap a smaller area was observed to be softened. This cap side softened region extended from 1.75 mm (0.079 in.) from the fusion line to 3.5 mm (0.14 in.) from the fusion line. The definition of the outer boundary of the soft zone could easily be shifted by 0.5 mm (0.02 in.).

Hardness measurements taken from this softened zone were compared with hardness measurements taken at 5 to 6.5 mm (0.20 to 0.26 in.) from the fusion line, which represent the base metal hardness. The mean hardness for the base metal region was 267.9 HV 0.5 kg with a standard deviation of 12.2. The mean hardness of the softened region was 257.3 HV 0.5 kg with a standard deviation of 12.0.

A student's t-test was applied to judge if the hardness data recorded in the softened zone could reasonably be described as the same as the base metal hardness, as represented by the data from 5 to 6.5 mm (0.20 to 0.26 in.) from the fusion line. The probability was very low, less than 0.00001.

The variation of hardness in the softened zone is very similar to the variation in hardness in the base metal. Since the mean hardness of the softened region is within one standard deviation of

the base metal hardness, multiple tests of the HAZ hardness would be required to demonstrate that an individual weld had a softened HAZ.

The results described here for one X-100 plate material provide an example of demonstration of softening, but cannot be considered as representative of this grade, either as plate or as pipe.

The results from hardness testing do not directly give the matching conditions for yield strength or ultimate strength that are appropriate for strain-based design analysis. Several effects should be considered. Hardness measures deformations in compression with considerable local plasticity. Thus, the results correlate with yield strength and ultimate strength, but do not directly measure the same property. Flow strength defined as the average of yield and ultimate would be closer to the value measured by hardness. However, the differences between compressive and tensile yielding will still create differences in the trends between hardness and any measured tensile mechanical property. While the weld metal and the visible HAZ will tend to have nearly isotropic mechanical behavior, the SCHAZ and the base metal of pipe can have mechanical properties that differ with direction. The hoop direction properties for both yield and ultimate strength are usually noticeably higher than in the pipe longitudinal direction, because of the deformation induced by the pipe production process. When hardness measurements are taken on the weld cross section, the measurements from the SCHAZ will be influenced by the stronger hoop direction properties. This occurs even though the appropriate comparison for matching of the yield properties in strain based design is in the longitudinal direction.

The use of plate rather than pipe as base metal for these tests minimized the effect of differing properties based upon direction. The plate properties will be closer to those observed in the longitudinal direction of X-100 pipe produced for field service than to the hoop direction of that pipe.

4.3 Testing of Softened Region Properties Using X-100 Pipe as Base Metal

EWI performed more extensive testing on three selected welds in X-100 pipes. The pipes and girth welds were provided to EWI by PRCI member companies. One company provided a single girth-welded section (Weld 1). The other company provided two sections of girth weld with different procedures that were applied on two halves of the same girth weld. These were designated Weld 2a for the weld using the dual torch procedure and Weld 2b for the weld using the tandem welding procedure. Dual torch welding uses two welding torches separated along the direction of travel of the torches. Tandem welding uses two wires feeding into a single torch into a single weld pool.

EWI performed six types of testing on girth-welded X-100 pipes supplied in 2005. These were base metal tensile testing, microhardness traverses, microhardness matrices, cross-weld tensile, stub tensile, and micro-tensile testing. The stub and micro-tensile specimens were non-standard specimens used to obtain information useful to study of the HAZ strength.

Base metal testing used specimens of round cross section without flattening.

The stub tensile specimens had a 10-mm (0.39-in.) square cross section, except for the radiused notch near the center of the specimen length. This radiused notch left a round cross section with a minimum diameter of 6.35 mm (0.25 in.). There was no uniform diameter section in the middle of the specimen length, as shown in Figure 12. Instead, the specimens were designed with a curved notch surface of 9.53-mm (0.375-in.) radius. Five locations were tested: one in the hoop direction in the base metal, one in the axial direction in the base metal, and three near the fusion line (FL) in the pipe axial direction. The three locations were defined by the plane of the center of the notch as FL + 2 mm, FL + 3 mm, and FL + 4 mm. Extension was measured using points on the square cross sections adjacent to the notch with a gage length of 12.5 mm (0.49 in.).

The micro-tensile specimens were taken in and adjacent to the weld in the pipe hoop direction. Figure 13 shows two specimens allowing a comparison of the specimen before and after testing. Specimens were designed to be 0.5-mm (0.02-in.) thick and 2.0-mm (0.08-in.) wide in the reduced section, taken from the center of the pipe thickness. The position of the specimens compared to the girth weld is shown in Figure 14. The specimen area was machined from the pipe as a block, 75-mm (3.0 in.) long and 4-mm (0.16-in.) thick. The reduced section [12.7-mm long (0.5 in.) and 2-mm (0.08-in.) thick] and radii of 1 mm (0.04 in.) were machined before the individual specimens were cut. The individual specimens were cut with a 0.5-mm (0.02-in.) kerf slitting saw, beginning closest to the weld centerline and moving toward the base metal taking off one specimen with each cut. Machining and slitting were done with cooling fluid, so the specimens could be used without additional surface preparation.

4.3.1 Weld 1

Figure 15 shows a cross section of Girth Weld W1 in 914-mm-(36-in.)-diameter X-100 pipe.

The stress-strain curves for the base metal are shown in Figure 16 and summarized in Table 7. These show the expected differences between the hoop and axial direction. The yield point is sharper and higher in the hoop direction. Over the first two percent strain, the plastic strength is between 5 and 10% lower in the axial direction. The behavior at higher strains shows a lower

uniform elongation in the hoop direction, as well as lower elongation to failure. The cross-weld strap tensile had an ultimate strength of 774 MPa (112.2 ksi).

The stub tensile results are shown in Figure 17 and summarized in Table 8. Looking first at the base metal results, the overall form of the results is similar, but the stress values are approximately 20% higher than those from the standard specimens with a cylindrical length of reduced section. Bowker et al.[22] estimated an increase in stress for a waisted specimen of this ratio of minimum diameter to notch radius of 12.6% for X100. The minimum cross section was measured on the stub tensile specimens and used in the stress calculation. The failures are not planar failures at this cross section. Instead, the failures have a central nearly planar region surrounded by a shear lip that extends to larger diameter. Thus the area of the fracture surface is larger than for a specimen with a smooth reduced section of the same minimum diameter.

The microtensile results are shown in Figure 18 and summarized in Table 9. Specimens were taken every 1 mm (0.04 in.) starting at the weld centerline, going out 13 mm (0.51 in.). The highest ultimate strength was observed on the weld centerline (WCL). The adjacent specimen in the weld at WCL + 1 mm was observed to be slightly bent before testing. Some preliminary testing indicated to EWI that this bending could reduce the ultimate strength and uniform elongation, as shown in Figure 18. Lower yield strengths were observed on the WCL + 2 mm, WCL + 3 mm, and WCL + 4 mm specimens than on other specimens.

The microhardness matrices were measured with an automated system using a Vickers indenter and a 0.1-kgf (0.22-lbf) load. A rectangular matrix was used with a spacing of 0.25 mm (0.010 in.). The results are shown in Figure 19. Hardness reductions in the HAZ were about 10 to 20 HV. This resolution allows some finer features to be identified beyond the generally overmatched weld metal and undermatched HAZ. The internal root pass is shown to be lower hardness than the other weld passes and undermatched to the base metal. The undermatched area of the HAZ appears to be divided into two parts with a central strip of material with a hardness close to matching of the base metal. The slightly harder strip corresponds to approximately the boundary between the light and dark etching regions of the HAZ in Figure 15.

4.3.2 Weld 2a – Dual Torch

The dual torch weld had the specimen identification number D503276. A cross section of the weld is shown in Figure 20. Base metal chemistry measurements were provided for the pipe used adjacent to Welds 2a and 2b (Table 10).

Base metal properties were provided by the company supplying the girth weld. The testing was repeated at EWI to determine full stress-strain curves. The results from the supplier on 12.7-mm-(0.50-in.)-diameter round bars are shown in Table 11. The EWI results are shown in Figure 21. The cross-weld tensile test gave an ultimate strength of 793 MPa (115.0 ksi).

All weld-metal specimen tensile properties were also obtained both by EWI and from the supplier. The results of the testing for the supplier are shown in Table 12. These indicate that the weld metal is significantly stronger than the base metal in both the axial and hoop directions.

The stub tensile results are shown in Figure 22 and summarized in Table 13. As was noted above for Weld W1, the direct comparison of the base metal stub tensile to the standard waisted specimen in the axial orientation showed that the strengths are higher on the stub tensile. Little difference in the stress-strain curve of the stub tensile specimen was observed between the base metal hoop and axial direction. At strains above 5%, the HAZ area stub tensiles also show very similar behavior. The HAZ area stub tensiles did show somewhat lower plastic strength from yielding up to 5% strain, by about 69 MPa (10 ksi) from 1 to 3% strain.

The microtensile results are shown in Figure 23 and summarized in Table 14. These specimens were generally thicker than was used in for Weld W1. The weld metal microtensiles (WCL, WCL + 1 mm, and WCL + 3 mm) were overmatched compared to the base metal (WCL + 7 mm, up to WCL + 13 mm). The base metal specimens showed behavior generally similar to the hoop direction large tensile specimen, with an upper yield point followed by about 2% elongation without an increase in strength. The HAZ microtensile specimens showed a roundhouse stress strain curve, so that the yield strength was lower than the base metal, but the ultimate strength was in a similar range.

The hardness map shown in Figure 24 indicates that only a very modest hardness reduction in the HAZ can be found at the outside edge of the visible HAZ compared to the base metal. The weld metal is harder than the base metal by from about 10 to 50 HV. The highest hardnesses were in areas without the tempering effect of adjacent weld passes. As noted on Weld W1, the root pass has much lower hardness.

Overall, Dual Torch Weld W2a could be described as having minor HAZ softening. This would be particularly minor when compared to the axial direction properties of the base metal at higher strains.

4.3.3 Weld 2b – Tandem

The tandem weld had the specimen identification number D503274. A cross section of this weld is shown in Figure 25.

The base metal in Weld 2b was from the same pipe as Weld 2a. Stress-strain curves measured on full-size specimens are shown in Figure 26 for the hoop and axial directions. The cross-weld tensile test gave an ultimate strength of 800.5 MPa (116.1 ksi).

Weld metal tensile tests had also been completed for the company that supplied the weld and by EWI. The weld metal tensile properties reported from the supplier in Table 15 were higher than those observed in the pipe axial direction, but the yield strength was significantly lower than the strength in the pipe hoop direction.

The stub tensile results are shown in Figure 27 and summarized in Table 16. As noted for Weld W1, the stub tensile strengths were larger for the base metal specimens than the standard shape tensile specimens. The HAZ results bracketed the results for the base metal axial test.

The microtensile specimens gave stress-strain curve results shown in Figure 28. The specimens were generally thicker than those used for Weld W1. Two of the specimens, WCL + 1 mm and WCL + 10 mm, had been cut thin enough that an extensometer could not be applied. This lowered the data quality, particularly of the initial elastic phase. A summary of the results is provided in Table 17. The base metal results were very similar to those for Weld W2a, with a yield point at about 758 MPa (110 ksi) and no increase in strength thereafter. The weld metal results (WCL to WCL + 4 mm) showed roundhouse behavior with a similar yield strength to the base metal, but a higher ultimate strength by about 34 MPa (5 ksi). The HAZ specimens (WCL + 6 mm and WCL + 7 mm) showed curve shapes intermediate between those of the base metal and weld metal. However, the yield strength was about 793 MPa (115 ksi), approximately 34 MPa (5 ksi) higher than the base metal.

The hardness map in Figure 29 shows that the HAZ hardness is slightly lower on average for this weld compared to Dual Torch Weld W2a, with a visible variation on the left side of the weld related to re-heating. The average hardness of the weld metal was lower than that observed on Dual Torch Weld W2a, with only local areas of un-tempered material more than about 20 HV above the base metal hardness.

4.4 Summary

HAZ softening has been observed for welds on X-70, X-80, and X-100 steels. Cases with little or no softening have also been observed for other welds in these same grades. Higher heat inputs and larger weld volumes per pass associated with SAW as compared to GMAW have been correlated with greater softening in each of these pipe grades.

The width of the softened zone in the HAZ is commonly between 3 and 5 mm (0.12 in. and 0.20 in.) for multipass girth welds in pipeline, extending slightly beyond the outer edge of the visible HAZ. Hardnesses taken at or near the outside surface may provide a smaller estimate of softened width than measurements taken at or near the internal surface.

The width of the softened zone is a function of the heating history, as is the minimum hardness. The SAW welds with higher heat input per pass than GMAW gave the widest softened zones for each pipe grade.

The hardness reduction in softened zones averaged 10.6 HV 0.5 kg for the five welds in X-100 plate examined. The hardness in the softened zone for the five X-100 welds had a standard deviation of 12.0 HV, while the hardness of the base metal had a standard deviation of 12.2 HV. This indicates that multiple hardness measurements will commonly be needed to demonstrate hardness reduction in the HAZ, since the average reduction is less than the standard deviation in either the HAZ material or the base material unaffected by the weld heating.

Softening of the HAZ was also observed on X-100 pipe girth welds, with more softening on W1 and less softening on Dual Torch Weld W2a and Tandem Weld W2b. The softening adjacent to these last two welds is so limited that it would be difficult to define an amount of softening, particularly in the axial direction of the pipe.

5.0 Loading Mode Effects on Strain Concentration at Girth Welds

It was recognized in the first phase of this program that large strain concentrations could be created around girth welds where the axial strain was combined with a lower strength in the weld HAZ and with internal pressure in the pipe.

This finding was dependent upon finite-element models and example tests where the applied displacement was in tension along the axis of the pipe.

The displacement-controlled loadings on pipes, both for laying and during operation, commonly have an important off-axis component. That is, the displacement causes bending of the pipe. Pipe bending will also tend to localize the strains in areas of lower yield strength, but may do it with different concentration factors than for pipes in tension.

Pipe tension strains are nearly uniform around the circumference of the pipe. Pipe bending strains vary greatly around the pipe, reaching peak levels at the outer fiber and zero strain at the neutral axis. This variation of strain around the pipe can limit the strain concentration, by providing adjacent restraint.

This section provides comparisons to examine the relative effect of loading mode on the strain capacity of girth welds.

5.1 Finite-Element Models

Finite-element models were designed to assess loading mode effects using the weld configuration most heavily used in Phase 1 project.[1] This used a three-material model of one material for the base metal, one material for the HAZ and weld root, and one material for the remainder of the weld metal. The dimensions of the cross section, meshed cross section of the weld area and the overall model are shown in Figure 30.

The stress-strain curves were the same as in Phase 1 as shown in Figure 31.

The model built for this task differs from the two-dimensional model used in Phase 1. Instead, it is a three-dimensional model of ¼ of the pipe, with mirror symmetry at the weld center line (the 2-3 plane in Figure 30). The other perpendicular symmetry plane is used as the plane of bending (the 1-2 plane in Figure 30). Residual welding stresses were not included based on results from Phase 1 that indicated little effect of these stresses on strain distributions for large applied remote strains.

Three loading types were applied to this model. A uniform axial displacement of the ends to achieve 6% strain was applied so that a direct comparison could be made with the Phase 1 models. The 6% strain was applied as a displacement of the ends by 6% of the original length far away from the weld so that the local effects of the strain application do not affect the results. A uniform bending displacement of the ends was applied to reach 6% tension strain on one side of the pipe and 6% compression strain on the other. The third loading type combined axial displacement and bending displacement, so that the compression side stayed at 0% strain, while the tension side reached 6% strain.

The overall strain results are shown for tension, bending, and the combination loading in Figures 32 through 34, respectively. The areas around the weld in the area of peak tension are shown in greater detail in Figures 35 through 37.

5.2 Conclusions

All of the three loading types result in similar strain distributions on the peak tension side of the pipe. The local strain concentrations are not strongly affected by the remote loading mode. This indicates that data obtained with tension loading can be used for cases of bending loading and vice versa. It should be noted that effects of pipe bending versus pipe tension loading mode have been observed in strain-based assessment of pipes with flaws, for instance in Shimanuki and Inoue.[23]

6.0 Strain Concentrations at Girth Welds

EWI has performed finite-element analyses of girth welded areas to determine the effects of softened HAZ areas on strain distributions under conditions of interest for strain-based design. Primary variables examined are softened HAZ width, internal pressure, and pipe thickness. These models continue to use the three-material model described above with one set of mechanical properties for the weld metal, one set for the HAZ, and one set for the base metal. The following section describes models that use a more complicated distribution of mechanical properties.

6.1 Effect of Softened HAZ Width on 10-mm (0.39-in.)-Thick Pipe

A simple two-dimensional model was used to estimate the effect of softened HAZ width. The model uses cylindrical symmetry of the pipe and mirror symmetry across the plane of the weld centerline.

The basic pipe geometry assumed was 10-mm (0.39-in.) thick with outer diameter of 914 mm (36 in.). The distance from the point of strain application to the plane of mirror symmetry at the weld centerline was 1000 mm (39.4 in.).

Four geometry cases were used, as shown in Figures 38 through 41, with softened HAZ widths averaging 2, 3, 4, and 7 mm (0.08, 0.12, 0.16 and 0.28 in.). The weld metal profile was designed to simulate automated welding of on-shore pipelines. The softened HAZ profile is designed to follow the fusion line and be slightly wider at the root than at the cap.

The material properties were the same ones used in Phase 1. The stress-strain curves are shown in Figure 42. The red zone in Figures 38 through 41 is given the 10% lower strength properties, while the weld metal area is given the 10% higher strength properties.

Welding residual stresses were not included in the model based on results in Phase 1 that indicated little effect of residual stresses for large applied axial remote strains. The model used in Phase 1 to check for residual stress effects also included a different hardening model that had the capability of assessing stresses and strains that do not increase monotonically.

Two loading conditions were considered, one with axial strain of 4% applied at 100 mm (3.9 in.) from the weld centerline and one with internal pressure applied first and then 4% axial strain. The von Mises stress for the case with no internal pressure is shown in Figure 43 for each of the HAZ widths. The local axial strains and the plastic equivalent strains for this case are shown in Figures 44 and 45, respectively. The internal pressure case gave the results shown in Figure 46 for von Mises stress, Figure 47 for local axial strain, and Figure 48 for plastic equivalent strain. All of these figures are arranged in four parts with the 2-mm (0.08-in.) HAZ at upper left, the 3-mm (0.12-in.) HAZ at upper right, the 4-mm (0.16-in.) HAZ at lower left, and the 7-mm (0.28-in.) HAZ at lower right. All of the figures are shown with exaggerated displacements by a factor of 2.

The results indicate the greatest deformation of the HAZ occurs in the case of the widest HAZ, where the softened region is wide enough for a continuous shear band to extend from the internal root corner to the outer surface of the pipe while remaining in the lower strength material. The greater width of the HAZ near the root does not have an important effect on the regions of strain concentration. This appears to be because the shear bands that shift the weld cap toward the pipe wall centerline are favored compared to those that move the weld root toward the centerline. Thus, the shear bends that are favored are wider apart at the cap side compared to the root side.

For the axial strain only case, the peak strains are concentrated at the root edge of the weld. Only very small areas of the softened area have axial strain concentrations exceeding 2. In the weld metal and along the fusion line, the peak strains are below 1.5 times the remote strain.

For the pressure and axial strain case, the peak strain pattern is strongly dependent upon the HAZ width. For the wider HAZ, the area of peak strains above 8% progressively widens and deepens from a small area at the root weld toe. For the widest HAZ, it extends through the thickness of the pipe wall forming a 45-degree shear band. The material in the weld and along

the fusion line has strains that are not strongly affected by the width of the HAZ with strains less than twice the applied strain.

The area of the weld that has the highest strains is the about 3 mm (0.12 in.) from the root of the weld. The fusion line area with the highest strains is nearby, extending to the weld root.

6.2 Effect of Weld Metal Strength on 10-mm (0.39-in.)-Thick Pipe

A check case was performed with a lower weld metal strength to examine the effects of having a weld metal with strength no larger than the base metal. The internal pressure + 4% axial strain case gave the von Mises stress pattern in Figure 49, the local axial strain pattern in Figure 50, and the plastic equivalent strain pattern in Figure 51.

One of the differences between this case and the one with higher weld metal strength is the larger strains at the narrowest portion of the weld. This occurs because shear bands form that cross in this region. The severity of the strain concentration in this region is not strongly dependent upon the width of the HAZ. As the softened HAZ widens, additional strains are concentrated in shear bands parallel to those that cross in the weld metal but entirely in the softened HAZ and base metal.

Strain concentrations in the most severe shear bands exceed three times the nominal strain.

6.3 Effect of Pipe Thickness

A check case was done with a 20-mm-(0.79-in.)-thick pipe using the same cap and root widths as were used for the 10-mm (0.39-in.) pipe. The model essentially added 10 mm (0.39 in.) at the mid-thickness of the pipe wall. The material properties were the same as those used above for the original 10-mm (0.39-in.) pipe. The shapes of the four sizes of HAZ are shown in Figure 52.

The von Mises stresses are shown in Figure 53. The axial strains for the internal pressure + 4% axial strain case are shown in Figure 54. The equivalent plastic strains are shown in Figure 55.

The strains near the center of the thickness are much lower in this case than in the 10-mm-(0.39-in.)-thick case, particularly for the case of the widest HAZ. The surface deflections are also much smaller than those observed in the 10-mm-(0.39-in.)-thick case. This indicates that shear bands that formed in the 10-mm-(0.39-in.)-thick case were prevented from forming in the case with the larger thickness.

The region of the largest strains in this weld is much more diffuse than in the case of the 10-mm-(0.39-in.)-thick pipe. The region extends roughly from half the weld width below the cap to half the weld root width above the root. This center section does not have a strong variation of local strain. The very widest HAZ case did show a slight increase in the peak strain in the weld metal.

6.4 Effect of Lower Internal Pressure

The internal pressures chosen for use in the previous sections were at 70% of the pressure to cause yielding in the base metal by pressure alone. This is a common peak design pressure value, where no other restrictions on design pressure are applicable. Since an effect of internal pressure was observed, it is appropriate to check at lower pressures, particularly since some of the initial uses of X-80, X-100, and X-120 pipe have been at lower design factors.

Thus, three additional studies were completed with a pressure of half the pressure used in the previous sections, 35% of the pressure to yield by pressure alone. The pressure values used are 3.215 MPa (466 psi) for 10-mm (0.39-in.) thickness and 6.43 MPa (933 psi) for 20-mm (0.79-in.) thickness. The three cases were the case with a 10-mm-(0.39-in.)-thick pipe and overmatching weld, the case with a 10-mm-(0.39-in.)-thick pipe and even matching weld, and the case with a 20-mm-(0.79-in.)-thick pipe and overmatching weld.

The 10-mm-(0.39-in.)-thick pipe with overmatching weld metal was examined with the lower pressure. The internal pressure + 4% axial strain case gave the von Mises stress pattern in Figure 56, the local axial strain pattern in Figure 57, and the plastic equivalent strain pattern in Figure 58.

It is not surprising to see that the strains in the 45-degree shear bands in the HAZ are intermediate between those of the high pressure and no pressure cases. The strains in the weld metal and fusion line areas were also intermediate between these cases, tending to be higher on the inner half of the weld.

The 10-mm-(0.39-in.)-thick pipe case with the weld metal strength matching the base metal strength was examined at the same pressure. The internal pressure + 4% axial strain case gave the von Mises stress pattern in Figure 59, the local axial strain pattern in Figure 60, and the plastic equivalent strain pattern in Figure 61.

The 20-mm-(0.79-in.)-thick pipe case with overmatching weld metal was examined with the lower pressure. Because the thickness is greater, this leads to this case using the same

pressure as was originally used for the 10-mm-(0.79-in.)-thick pipe. The internal pressure + 4% axial strain case gave the von Mises stress pattern in Figure 62, the local axial strain pattern in Figure 63, and the plastic equivalent strain pattern in Figure 64.

6.5 Strains in the HAZ

The strains observed vary strongly across the HAZ in all cases. A choice much be made of the most interesting value of strain for comparison. In this section, the strain of interest is taken at 3 mm (0.12 in.) from the root surface, within the HAZ. The peak value on axial strain along the line originally at 3 mm (0.12 in.) from the ID surface is chosen. This 3-mm (0.12-in.) position was chosen based on other uses of the 3-mm (0.12-in.) position, such as the estimates where flaws in workmanship assessments of welds are assumed to have a maximum depth of 3 mm (0.12 in.).

For the analyses conducted, the choice of position avoids the artificially high strain concentration around the corner at the weld root. It also avoids areas that are strongly dependent upon the specifics of the transition in strength properties between the weld metal and HAZ and between the HAZ and the base metal. Peak strain values at two other locations are discussed in the following sections.

The HAZ strain values at 3 mm (0.12 in.) from the root, as determined for each model, are listed in Table 18. The strain concentrations for this location, the strain at this location divided by the average remote axial strain, are listed for each case in Table 19. Strain concentration may be helpful for comparison with cases where different remote axial strains are applied, since they are nearly constant with strain at the 4% strain value used here.

The results indicate that the axial strain at the 3-mm (0.12-in.) position in the HAZ is a function of internal pressure. Changing pressure changed the strain concentration for all the cases of HAZ size, thickness, and weld metal strength.

The 3-mm (0.12-in.) position axial strain can be a strong function or a weak function of the HAZ width depending on aspects of the geometry. A wider HAZ increases the strain concentration. The amount of that increase depends upon whether the increased width allows a more extensive shear band to form using the wider HAZ.

The 10-mm-(0.39-in.)-thick weld with the matching weld metal shown in Figures 49-51 did not show a large effect of HAZ size, because the weld in all four cases of HAZ size was large enough to allow a pair of shear bands to cross in the weld. Although no case with matching

weld metal was assessed for the 20-mm-(0.79-in.)-thick weld, the strain would not be expected to be as high because the same configurations of shear bands will not fit in that weld region.

6.6 Strains in the Weld Metal

The weld metal strains can be considered separately from those in the HAZ. The greater likelihood of discontinuities in the weld metal makes it appear to be a more severe site for localization of strain.

Looking generally at the figures presented in the last section, the weld metal strains are largest in approximately the inner third of the weld metal, but not including the root reinforcement. The largest strains generally occur near the weld centerline at approximately one half W_r toward the cap from the plane of the ID surface of the pipes. W_r is defined as the width of the root.

The peak strain values on the weld centerline are shown in Table 20. The strain concentration at this point, the peak strain divided by the average remote strain, is shown for each case in Table 21.

The peak strain magnification factor is commonly between 1.5 and 2. Higher values of this strain concentration are observed where the weld material matches the base metal, so that the strain concentration can be well above three in that region.

Effects of pressure were more important than effects of HAZ size on the observed strain concentration. When an extensive shear band formed in the HAZ, as in the case of the extra large HAZ with high internal pressure, the strain concentration in the weld metal dropped slightly, compared to welds with narrower HAZs.

For cases where shear bands do not form across the whole thickness, the peak strain in the center of the weld metal is similar to the strain in the HAZ at 3 mm (0.12 in.) from the surface. The largest differences occur for the 20-mm-(0.79-in.)-thick pipe, where the shear band formation is inhibited not only by the higher strength weld metal, but also by the weld bevel, which would not allow a full thickness shear bend even in a weld with a lower yield strength weld metal.

6.7 Peak Strain Concentrations

The discussion of strain concentrations above has tended to avoid the areas of peak strain concentration at the weld toes of the cap and root. These peak strains are greatest at the root,

where the weld material at the root transitions to the HAZ. The strain concentrations observed are a combination of the effects of the weld geometry and the sharp change of mechanical properties at the boundary between the weld and HAZ.

The peak strain values when 4% axial strain is applied are given in Table 22.

The two special effects at the root and cap toes, from the external geometry and from the switch from weld metal properties to HAZ properties, exaggerate the real effects. The models here assume a sharp weld toe and a sharp transition in strength at the same point. Weld toe radii tend to be closer to 0.5 mm (0.02 in.) rather than the sharp corner assumed in the model. The difference in strength would be expected to be smaller at the root because of tempering of the weld root area. At the cap, it is likely that the transition from overmatched to undermatched properties does not correspond to the position of the weld toe, but will be some distance into the HAZ.

The results in Table 22 should thus be used for comparative guidance rather than quantitative measurement.

7.0 Strain Concentrations at Girth Welds Using Finer-Grained Material Models

The past section looked at models that were generated using a three-material model of the girth weld area. The data generated in Section 4.3 can be used to create more realistic models with finer-grained material property distinctions. This section discusses results of models using these models.

The models in the previous section were designed to be used to check a wide range of possible conditions. The models discussed in this section are designed to be closer to those of most interest for future designs, with material properties more closely representing X-100 material, thicknesses in the range most commonly considered, and thinner HAZs. The properties measured on Weld 1 described in Section 4.3.1 were used as a basis.

The pipe used here was 20-mm (0.79-in.) thick, with a diameter of 934.5 mm (36.8 in.) and a distance across the weld cap of 14.4 mm (0.567-in.).

7.1 Model Assumptions

As in the previous section, the models were cylindrically symmetric around the pipe axis as well as having mirror symmetry at the weld centerline.

The models were designed with five regions, so that each of the five regions could have a specific set of material properties. These five regions are shown in Figure 65. As before, uniform material properties were used in the base metal.

No welding residual stresses were included in the model. This was based on experience from Phase 1 models where addition of residual stresses had had a very minor effect on stress and strain distributions at large plastic axial strains.

7.1.1 Material Stress-Strain Properties

EWI used the general-purpose finite-element code ABAQUS for modeling. This includes a flexible, but not all-inclusive, method of setting the material properties in the individual elements.

A two-stage elastic plastic model of mechanical behavior was used for this portion of the assessment. This differs from the Ramberg-Osgood representation of stress-strain behavior used in the previous sections. The Ramberg-Osgood method provides a smooth curve through the yield point. The two-stage method has a sharp yield point where the elastic relationship between stress and strain switches to the plastic relationship.

As shown in the test results in Section 4.3, the plastic portion of the stress-strain curve of the pipe base material has a different shape in the axial and hoop directions. Thus, to model this behavior, it would be advantageous to have as much control as possible, of both the shape of the yield curve and the relationship of the yield curve with direction.

The ABAQUS material models for Ramberg-Osgood materials allow a proportional change in strength with direction. That is, the strength is always a given percentage lower or higher in one direction for any given value of strain. This does not allow the differing shape of the stress-strain curve with direction that was observed for the hoop and axial behavior in the base pipe.

The elastic plastic models of the stress-strain behavior were derived from Ramberg-Osgood models of the material behavior fit to the measured behavior in five regions:

- Weld metal
- Fusion line to the fusion line plus 1 mm (0.04 in.)
- Fusion line plus 1 mm (0.04 in.) to the fusion line + 2 mm (0.08 in.)
- Fusion line + 2 mm (0.08 in.) to the fusion line + 3 mm (0.12 in.)
- Base metal.

The fit of the Ramberg-Osgood models to the tested stress-strain curves is shown in Figure 66. The elastic plastic model curves were then fit to the Ramberg-Osgood representations, converted to true-stress/true-strain. The elastic-plastic engineering-stress/engineering-strain curves for uniaxial loading are shown in Figure 67. The curves for true-stress/true-strain are shown in Figure 68.

The Ramberg-Osgood fits extend to higher strain than the failure strain of the microtensile specimens. The microtensile results tended to give lower failure strains than the standard tensile specimens because of localized shear failure of the small cross section. The Ramberg-Osgood models need to extend to strains above the average failure strains to allow for reasonable modeling of the areas of strain concentration.

The elastic-plastic two-stage representation allows the plastic properties to be orthotropic rather than isotropic. In addition to isotropic behavior of all the material regions, two types of orthotropic representations were used in these assessments. In the first orthotropic model, all of the materials are orthotropic with the axial and radial strengths in the plastic region lower by 5%. In the second orthotropic model, only the base metal region has the axial and radial plastic strength properties lower by 5%. The orthotropic yield stress was implemented using the Hill yield criteria. This was implemented using the *POTENTIAL keyword in ABAQUS/Standard. The coefficients for the *POTENTIAL option were 0.95, 0.95, 1, 0.95, 0.975, 0.975 with the x-axis as the axial direction.

7.2 Effects of Pressure and 4% Axial Strain

The models were loaded first with internal pressure and then with an axial displacement of the ends to achieve an average of 4% strain over the pipe length. The modeled section of pipe was long enough that displacing the ends to 104% of their spacing after pressurization provides very similar results to displacing the ends sufficient to achieve a 4% strain remote to both the weld and the ends. Three levels of internal pressure were used:

- 0 MPa (0 psi) to achieve 0% of the standard minimum yield strength (SMYS) as hoop stress in the pipe
- 9.59 MPa (1390 psi) to achieve 35% of the SMYS as hoop stress in the pipe
- 19.18 MPa (2780 psi) to achieve 70% of the SMYS as hoop stress in the pipe.

The results for local axial strain around the weld for the case of isotropic material properties are shown in Figure 69. The results for local axial strain for the case of all materials with orthotropic properties are shown in Figure 70. The results for local axial strain for the case where only the base metal has orthotropic properties and the other materials have isotropic properties are shown in Figure 71. In each of these figures, the left-hand result is for no internal pressure, the middle result is for internal pressure of 9.59 MPa (1390 psi) and the right-hand result is for internal pressure of 19.18 MPa (2780 psi).

None of these results shows full thickness shear bands. The weld geometry, chosen to be representative of automatic GMAW weld fusion area, is not conducive to their formation in this pipe wall thickness. The greatest local strains are observed at the weld root toe. Shear bands extending from this location can be observed starting from this location and reaching both into the base metal and into the weld centerline, but further extension toward through thickness is not observed.

As noted above, the two regions of shear banding near the root of the weld can be quantitatively compared based on local strain parameters. The local strain in the HAZ at 3 mm (0.12 in.) from the root surface can be used for the shear band on the base metal side. The local strain at the point where the shear bands cross at the weld centerline can be used for the shear band on the weld metal side. These are the same definitions used above.

The peak local strains in the HAZ at 3 mm (0.12 in.) from the root are provided in Table 23 for each of the nine cases. Both the isotropic and fully orthotropic cases show some strain concentration when pressure is applied, by about 40% over the results without internal pressure. The case where only the base metal had orthotropic properties had almost no increase in strain over the internal pressure case.

The peak local strains along the weld centerline were also very similar for the isotropic and fully orthotropic cases, as shown in Table 24. Again, a roughly 40% increase in peak local strain was observed with internal pressure compared to the case with no internal pressure. The behavior with orthotropic behavior only in the base metal again showed much less strain concentration.

Of the three material behavior cases examined, the one that most closely represents the actual pipe is the one where the base metal is the only region where the orthotropic properties are applied. The difference in strength between the hoop and axial directions will come out of the forming process to create the pipe from flat plate and the subsequent expansion step to improve its match to the desired dimensions. Neither of these processes will be applied after the welding of girth welds, so the girth weld and HAZ would only have departures from isotropic behavior based on the welding conditions and microstructural evolution during cooling. Thus, the best estimate of strain concentration would be the one from the base metal orthotropic analysis, rather than a strain concentration of 40%, which would appear to be unrealistically conservative for welds in the X-100 pipe represented by the models. The orthotropic properties chosen were relevant to pipe with an axial long seam. The different relation between axial and hoop properties of spiral pipe may cause the estimates here to be invalid for the spiral pipe case.

7.3 Constraint as a Function of Internal Pressure

The models discussed above can also be used to provide some initial ideas for on the constraint for models of fracture for the weld area. These ideas are further developed in the sections below.

The following three sections discuss basic ideas about constraint, hoop stress, and triaxiality parameters.

The models were also used to examine the hoop stresses in the weld area. The hoop stresses are induced by a combination of the direct stresses from the internal pressure and the Poisson stresses induced by the axial strain.

7.3.1 Constraint Descriptions

Most simple fracture estimates assume that the driving force of a flawed body to fracture is proportional to a single parameter, such as the stress intensity factor or applied crack-tip open displacement (CTOD). Testing of many configurations of specimens has indicated that a two-parameter method can give a better representation of the driving force to fracture. The second parameter defines a constraint level, which tends to be low for specimens tested in tension and high for specimens tested in bending.

Several numerical parameters have been suggested to act as the second parameter in describing driving force to fracture. Parameters such as Q are appropriate to situations with extensive yielding, but are relatively difficult to estimate without a model of the crack in the

structure. A related parameter, the T-stress, is very useful here, since its definition can be directly related to hoop stress. The T-stress is the stress parallel to the crack surfaces and perpendicular to the crack tip. The T-stress can be normalized to a non-dimensionalized parameter by dividing by the remote applied stress perpendicular to the crack. T-stress methods have a solid mathematical basis for small-scale yielding, but other methods such as those using the Q-parameter have been preferred for defining constraint under conditions with larger regions of crack tip yielding. Application of the T-stress to fully plastic loading situations has been the subject of recent research by Jayadevan et al.[24] with strong indications that T-stress methods will still be applicable for defining constraint in pipe geometries. Wang et al.[25] have discussed the T-stress as a parameter for strain-based design of flawed pipeline girth welds.

Tensile values of the T-stress indicate a high constraint. Compressive values of the T-stress have been noted in assessments of circumferential flaws in un-pressurized pipe. The hoop stresses observed in pressurized pipe are parallel to the crack faces and parallel to the crack tip. These stresses, perpendicular both to the primary axial stresses and to the T-stress, would appear to have little direct effect on constraint when comparing pressurized and un-pressurized pipe.

7.3.2 Hoop Stress

Figures 72 through 74 show the hoop stresses around the welds for the fine-grained models with, respectively: isotropic properties, orthotropic properties throughout, and orthotropic properties only in the base metal. Each of these figures shows the no pressure case on the left-hand side and two higher internal pressure cases on the right-hand side.

These figures show that the no-pressure case does not generate large stresses in the weld area in the hoop direction, except at the root and cap. Large compressive stresses are observed in the root and cap reinforcement material. The stresses in the weld and HAZ increase nearly proportionally to the increase in internal pressure, though some additional stress concentration occurs, particularly adjacent to the weld root toes.

This indicates that internal pressure can provide a stress input that affects the stress state at the crack tip even around a weld that has a softened HAZ and weld metal yield strength greater than the pipe base metal axial strength.

7.3.3 Ductile Failure Parameters

Other parameters have also been used to estimate the constraint. Kuwamura[26] has described a method of estimating the resistance of steel to ductile crack initiation that uses three parameters, the peak stress triaxiality τ_{peak} in the area of interest, the crack initiation strain ε_c and the uniform elongation ε_u of the material. The peak stress triaxiality is the peak value of the ratio of the hydrostatic stress to the von Mises equivalent stress. The crack initiation strain is the local averaged strain across the plane perpendicular to the largest strain. Kuwamura averaged the value across the minimum diameter of a notched tensile specimen.

These three parameters are related by the equation

$$\tau_{peak}\sqrt{\varepsilon_c / \varepsilon_u} = 1 \tag{1}$$

on average at failure, with minimum values of about 0.8 and maximum values of about 1.3.

The stress triaxiality for the isotropic case at 4% remote strain is shown in Figure 75, while the stress triaxiality for the base metal orthotropic case is shown in Figure 76. The peak values are between 0.72 and 0.84 for the isotropic cases and between 0.76 and 0.88 for the base metal orthotropic cases. These values are somewhat dependent upon the remote strain, with higher peak values expected for lower remote strain. The peak triaxialities are higher for the pressure cases, but not by large amounts compared to the no pressure cases.

Stress triaxialities have not been routinely calculated for cracked geometries, even though a linear elastic analysis of the crack tip area stresses indicates that this ratio is independent of distance from the crack tip. The stress triaxiality can be strongly dependent upon the position around the crack tip and the Poisson's ratio. For the peak triaxiality position ahead of the crack tip, the value for a Poisson's ratio of 0.3, tends to 2.17 close to the crack tip. This value can increase with distance from the crack tip if stresses along the crack front direction are present. However, with higher Poisson's ratio of 0.5 representing plastically deforming materials, the peak triaxiality can become meaningless, because the plane ahead of the sharp crack would have zero von Mises equivalent stress, resulting in a peak triaxiality of infinity.

The Kuwamura method can be used to predict whether the 4% remote strain might result in initiation of ductile cracks. The crack initiation strain can be roughly estimated by the peak strain at 3 mm (0.12 in.) from the root, as listed in Table 23 for instance. The material uniform

elongation must be estimated also, since the area of interest is in the HAZ. Averaging the HAZ microtensile elongations at the ultimate strength gives a value of about 5% strain. However, the comparison of the microtensiles in base metal and the larger standard specimens tested in base metal in the same hoop direction indicates that the microtensiles give somewhat lower values of the elongation at ultimate strength than the standard specimens. The uniform elongation of the larger base metal specimens was larger than the corresponding microtensiles by at least 1%.

Using values of crack initiation strain of 6.7% for the isotropic case and 6% for the uniform elongation still gives a value of the combined parameter less than 1, at 0.92, indicating that ductile crack initiation is not expected. The base metal orthotropic case had a much lower peak strain at 3 mm (0.12 in.) from the root, 4.4%, so the combined parameter is only 0.75, well below the expected initiation value of 1.0.

7.4 Effect of Weld Misalignment Due to Ovality

A small amount of high-low misalignment was observed on the weld cross sections in Figures 15, 20, and 25. No high-low was included in any of the finite-element models discussed earlier. It was thus considered valuable to examine high-low misalignment as an additional strain concentrator.

Mohr's guidance on strain-based design[(1)] included a guide on the acceptable misalignment. This limit is shown schematically in Figure 77 along with the misalignment in two example cases that are discussed below.

7.4.1 Ovality for X-100 Pipe

A check of the effect of high-low was performed by taking one of the two-dimensional models from the previous two sections and creating a three-dimensional model with high-low. One of the two pipes being joined at the girth weld was assumed to have a perfectly circular cross section, while the other pipe was assumed to have an elliptical cross section with the minor axis smaller than the circle and the major axis larger than the circle. The maximum misalignment was 1.5 mm (0.06 in.) at the two symmetry planes of the model. This amount of misalignment would be less than the maximum allowed for this pipe thickness of 20 mm (0.79 in.) for most pipeline specifications.

Figure 78 shows the cross section of the model at the maximum high-low.

Figure 79 shows the axial strain around an area of peak misalignment. Equivalent strain concentration was observed where the oval pipe was on the outside rather than the inside.

A mild shear band can be observed that runs from the root corner on the high side of the weld to the outer surface adjacent to the weld toe on the low side of the weld. The positioning of this band is no surprise, since a band at this location tends to straighten the weld area, reducing the misalignment. The other shear bands observed above for cases without high-low are minimized.

The deformation induced by the high-low tends to be more localized when additional internal pressure is applied. Figure 79 shows that the deformation of the base metal adjacent to the weld forms a sharper curve with the highest pressure than with the intermediate pressure, while the no pressure case is smoother than either of these.

The peak axial strains at 3 mm (0.12 in.) from the root on the high side are given in Table 25. These values are strongly dependent upon the internal pressure and weakly dependent upon the material models, either orthotropic or isotropic for all the material regions or with the base metal only orthotropic. The peak axial strains at the weld centerline are given in Table 26. These follow the basic trends in the previous table, but with lower magnitudes. The straightening deformation is distributed in three parts, one near the inside of the high side of the weld, one near the outside on the low side of the weld and the diagonal area in the weld metal and HAZ between them.

The peak axial strains for the misaligned case can be divided by the peak axial strains without misalignment to get a strain concentration due to the misalignment. These values are given in Table 27 for the position at 3 mm (0.12 in.) from the root of high side of the weld. The values at the weld centerline are given in Table 28.

As was shown in the previous section for the case without high-low, the hoop stress distribution continues to provide constraint even in areas with high strains in the axial direction.

High-low of 1.5 mm (0.06 in.) is a reasonable amount as an upper limit for critical applications. Special applications, such as risers, have been fabricated with maximum high-low of 0.5 mm (0.02 in.).

A second case of misalignment with maximum high-low of 0.75 mm (0.03 in.) was examined. The model configuration is shown in Figure 80.

The axial strain for the case with 0.75 mm (0.03 in.) high-low misalignment is shown in Figure 81. These strains, while lower in magnitude than the larger high-low case, follow the same general pattern.

7.4.2 Ovality for X-65 Pipe

The strength properties for X-65 pipe, HAZ, and weld material were defined based on the information provided by Kim et al.[8] in their microtensile study of the HAZ. The stress-strain curves are given in Figure 82.

The same model configuration as for the X-100 was used, which was shown in Figure 78.

Figure 83 shows the axial strain around an area of peak misalignment. Equivalent strain concentration was observed where the oval pipe was on the outside rather than the inside. As for the X-100, the strain is concentrated in three areas, adjacent to the root on the high side, adjacent to the cap on the low side and in a diagonal band across the weld metal from the root on the high side to the cap on the low side.

The peak axial strains at 3 mm (0.12 in.) from the root on the high side are given in Table 29. These values are strongly dependent upon the internal pressure and weakly dependent upon the three material models. The peak axial strains at the weld centerline are given in Table 30. These follow the trends in the previous table at somewhat lower magnitudes, since the weld area deformation is limited by the greater overmatch of the weld area.

As was shown in the previous section for the case without high-low, the hoop stress distribution continues to provide constraint even in areas with high strains in the axial direction.

The much lower yield strength and greater work hardening of the X-65 compared to the X-100 pipe did not create a large difference in either strain pattern or amount of strain concentration due to misalignment.

7.4.3 Estimating Effects of Ovality

Current standards provide guidance on the stress concentration factor (SCF) to be expected at misaligned girth welds. This is particularly important for fatigue standards, since fatigue lifetime and crack position are particularly sensitive to stress concentration. The strain concentration factor, estimated by squaring the stress concentration factor, can be compared with the results in the previous section.

The calculation of SCF in DNV RP-C203[27] uses

$$SCF = 1 + \frac{6\left(\delta_t + \delta_m\right)}{t} \frac{1}{1 + \left(\frac{T}{t}\right)^{2.5}} e^{-\alpha} \tag{2}$$

where

$$\alpha = \frac{1.82L}{\sqrt{Dt}} \frac{1}{1 + \left(\frac{T}{t}\right)^{2.5}}$$

δ_t is the difference in base metal center of wall due to different thickness,

δ_m is the distance of wall center misalignment,

t is the smaller thickness of base metal,
T is the larger thickness of base metal,
L is the width of the thickness or misalignment transition, and
D is the outer diameter of the lower diameter section.

The 1.5-mm (0.06-in.) high-low case has a calculated SCF of 1.205, so the strain concentration factor is 1.451. The 0.75-mm (0.03-in.) high-low case has a calculated SCF of 1.103, so the strain concentration factor is 1.216.

These values of strain concentration factor are conservative with respect to the results for the cases without internal pressure. However, when internal pressure is included, the results become non-conservative for the base-metal orthotropic case. The concentration of strain in the shear bands created by the internal pressure can nearly double the strain concentration factor.

8.0 Strain Concentrations in Specific X-65 Pipes

The assessment methods discussed above can be used to check the effects of modifications to weld region properties. In this section the effect of changing the material properties for girth welds in X-65 pipes is examined. The specific pipes have service with either zero pressure or pressure to 80% of yield an outside diameter of 324 mm (12.75 in.) and wall thickness of 12.7 mm (0.5 in.).

As noted in the last sections, EWI has defined stress-strain curves that can reasonably model the weld and HAZ areas in X-65, based on tests of weld properties by Kim et al.[8] Thus,

preliminary estimates can be made for the strain concentrations expected around these girth welds.

Two material property variants are checked, one for higher strength in the weld area by 25% compared to that measured by Kim et al., and one with a lower yield to tensile ratio for the base pipe of 0.85.

Strain concentrations for generic X-65 girth welds can give an idea of the determination of strain concentration on the un-notched examples needs fewer test cases, since notch location is not included.

The modeling of the weld area was done with models very similar to those used for the two-dimensional fine-grained models in Section 7.1. These have five material regions, a base metal region, a weld metal region, and three HAZ regions. The HAZ regions are 1-mm (0.04-in.) thick. The model is shown in Figure 84. The stress strain curves are shown in Figure 85. The material properties are assumed to be isotropic. Checks with orthotropic properties indicated that this change did not greatly change the strain distribution. Again residual welding stresses were not considered.

Loading was applied as in previous sections, with any internal pressure loading applied first and then a 4% axial strain gradually applied in tension.

The axial strain results are shown in Figure 86 for the baseline cases with no pressure and pressure to 80% of SMYS. The baseline cases indicate that very similar distributions of strain can be found near the toe of the weld on the internal surface and the toe of the weld on the external surface. A greater difference is observed in the axial strains in the weld area. The weld strains tend to be highest between the mid-thickness and the internal surface.

The strain pattern for the weld centerline with pressure but without misalignment is similar to the pattern observed above for misalignment, with a strain peak between mid-thickness and the inner surface of the pipe. Lower strains are observed between mid-thickness and the outside surface at the cap as well as in the region of overfill at the root.

The axial strain results are shown in Figure 87 with no pressure and 80% of SMYS pressure for greater overmatch in the weld metal. The greater overmatch tends to direct the strain away from the weld metal, particularly when pressure is applied. Somewhat greater strains are observed in the base metal, approximately one thickness away from the weld. This tends to limit any differences between strains near the root and strains near the cap.

The axial strain results are shown in Figure 88 with no pressure and 80% of SMYS with lower yield-to-tensile base pipe material, but no other changes in the material properties. The changes in strain concentrations from the baseline cases are quite mild.

Overall, these results indicate that strain concentrations due to pressure and mismatch of weld area properties in X-65 are mild. The HAZ shapes modeled here were not of the unfavorable shape that would promote shear band formation in the HAZ under remote strain. The HAZ strain concentrations are about the same adjacent to the outside surface and the inside surface, suggesting that HAZ notches may be representatively tested using external notches. The area of strain concentration in the weld metal tends to be in the inner half of the weld, so for this case external notches may not provide a conservative result compared to internal notches. Higher overmatch was observed to push strain away from the weld metal without localizing the strain excessively in the adjacent HAZ. The peak strain areas appeared to be roughly one pipe thickness away from the weld.

9.0 An Estimating Tool for Full-Thickness Shear Bands

The analysis using finite-element model has shown the formation of shear bands around the girth weld as the primary mechanism for severe localized deformation. The most severe strains occur when the shear bands can stay within the softened area, as occurred in the 10-mm-(0.39-in.)-thick pipe with 7-mm (0.28-in.) HAZ case for the axial strain + pressure as well as for the lower strength weld case when the HAZ was narrower.

The cases of weld geometry and pipe wall thickness where a shear band can stay within the softened zone can be determined by simple geometry. The shear band is assumed to keep a 45-degree angle with respect to the original surface and start at the corner of the weld root. Another assumption is that the cap and root have the same centerline. In this analysis the shear band has no required width.

Defining W_c as the cap width, W_r as the root width, h as the soft zone width on the cap side and t as the pipe wall thickness allows us to define two inequalities that define whether a shear band can form in a particular position:

$$t < \frac{W_c}{2} - \frac{W_r}{2} + h \tag{3}$$

and

$$t > \frac{W_c}{2} - \frac{W_r}{2} \tag{4}$$

If both of these are true, a shear band can form in the HAZ on each side of the weld. It is also possible for a shear band to cross from the root on one side of the weld to near the cap on the other side. This will only be favored if the weld metal is less than a few percent stronger than the base metal. The inequalities change for this case to

$$t < \frac{W_c}{2} + \frac{W_r}{2} + h \tag{5}$$

and

$$t > \frac{W_c}{2} + \frac{W_r}{2} \tag{6}$$

These parameters and the two types of shear band positions are shown in Figure 89.

As shown in Figure 89, it may take a relatively wide HAZ for a shear band at 45 degrees to the pipe axis to fit within the lower strength HAZ. If the weld is not overmatched, the shear band can also cross the weld metal, emerging at the cap HAZ on the other side of the weld.

These inequalities can be used for the initial finite-element model of the 10-mm-(0.39-in.)-thick pipe.

This becomes easier to visualize if the W_c and W_r values are described in term of the pipe thickness t. For a standard weld bevel (60-degree included angle), we can estimate the root bead width as 2 to 4 mm (0.08 to 0.16 in.) and the cap width as $t + 1.6\ mm$ to $t + 4.8\ mm$. The 1.6 to 4.8 mm (0.085 to 0.189 in.) is the estimate of the additional width of the cap beyond the bevel. For a narrow bevel, such as the CRC bevel that is used for automatic welding of thicker section pipe, the root bead width may be slightly larger, 2.5 to 4.5 mm (0.10 to 0.18 in.), while the cap width is smaller, $0.175\,t + 5.68\ mm + 1.6\ mm$ to $0.175\,t + 5.68\ mm + 4.8\ mm$. These rough approximations can allow us to fill in the inequalities from the previous paragraph and thus plot the cases where the shear band can fit in the lower strength HAZ as in Figure 85 for the standard weld bevel and the CRC bevel. The same can be done for the case of undermatching welds, as shown in Figure 86.

The ranges of values for cap HAZ width in Figures 90 and 91 go beyond what would normally be expected. A cap HAZ softened width of 3.5 mm (0.14 in.) was discussed above and may be considered to be near the upper limit of softened width due to common procedures.

Assuming a cap HAZ softened width of between 1 and 3.5 mm (0.04 and 0.14 in.) allows us to recognize that many cases considered for application will not show the behavior with shear bands running through the HAZ. Many cases examined for use of high-strength pipe, X-80 and higher, have looked at thicknesses for 14 mm (0.55 in.) and greater and automatic welding for the great majority of welds. This combination, given that bevels like the CRC bevel would be preferred, falls into the area where the shape of the HAZ prevents the formation of full thickness shear bands.

The results of this simple analysis show that some pipes do not form full shear bends in the softened HAZ unless the HAZ is unusually wide. Pipes larger than 16-mm (0.63-in.) thick and pipes with narrow bevels that are larger than 13-mm (0.51-in.) thick do not form shear bands in soft material that go across the entire pipe thickness.

If the interior shear bands that cross near the weld root are inhibited by higher strength weld metal, then the rules of thumb from the previous paragraph can be tightened down further. Pipes larger than 11-mm (0.43-in.) thick and pipes with narrow bevels larger than 8-mm (0.31-in.) thick do not form shear bands in the soft HAZ alone.

Cases where the pipe is not sufficiently thick to inhibit the formation of shear bands will be the ones that can get the most advantage from reducing the HAZ softened zone width.

9.1 An Estimating Tool That Includes Root Flaws

The estimating tool described in the last section can also be modified to account for the presence of a root discontinuity. The tip of the root discontinuity is chosen as the initiating point for the shear band rather than the corner at the edge of the weld root.

Figure 92 shows a schematic of a weld with a root flaw. The flaw tip is defined in position by the two parameters: a the flaw depth and g the offset toward the weld center from the root corner. The position of the flaw in Figure 92 is designed to provide an illustration, but does not describe a realistic case of flaw position.

In the models used above for the 10-mm-(0.39-in.)-thick pipe and the 20-mm-(0.79-in.)-thick pipe, a fusion line flaw that was 3-mm (0.12-in.) deep originating at the root corner would have an offset g of very close to zero. The depth of 3 mm (0.12 in.) has been a common one for estimating of pipeline resistance to flaws, as it has been used in standards such as CSA Z662.

Figure 93 shows the plot of when a shear band can fit in the HAZ when it begins from a 3-mm-(0.12-in.)-deep fusion line flaw. The parameter g is assumed to be 0.

Figure 94 shows the modified plot of when the shear band can fit into the lower strength material of the HAZ and weld, for cases where the weld is not overmatched compared to the base material. The values of a of 3 mm (0.12 in.) and g of 0 mm (0 in.) are assumed.

This model indicates that shear bands within the weak material around the girth weld become a preferred mode of deformation for a wider variety of thicknesses and HAZ sizes when a root flaw is present.

However, the initial primary thicknesses of use for high-strength steels, in the range from 15 to 20 mm (0.59 to 0.79 in.), with automated welds still fall outside the range where the shear band in the softer material can reach across the entire thickness from a root flaw of 3-mm (0.12-in.) depth.

One of the limitations of the model is that it assumes that the 45-degree orientation of the shear bands compared to the pipe axis remains constant in the case with the flaw. Cases with deep flaws would have some rotation of the pipe wall around the flaw and thus could be expected to change the angle. This would also happen because the shear analysis assumed a roughly symmetric deformation pattern on both sides of the weld.

10.0 Constraint Effects of Pressure and Axial Loading

The discussion above in Section 7.3 described some of the parameters related to constraint and compared the model results for X-100 girth welds to the parameters of interest in these models.

Constraint is primarily used as a parameter not for assessing un-cracked structures, but for assessing crack-like flaws in structures. If constraint is high, as in standard fracture toughness specimens, deformation tends to be localized around the crack tip. For lower constraint cases, the deformation is less localized, perhaps with more deformation of a nearby free surface.

10.1 Constraint Effects on Previous Fracture Measurements

The available tests in the literature have not been on pipeline materials. Biaxial testing has been completed on pressure vessel plate for nuclear reactors. Garwood[28] reported tests at room temperature of large cruciform specimens and wide plate specimens of A533B steel with central sections 25-mm (0.98-in.) thick. Tests were done under tension loading both uniaxially

and biaxially. Crack growth resistance was found to be the same in terms of CTOD for the uniaxial and biaxially loaded cases until the crack grew to through thickness. At that point noticeable differences emerged.

The Garwood tests did show changes in the forces required to achieve a particular CTOD value for uniaxial and biaxial loading. Indeed, the 25-mm (0.98-in.) thickness was a compromise designed to allow the center section to achieve full failure of the flawed section without yielding in the 50-mm-(1.97-in.)-thick arms under the biaxial loading conditions.

The Garwood tests have been used by others as a justification for only testing biaxial constraint effects in a relatively narrow temperature range. Bass et al.[29] chose to perform testing on surface cracks and limited their testing to the transition temperature range. They expected that biaxial constraint effects would not be important either at much lower temperatures without much crack tip ductility and would not be important where ductile failure modes dominated. Some testing in the lower part of the transition temperature regime indeed showed little effect of constraint.

10.2 Constraint Parameters

Three types of constraint parameters have been used for assessments of model girth welds. These are T, Q and variants of Q, and Weibull stress.

T-stress is computationally the simplest, but not easily converted to a parameter appropriate for distributed plastic strain. The T-stress is the component of stress parallel to the crack surfaces and perpendicular to the crack tip in the region around the crack tip. There is no singularity in this direction, so T can be averaged over a region around the crack tip. It is common to normalize the T-stress by dividing it by the remote stress perpendicular to the crack surfaces, as T/σ_r .

Jayadevan et al.[24] have calculated the T-stress around the crack tip for external surface cracks in a variety of pipe sizes with axial loading. They showed that the ratio of T-stress to the remote axial stress tended to be between -0.5 and -0.6 for most cases of interest to pipeline construction assessment.

Q stress is also a normalized stress, usually defined as the difference between the stress condition ahead of the crack tip in the actual situation and the stress condition in a case where the yielding around the crack tip is small in scale compared to the surrounding material. These stress conditions can be defined as the ratio of the stress to the yield strength at a location of

interest which is usually chosen as a distance of $2J/\sigma_y$ ahead of the crack tip. Q can be defined using either the hydrostatic stress or the stress perpendicular to the crack plane. Q can be determined for both elastic and elastic-plastic cases, but requires two different finite-element models, with the additional model used for the small-scale yielding case.

One of the weaknesses of Q is the definition of a location ahead of the crack tip may not be at the area of highest hydrostatic stress at that distance from the crack tip. Figure 95 shows an example where another point can be found with higher hydrostatic stresses for the plane strain case.

Weibull stress methods describe the crack tip stresses by integrating a stress parameter in the plastic zone ahead of the crack tip. Test specimens results are considered most relevant to service conditions when they match in Weibull stress rather than in CTOD or J. Different methods of defining the appropriate integral have been used. The most common stress in the integral is the maximum principal stress for the element. However, the most extensive analysis of the Weibull stress for pressurized pipe used a more complicated stress formula, imagining tiny penny-shaped cracks at all possible orientations within the elements and defining the normal stress and the peak shear stress on these microcracks. Shimanuki and Inoue[23] used an equivalent CTOD method based on local Weibull stress around the crack tip to get a single parameter that could be used with specimens of differing constraint.

10.3 Elastic Model Results

Elastic models are a way of easily determining general effects, although they cannot represent the conditions of yielded material most interesting for strain-based design. A particular advantage of elastic models is that T-stress can be easily and directly calculated. Standard routines are available in general-purpose finite-element programs such as ABAQUS.

T-stress calculations are also available in summary form in Sherry et al.'s compendium of solutions.[30] While none of these directly address the issue of biaxial loading of pipe, some of the listed cases can give guidance and compare with the testing already mentioned.

Center cracked panel results are available from the T-stress compendium which include both uniaxial and equal biaxial loadings. The T/σ_r values are all smaller than -1 for the uniaxial loading case, while they are between 0 and -0.5 for the equal biaxial load in the plane of the plate. This corresponds to the case where Garwood observed a large constraint effect.

Results for an internal crack in a cylinder are only available in Sherry's compendium for the uniaxially loaded case, which for small crack depths is very similar to the edge crack in a plate, regardless of diameter-to-thickness ratio.

Models comparing uniaxial and biaxial loading were designed for an internally cracked cylinder [D = 1000 mm (39.3 in.)] with crack depth of 20% of the wall thickness of 10 mm (0.39 in.), as shown in Figure 96.

Different boundary conditions were used to check their effects. The axial strain was applied three different ways:

- Applying an end strain
- Applying an end stress
- Applying an internal pressure while the ends were held fixed.

This last case causes the pipe to have axial stress since shortening of the pipe length is prevented. Each of these cases gave a constant ratio of T/σ_r as the loading was increased to its final value, as shown in Figure 97. The values for these three cases were all within a narrow band between -0.55 and -0.65. It may come as a surprise that the most negative of these three cases was the one with applied pressure, even though pressure adds a stress in the hoop direction.

Some additional combination cases were run with the following loading orders: pressure was applied after the end strain was applied, pressure was applied after end stress was applied, end strain was applied to pressurized pipe where the ends had been fixed, and end stress was applied to pressurized pipe where the ends had been free. These are shown on Figure 97, as well. Because the model was elastic, the order of axial loading and pressurization did not matter for the final J and T results. Also, little difference was observed in T/σ_r, which remained in the range from -0.55 to -0.65. However, the J value was quite different between the different methods of application.

10.4 Plastic Model Results

A simple stress strain curve was chosen for the elastic-plastic models, as shown in Figure 98. A linear increase in strength was used for the work hardening above a yield strength of 600 MPa (87.0 ksi). Below yield the material was elastic with an elastic modulus of 200000 MPa (29000 ksi) and a Poisson's ratio of 0.3.

When the applied strain in the axial direction is small, plasticity changes the J results and hydrostatic stress contours very little compared to the elastic cases described above. Figures 99 through 102 show the hydrostatic stresses around the crack tip. Figure 99 shows the case of an axial strain of 0.1%. The hydrostatic stresses around the crack tip for the pressure case in Figure 100 are similar, although the overall strain and J value are lower. Figures 101 and 102 show the hydrostatic stresses for combinations of axial strain and pressure with the stain applied first in Figure 101 and of axial strain and pressure with the pressure applied first in Figure 102. There is little difference between these last two figures. The progression of J as the loading is applied for the two orders of loading is shown in Figure 103.

However, large plastic strains, here 4% remote strain, can cause very significant differences from the elastic results. Significant differences are also observed based on the order of loading, between axial strain first followed by internal pressure and internal pressure on a pipe with fixed ends followed by axial strain applied through those ends. The J progression results are shown in Figure 104. Here, J is shown to be little changed by following the axial strain with the application of internal pressure. However, the effect of pressure applied first is to greatly increase the J value from the axial loading.

While T-stress cannot be reliably calculated for such high plastic strains, the relative constraint can be measured by comparing the hydrostatic stresses around the crack tips.

Figure 105 shows the axial stress both for 4% axial strain alone and for 4% axial strain followed by pressure the ends fixed in position. There is little difference caused by the addition of pressure.

Figure 106 shows the hydrostatic stresses for the same two cases. These are much larger around the crack tip. Since there is little difference in J between these two cases, the Q can be estimated to be higher (more positive) for the case with internal pressure.

Figure 107 shows the axial stress both for 4% axial strain and internal pressure, both with the strain applied first and with the axial strain applied second. The crack mouth opening is much larger in the second case, with correspondingly greater stresses around the crack tip.

Figure 108 shows the hydrostatic stresses for the same two cases. These are quite similar. This indicates little effect of the pressure on constraint, although there may be an effect related to the higher J moving the measurement point for Q.

10.4.1 J-Q Calculations

Calculations where both J and Q were obtained were performed by using two finite-element models in combination. Figure 96 shows the model for the pipe with a 20% wall internal notch. Figure 109 shows the additional model needed for calculating Q. This model, a circle with a crack tip at the center, is loaded using tractions at the outside surface. The circle is reduced to a half circle using symmetry along the crack plane in the figure. The tractions on the outer surface are defined by the equations of a crack tip in an infinite space with elastic loading.

Two methods of calculating Q from the two models are used below. Both define a position ahead of the crack tip by a distance r where and evaluate quantities on both models at that position. The Q value is the difference between the ratio of the stress at that location in the cylinder model to the yield strength and the same ratio from the circle model. An optional method was used for comparison that used hydrostatic stress at this location, rather than stress across the crack tip. The Q_h value, using the optional method, is the ratio of the hystrostatic stress at that location in the cylinder model to the yield strength and the same ratio from the circle model.

The point ahead of the crack tip that is used for calculating Q depends on the value of J. As was noted above, J can change significantly for cases where internal pressure is added. So Q will also be changed due to the change of position for its calculation.

Calculations were performed for a range of axial strains up to 4%, both for cases with no pressure initially and for cases with internal pressure applied before the axial strain. The results are shown in Figure 110 as a function of applied strain, using the primary method for calculating Q. Increasing the axial strain increased J and made Q more negative for both the pressure and no pressure cases. Figure 111 shows the relation between J and Q for both the pressure and no pressure cases.

These results show similar behavior to that observed for the elastic T-stress. The addition of internal pressure does not have a large influence on Q. Q was slightly more negative for the added pressure case at constant applied strain.

As a further check, the hydrostatic method was used to calculate Q. The results are shown in Figure 112 as a function of applied strain. The difference between the pressure and no pressure cases was slightly smaller using this calculation method. Figure 113 shows the relation between J and Q_h for both the pressure and no pressure cases.

An unexpected feature of the relationship of J and Q is that the pressure reduces constraint for low J values and increases constraint for higher J values. The switch occurred between J of 400 and 600 N/mm.

Further checks were performed with the model size doubled, and thus with radius 2000 mm (78.7 in.), thickness 20 mm (0.79 in.) and notch depth 4 mm (0.16 in.). The results indicated very little change in Q versus applied strain, as shown in Figure 114. The J values did increase with the greater flaw depth, roughly as the square root of flaw depth. Hydrostatic calculation of Q did not change the Q results significantly, as shown in Figure 115.

10.5 Conclusions

It should be recognized that internal pressure can create major changes in the relation of applied axial strain and CTOD.

Hoop stress from pressure should not be expected to have a major effect on the T-stress, when that stress is used as a measure of constraint. Indeed, hoop pressure stress can be shown for elastic cases to make the T-stress slightly more negative, rather than more positive.

Q calculations of plastic constraint indicate that internal pressure applied before the axial strain can lower constraint slightly rather than raising constraint for a given remote applied strain.

11.0 ECA Methods for Strain-Based Design of Girth Welds

The design process for girth-welded pipelines that can experience high applied strains will usually need to include an ECA to demonstrate that the choices made regarding the girth weld area provide sufficient resistance to fracture under the peak strains. The methods that are used for the ECA must be applicable to the situation. Today's situation in ECA methods is that routine methods are available for strains up to the yield strain in tension and extensions of these methods have been used for higher strain, although the methods have not become routine standard methods. As the strain in the pipe design is increased up to 2% strain and beyond, very few methods are available and these methods may not cover all the required behavior.

The area of high strain ECA methods has been and is currently an active area of research. This section is designed as a summary. More extensive work in this area has been completed by Wang et al.[31-33]

High strain for a pipeline may mean either high strain in compression, high strain in tension or both in a given length of pipe. The ECA methods examined in this section relate to the tension strain. The compression strain area of the pipe can fail by cracking or rupture, but the methods for demonstrating sufficient resistance are related to the previous behavior of pipe wrinkling under the compression straining. So compression strain will not be considered here, except as part of cycles of strain.

11.1 Basic Methods

The basic methods for ECA have been built up over the years by combining methods for assessing brittle fracture, ductile fracture, and local and global plastic collapse. Much of the work underlying these methods has been done in load control. Methods more appropriate to displacement control or combinations of load and displacement control are the focus of this discussion.

11.2 Inputs to the Assessment

11.2.1 Toughness

The toughness input to assessments for high strain design must be applicable to the material being assessed, the temperature, and the constraint of the imperfections to be assessed. It has been common to use toughness values correlated from Charpy tests for the lowest strain cases. For higher strains, directly measured toughness values of CTOD or full resistance curves where CTOD is measured as a function of crack advancement are needed.

The constraint requirement has usually been met by choosing a specimen known to have high constraint, such as a single-edge notched bend specimen, with a crack tip near the center of the specimen thickness. Recently, this approach to providing sufficient constraint has been recognized as an important source of conservatism in ECA. Other specimen types, particularly the single-edge notched tension (SENT) specimen with a notch depth at least equal to the imperfection depth to be assessed, have been proposed to avoid the additional conservatism. This approach has particularly been applied to cases of reeled pipe installation, where the peak strains are well controlled and known to be in axial tension in the pipe wall.

One of the ways of accounting for the differences in constraint is use an apparent CTOD toughness rather than the measured result of the CTOD test when done in bending. The multiplier has been found to depend upon the mode of failure in the CTOD test. The mode of failure is listed on the test result as δ_c, δ_u, and δ_m. The last of these cases is the maximum

load case, where the crack is still advancing in a ductile manner even after the peak load in the test has been reached. For this case the apparent toughness cannot be estimated higher than the testing result of the bending CTOD test.[33] For highly ductile materials this may give an advantage to testing methods applying tension directly rather than correlating with the bending CTOD test. On the other hand, the other two cases, which both include sudden crack advance, will be affected by the constraint and thus can have a higher apparent CTOD in the pipeline than in the bending CTOD test. The multiplier has been estimated at 2 to 3. Wang has provided a justification for a value of 3.

11.2.2 Flaw Size, Position, and Type

The characteristics of the imperfection being assessed are critical to the assessment results. This includes its position with respect to the weld and with respect to the loading conditions. The type of flaw such as volumetric, planar perpendicular to the pipe axis, planar perpendicular to the weld axis, and planar perpendicular to the pipe radius, can also be an important influence.

It has been standard to assess pipe girth welds using assumed flaw sizes, shapes, and positions as part of determining the allowable flaw sizes that can be accepted during the post-weld inspection. These assumed flaws are generally chosen to be crack-like, oriented perpendicular to the largest stresses, with sharp tips, where fracture assessment is appropriate. Assessments may be completed for any or all of the following choices:

- Surface at root or surface at cap or embedded
- Long flaw in the hoop direction or short flaw in the hoop direction
- Weld metal centerline or fusion line flaw position.

Many projects use an approach of setting conservative limits on flaw sizes for acceptance criteria by assessing only the more conservative choice, surface flaws rather than embedded, long flaws rather than short ones, and flaws at the lower strength material of either base metal or weld metal.

11.2.3 Strength

Both strength for the area of interest and relative strength of the different components of the weld area are important to the assessment.

It has been common practice to assess the weld area as though there were only two materials in the weld area from a strength perspective: a base metal strength behavior that extends to the fusion line and a uniform weld metal strength behavior that includes the entire region within the fusion line. If the weld metal strength is undermatched, then the HAZ is assumed to have the behavior of the weld metal, thus moving the boundary from the fusion line to the outer edge of the HAZ. This practice was included in BS7910:1999, but was updated to account for HAZ softening in the 2005 edition.

The strength assumption used can, in many ECA methods, affect the assumed residual stress from welding. This is of less interest to the strain-based design assessment ECA method, since the strain in excess of yield will relieve residual stresses at the weld joint.

As noted above, the strength properties of pipe can differ between the hoop direction and the axial direction. For the girth weld assessments discussed here, the strength of interest for the base pipe would be the axial direction strength, even though this may be below the strength in the hoop direction or even below the SMYS required for the hoop direction.

Two methods of inputting the strength behavior are widely used. In the simplified method only a small number of standard parameters are input, such as yield strength, tensile strength, and elastic modulus. The other method is to provide the stress-strain curve as a point-by-point representation so that the ductile fracture resistance can be accounted for more exactly. DNV has mentioned that they have used an intermediate method where the standard parameters, with the addition of the uniform elongation, the elongation at the ultimate tensile stress, are converted to a full stress-strain curve of Ramberg-Osgood form and then applied as though the point-by-point stress-strain curve were available.

11.3 Failure Assessment Diagram (FAD) Choice

There are seven methods of fracture assessment codified in BS7910 arranged at three levels from 1 to 3. These levels are 1A simplified method, 1B simplified method for manual calculation, 2A normal method with assumed stress-strain behavior, 2B normal method with measured stress-strain behavior, 3A tearing analysis with assumed stress-strain behavior, 3B tearing analysis with measured stress-strain behavior, and 3C J-integral tearing analysis. All but method 1B use a FAD for showing the acceptable region when comparing against multiple modes of possible failure. While the Levels 1A and 1B methods can account for strains above the yield strain, the simplifications used in these methods avoid some of the complications in combining fracture modes and may become less applicable at high strains.

The other five levels are each designed as a specific procedure to account for specific combinations of resistance to brittle and ductile fracture, as well as local and global collapse.

DNV F108[34] has recommended that Level 3B be the primary assessment level for strain-based design, since it combines a physically reasonable recognition of ductile tearing as a participating mechanism during fracture, a reasonable recognition that the stress-strain curve is appropriate tuning technique for making the assessment specific to the pipe material, and does not require extensive finite-element modeling of cracked bodies.

However, DNV[35] has also recognized that the primary basis for each of these five levels is analysis done with the assumption of load control. So features of the assessment must be modified to allow for a strain-based assessment that is based upon displacement-controlled loading, or at least a combination of load control and displacement control where all load-controlled failure modes have been demonstrated not to apply.

Modifications to the plastic collapse criteria are important for applications to high strains. The assumption in BS7910 is that plastic collapse failure occurs when the reference stress equals the flow strength of the material, the average of yield strength and ultimate strength. DNV F108 has recommended replacing this assumption with one where plastic collapse failure occurs when the representative stress reaches the ultimate strength of the material.

11.3.1 Non-FAD Methods

Non-FAD methods are available from some standards for pipelines. The methods are designed to check only a single failure mode and to eliminate others by specifying parameters that guarantee sufficient resistance to the other modes.

11.4 Applied Strains

For a strain-based assessment, the general applied strain must be carried to the local area where the imperfection is being assessed. This can involve several corrections to account for specific features of the local welded area: the variation of strength with position, the welding residual strains, the local strain concentrations due to the existing or planned geometry of the weld area, and the local strain concentrations due to the allowed variations of the geometry of the weld area.

11.4.1 Variation of Strength and Thus Strain with Position

Variation of strength in the weld area, as has been mentioned before, has been accounted for in BS7910 by the two-material assumption. Other sections of this report deal with the idea that this assumption may not be adequate for the higher-strength base metals where the lowest strength material can be found in the weld root area or, more likely, in the HAZ material.

The effect of the lower strength region in the HAZ area is made more important for the case where the pipe is under internal pressure during the axial straining.

11.4.2 Welding Residual Stress or Strain

BS7910 has many useful estimates of the welding residual stress for different situations. One of these is commonly applied to as-welded joints to cover a wide variety of situations. This assumes that anywhere in the weld area and into the HAZ the residual stress parallel to the weld is at the magnitude of the yield strength in tension for the material in which the flaw is located. The residual stress perpendicular to the weld is chosen based on the lower of the yield strength of the weld metal and the base metal. There is a note relating to the need to get mechanical properties of the HAZ if HAZ softening is present. An option is included in BS7910 for cases of high applied stress, where the residual stress estimate is allowed to be reduced to $\left(1.4-\sigma_{ref}/\sigma'_f\right)\sigma'_Y$ where the reference stress is the stress from the plastic collapse analysis at the net section, and the flow strength and the yield strength are indicated by the prime as being at the appropriate temperature.

For nearly all cases where strain-based design will be useful, the ratio of the reference stress to the flow strength will be greater than 0.9, so the standard prediction for residual stress would be at 0.5 times the yield strength or smaller.

Bratfos[35] has recommended that the residual welding strain for as-welded joints be estimated as the yield strain, in their definition the elastic strain at yield plus 0.2%. For common pipe grades, this works out to adding about 0.5% strain to the applied strain in the weld and HAZ. This is more conservative than is recommended by BS7910.

Residual strain from welding will, of course, be the consequence of self-equilibrated stress distribution. The distribution is the consequence of the weld metal and neighboring areas shrinking as the weld cools. The primary direction of residual stress generation in girth welds is the hoop direction, but several features of girth welding also induce residual stress in the pipe axis direction.

11.4.3 Geometrical Strain Concentration

The local strain concentrations due to geometry can include misalignment across the weld, differences in stiffness of the pipes being joined, and thickness variations introduced by machining, such as counterbore. Estimates of the stress concentration factors for such geometrical conditions are widely available for the elastic case. The conversion of these estimates is required to strain concentration factors (SNCFs) that are applicable both when part of the cross section has yielded and when the entire cross section has yielded. The most common method has been to use the Neuber hypothesis[36] in a simple version, that the strain concentration factor is the square of the elastic SCF.

Neuber's hypothesis can also be applied in a slightly more complicated form, where SNCF is equal to the square of the elastic stress concentration factor K_t times the ratio of the nominal stress σ_n to the actual local stress σ_k. Furthermore, Neuber also had a mild notch version of the calculation of SNCF.

$$SNCF = 1 + \frac{\sigma_n}{\sigma_k} K_t \left(K_t - 1 \right) \tag{7}$$

This results in a substantial drop in SNCF, where the material strain hardens or where the stress concentration factor is close to 1.

Both of these are intended only when the plasticity is confined by surrounding elastic material. When the net section has yielded, different local strains are expected. Seeger and Heuler[37] have proposed a method for accounting for plasticity and strain-hardening in the net section. The proposed correction reduces the strain concentration, so it will be conservative not to include it.

Another geometrical effect can also reduce the plastic strain concentration factor. Misalignment of an area around the weld that is loaded in transverse tension can be drastically reduced once plastic hinges form. The plastic hinges allow the area to straighten out, thus limiting the bending strain at the plastic hinge to that which removes the original misalignment. This is most easily seen in the testing of misaligned plate joints. Misaligned pipes are more greatly restrained in the radial direction than the plates are in the thickness direction. This further limits the strain concentration that can be generated by misalignment.[38]

11.4.4 Applied Stress

To complete the assessment, the applied strains must be converted to applied stresses, which are used directly in most forms of assessment. This is done at the stage where the local modifications to the strain discussed in the last section have been included.

The conversion uses the stress-strain curve appropriate for the material around the flaw in the direction perpendicular to the flaw faces. The stress-strain curve should be the true-stress/true-strain curve rather than the one using engineering stress and strain. This will prevent a non-conservative estimate of the stress, particularly at relatively high applied strains.

11.5 Effect of Internal Pressure

The effect of internal pressure on the resistance of cracked bodies to fracture has only recently become a focus of study. Some general studies and current research activities can provide guidance. Section 10 discusses the effect of internal pressure on fracture resistance.

11.6 Additional Behavior – Crack Growth into Different Material

Cracks that occur at the fusion line can grow in different directions and thus enter different types of material. Methods that account for ductile tearing must deal with this complicating factor. Methods that use initiation toughness only avoid these complications. Yet for high strain applications, the real behavior of the component with a flaw would be expected to be a combination of crack tip blunting, ductile tearing from the crack tip, and ductile failure, provided that other failure modes, such as brittle fracture, plastic collapse, and failure from another location do not intervene. This was the primary reason in DNV F108 for preferring the FAD 3B method from BS7910.

As a crack extends by ductile tearing into a different material region, the material stress-strain behavior will depend upon the location of the crack tip. The ductile tearing resistance will, in turn, depend upon the material stress-strain behavior.

11.7 Additional Behavior – Cyclic Loading

Multiple-cycle loading places additional demands on the ECA, since the consequences of earlier cycles must be carried forward to the subsequent cycles. For multiple-cycle loading, the three primary ways to account for changes on the previous cycles are by updating the crack size, by updating the stress-strain curve, and by updating the toughness.

As with ductile tearing, assessment of cyclic loading also needs to account for the change in material stress-strain curve as the crack tip moves. The crack tip can move its plastic zone into different material as it grows.

12.0 Comparisons to Installed Capacity in High-Strength Steel Pipelines

High-strength steel pipelines with grade X-80 and higher are becoming more widely used. As discussed above, they are also the pipelines where some HAZ softening can be routinely expected. The results described in the previous sections show that specific combinations of HAZ softening, internal pressure, pipe and weld geometry, and longitudinal strain can cause high strain concentrations in the HAZ.

Table 33 shows several examples from around the world of pipelines in higher-strength steels. The primary applications have been on pipes with wall thicknesses above 12 mm (0.47 in.) with pipe diameters of more than 762 mm (30 in.). The Roma to Brisbane loop in Australia is an important exception, with a wall thickness of only 8.8 mm (0.35 in.).

This Roma to Brisbane line falls into a range of thickness where the mechanism of failure is more likely to be a shear band through the HAZ when the pipe is loaded in high strain service.

The other pipes, given their larger diameter, would not fall into the case where this failure mode was probable, unless unusual conditions were met. Higher-strength pipelines have been designed in this thickness range with the expectation of overmatched welding consumables, primarily automated welding with narrower bevels than the standard bevel, and inspection to demonstrate that welds do not include initial flaws approaching the 3-mm (0.12-in.) depth.

13.0 Path Forward

The path forward toward standardization of strain-based design procedures can be sketched, based upon the current state of technology, the current standards, and the plans of the pipeline industry.

Strain-based design pipelines have become part of the toolkit of pipeline builders in many environments: arctic on-shore, arctic on-shore, deepwater subsea, and on-shore in areas of unstable soil or subsoil.

For offshore applications, there are three cases of interest, one where the pipe laying process uses strain-based design, one where the pipe is in an operating condition when the plastic strain is applied, and one where strain-based design is applied both to the laying and to subsequent service.

13.1 Institutional Hurdles

Some national standards bodies have a single primary document that can be referenced for pipeline design and construction. Under these conditions it is obvious where new provisions standardizing strain-based design should go. Adding these provisions may still require a difficult process, since usually only a small fraction of future projects will use strain-based design pipelines.

The U.S. pipeline standards system is much more complicated, because several organizations provide standards that are used over part of the range of pipeline design and construction. Fabrication is separated out in API 1104. Design is covered by the ASME B31 series of documents. Government regulations have provided their own particular rules, referring to some provisions of the industry documents, but not to others. There have been recent efforts at improving the working relationship of the government with the standards organizations in the area of pipeline standards.

It is possible to take the guidance overall for strain-based design and break it into areas that fall primarily into design and areas that fall primarily into fabrication. The design areas would be strain demand, and strain capacity in compression. The fabrication areas would be material property characterization and strain capacity in tension.

Strain capacity in compression is placed in the design area rather than the fabrication area, since it is not strongly dependent upon the fabrication variables, with buckling modes usually initiating in the pipe base metal rather than in welded areas.

The material property characterization and strain capacity in tension are placed in the fabrication area, since tension capacity is strongly dependent upon the variation of material properties around girth welds and the failure modes usually initiate in weld areas.

The problem areas in this approach tend to be ones where material property characterization is important to strain demand in compression and where both tension and compression capacity may need to be checked against the strain demand.

Strain capacity during pipe laying operations appears to fall into a separate category, one that has been primarily been served by standards or similar documents from offshore classifications societies. API RP 1111 also covers allowable strains during pipe laying processes.

Some moves forward to improve coverage of strain-based design have already been made by the standards committees. API 1104 committees have authorized a sub-committee to look at the ECA acceptance of welding imperfections for strains above the current limit of 0.5%, thus entering the region of strain-based design.

13.2 Technical Hurdles

Some of the technical hurdles that must be met on the way to a standardized strain-based design process have been noted in earlier sections of this report. The primary area that must be defined is a complete method for defining the tensile capacity, given that tensile capacity is sensitive to many parameters and local variations in properties.

An area that is now receiving much interest is transferability of small-scale data to the full pipe strain-based design for resistance to tensile failure in flawed girth welds. Current methods of strain-based design assume one of three answers related to transferability: assuming direct transferability of curved wide plate test results to full pipe strain-based design, assuming direct transferability of CTOD measured on small-scale high constraint specimens such as SENB, and assuming indirect transferability of CTOD with a correction for lower constraint in the full pipe. The lower constraint method has been implemented in some standards by recommending another test specimen design than the SENB specimen.

One area that has not been extensively studied is the addition of other strain concentrations in the weld area, such as thickness variation or misalignment. It appears from this project that there can be interactions between internal pressure and strain concentration from misalignment.

The strain concentration approach can also be extended to account for welding residual stresses, which were not included in the assessments in this report. To a first approximation, these residual stresses should be extensively relieved by the plastic strains around the girth weld. A closer look at this process would quantify the relief of residual stress under the combination of pressure loading and axial strain. The residual stress models would need to include a hardening model for the materials that is more complicated than that used in this study, since the Bauschinger effect will be important in describing stress and strain fields that change sign during the loading history. The residual stress effects would appear to be more important for cases with moderate amounts of plastic strain applied and limited toughness

against brittle fracture, since residual stresses are recognized as having more effect on brittle than on ductile fracture.

Outside the primary area of tensile capacity, the main technical hurdles relate to interaction of failure modes and to reliability methods. Compression strain capacity may be much larger for single events than for repeatedly cycles of displacement controlled loading. The question of whether early cycles with plastic strain have a damaging effect on future fatigue performance has been answered for risers with demonstrations of no effect. But the intermediate range where subsequent cycles are plastic but not as large as those early cycles has not been a focus of full study.

Reliability methods can be confidently applied where all the important variables have been captured and documented for the failure modes. Reliability methods for dealing with the demand side of strain-based design may be the hardest to standardize.

14.0 Conclusions

Previous work by EWI had indicated that a combination of softened HAZ and internal pressure could cause high strain concentrations at the HAZ under conditions with plastic axial strains. Work in this project has been directed to further understand this behavior and its limits.

HAZ softening has been observed for welds on X-70 and X-80 steels. Cases with little or no softening have also been observed for other welds in these same grades. This project extended these findings to X-100 steels, with cases of obvious softening and little or no softening observed. Higher heat inputs and larger weld volumes per pass associated with SAW as compared to GMAW have been correlated with greater softening in each of these pipe grades.

This project has demonstrated that the conditions required for the high strain concentration in the HAZ are dependent upon the configuration of the weld. Welds that meet the other criteria for high strain concentration but cannot fit a shear band at 45 degrees to the pipe axial direction into the softer material will not see the high strain concentration that was observed in the previous project.

The 45-degree shear band hypothesis means that some areas of the HAZ are more important to the formation of high strain concentrations and others are less important. The most important regions are those near the fusion line at the root of the weld and those in the SCHAZ just

outside the visible HAZ on the cap side. Neither the width of the HAZ at the root, nor the amount of softening at the cap adjacent to the fusion line was found to be important parameters.

Manual welds will be more likely to be susceptible to the elevated strain concentration in the HAZ than automatic welds for a combination of geometrical reasons. Manual welds are commonly designed with wider bevel openings, which place the HAZ closer to a 45-degree angle with the pipe axis. Manual welds may also be made with lower strength consumables in the root that extend the region of lower strength material beyond the HAZ.

Many girth weld configurations, particularly those in large thicknesses, will not be likely to form shear bands at the girth weld areas under the applied combination of strains and pressures in service.

Examinations of models for pipes greater than about 14-mm (0.55-in.) thickness suggested that strain concentration factors of about 1.5 are reasonable approximations for both weld centerline and HAZ areas. Smaller strain concentrations may be appropriate for specific cases, particularly in pipes with a significant difference between the hoop yield strength and axial yield strength.

Internal pressure increases crack opening for a given applied strain. It does not increase constraint around girth weld flaws. This should be considered when ECA are performed.

High-low misalignment can increase the strain concentration for combinations of internal pressure and axial strain. Some strain concentration is observed with high-low and axial strain alone, but the addition of internal pressure tends to localize the strain into a single narrow shear band from the high side of the root to the low side of the cap.

15.0 References

1. Mohr, W. C., “Strain-Based Design of Pipelines”, report to Minerals Management Service, Project Number 434, (www.mms.gov/tarprojects/434.htm), October 2003.

2. Hukla, K., Heisterkamp, F., and Frantov, Y., “An Economic Approach to Pipe Steels with High Toughness and Good Weldability”, Pipeline Technology Conference, Oostende, Belgium, Vol. A, pp. 4.43-4.51, October 1990.

3. Lillig, D. B., Hoyt, D. S., Hukle, M. W., Dwyer, J. P., Horn, A. M., and Manton, K., “ Materials and Welding Engineering for ExxonMobil High Strain Pipelines”, Proceedings of the Sixteenth International Offshore and Polar Engineering Conference, San Francisco, Vol. 4, pp. 8-17, 2006.

4. Kim, C. M., Lee, J. B., and Yoo, J. Y., “A Study on Metallurgical and Mechanical Characteristics of the Weld Joint of X80 Steel”, International Offshore and Polar Engineering Conference, Seoul, South Korea, pp. 158-162, June 2005.

5. Johnson, M. Q., “Evaluation of Welding Consumables and Processes for X100 Line Pipe Steel”, Pipeline Research Council International Final Report PRCI-185-9829, October 2003.

6. Widgery, D. J., “Welding High Strength Steel Pipelines – A Consumable Manufacturer’s View”, 3rd International Conference on Pipeline Technology, Brugge, Belgium, Vol. II, pp. 499-508, May 2000.

7. Adeeb, S., Horsley, D., Yan, J., Sutton, M. A, and Reynolds, A. P., “Local Stress-Strain Response of an Axial X100 Girth Weld under Tensile Loading using Digital Image Correlation”, Proceedings of the International Pipeline Conference, Calgary, Alberta, paper IPC2006-10330, 2006.

8. Kim, W. S., Baek, J. H, and Kwon, D., “Failure Assessment Diagram for Assessing Cracks in the Weldment Heat Affected-Zone of a Natural Gas Pipeline”, Pipeline Technology Conference, Ostend, Belgium, Vol. 3, pp. 1503-1516, 2004.

9. Düren, C. F. and Niederhoff, K. A., “Hardness in the Heat Affected Zone of Pipeline Girth Welds”, Welding and Performance of Pipelines, London, England, Vol. 1, Paper 20, November 1986.

10. Baek, J. H., Kim, Y. P., and Kim, W. S., “Effect of Orbital Automatic Welding on the Weld Metal Mechanical Properties in API 5L X65 Natural Gas Transmission Pipe”, 2000 International Pipeline Conference, Calgary, Vol. 1, pp. 177-184.

11. Ishikawa, N., Shinmiya, T. and Igi, S., “Toughness Evaluation on Seam Weld HAZ of High Strength UOE Linepipe”, Proceedings of the International Pipeline Conference, Calgary, Alberta, paper IPC2006-10245, 2006.

12. Masuda, T., Watanabe, T., Hagiwara, N., Yatabe, H., Kawaguch, S., Motohashi, H., and Fukuda, N., “Application of X80 in Japan: Summary”, 4th International Conference on Pipeline Technology, Ostend, Belgium, Vol. 1, pp. 31-39, May 2004.

13. Ishikawa, N., Endo, S., Igi, S., Glover, A., Horsley, D., Ohata, M., and Toyoda, M., “Ductile Fracture Behavior of Girth-Welded Joints and Strain-Based Design for High-Strength Linepipe”, 4th International Conference on Pipeline Technology, Ostend, Belgium, Vol. 1, pp. 81-97, May 2004.

14. Laing, B. S., Dittrich, S., and Dorling, D. V., ”Mechanized Field Welding of Large Diameter X-80 Pipelines”, 2nd International Conference on Pipeline Technology, Ostend, Belgium, Vol. 1, pp. 505-512, September 1995.

15. Kawanishi, Y., Masuda, T., Toyoda, M., Suzuki, N., Yatabe, H., and Nose, T., “Full-Scale Large Deformation Tests and Ultra Low Cycle Fatigue Tests for Evaluating X-80 Linepipe

Performance", 4th International Conference on Pipeline Technology, Ostend, Belgium, Vol. 4, pp. 1881-1894, May 2004.

16. Huang, Z., Kai, M., Liu, J., Kong, J. and Wang, Y., "Adaptability of X80 Steel and its SAW Welding Wire to the Welding Procedure", Proceedings of the International Pipeline Conference, Calgary, Alberta, paper IPC2006-10193, 2006.

17. Hamad, F., Chen, X., and Collins, L., "High Toughness, Submerged Arc Girth Weld for Northern Pipeline Applications", Proceedings of the International Pipeline Conference, Calgary, Alberta, paper IPC2006-10168, 2006.

18. Hamada, M., Okaguchi, S., Shitamoto, H., and Komizo, Y., "Tensile Properties and Deformation Behavior at the Weld Position of X100 Line Pipe Steel", Pipe Dreamer's Conference, Yokohama, Vol. 1, pp. 289-305, November 2002.

19. Hammond, J., Blackman, S. A., and Hudson, M. G., "Challenges of Girth Welding X100 Linepipe for Gas Pipelines", Pipe Dreamer's Conference, Yokohama, Vol. 1, pp. 931-955, November 2002.

20. Hammond, J. and Millwood, N. A., "Construction of Ultra High Strength Steel Pipelines", 3rd International Conference on Pipeline Technology, Brugge, Belgium, Vol. 1, pp. 69-88, May 2000.

21. Rajan, V. and Hartman, D., "Metal Cored Welding GMAW Consumables Development for Girth Welding of X-100 Pipe", Proceedings of the International Pipeline Conference, Calgary, Alberta, paper IPC2006-10358, 2006.

22. Bowker, J. T., Gianetto, J. A., Shen, G., Tyson, W. and Horsley, D., "Cross-Weld Tensile Properties of Girth Welds for Strain-Based Designed Pipelines", Proceedings of the International Pipeline Conference, Calgary, Alberta, paper IPC2006-10400, 2006.

23. Shimanuki, H. and Inoue, T., "Assessment of Brittle Fracture in Girth Weld Joint of Pipelines Subjected to Internal Pressure and Bending Load", Pipe Dreamer's Conference, Yokohama, Japan, November 2002, revised version in addendum.

24. Jayadevan, K. R., Thaulow, C., Østby, E., Berg, E., Skallerud, B., Holthe, K., and Nyhus, B., "Structural Integrity of Pipelines: T-Stress by Line-Spring", Fatigue Fract. Engng. Mater. Struct., Vol. 28, 467-488, 2005.

25. Wang, Y.-Y., Liu, M., and Horsley, D., "Application of Constraint-Sensitive Fracture Mechanics to the Assessment of Girth Weld Integrity", Proceedings of the International Pipeline Conference, Calgary, Alberta, paper IPC2004-0525, 2004.

26. Kuwamura, H., "Fracture of Steel During an Earthquake – State-of-the-Art in Japan", Engineering Structures, Vol. 20, Nos. 4-6, pp. 310-322, 1998.

27. DNV RP-C203, "Fatigue Strength Analysis of Offshore Steel Structures", DNV, 2000.

28. Garwood, S. J., “The Significance of Biaxial Loading on the Fracture Performance of a Pressure Vessel Steel”, Pressure Vessel Integrity, ASMEPVP, Vol. 213, MPC Vol. 32, pp. 113-123.

29. Bass, B. R., McAfee, W. J., Williams, P. T., and Pennell, W. E., “Fracture Assessment of Shallow-Flaw Cruciform Beams Tested Under Uniaxial and Biaxial Loading Conditions”, Nuclear Engineering and Design, Vol. 188, pp. 259-288, 1999.

30. Sherry, A. H., France, C. C., and Goldthorpe, M. R., “Compendium of T-Stress Solutions for Two and Three Dimensional Cracked Geometries”, *Fatigue and Fracture of Engineering Materials and Structures*, Vol. 18, pp. 141-155, 1992.

31. Wang, Y. Y., Liu, M., and Horsley, D. J., “Some Aspects of Material and Welding Specifications for Strain-Based Design of Pipelines”, Proceedings of EPRG-PRCI-APIA 15th Joint Technical Meeting on Pipeline Research, Orlando, FL, 2005.

32. Liu, M., Wang, Y. Y., and Horsley, D. J., “Significance of HAZ Softening on Strain Concentration and Crack Driving Force in Pipeline Girth Welds”, 24th International Conference on Offshore Mechanics and Arctic Engineering, Halkidiki, Greece, 2005.

33. Wang, Y. Y., Horsley, D. J., Cheng, W., Glover, A., McLamb, M., and Zhou, J., “Tensile Strain Limits of Girth Welds with Surface-Breaking Defects – Part 2: Experimental Correlation and Validation”, Pipeline Technology Conference, Ostend, Belgium, Vol. 1, pp. 251-266, 2004.

34. Det Norske Veritas, “Recommended Practice DNV-RP-F108, Fracture Control for Pipeline Installation Methods Introducing Cyclic Plastic Strain”, January 2006.

35. Bratfos, H. A., “Use of Strain-Based ECA for the Assessment of Flaws in Pipeline Girth Welds Subjected to Plastic Deformations”, Pipe Dreamer’s Conference, Yokohama, Japan, pp. 957-986, November 2002.

36. Neuber, H., Über die Berücksichtigung der Spannungskonzentration bei Festigkeitsberechnungen, Konstruktion, Vol. 7, pp. 245-251, 1968.

37. Seeger T. and Heuler, P., “Generalized Application of Neuber’s Rule”, *Journal of Testing and Evaluation*, Vol. 8, No. 4, pp. 199-204, July 1980.

38. De Waele, W., Denys, R. M., and Lefevre, A., “Fitness-for-Purpose Assessment of Misaligned Welds”, Materials Science Forum, Vols. 475-479, pp.2663-2666, 2005.

Table 1. Laing et al.[14] Vickers 10 kg Hardness Data for 1980s and 1990s Vintage X-80

Pipe	Weld HV 10 Range	HAZ HV 10 Range	Parent Metal HV 10 Range
A	229-260	237-303	230-258
B	258-270	213-299	228-247
C	210-239	226-280	207-249

Table 2. Summary of Welding Procedures

Weld Name	Current (A)	Voltage (V)	Arc Speed		Arc Energy		Max. Interpass	
			(ipm)	(mm/min)	(kJ/in.)	(kJ/mm)	(°F)	(°C)
Automatic								
W1	245	24	18	457	19.6	0.77	302	150
W2	240	24	18	457	19.2	0.76	302	150
W3	245	24	18	457	19.6	0.77	302	150
W4	240	24.5	16	406	22.1	0.87	257	125
W5	225	24	16	406	20.3	0.80	257	125
W6	240	24	16	406	21.6	0.85	257	125
W7	161	21	13	330	15.6	0.61	302	150
W8	180	22.5	12	305	20.3	0.80	302	150
W9	200	22.5	13	330	20.8	0.82	302	150
W10	160	21	12	305	16.8	0.66	302	150
W11	Note 1	Note 1	Note 1	Note 1	Note 1	Note 1	302	150
Semi-Auto.								
SA-1	260	18.5	15	381	19.2	0.76	302	150
SA-2	175	20	15	381	14.0	0.55	302	150
Manual								
SMAW	185	20	9	229	24.7	0.97	302	150

Note 1: See Figure 5 for welding parameters

Table 3. Summary of HV 1-kg Hardness Data Compiled from Hardness Traverses in the Weld Metal and HAZ on X-100 Plate

	Root		Mid-Thickness		Cap	
Weld	**Weld**	**HAZ (Max/Min)**	**Weld**	**HAZ (Max/Min)**	**Weld**	**HAZ (Max/Min)**
W1	266	277/236	293	279/238	308	304/269
W2	257	282/231	268	258/246	300	291/242
W3	318	293/245	365	269/249	427	312/254
W4	250	236/223	268	251/231	270	286/222
W5	269	256/235	276	284/232	283	297/243
W6	301	251/236	357	261/220	417	302/246
W7	247	240/230	296	297/246	305	308/269
W8	257	251/232	280	254/233	290	269/243
W9	253	253/239	290	282/248	306	304/270
W10	262	266/236	297	255/236	316	308/256
W11	252	229/223	254	239/218	248	252/221
SA-1	300	302/256	273	276/246	290	304/269
SA-2	267	295/256	280	284/243	272	302/270
SMA	266	240/225	278	283/225	285	295/225

Table 4. Hammond et al.[19] Hardness (HV 10 kg) Results for X-100 Welds

			Av. Hardness (2 mm above root)			Av. Hardness (2 mm below cap)		
Weld	Consumable	Position	Weld Metal	HAZ	Base Metal	Weld Metal	HAZ	Base Metal
ML-B-DT-1	ER110S-G ER70S-6 root	3 o'clock	269 268	256 299	286 283	304 290	287 347	286 281
ML-B-DT-2	ER90S-G ER70S-6 root	3 o'clock seam	264 276	253 294	282 282	303 291	255 333	303 276
ML-B-7 and ML-B-8	ER100S-G ER70S-6 root	3 o'clock seam	268 268	267 331	295 287	303 315	261 303	272 290
ML-B15-1	ER120S-G ER70S-6 root	3 o'clock seam	238 232	265 314	288 292	364 370	304 347	275 289
ML-B15-3	ER100S-G ER70S-6 root	3 o'clock seam	216 251	257 306	297 282	302 300	268 322	280 286
SMAW single pass backweld	E11018-M	12 o'clock	305	262	273			
GMAW single pass backweld	ER100S-G	12 o'clock	273	259	288			
MPBW 2 pass backweld	E11018-M	12 o'clock	305	255	278			
MPBW 2 pass backweld	ER100S-G	12 o'clock	274	271	298			
SMAW cap repair	E11018-M	3 o'clock				378	290	279
FCAW[a] cap repair	E111-T1	3 o'clock				293	253	273
Partial penetration repair	E111-T1	3 o'clock	259	245	257	311	252	281
Full penetration repair	E11018-M(r+h) E111-T1(f+c)	5 o'clock	231	245	264	317	255	264
ML-B-9 Tie-in	E11018-M(r+h) E111-T1(f+c)	3 o'clock seam	233 238	228 295	276 275	281 266	259 291	271 276

(a) Flux-cored arc welding

Table 5. Summary of Welding Procedures

Automatic	Current (A)	Voltage (V)	Arc Speed		Arc Energy		Max. Interpass	
			(ipm)	(mm/min)	(kJ/in.)	(kJ/mm)	(°F)	(°C)
W1	245	24	18	457	19.6	0.77	302	150
W3	245	24	18	457	19.6	0.77	302	150
W7	161	21	13	330	15.6	0.61	302	150
W8	180	22.5	12	305	20.3	0.80	302	150
W10	160	21	12	305	16.8	0.66	302	150

Table 6. Summary of HV 1-kg Hardness Data Compiled from Hardness Traverses in the Weld Metal and HAZ on X-100 Plate

	Root		Mid-Thickness		Cap	
Weld	Weld	HAZ (Max/Min)	Weld	HAZ (Max/Min)	Weld	HAZ (Max/Min)
W1	266	277/236	293	279/238	308	304/269
W3	318	293/245	365	269/249	427	312/254
W7	247	240/230	296	297/246	305	308/269
W8	257	251/232	280	254/233	290	269/243
W10	262	266/236	297	255/236	316	308/256

Table 7 Base Pipe Tensile Testing Results Adjacent to Weld W1

Direction	Yield Strength at 0.2% Offset (MPa)	Ultimate Strength (MPa)	Elongation to Failure (%)	Uniform Elongation (%)
Hoop (Longitudinal to Weld)	753	801	25	4.5
Axial (Transverse to Weld)	672	782	21.4	6.7

Table 8. Stub Tensile Data for Weld W1

Location	Diameter [mm (in.)]	Gage Length [mm (in.)]	Ultimate Strength		0.2% Offset Yield Strength		% Elong-ation	% Reduction of Area
			(MPa)	(ksi)	(MPa)	(ksi)		
Hoop	6.40 (0.252)	12.7 (0.500)	999	145	863	125	18.2	61.7
Axial	6.38 (0.251)	12.73 (0.501)	970	141	803	117	21.4	74.8
FL+2 mm	6.35 (0.250)	12.70 (0.500)	910	132	814	118	20.6	58.5
FL+3 mm	6.50 (0.256)	12.67 (0.499)	872	127	803	116	20.8	56.4
FL+4 mm	6.35 (0.250)	12.62 (0.497)	930	135	833	121	20.9	57.0

Table 9. Microtensile Testing Results for Weld W1

Spec.	Width [mm (in.)]	Thick-ness [mm (in.)]	Ultimate Strength		0.2% Yield Strength		Elong. (%)	Red. of Area (%)	Note
			(MPa)	(ksi)	(MPa)	(ksi)			
13 WCL	1.52 (0.060)	0.51 (0.020)	745	108	683	99	4.7	80.2	
14 WCL+1	1.55 (0.061)	0.33 (0.013)	697	101	662	96	2.5	31.1	1
15 WCL+2	1.55 (0.061)	0.51 (0.020)	662	96	579	84	9.5	82.2	
16 WCL+3	1.52 (0.060)	0.64 (0.025)	690	100	621	90	9.6	66.1	
17 WCL+4	1.55 (0.061)	0.58 (0.023)	690	100	607	88	6.9	82.0	
18 WCL+5	1.55 (0.061)	0.51 (0.020)	724	105	641	93	8.1	81.3	
19 WCL+6	1.57 (0.062)	0.53 (0.021)	717	104	641	93	7.3	86.4	
20 WCL+7	1.57 (0.062)	0.56 (0.022)	710	103	655	95	7.1	86.9	
21 WCL+8	1.60 (0.063)	0.56 (0.022)	717	104	655	95	7.1	82.0	
22 WCL+9	1.57 (0.062)	0.56 (0.022)	724	105	662	96	8.2	80.3	
23 WCL+10	1.60 (0.063)	0.46 (0.018)	717	104	628	91	8.7	77.8	
24 WCL+11	1.55 (0.061)	0.58 (0.023)	703	102	655	95	8.5	84.4	
25 WCL+12	1.52 (0.060)	0.66 (0.026)	697	101	662	96	6.7	88.6	
26 WCL+13	1.60 (0.063)	0.56 (0.022)	690	100	641	93	7.6	91.2	

Note 1: This specimen was bent before testing, reducing elongation and reduction of area.

Table 10. Base Metal Chemistry for Pipe Adjacent to Welds 2a and 2b

Element	C	Si	Mn	P	S	Nb	V	Ti
Wt%	0.043	0.24	1.92	0.008	0.0008	0.047	0.061	0.012
Element	Al	Ni	Cu	Cr	Mo	B	N	O
Wt%	0.004	0.46	0.49	0.42	0.41	0.0000	31 ppm	16 ppm

Table 11. Base Metal Tensile Testing Results for Welds 2a and 2b as Provided by Supplier Company

Direction	Yield Strength at 0.5% Strain (MPa)	Ultimate Strength (MPa)	Elongation to Failure (%)	Uniform Elongation (%)
Hoop (Longitudinal to Weld)	683	774	22	5.6
Axial (Transverse to Weld)	777	810	20	4.0

Table 12. Weld Metal Tensile Testing Results for Weld 2a as Provided by Supplier Company

Yield Strength at 0.2% Offset (MPa)	Yield Strength at 0.5% Strain (MPa)	Ultimate Strength (MPa)	Elongation to Failure (%)
868	792	942	16

Table 13. Weld Metal Stub Tensile Data for Weld 2a

Location	Diameter [mm (in.)]	Gage Length [mm (in.)]	Ultimate Strength		0.2% Offset Yield Strength		% Elong-ation	% Reduction of Area
			(ksi)	(MPa)	(ksi)	(MPa)		
276Ax	6.38 (0.251)	12.5 (0.491)	146.8	1012	120.8	833.1	22.0	63.3
276HP	6.38 (0.251)	12.6 (0.497)	148.0	1021	137.0	944.8	18.5	67.1
276+2	6.59 (0.259)	12.8 (0.502)	135.9	937	109.3	753.8	17.7	66.9
276+3	6.30 (0.248)	12.6 (0.498)	141.0	972	121.3	836.6	19.9	61.4
276+4	6.53 (0.257)	12.5 (0.492)	138.6	956	116.3	802.1	20.3	68.6

Table 14. Microtensile Testing Results for Weld W2a

Spec.	Width [mm (in.)]	Thick-ness [mm (in.)]	Ultimate Strength		0.2% Yield Strength		Elong. (%)	Red. of Area (%)	Note
			MPa	(ksi)	(MPa)	(ksi)			
276-1 WCL	2.06 (0.081)	0.99 (0.039)	805.5	116.8	740.7	107.4	9.9	59.6	
276-2 WCL+1	2.06 (0.081)	0.69 (0.027)	793.1	115.0	778.6	112.9			1 and 2
276-3 WCL+3	2.11 (0.083)	1.14 (0.045)	797.2	115.6	754.5	109.4	11.7	67.4	
276-4 WCL+4	2.01 (0.079)	1.09 (0.043)	784.8	113.8	728.3	105.6	11.5	72.9	
276-5 WCL+6	2.11 (0.083)	0.86 (0.034)	800.7	116.1	784.8	113.8	8.8	65.3	
276-6 WCL+7	2.08 (0.082)	1.07 (0.042)	809.0	117.3	800.7	116.1	10.8	71.5	
276-7 WCL+9	2.08 (0.082)	1.09 (0.043)	780.0	113.1	762.1	110.5	9.7	66.6	
276-8 WCL+10	2.11 (0.083)	0.74 (0.029)	751.7	109.0	751.0	108.9	5.9	67.1	1
276-9 WCL+12	2.16 (0.085)	1.17 (0.046)	765.5	111.0	758.6	110.0	9.4	72.4	
276-10 WCL+13	2.24 (0.088)	1.07 (0.042)	785.5	113.9	769.7	111.6	9.4	68.2	

Note 1: Sample was tested without an extensometer due to small sample size. This limits accuracy of the results, particularly of yield strength and measurement of the strain at the tensile strength.
Note 2: Sample failed outside of gage length, so no elongation or reduction of area is recorded.

Table 15. Weld Metal Tensile Testing Results for Weld W2b as Provided by Supplier Company

Yield Strength at 0.2% Offset (MPa)	Yield Strength at 0.5% Strain (MPa)	Ultimate Strength (MPa)	Elongation to Failure (%)
781	756	827	20.5

Table 16. Weld Metal Stub Tensile Data for Weld W2b

Location	Diameter [mm (in.)]	Gage Length [mm (in.)]	Ultimate Strength		0.2% Offset Yield Strength		Elong-ation (%)	Reduction of Area (%)
			(ksi)	(MPa)	(ksi)	(MPa)		
274Ax	6.45 (0.254)	12.4 (0.490)	142.9	986	114.5	789.7	20.8	67.0
274Hp	6.43 (0.253)	12.6 (0.497)	151.1	1042	117.3	809.0	17.7	61.5
FL+2	6.43 (0.253)	12.5 (0.493)	145.8	1006	128.6	886.9	17.4	62.5
FL+3	6.38 (0.251)	12.5 (0.494)	144.2	994	125.2	863.4	21.5	68.4
FL+4	6.43 (0.253)	12.6 (0.496)	142.6	983	109.8	757.2	22.8	71.1

Table 17. Microtensile Testing Results for Weld W2b

Spec.	Width [mm (in.)]	Thick-ness [mm (in.)]	Ultimate Strength		0.2% Yield Strength		Elong. (%)	Red. of Area (%)	Note
			(MPa)	(ksi)	(MPa)	(ksi)			
274-1	2.01 (0.079)	0.84 (0.033)	902.8	130.9	855.2	124.0	7.5	42.7	
274-2	2.03 (0.080)	0.99 (0.039)	875.2	126.9	814.5	118.1	8.9	61.0	
274-3	2.06 (0.081)	0.94 (0.037)	860.0	124.7	785.5	113.9	9.1	66.4	
274-4	2.08 (0.082)	1.02 (0.040)	784.1	113.7	720.0	104.4	14.2	74.6	
274-5	2.11 (0.083)	0.99 (0.039)	762.8	110.6	730.3	105.9	11.3	79.1	
274-6	2.11 (0.083)	1.02 (0.040)	779.3	113.0	766.2	111.1	11.2	81.4	
274-7	2.11 (0.083)	1.09 (0.043)	782.8	113.5	771.0	111.8	9.4	71.8	
274-8	2.08 (0.082)	1.02 (0.040)	760.0	110.2	753.8	109.3	10.0	78.0	
274-9	2.11 (0.083)	0.94 (0.037)	795.2	115.3	783.4	113.6	8.7	69.7	
274-10	2.08 (0.082)	1.09 (0.043)	795.2	115.3	789.0	114.4	9.2	78.2	

Table 18. Peak HAZ Strain Observed at 3 mm (0.12 in.) from Root Under 4% Remote Loading

Thick-ness	Weld Strength	Pressure	Small HAZ Peak Strain (%)	Medium HAZ Peak Strain (%)	Large HAZ Peak Strain (%)	Extra Large HAZ Peak Strain (%)
10	10% overmatched	None	4.6	4.7	4.8	5.4
10	10% overmatched	6.43	7.6	8.0	9.4	21
10	10% overmatched	3.2	5.6	5.9	6.1	11
10	Even matched	6.43	18	18	18	20
10	Even matched	3.2	10	11	11	12
20	10% overmatched	12.8	6.5	7.9	9.3	13
20	10% overmatched	6.43	5.2	5.9	6.6	8.5

Table 19. HAZ Strain Concentration Observed at 3 mm (0.12 in.) from Root

Thick-ness	Weld Strength	Pressure	Small HAZ Peak Strain (%)	Medium HAZ Peak Strain (%)	Large HAZ Peak Strain (%)	Extra Large HAZ Peak Strain (%)
10	10% overmatched	None	1.15	1.17	1.19	1.35
10	10% overmatched	6.43	1.90	2.00	2.35	5.25
10	10% overmatched	3.2	1.40	1.48	1.52	2.80
10	Even matched	6.43	4.45	4.61	4.62	5.06
10	Even matched	3.2	2.58	2.69	2.75	2.89
20	10% overmatched	12.8	1.63	1.98	2.34	3.21
20	10% overmatched	6.43	1.30	1.47	1.66	2.11

Table 20. Peak Strain at Weld Centerline Observed Under 4% Remote Loading

Thick-ness	Weld Strength	Pressure	Small HAZ Peak Strain (%)	Medium HAZ Peak Strain (%)	Large HAZ Peak Strain (%)	Extra Large HAZ Peak Strain (%)
10	10% overmatched	None	4.5	4.6	4.7	4.9
10	10% overmatched	6.43	7.3	8.3	8.6	7.4
10	10% overmatched	3.2	5.4	5.8	6.1	6.2
10	Even matched	6.43	17	19	20	17
10	Even matched	3.2	10	11	11	11
20	10% overmatched	12.8	5.6	5.8	6.2	7.9
20	10% overmatched	6.43	4.6	4.8	4.9	5.8

Table 21. Peak Strain Concentration Observed at Weld Centerline

Thick-ness	Weld Strength	Pressure	Small HAZ Peak Strain (%)	Medium HAZ Peak Strain (%)	Large HAZ Peak Strain (%)	Extra Large HAZ Peak Strain (%)
10	10% overmatched	None	1.13	1.15	1.18	1.21
10	10% overmatched	6.43	1.82	2.07	2.14	1.86
10	10% overmatched	3.2	1.36	1.46	1.53	1.56
10	Even matched	6.43	4.25	4.74	4.88	4.37
10	Even matched	3.2	2.57	2.71	2.82	2.84
20	10% overmatched	12.8	1.41	1.46	1.54	1.98
20	10% overmatched	6.43	1.16	1.19	1.24	1.46

Table 22. Peak Strain Observed Under 4% Remote Loading

Thick-ness	Weld Strength	Pressure	Small HAZ Peak Strain (%)	Medium HAZ Peak Strain (%)	Large HAZ Peak Strain (%)	Extra Large HAZ Peak Strain (%)
10	10% overmatched	None	14	15	16	18
10	10% overmatched	6.43	31	38	47	72
10	10% overmatched	3.2	21	24	28	40
10	Even matched	6.43	43	51	61	84
10	Even matched	3.2	28	32	36	47
20	10% overmatched	12.8	29	33	36	47
20	10% overmatched	6.43	19	21	23	28

Table 23. X-100 Finer-Grained Model Results for Local Strain at 3 mm from Root

	Local Strain under 4% Axial Remote Strain (%)	Local Strain under Internal Pressure to 35% SMYS and 4% Axial Remote Strain (%)	Local Strain under Internal Pressure to 70% SMYS and 4% Axial Remote Strain (%)
Isotropic Properties	4.7	6.0	6.7
Orthotropic Properties	4.8	6.3	6.8
Base Metal Orthotropic	4.3	4.4	4.4

Table 24. X-100 Finer-Grained Model Results for Peak Local Strain at Weld Centerline

	Local Strain under 4% Axial Remote Strain (%)	Local Strain under Internal Pressure to 35% SMYS and 4% Axial Remote Strain (%)	Local Strain under Internal Pressure to 70% SMYS and 4% Axial Remote Strain (%)
Isotropic Properties	4.7	6.0	6.7
Orthotropic Properties	4.8	6.3	6.8
Base Metal Orthotropic	4.3	4.4	4.4

Table 25. X-100 Finer-Grained Model Results for Local Strain at 3 mm (0.12 in.) from the Root with 1.5-mm (0.06-mm) High-Low

	Local Strain under 4% Axial Remote Strain (%)	Local Strain under Internal Pressure to 35% SMYS and 4% Axial Remote Strain (%)	Local Strain under Internal Pressure to 70% SMYS and 4% Axial Remote Strain (%)
Isotropic Properties	6.0	7.6	9.1
Orthotropic Properties	6.2	8.0	9.5
Base Metal Orthotropic	6.1	7.4	8.6

Table 26. X-100 Finer-Grained Model Results for Peak Local Strain at Weld Centerline with 1.5-mm (0.06-in.) High-Low

	Local Strain under 4% Axial Remote Strain (%)	Local Strain under Internal Pressure to 35% SMYS and 4% Axial Remote Strain (%)	Local Strain under Internal Pressure to 70% SMYS and 4% Axial Remote Strain (%)
Isotropic Properties	4.8	5.6	6.5
Orthotropic Properties	4.9	5.9	6.7
Base Metal Orthotropic	4.8	5.4	6.0

Table 27. X-100 Finer-Grained Model Results for Local Strain Concentrations at 3 mm (0.12 in.) from the Root Due to 1.5-mm (0.06-in.) High-Low

	Local Strain Concentration for No Pressure (%)	Local Strain Concentration for Internal Pressure to 35% SMYS (%)	Local Strain Concentration for Internal Pressure to 70% SMYS (%)
Isotropic Properties	6.0/4.7=1.28	7.6/6.0=1.27	9.1/6.7=1.36
Orthotropic Properties	6.2/4.8=1.29	8.0/6.3=1.27	9.5/6.8=1.40
Base Metal Orthotropic	6.1/4.3=1.42	7.4/4.4=1.68	8.6/4.4=1.95

Table 28. X-100 Finer-Grained Model Results for Local Strain Concentrations at 3 mm (0.12 in.) from the Root Due to Internal Pressure for the Case of 1.5-mm (0.06-in.) High-Low

	Local Strain Concentration for No Pressure (%)	Local Strain Concentration for Internal Pressure to 35% SMYS (%)	Local Strain Concentration for Internal Pressure to 70% SMYS (%)
Isotropic Properties	1	7.6/6.0=1.27	9.1/6.0=1.52
Orthotropic Properties	1	8.0/6.2=1.29	9.5/6.2=1.53
Base Metal Orthotropic	1	7.4/6.1=1.21	8.6/6.1=1.41

Table 29. X-100 Finer-Grained Model Results for Local Strain at 3 mm (0.12 in.) from the Root with 0.75-mm (0.03-in.) High-Low

	Local Strain under 4% Axial Remote Strain (%)	Local Strain under Internal Pressure to 35% SMYS and 4% Axial Remote Strain (%)	Local Strain under Internal Pressure to 70% SMYS and 4% Axial Remote Strain (%)
Isotropic Properties	5.0	5.9	7.1
Orthotropic Properties	5.1	6.2	7.3
Base Metal Orthotropic	5.0	5.8	7.3

Table 30. X-100 Finer-Grained Model Results for Peak Local Strain at Weld Centerline with 0.75-mm (0.03-in.) High-Low

	Local Strain under 4% Axial Remote Strain (%)	Local Strain under Internal Pressure to 35% SMYS and 4% Axial Remote Strain (%)	Local Strain under Internal Pressure to 70% SMYS and 4% Axial Remote Strain (%)
Isotropic Properties	4.5	5.0	5.6
Orthotropic Properties	4.6	5.1	5.7
Base Metal Orthotropic	4.5	4.8	5.7

Table 31. X-65 Finer-Grained Model Results for Local Strain at 3 mm (0.12 in.) from the Root with 1.5-mm (0.06-in.) High-Low

	Local Strain under 4% Axial Remote Strain (%)	Local Strain under Internal Pressure to 35% SMYS and 4% Axial Remote Strain (%)	Local Strain under Internal Pressure to 70% SMYS and 4% Axial Remote Strain (%)
Isotropic Properties	6.3	7.6	8.2
Orthotropic Properties	6.5	7.8	8.3
Base Metal Orthotropic	6.3	7.3	7.9

Table 32. X-65 Finer-Grained Model Results for Peak Local Strain at Weld Centerline with 1.5-mm (0.06-in.) High-Low

	Local Strain under 4% Axial Remote Strain (%)	Local Strain under Internal Pressure to 35% SMYS and 4% Axial Remote Strain (%)	Local Strain under Internal Pressure to 70% SMYS and 4% Axial Remote Strain (%)
Isotropic Properties	4.6	4.9	5.3
Orthotropic Properties	4.6	5.0	5.4
Base Metal Orthotropic	4.6	4.6	5.0

Table 33. Examples of Pressurized Pipelines of X-80 and Higher Strength

Country	Pipe OD. in. (mm)	WT in. (mm)	Grade	P (kPa)	Pressure Stress/SMYS	Comment
Canada	36 (914)	0.51 (13)	550	12500	0.80	
Canada	36 (914)	0.56 (14.3)	690	12500	0.58	
Canada	48 (1219)	0.472 (12.0)	550			Eastern Alberta Mainline Loop
Canada	48 (1219)	0.63 (16.0)	550			
Canada	42 (1067)	0.42 (10.6)	550			Empress East
China	40 (1016)	0.60 (15.3)	560		0.72	Jia Ning
Australia	16 (406)	0.35 (8.8)	X-80	5165	0.22	Roma-Brisbane Loop
Japan	31 (782)	0.69 (17.5)	X-80			Tests for Tokyo Gas
U.S	36 (914)	0.464 (11.8)	X-80		0.72	Cheyenne Plains
U.S	36 (914)	0.667 (16.9)	X-80		0.50	Cheyenne Plains
U.S	30 (762)	0.386 (9.8)	X-80		0.72	Cheyenne Plains
U.K.	48 (1220)	0.63 (15.9)	X-80	94bar (9390)	0.67	Aberdeen-Lochside
U.K.	48 (1220)	0.90 (22.9)	X-80	94bar (9390)	0.67	Aberdeen-Lochside
Germany	44 (1118)	0.54 (13.6)	X-80	8000	0.60	MEGAL II
Germany	48 (1219)	0.72 (18.3)	X-80	100bar (10000)		Ruhrgas
Slovakia	56 (1420)	0.61 (15.5)	X-80	7500	0.62	

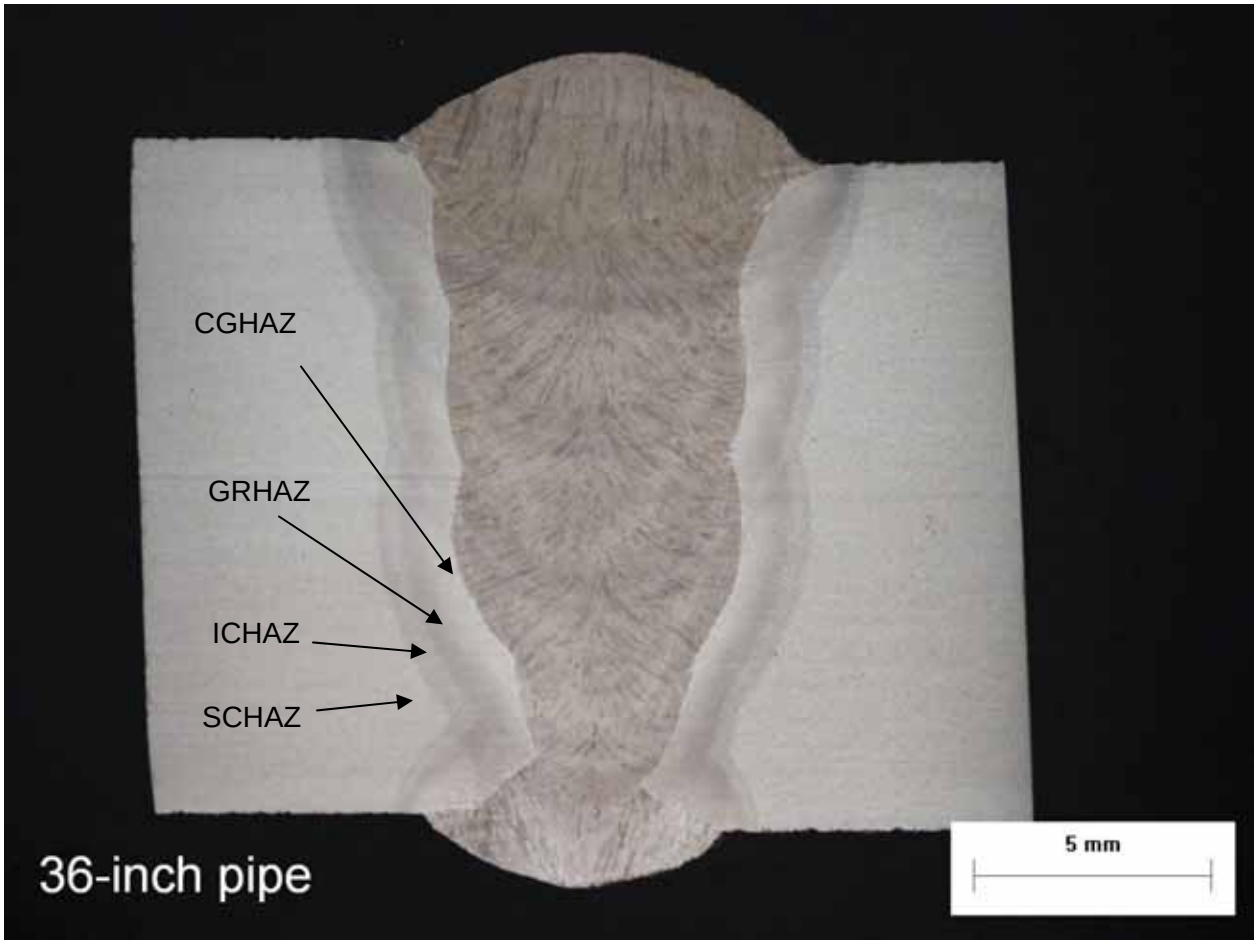

Figure 1. HAZ Regions in a Multipass Weld

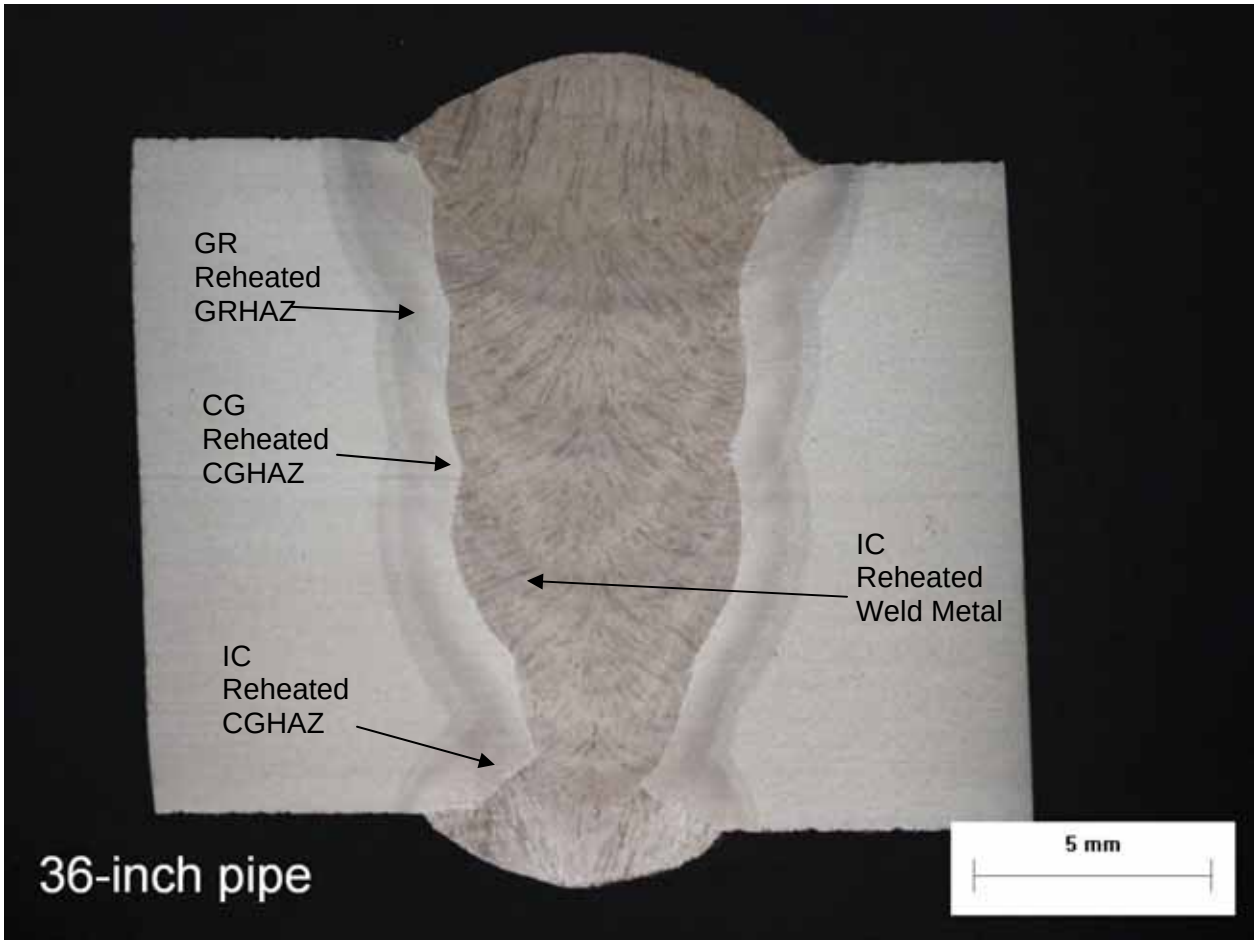

Figure 2. Example Regions in a Multipass Weld Where Structure is Affected by Multiple Heating Cycles

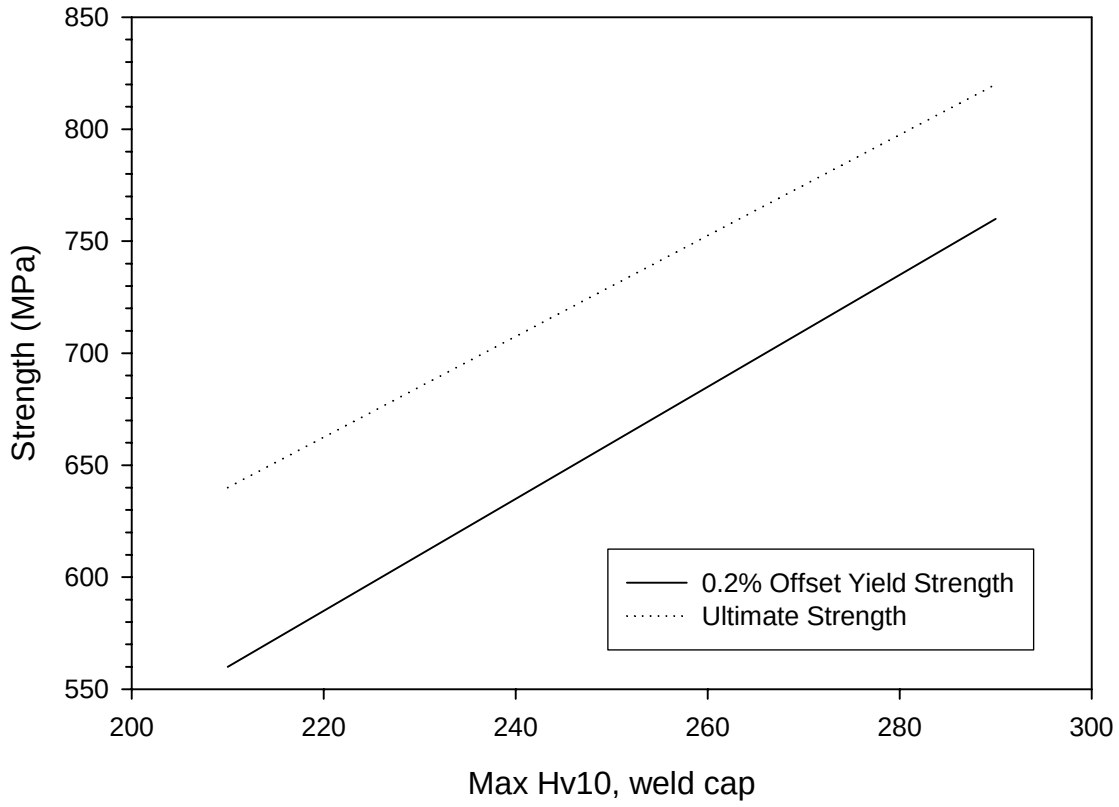

Figure 3. Widgery Hardness Conversion

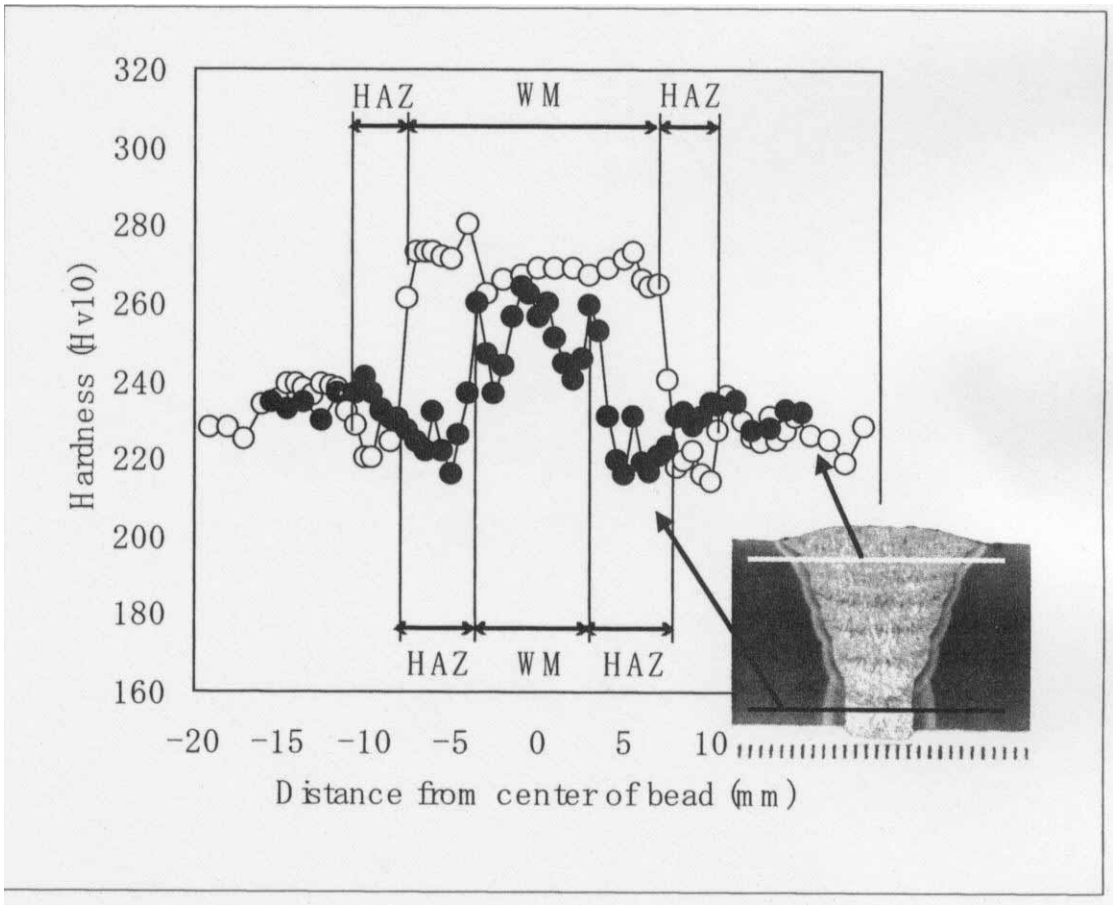

Figure 4. Tokyo Gas Example of Softening Adjacent to Girth Weld in X-80

CRC-EVANS **AUTOMATIC WELDING**

This information is the proprietary property of CRC-Evans Automatic Welding which contains trade secrets and or know how and may only be used in conjunction with equipment rented from CRC-Evans Automatic Welding.

PGMAW WELDING TECHNIQUE SHEET (P-500)

Project:	Plate Welds WO#10072	Issue Date:	March 14, 2000
Customer:	Edison Welding Institute	Electrode T/N :	Spoolarc 95
Weld Number:	547-D	Electrode Mfr.:	ESAB
Material Specification:	X-100	Electrode Heat No.:	195316
Technical Spec.:	None	Shielding Gas(%):	85Ar/15 CO_2
Plate Length:	27.5"	Electrical Current:	Direct Current
Plate Thickness:	0.780" (20.0mm)	Polarity:	Electrode Positive
Preheat:	100°C	Position:	1G
Interpass Temperature:	125°C	PWHT:	N/A

Pass No.	Root	Hot Pass	Fill 1-4	Fill 5	Split Cap		
Process	PGMAW	PGMAW	PGMAW	PGMAW	PGMAW		
Travel Speed (IPM)	28	50	16	13.0-19.0	8.3-9.5		
Electrode Diameter	0.035"	0.035"	0.035"	0.035"	0.035"		
Wire Feed Speed (IPM)	380	500	575 Lead Torch 575 Trail Torch	500 Lead Torch	380 Lead Torch 380 Trail Torch		
Gas Flow Rate (CFH)	45-50	34 – 53	34 – 53 27 - 46	34 – 53 27 - 46	34 – 53 (Lead) 27 – 46 (Trail)		
Shielding Gas Type (%)	85Ar / 15 CO_2	85Ar / 15CO_2	85Ar / 15CO_2	85Ar / 15CO_2	85Ar / 15CO_2		
C.T.W.D. (Inch)	0.300" - 0.500"	0.300" - 0.500"	0.300" - 0.500"	0.300" - 0.500"	0.500 Lead Torch 0.625 Trail Torch		
Amps	167 – 199	192 – 210	208 – 226 175 – 185	183 - 190	141 – 150		
Volts	21.2 – 23.4	22.6 – 23.7	25.5 – 29.5	22.5 – 24.5	27.9 – 29.9		
Oscillation Rate (BPM)	----	----	160	160	110		
Oscillation Width (Inch)	----	----	As Required	As Required	As Required		
Left/Right Dwell (Setting)	----	----	0.020 – 0.020	0.020 – 0.020	0.035 – 0.035		
Arc Length Setting	.100	.500	.500	.500	.100		
Head Angle	0° – 4° Lead	0° -4° Lead	0° -4° Lead	0° -4° Lead	0° -4° Lead		
Heat Input (kJ/mm)	0.29-0.39	0.21-0.24	0.79-0.98	0.60-1.05	0.97-1.27		

Joint Design

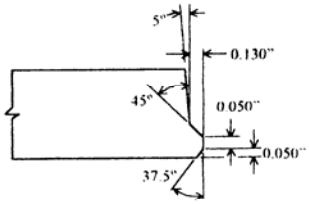

Dimensional Tolerance: ± 0.007", ±0.5°

FOR INFORMATION ONLY

Pass Sequence

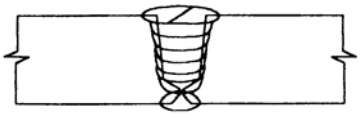

Comments

CDT program number: Thyssen X-90

All passes welded with the **P-500 Dual Torch.**

G:\DEPT353\WELDPROC\WELDFILE\FILES\547 EWI plate welds\January Plate Welds\EWI ESAB ConsumableP-500.doc Prepared By:

Figure 5. Procedure Description for W11

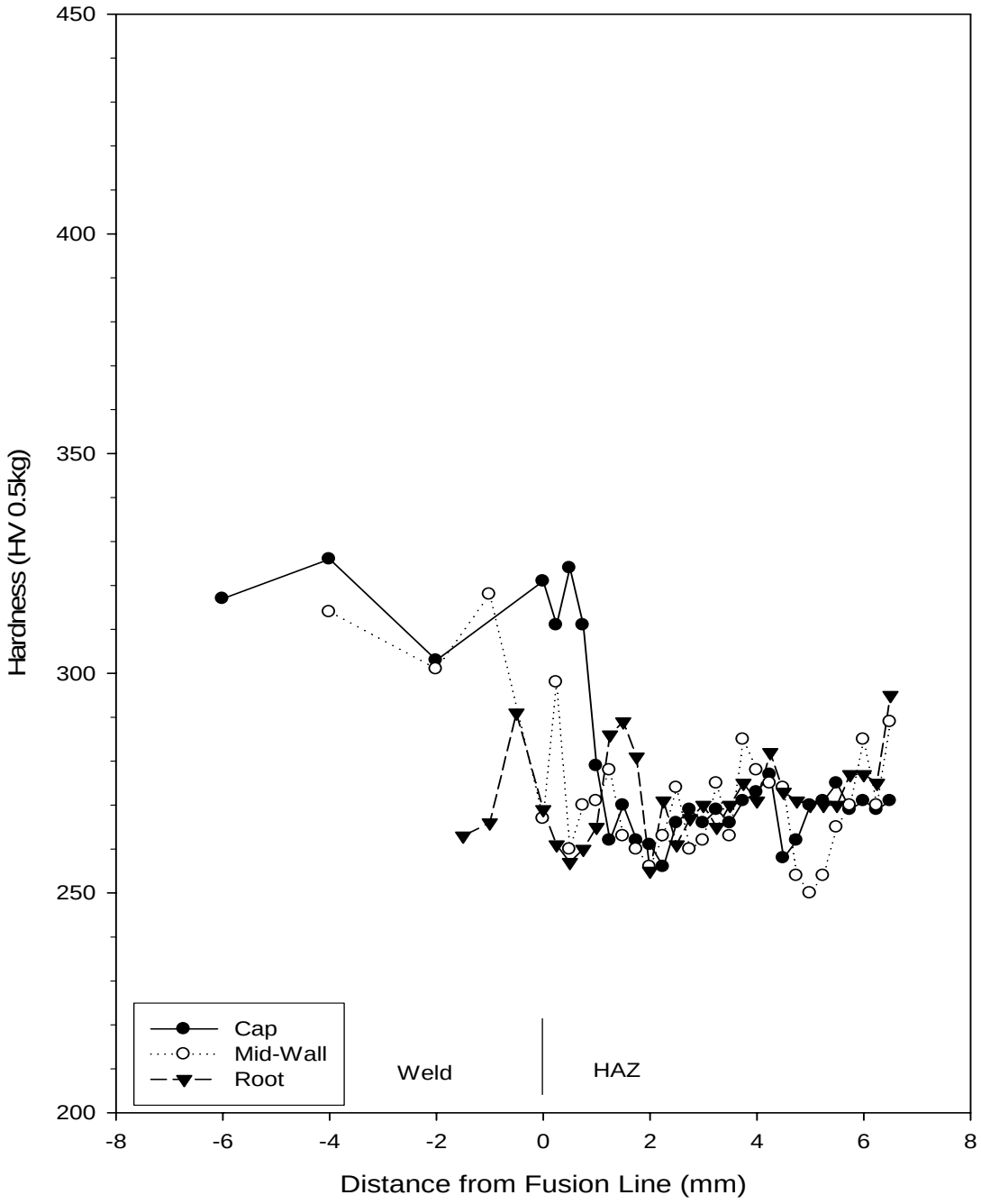

Figure 6. Extended Hardness Traverse for Weld W1 in X-100 Plate

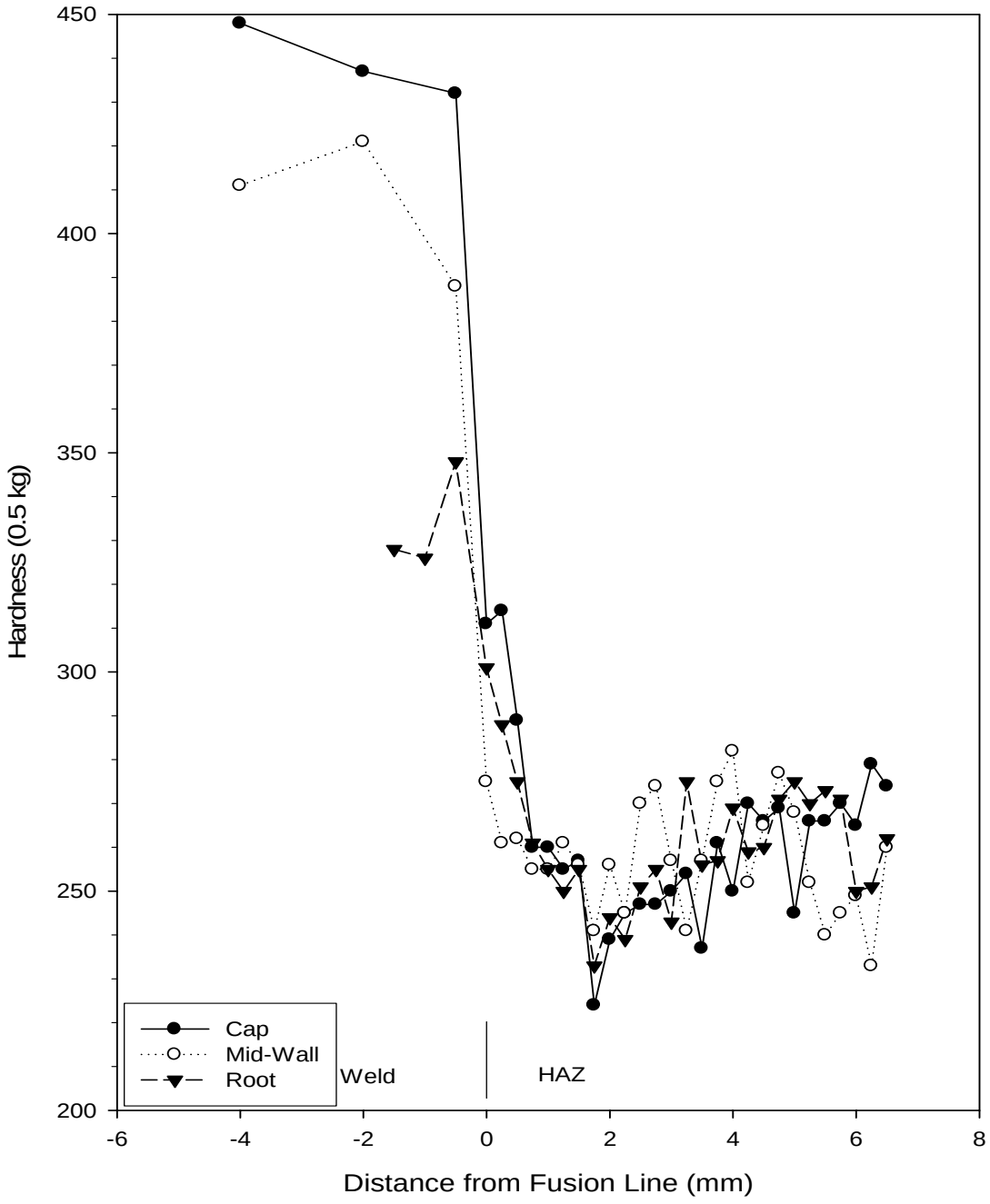

Figure 7. Extended Hardness Traverses for Weld W3 in X-100 Plate

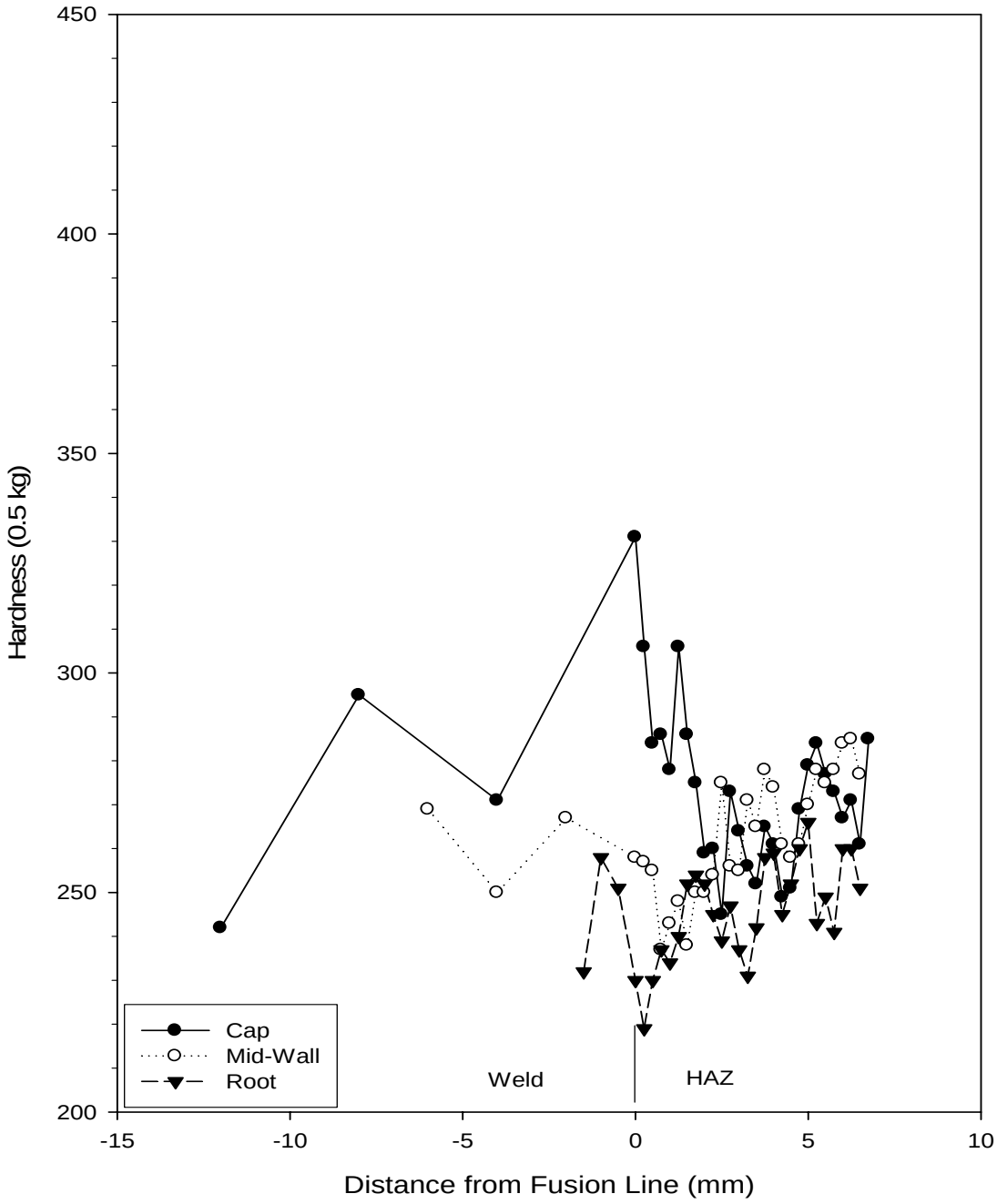

Figure 8. Extended Hardness Traverses for Weld W7 in X-100 Plate

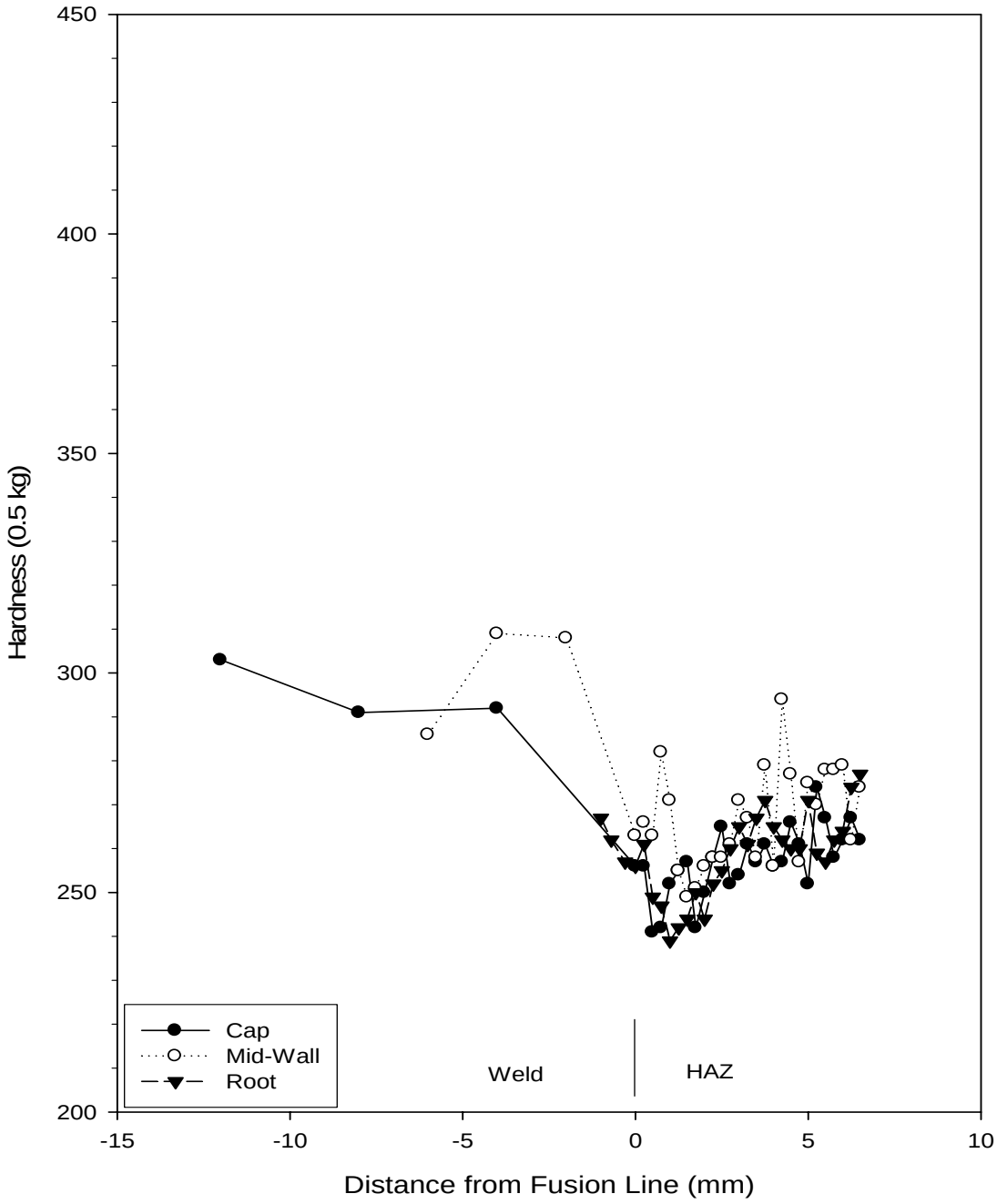

Figure 9. Extended Hardness Traverses for Weld W8 in X-100 Plate

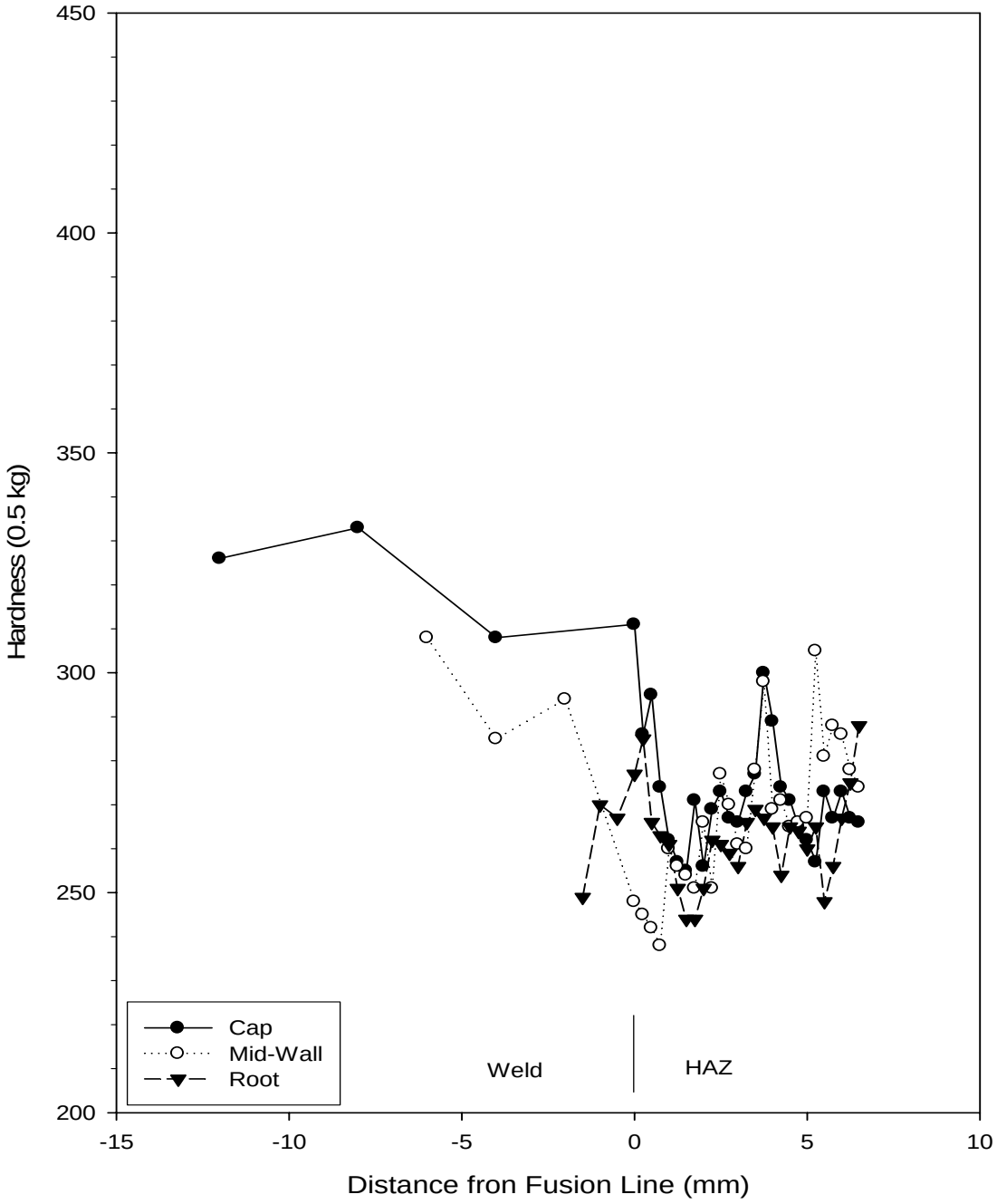

Figure 10. Extended Hardness Traverses for Weld W10 in X-100 Plate

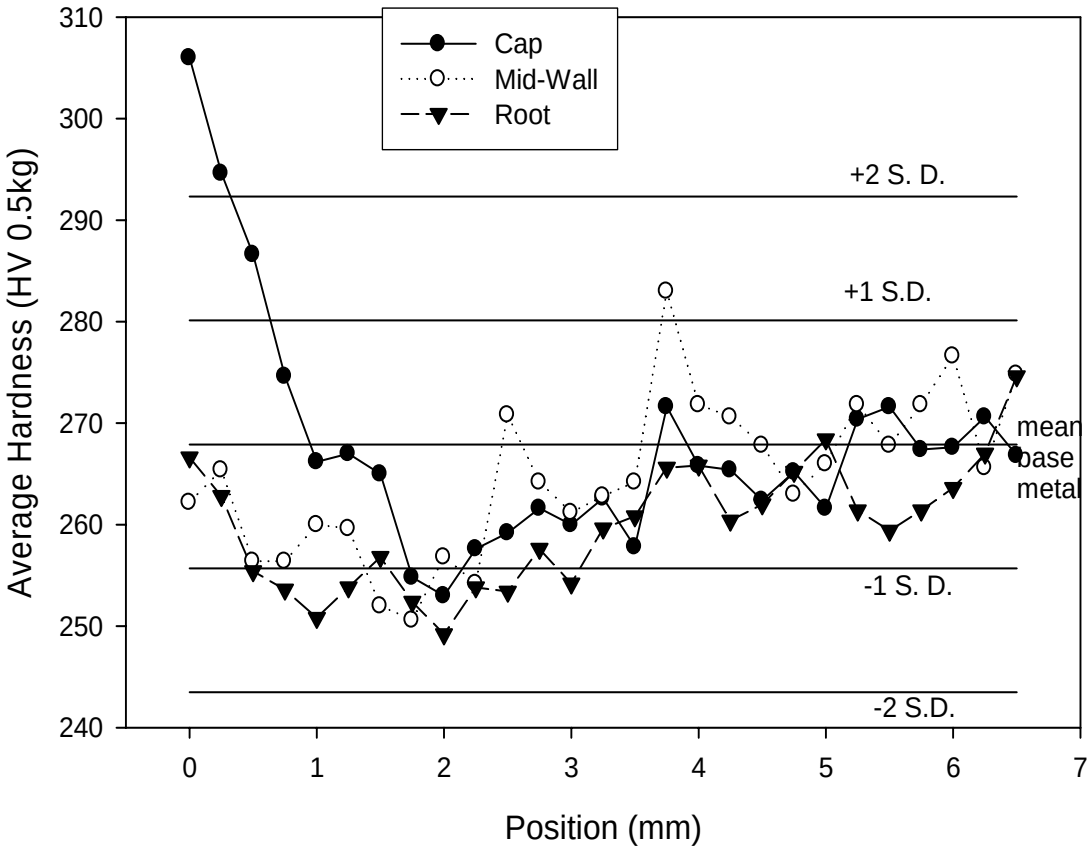

Figure 11. Average Hardness Values by Position in HAZs of X-100 Plate for Welds W1, W3, W7, W8, and W10

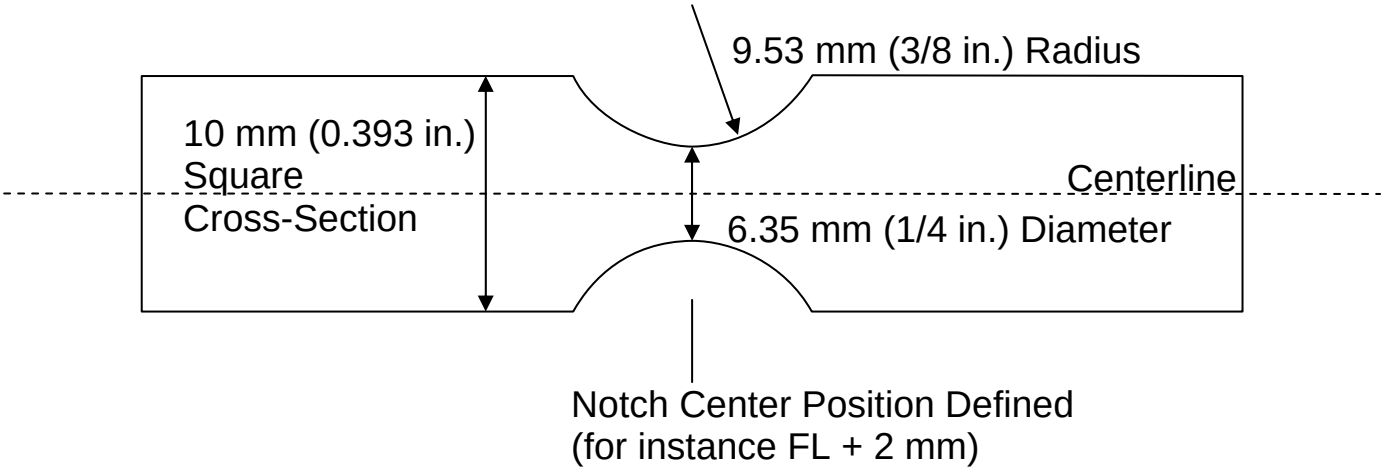

Figure 12. Design of Stub Tensile Specimen

Figure 13. Examples of Microtensile Specimen Before and After Tensile Testing

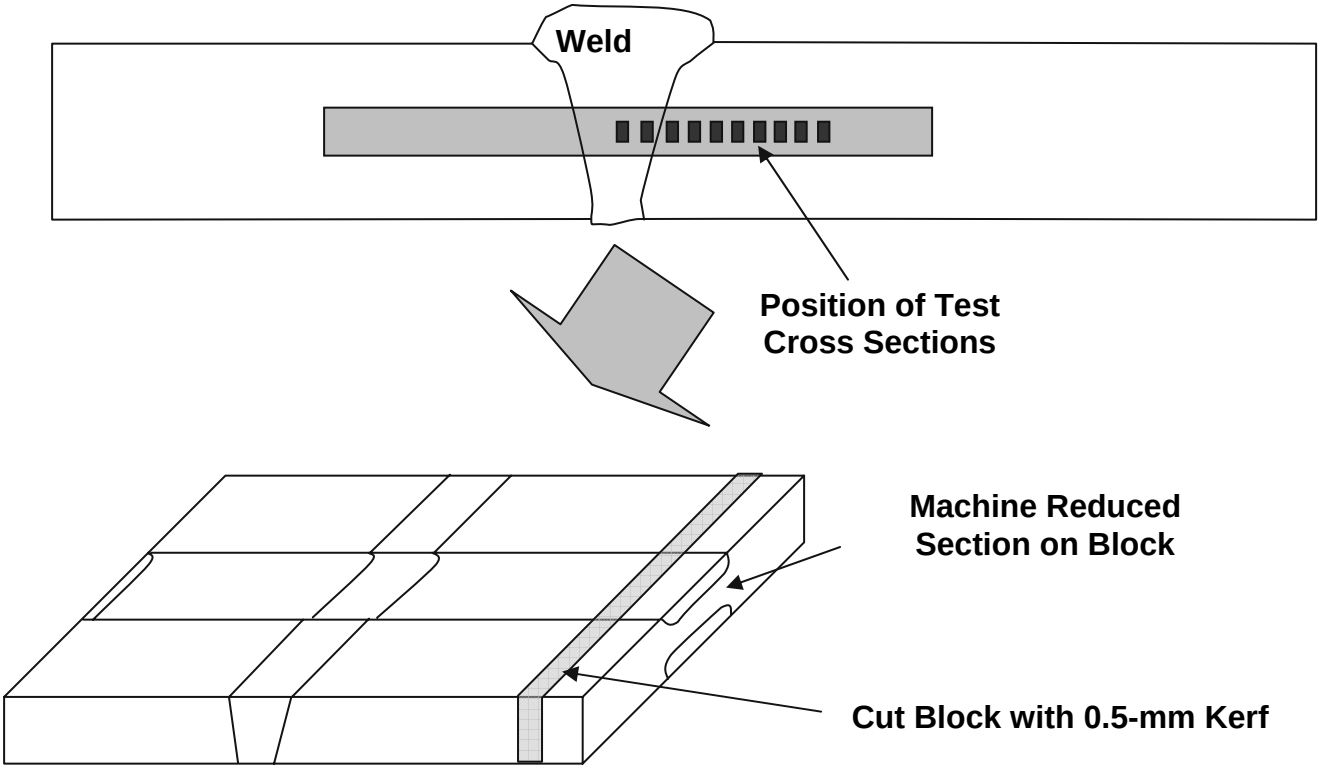

Figure 14. Position of Microtensile Specimens

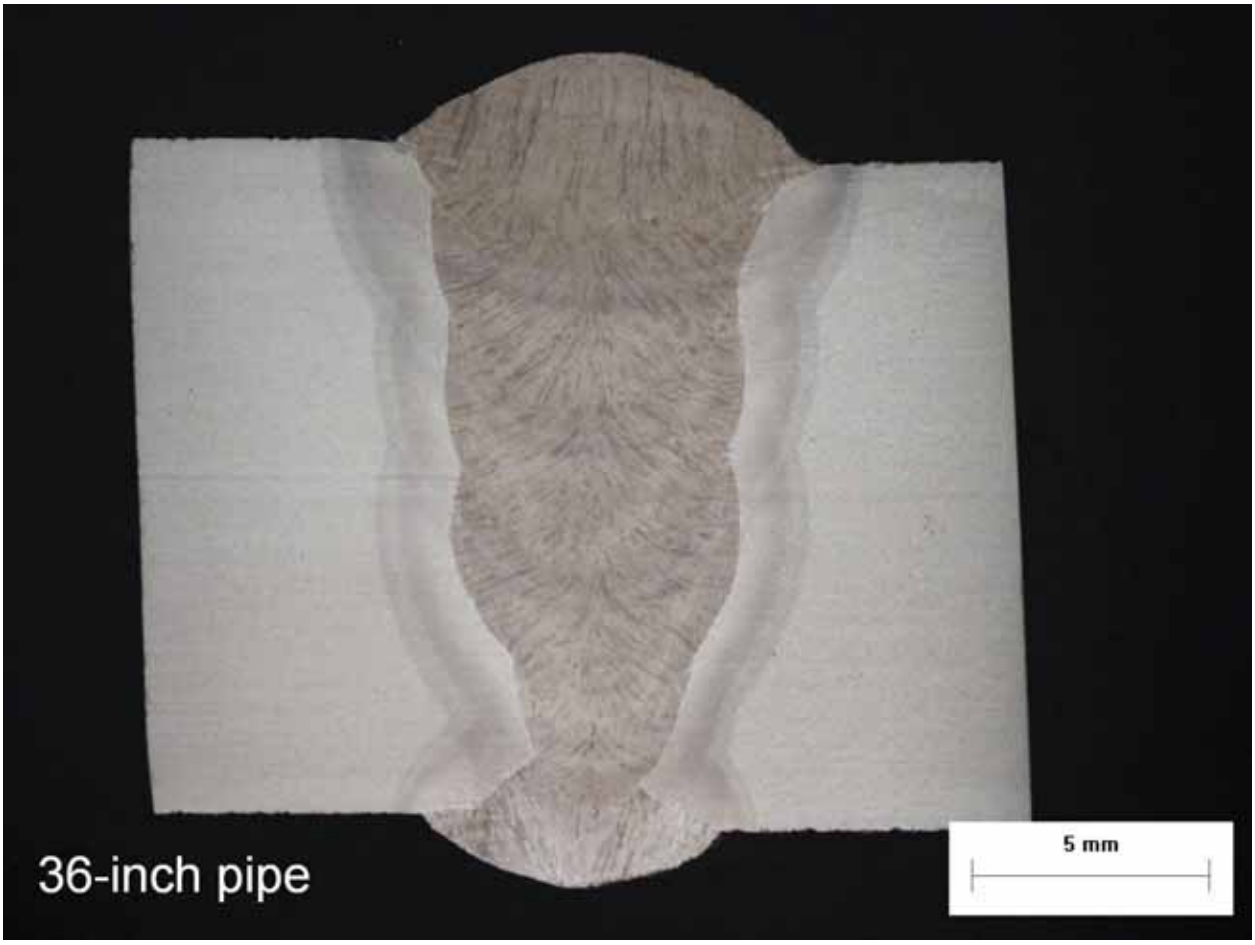

Figure 15. Cross Section of Weld W1 in 914-mm (36-in.)-Diameter Pipe

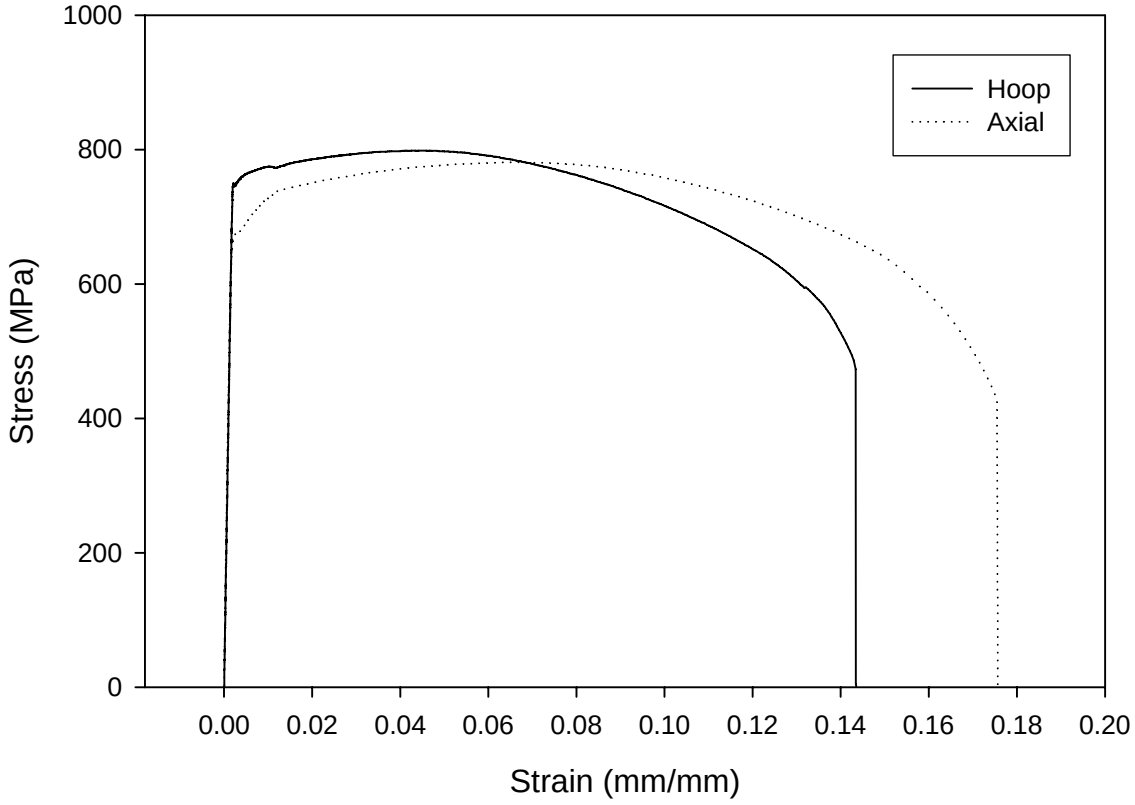

Figure 16. Base Metal Stress-Strain Properties for Pipe Adjacent to Weld W1

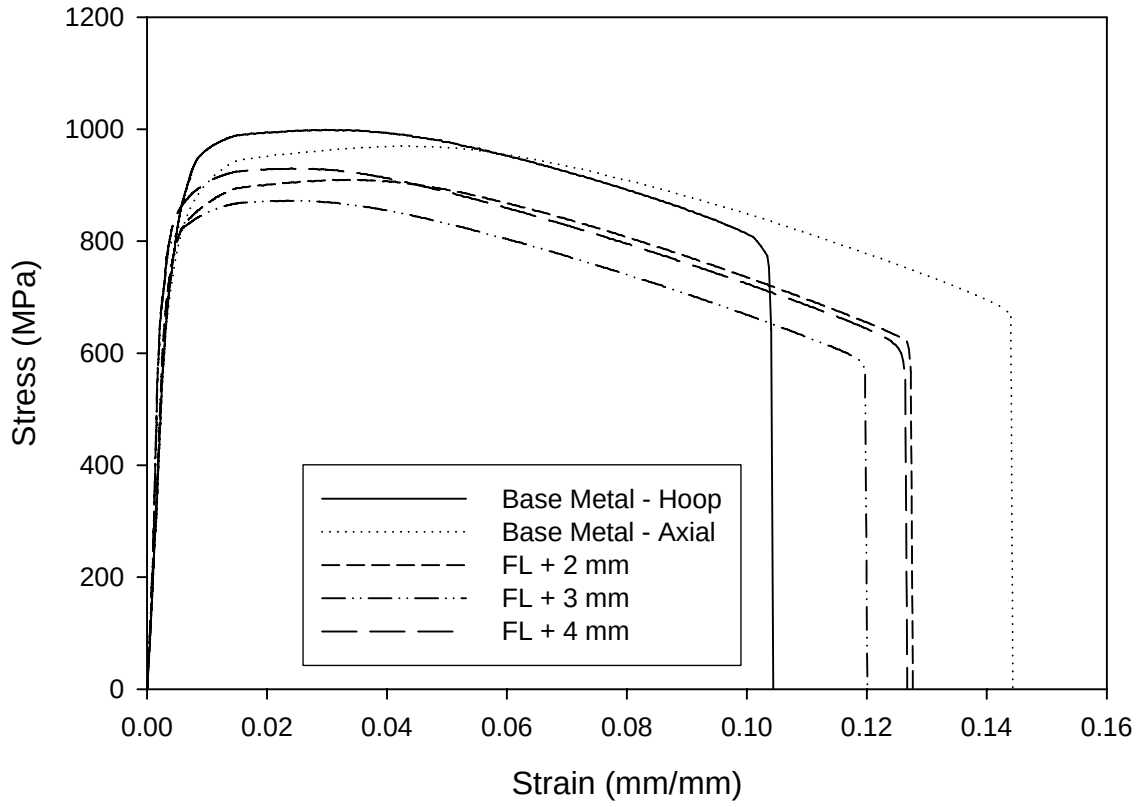

Figure 17. Stress-Strain Curves for Stub Tensile Specimens for Weld W1

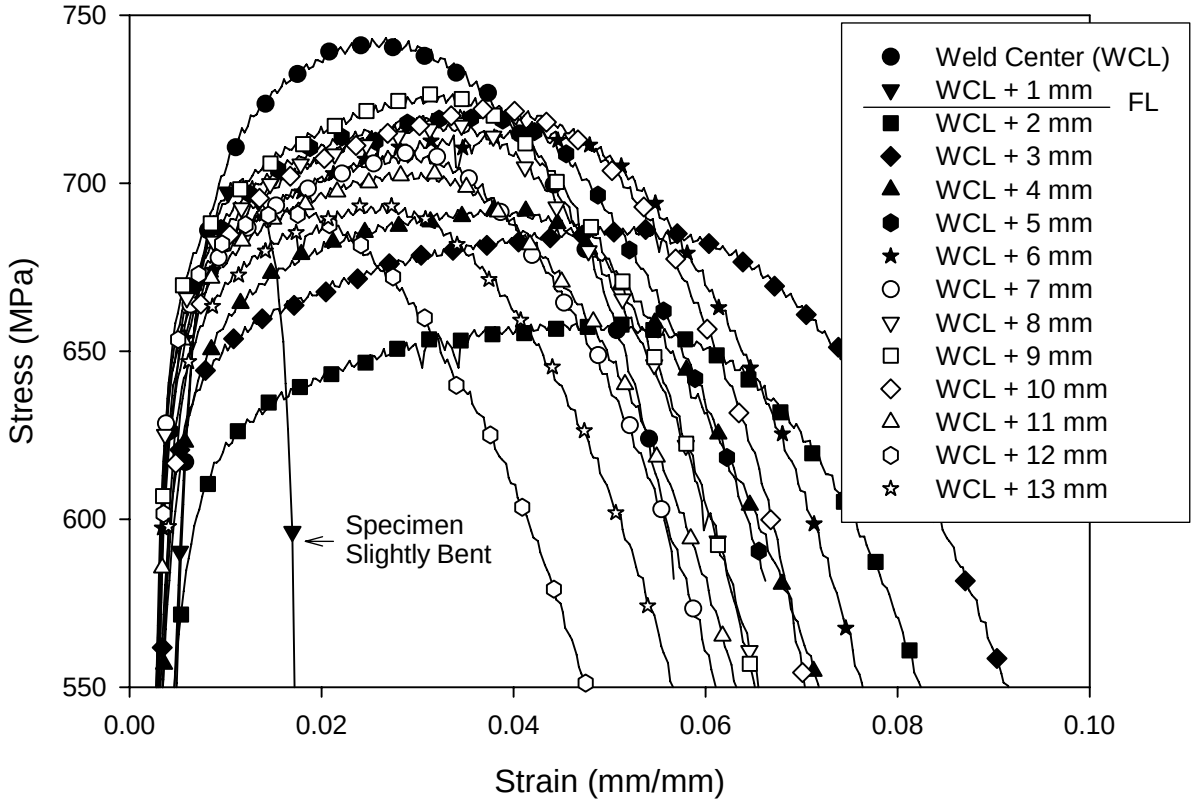

Figure 18. Microtensile Test Results for Weld W1

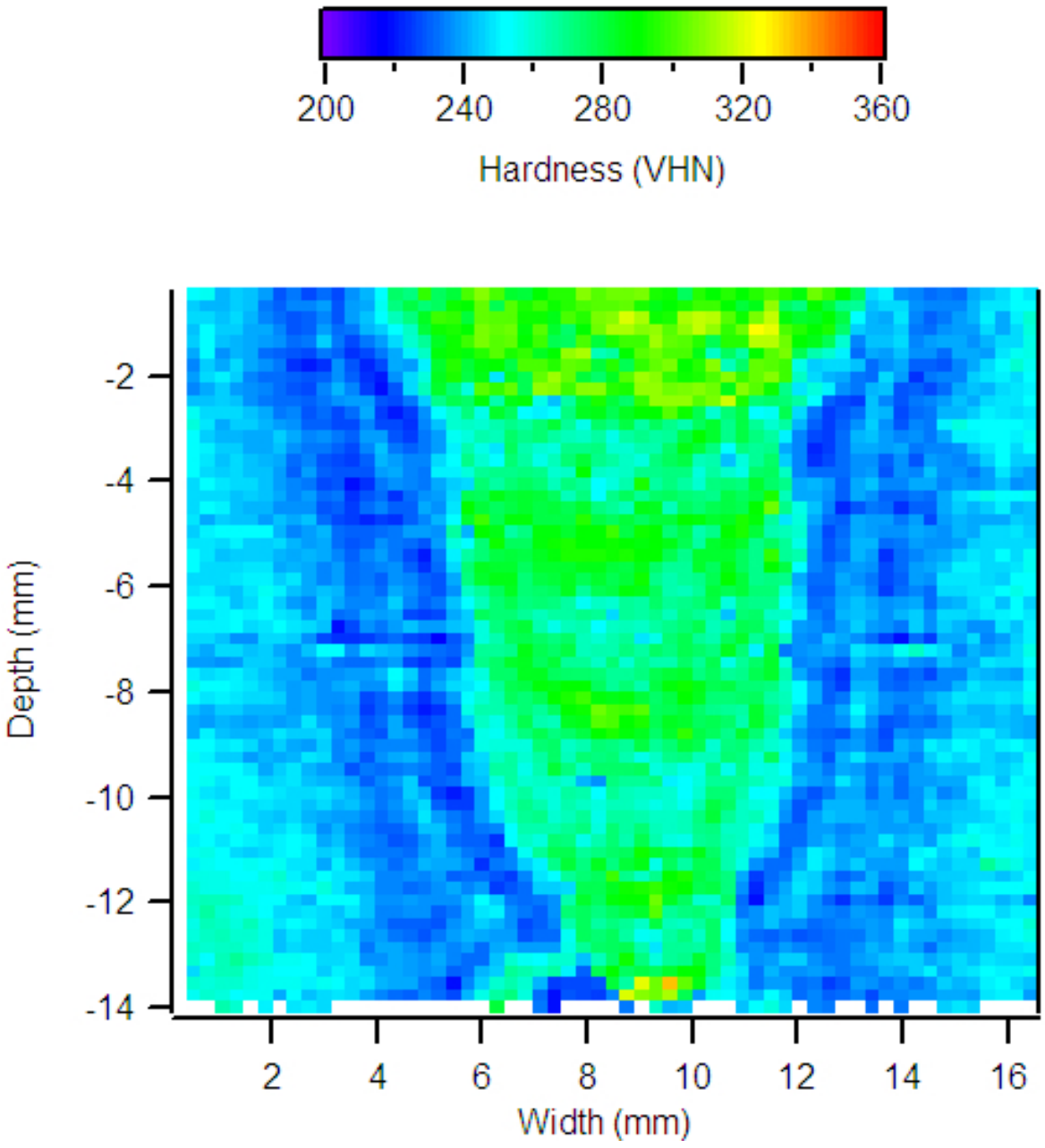

Figure 19. Hardness Matrix for Girth Weld W1

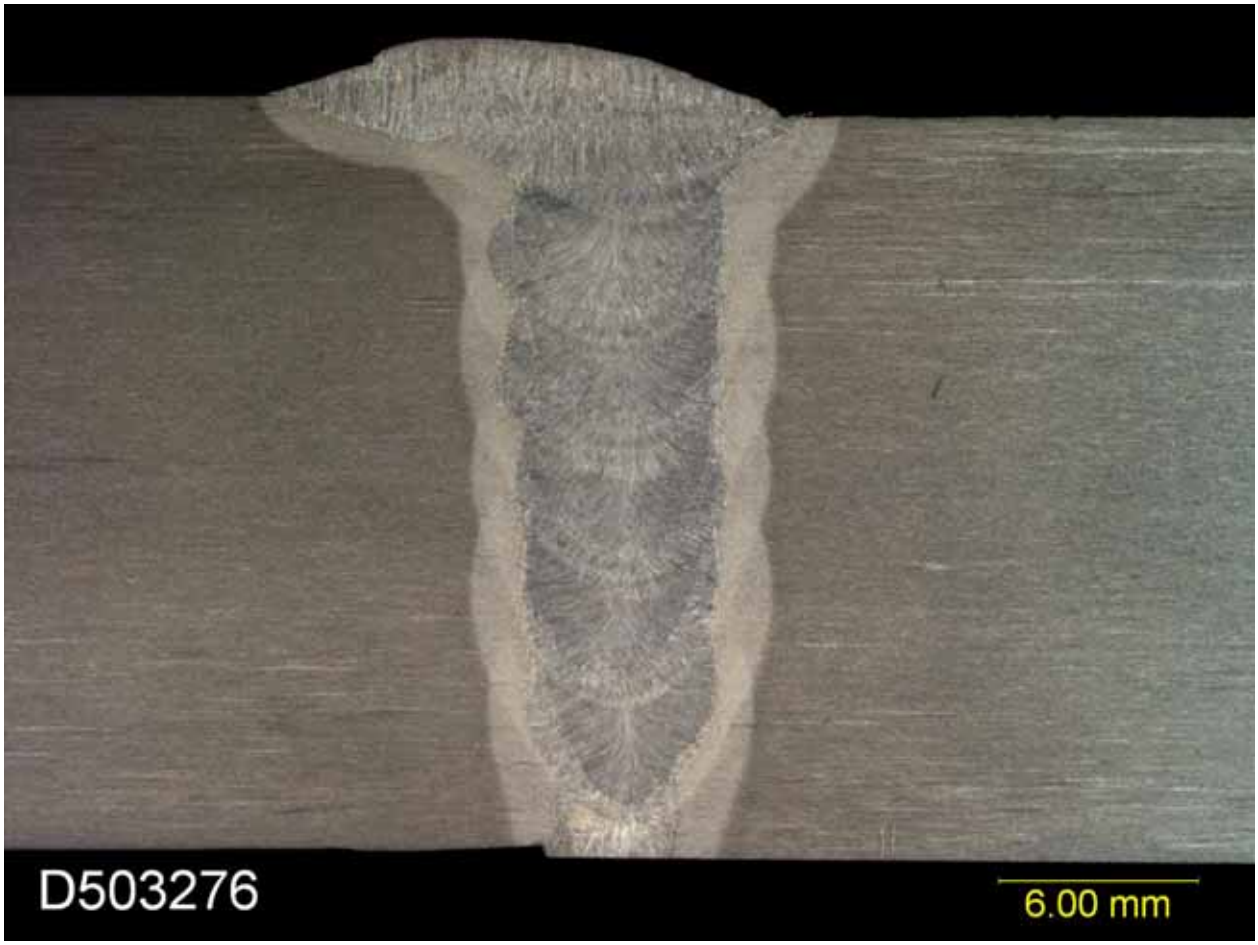

Figure 20. Cross Section of Dual Torch Weld W2a

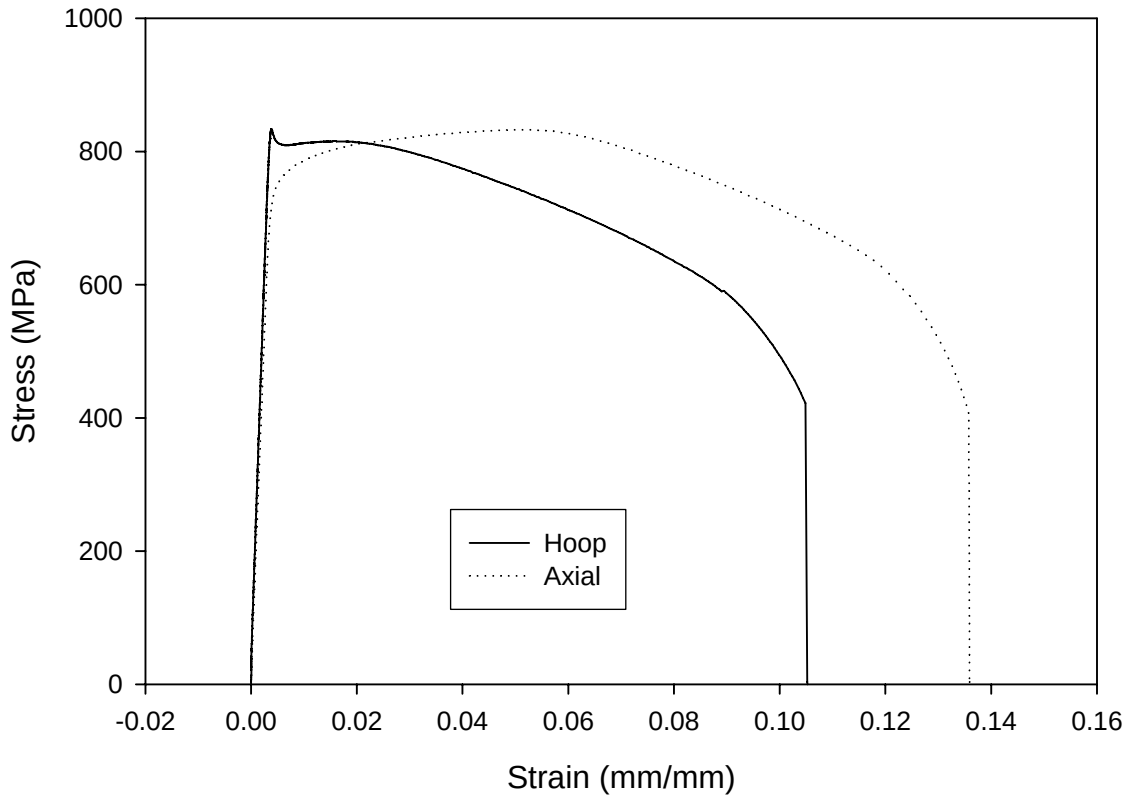

Figure 21. Base Metal Tensile Test Results Adjacent to Weld W2a

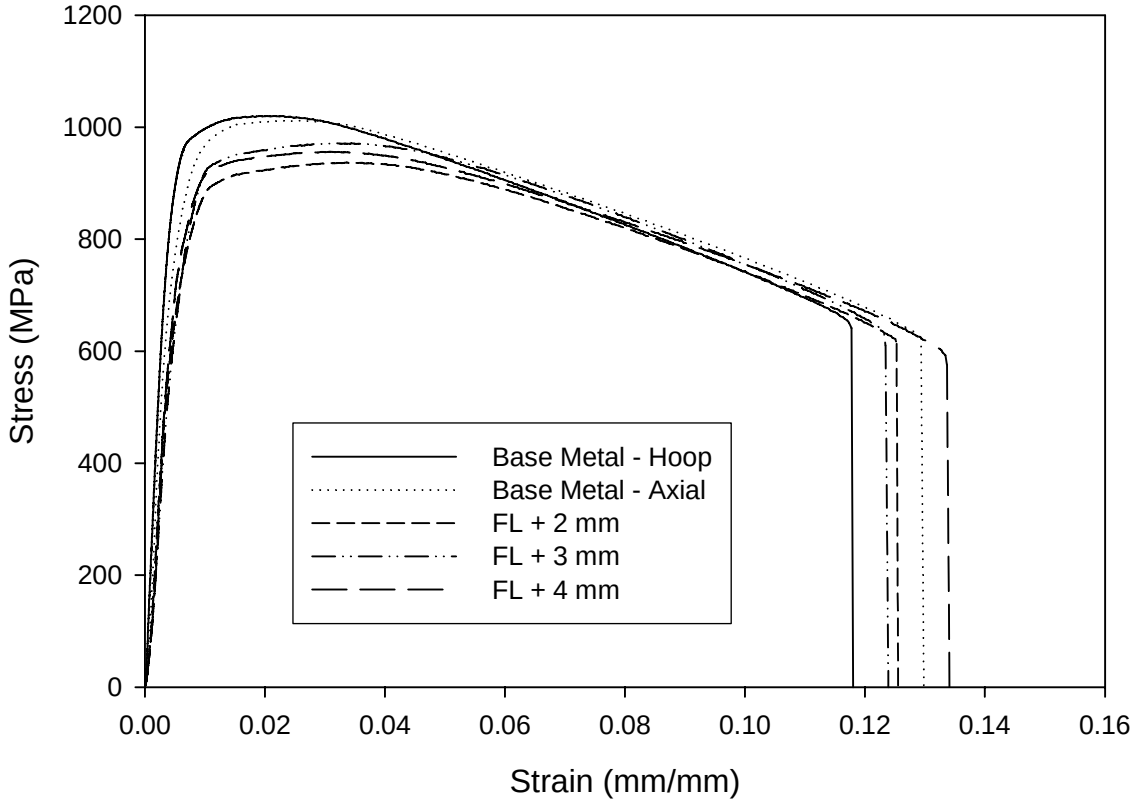

Figure 22. Stub Tensile Results for Dual Torch Weld W2a

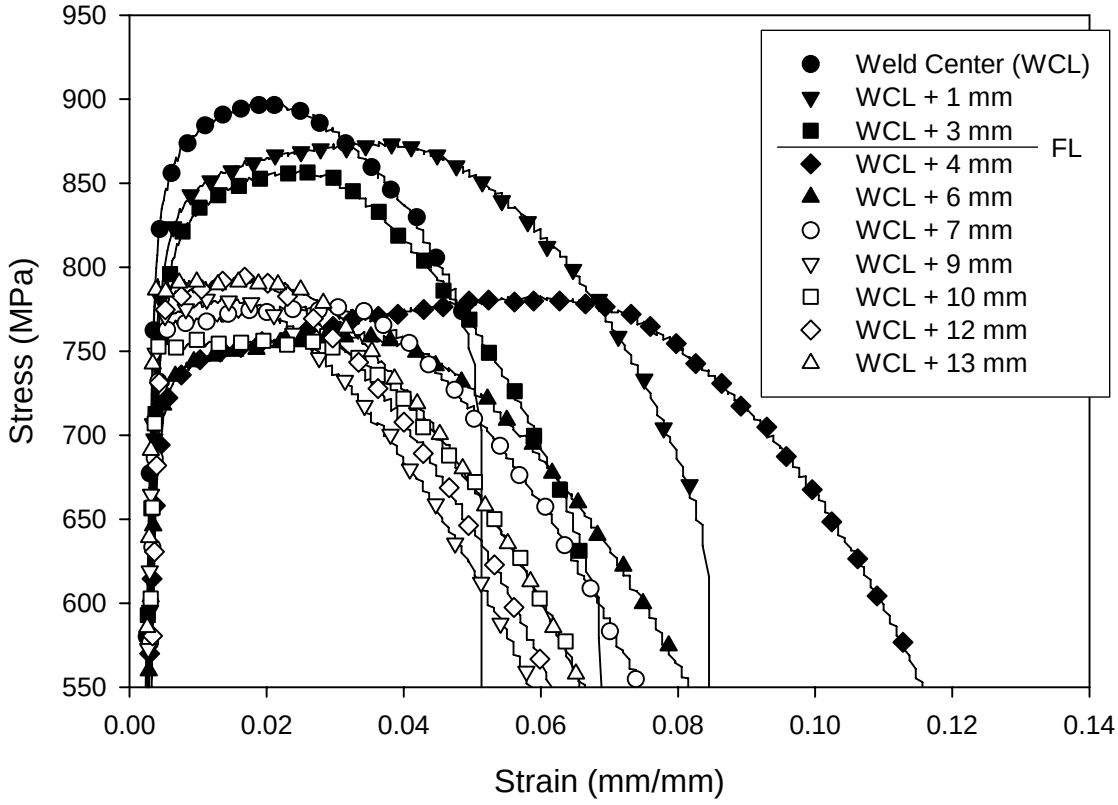

Figure 23. Microtensile Results for Dual Torch Weld W2a

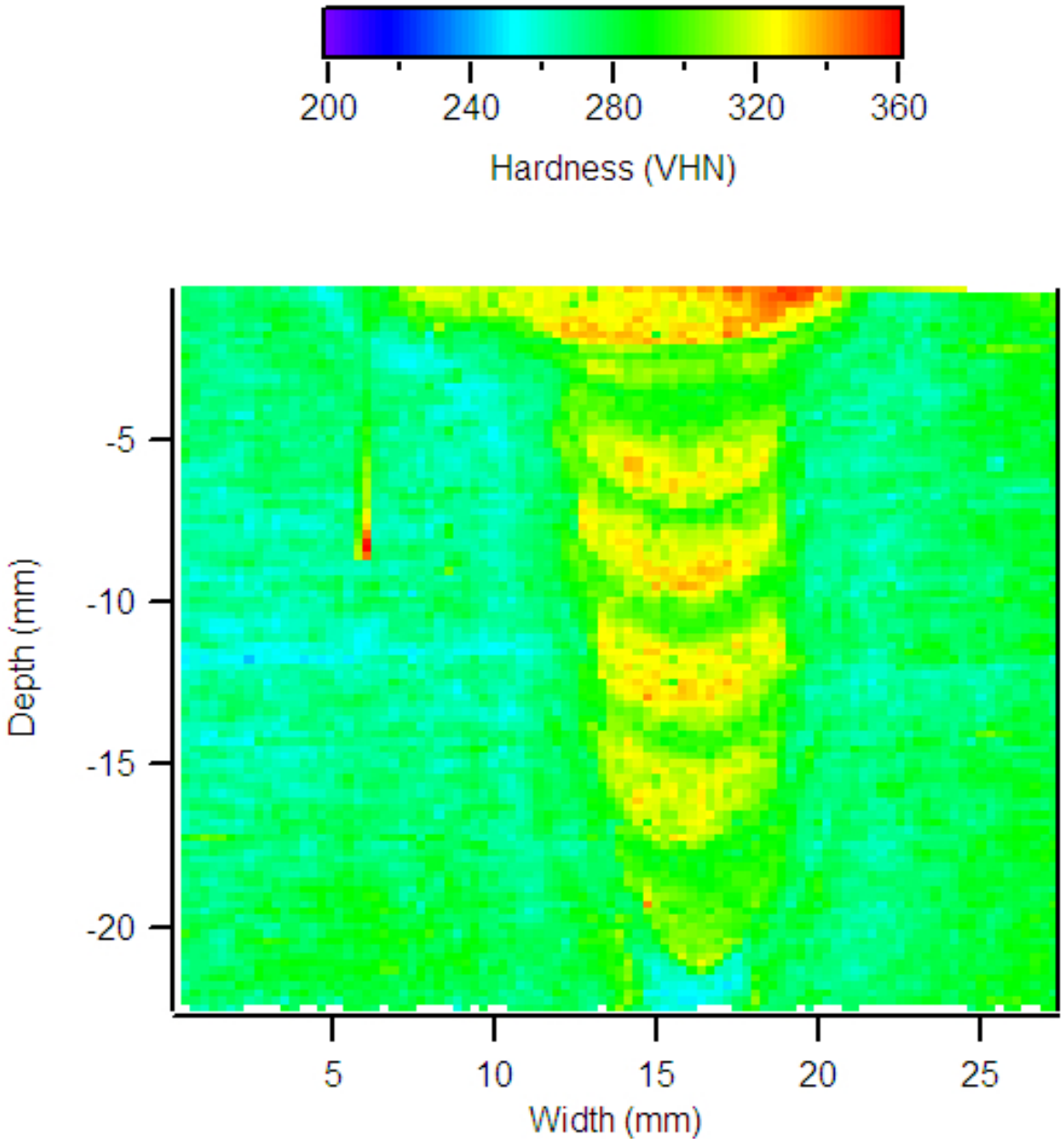

Figure 24. Hardness Map for Dual Torch Weld W2a

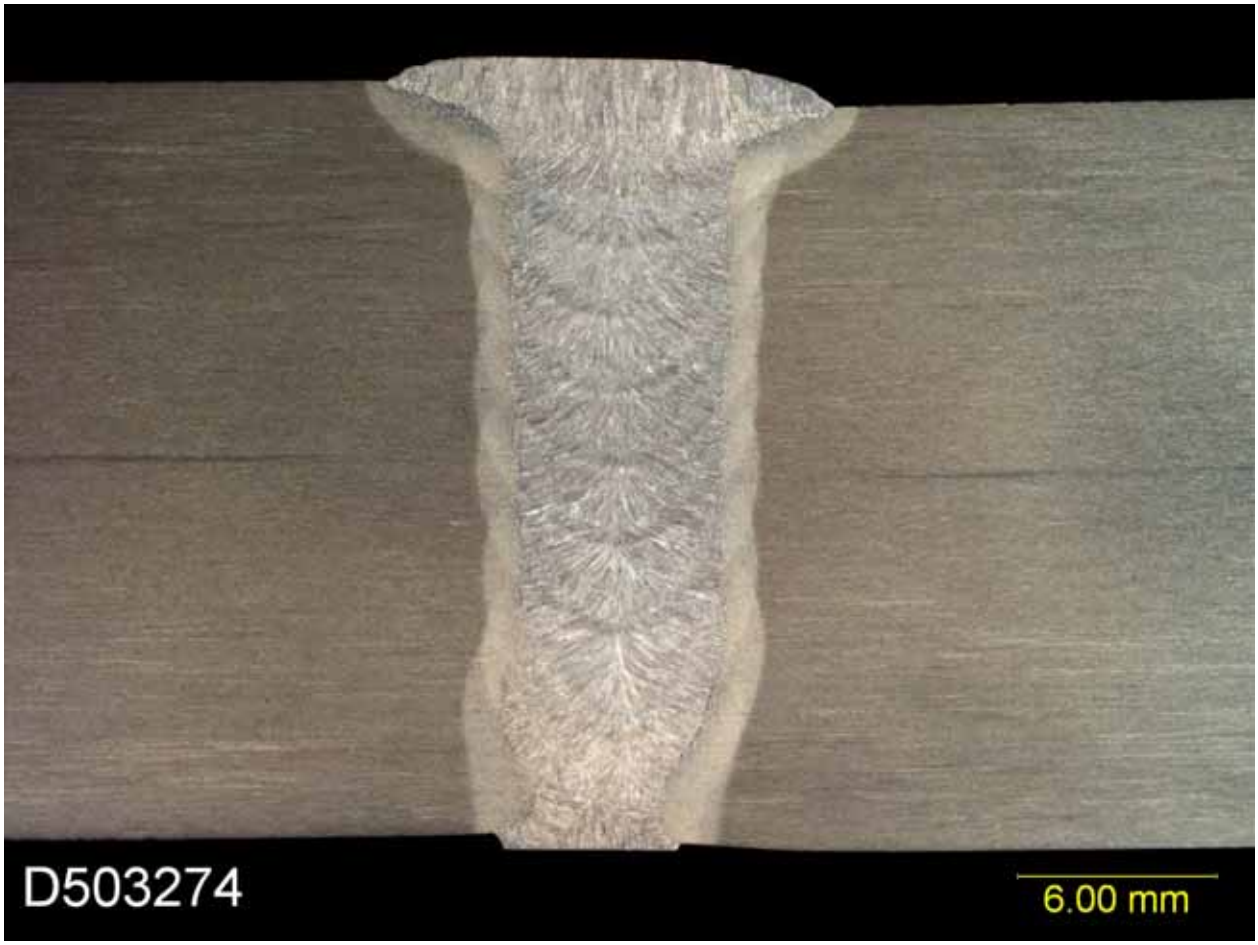

Figure 25. Cross Section of Tandem Weld W2b

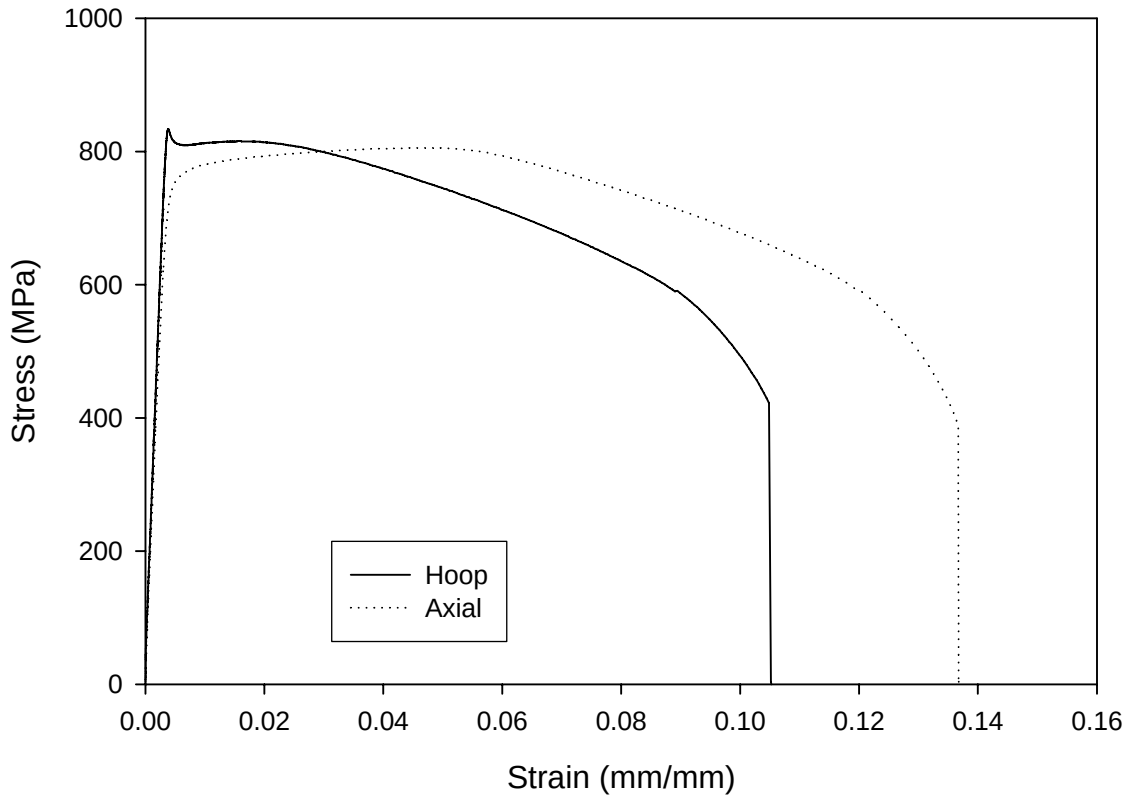

Figure 26. Base Metal Tensile Test Results Adjacent to Tandem Weld W2b

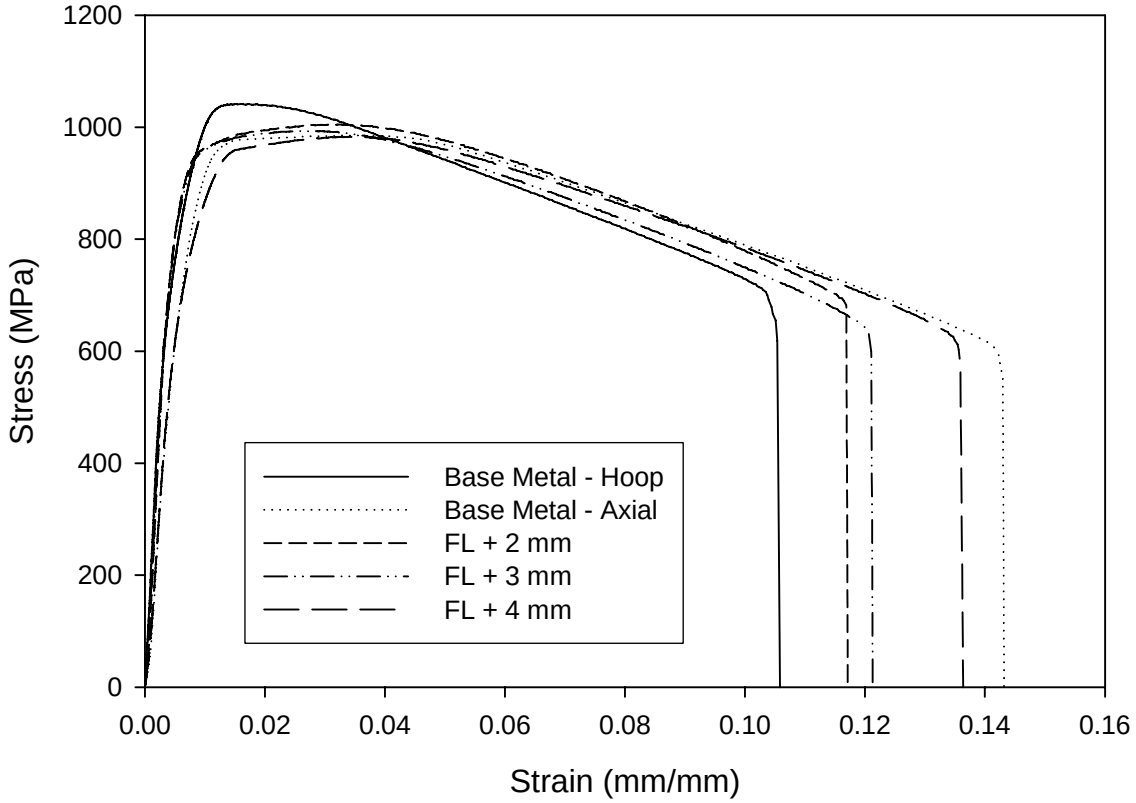

Figure 27. Stub Tensile Results for Tandem Weld W2b

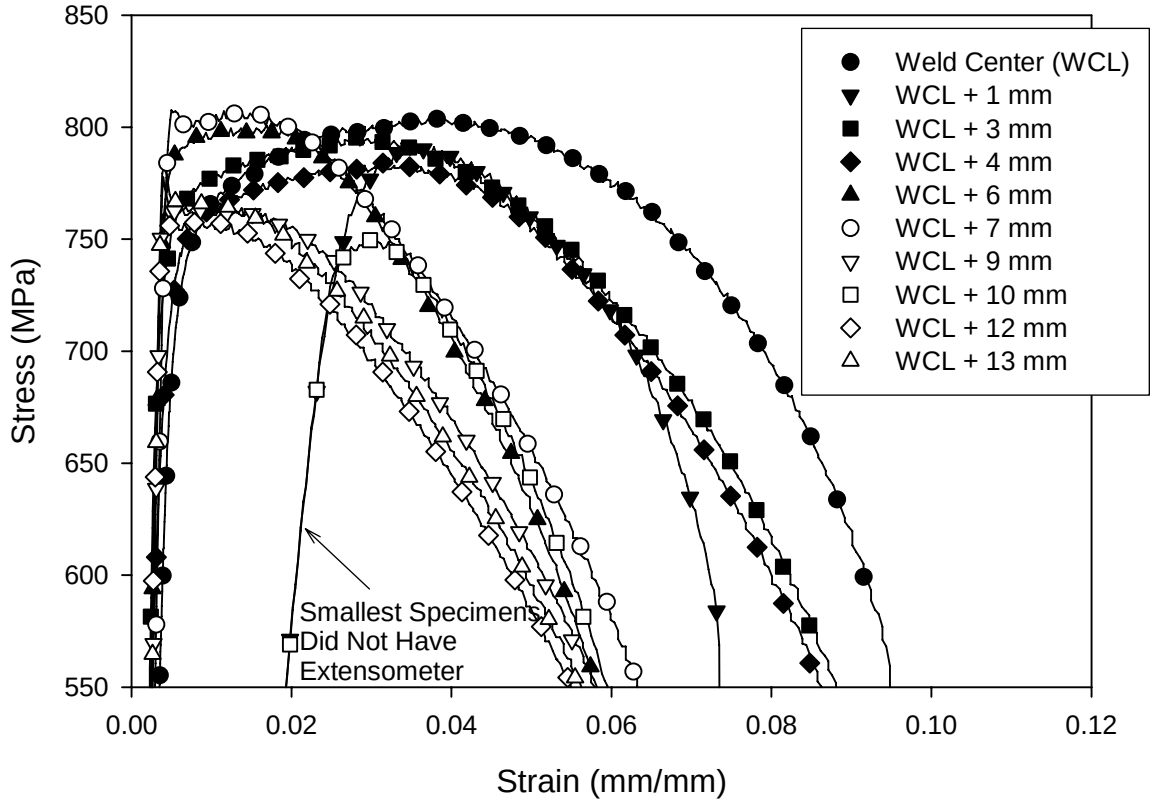

Figure 28. Microtensile Results for Tandem Weld W2b

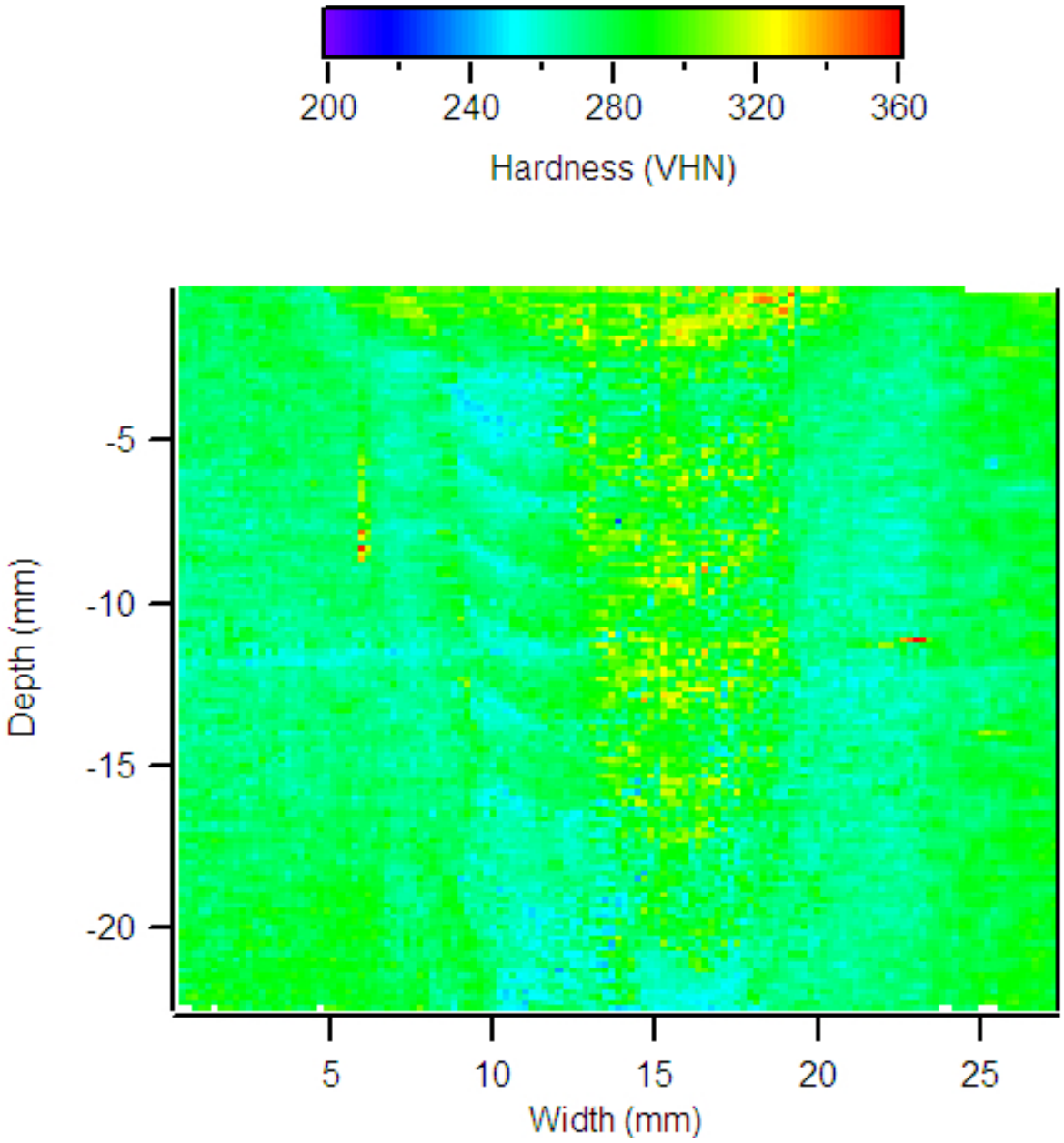

Figure 29. Hardness Map for Tandem Weld W2b

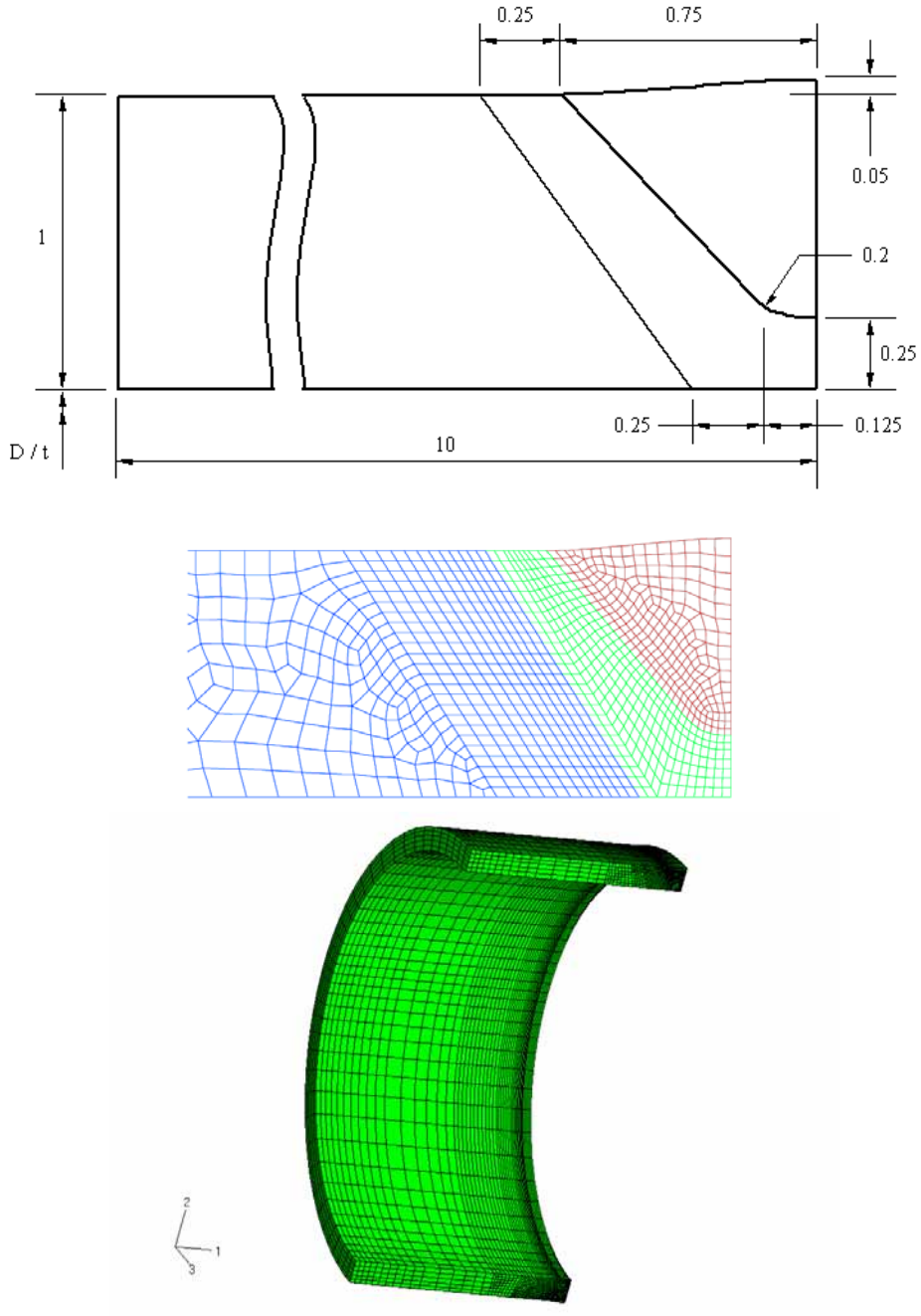

Figure 30. Drawing, 2D, and 3D Mesh for Finite-Element Modeling Assessment with Weld on Right

(Note all dimensions in top drawing are normalized by the base pipe thickness.)

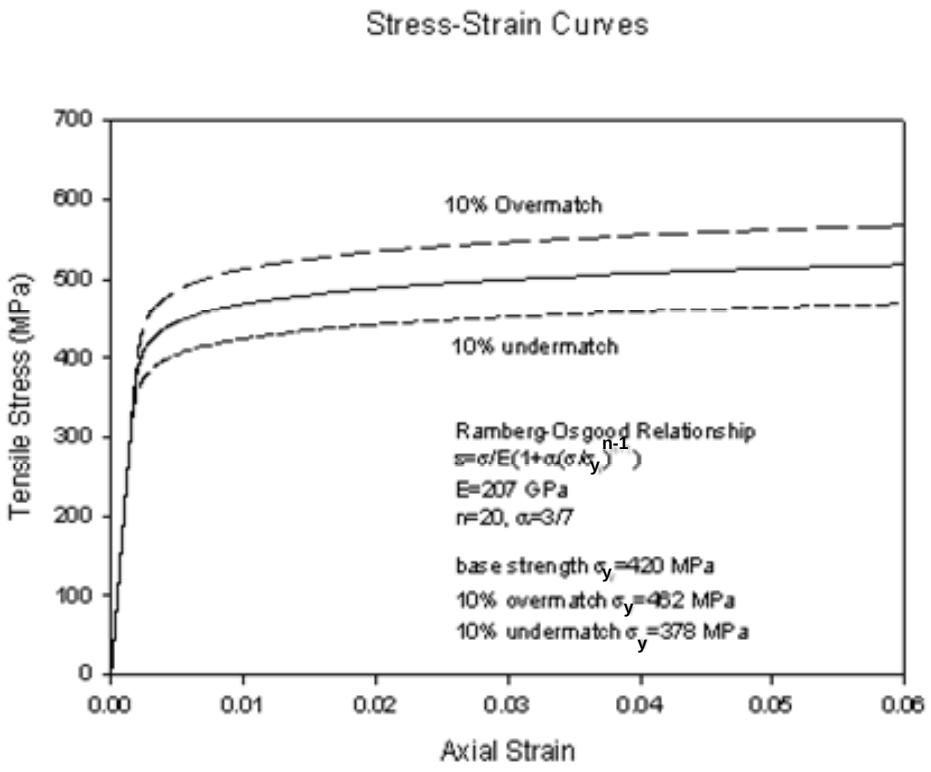

Figure 31. Stress-Strain Curves for Assessment of Loading Type Effect

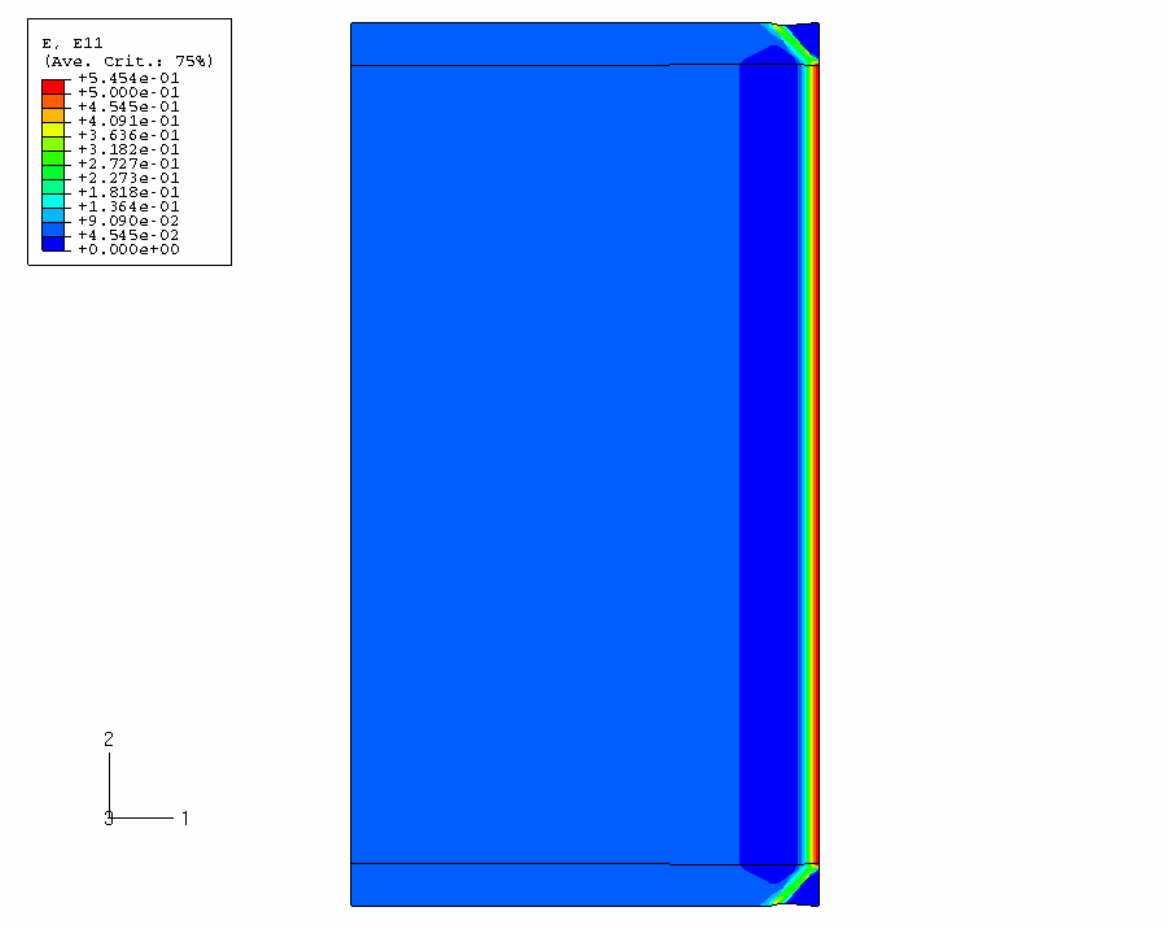

Figure 32. Strain Distribution Under Tension Loading to 6% Remote Strain

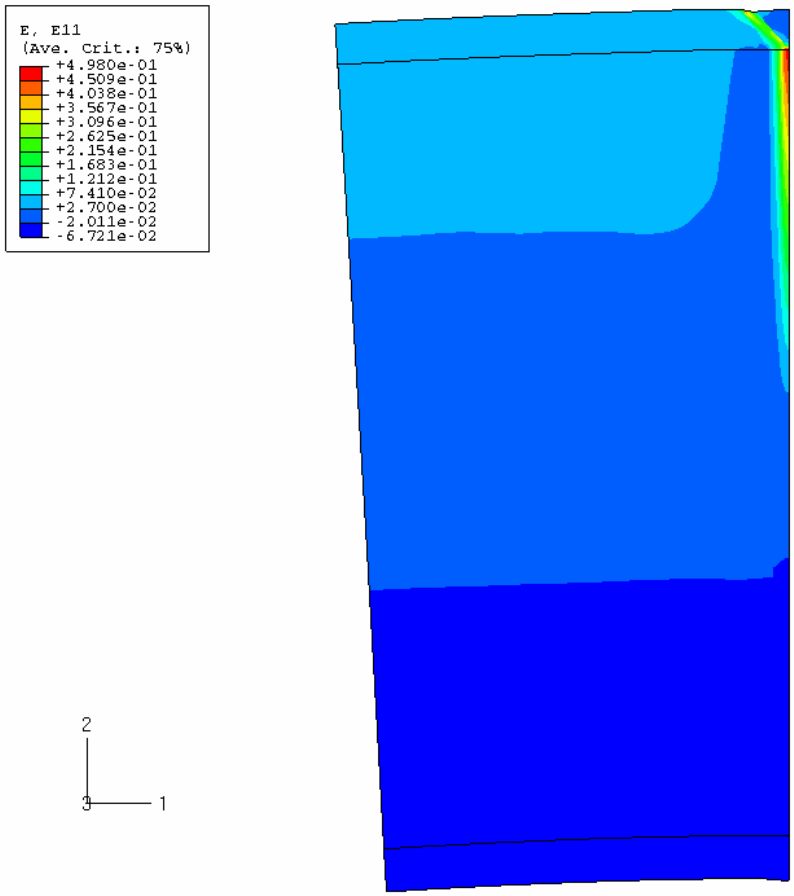

Figure 33. Strain Distribution Under Bending Loading to 6% Remote Strain

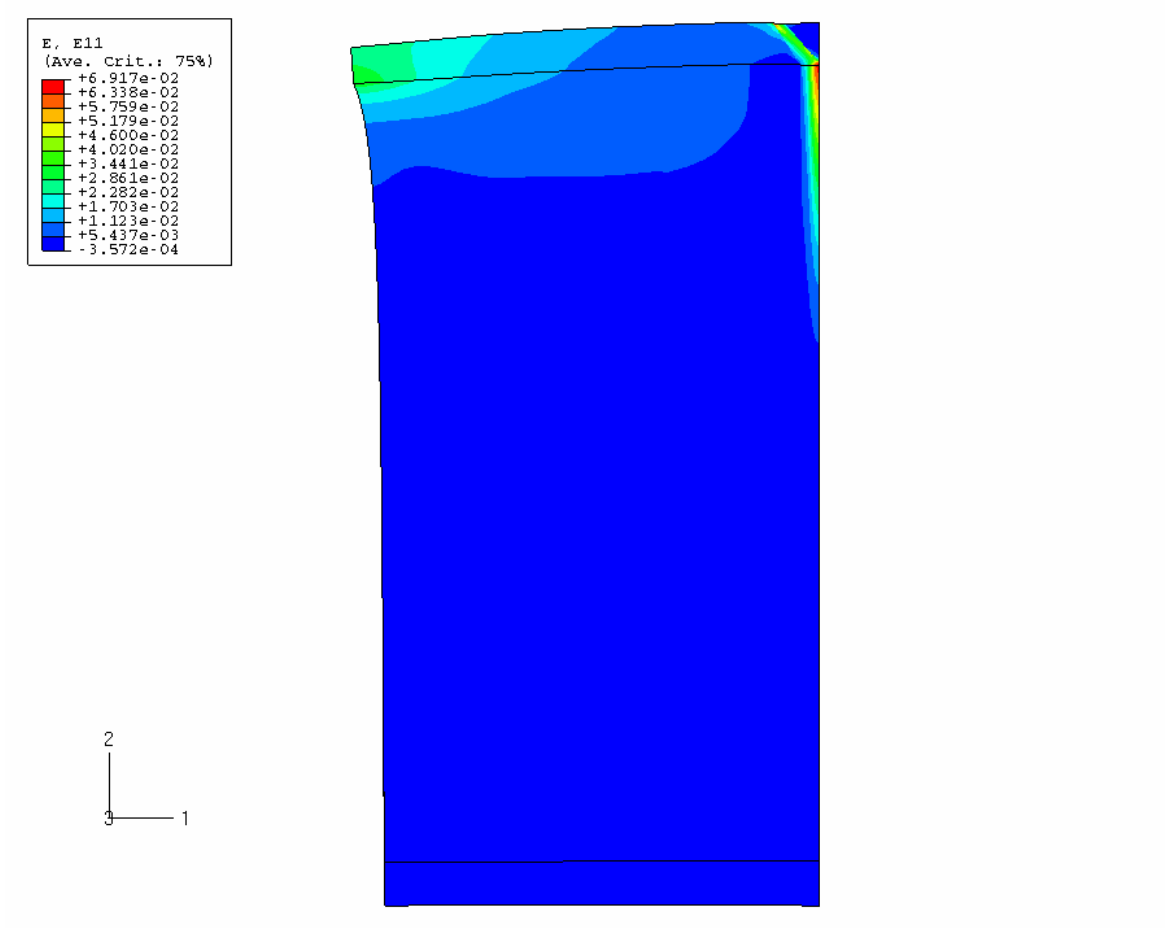

Figure 34. Strain Distribution Under Combination Loading to 6% Remote Strain

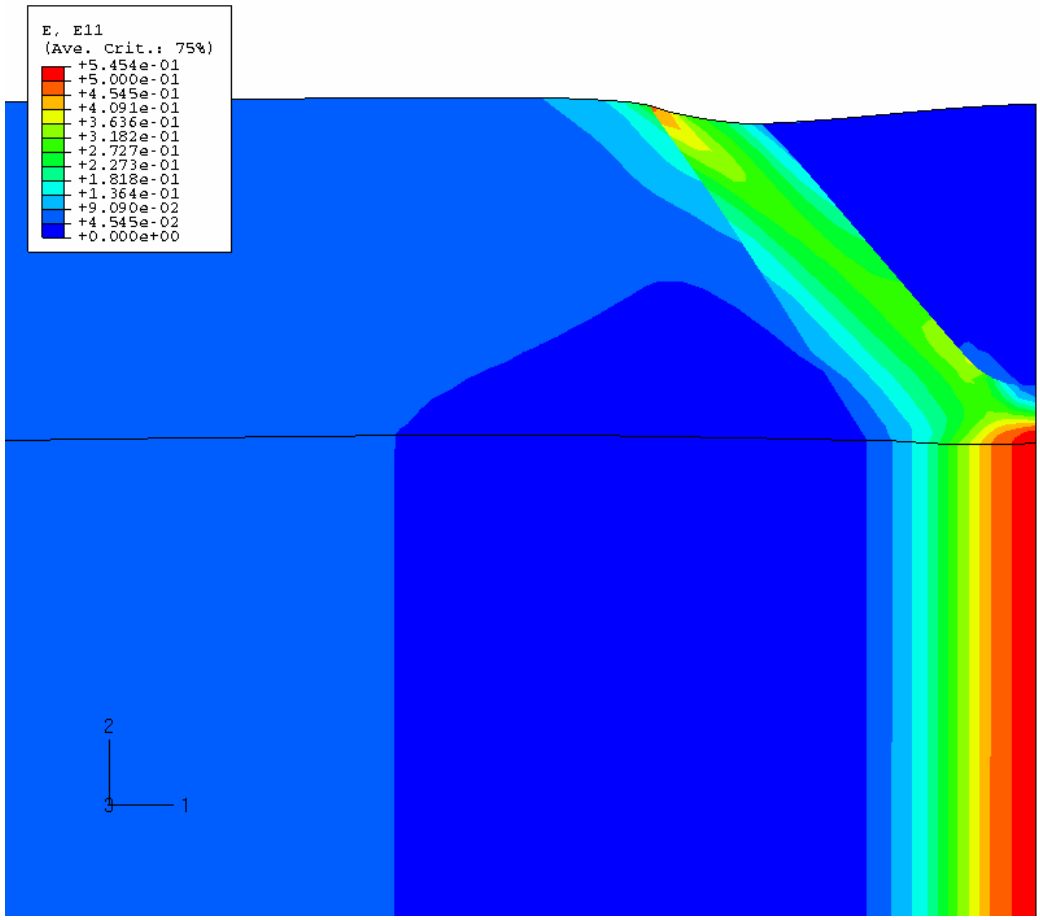

Figure 35. Local Strain Distribution at Weld Under Tension Loading

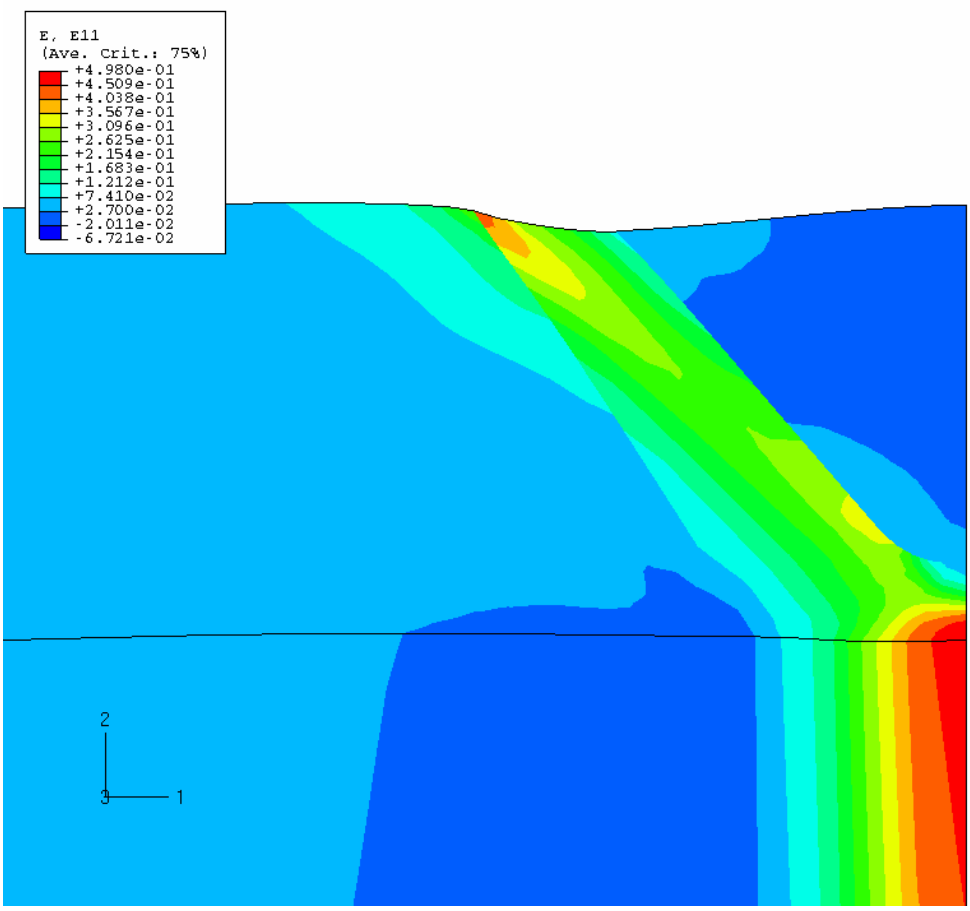

Figure 36. Local Strain Distribution at Tension Side of Weld Under Bending Loading

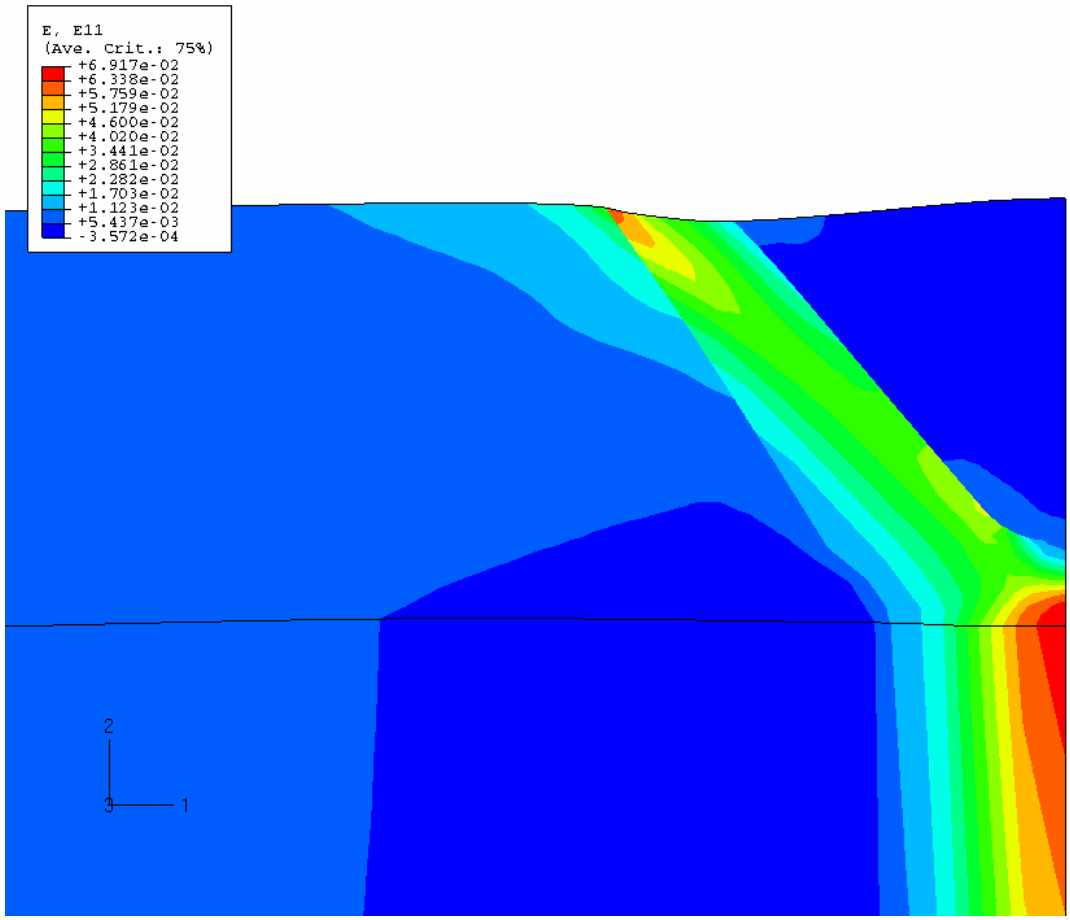

Figure 37. Local Strain Distribution at Peak Tension Side of Weld Under Combination Loading

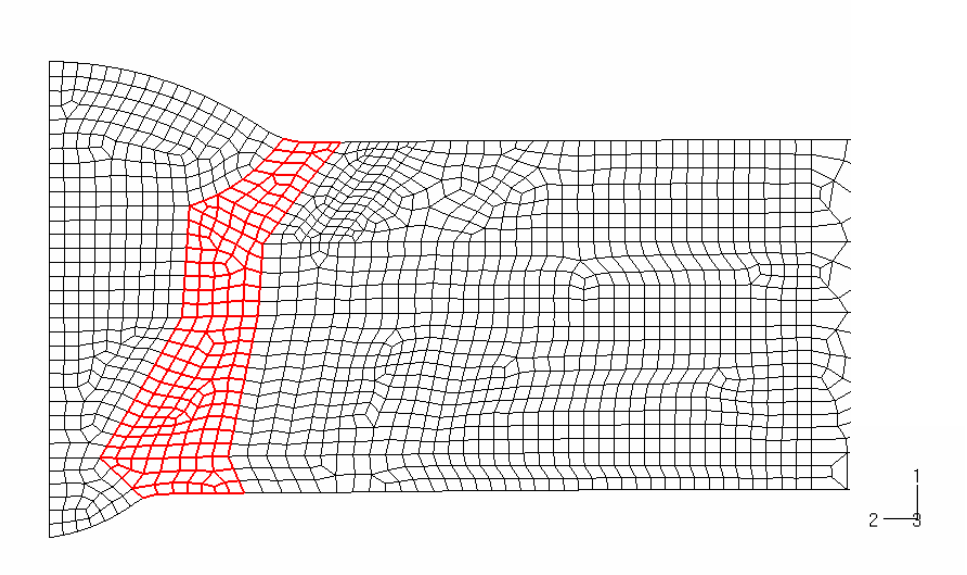

Figure 38. Two-Dimensional Model With Softened Zone Width About 2 mm (0.08 in.)
[1.5 mm (0.06 in.) at cap]

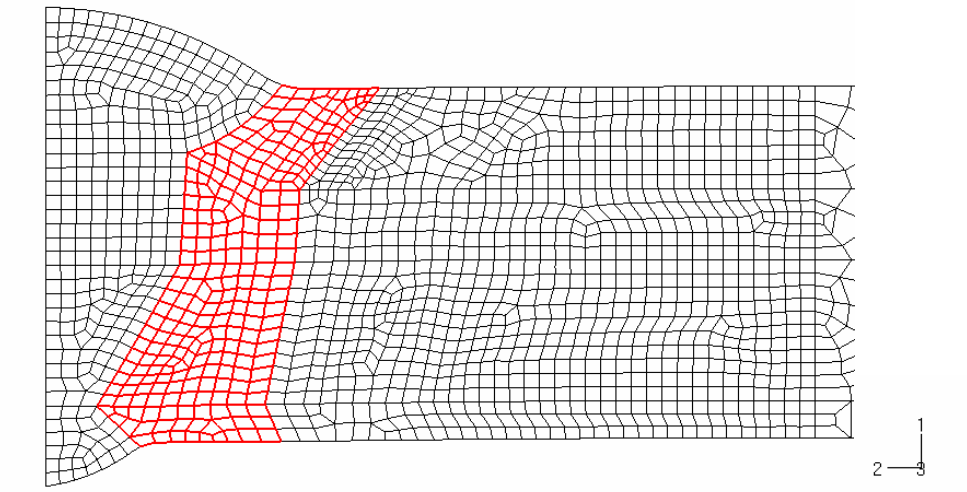

Figure 39. Two-Dimensional Model With Softened Zone Width About 3 mm (0.12 in.)
[2.5 mm (0.10 in.) at cap]

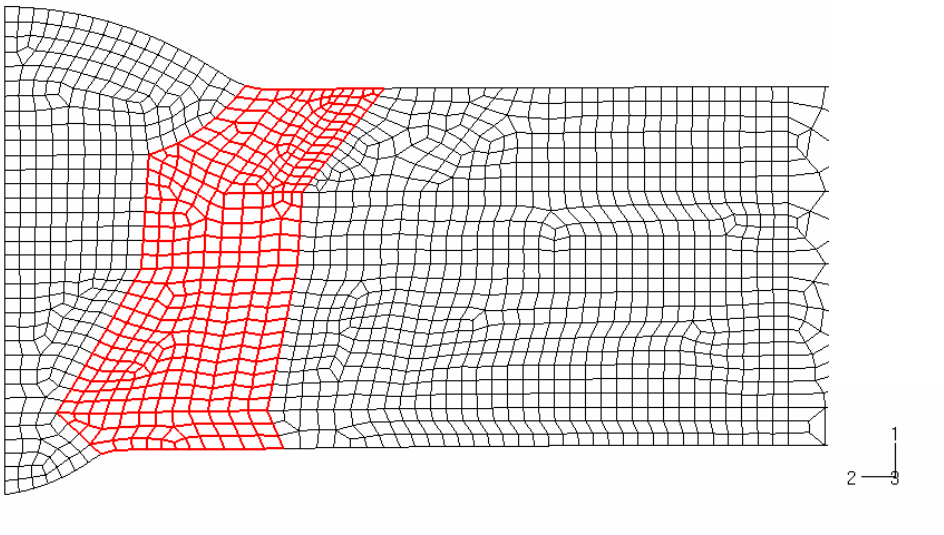

Figure 40. Two-Dimensional Model With Softened Zone Width About 4 mm (0.16 in.)
[3.5 mm (0.14 in.) at cap]

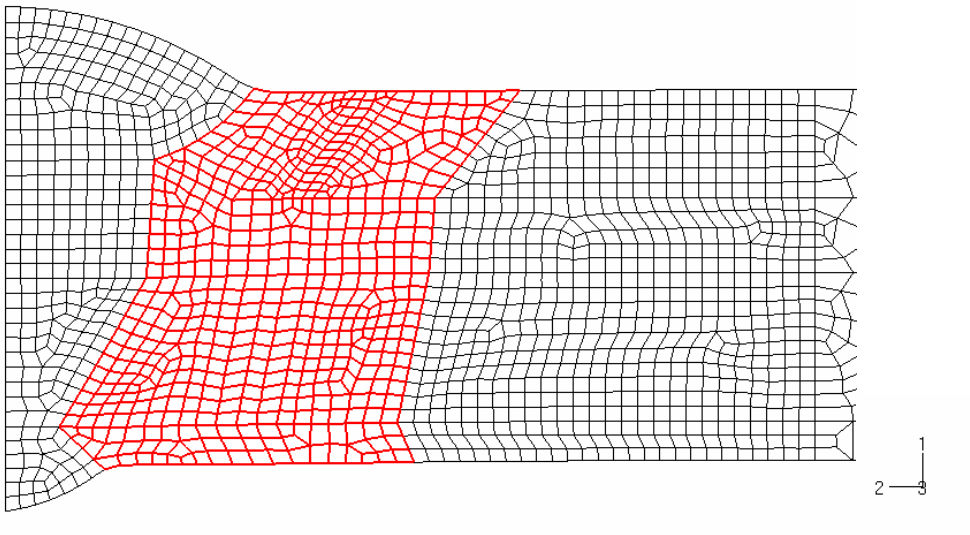

Figure 41. Two-Dimensional Model With Softened Zone Width About 7.5 mm (0.30 in.)
[7 mm (0.28 in.) at cap]

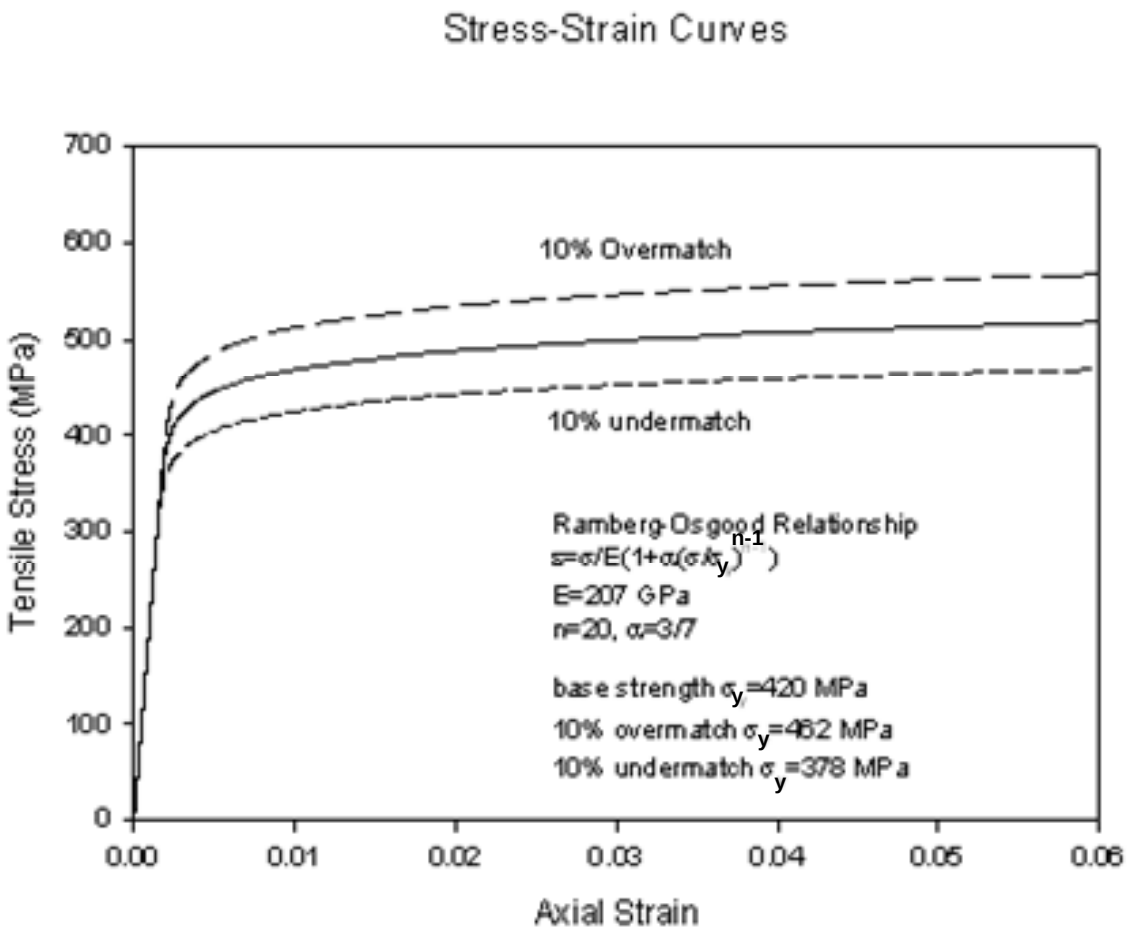

Figure 42. Stress-Strain Curves for Three-Material Model

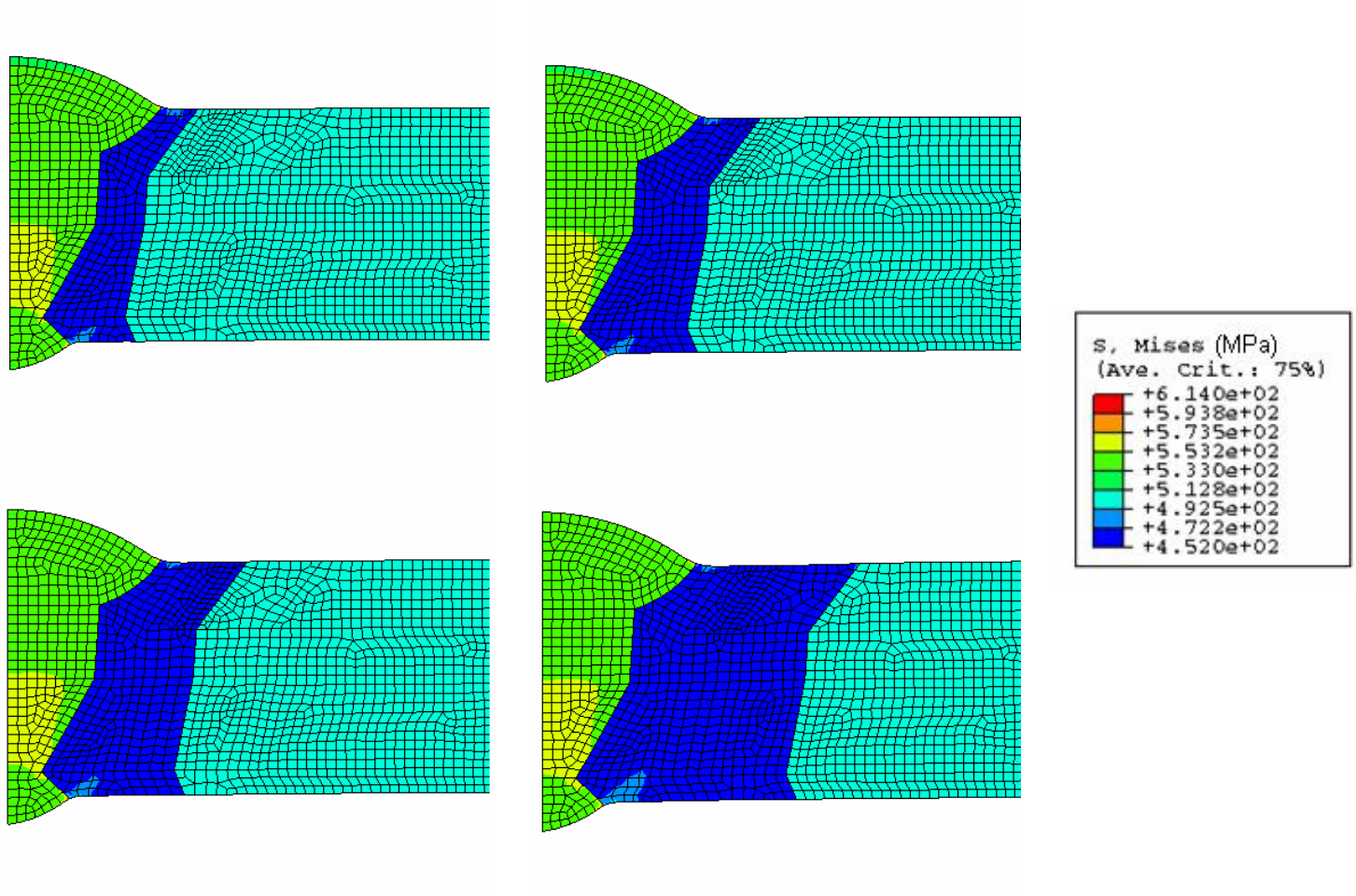

Figure 43. von Mises Stress for Axial Strain of 4% and No Internal Pressure [Upper left HAZ ~2 mm (~0.08 mm), upper right HAZ ~3 mm (~0.12 in.), lower left HAZ ~4 mm (~0.16 in.), lower right HAZ ~7 mm (~0.28 in.)]

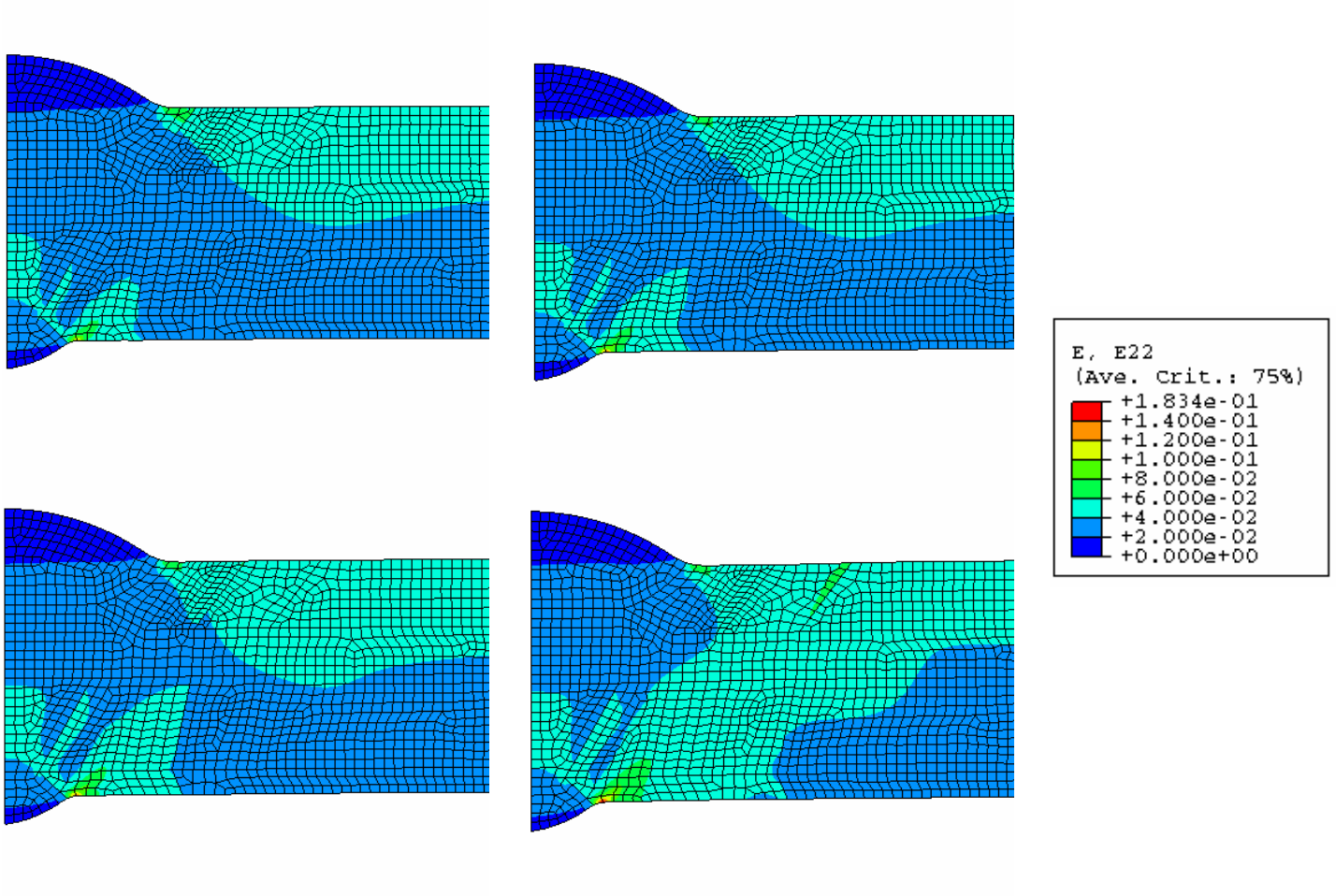

Figure 44. **Axial Strain for Remote Axial Strain of 4% and No Internal Pressure** [Upper left HAZ ~2 mm (~0.08 in.), upper right HAZ ~3 mm (~0.12 in.), lower left HAZ ~4 mm (~0.16 in.), lower right HAZ ~7 mm (~0.28 in.)]

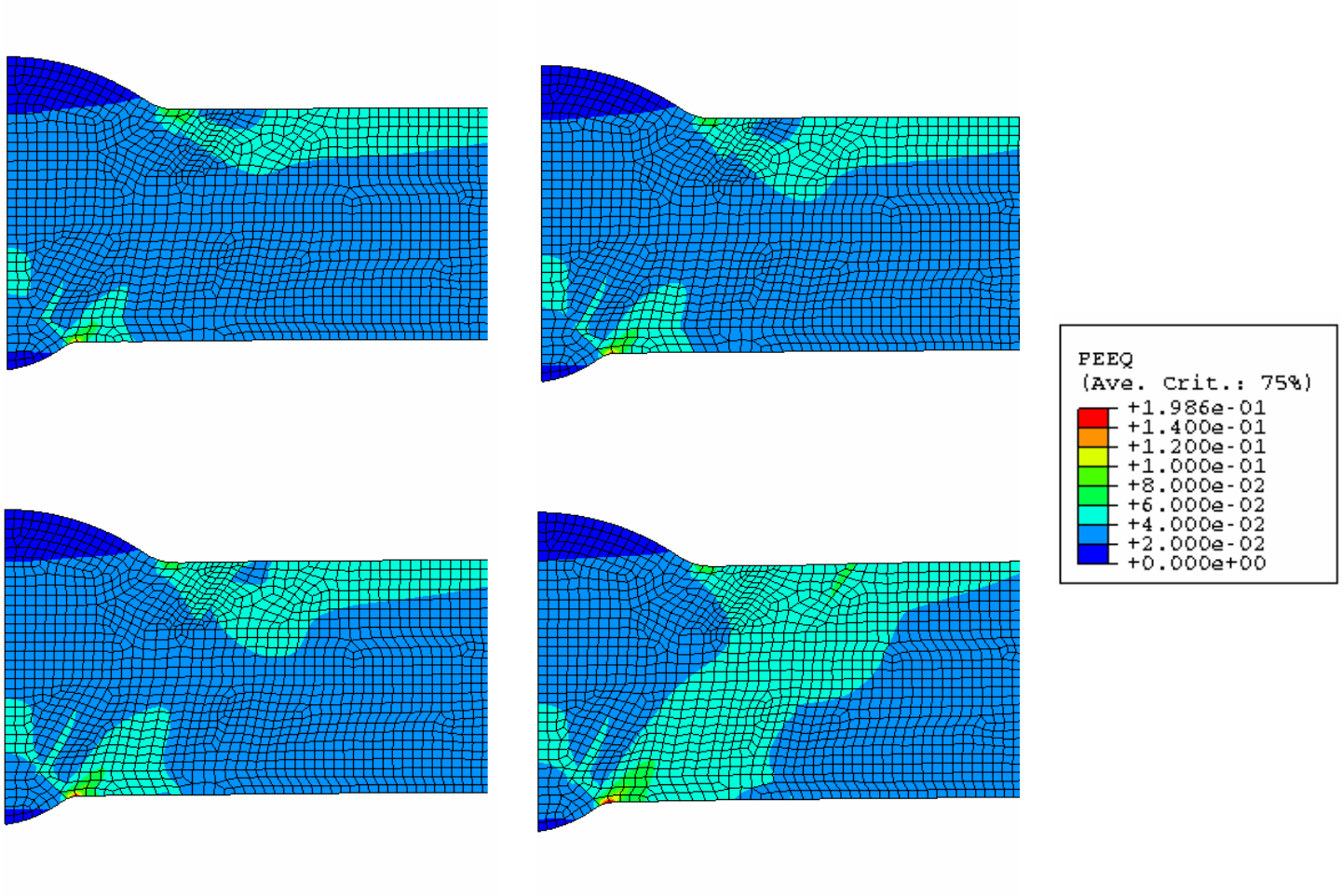

Figure 45. Equivalent Plastic Strain for 4% Remote Strain and No Internal Pressure [Upper left HAZ ~2 mm (~0.08 in.), upper right HAZ ~3 mm (~0.12 in.), lower left HAZ ~4 mm (~0.16 in.), lower right HAZ ~7 mm (~0.28 in.)]

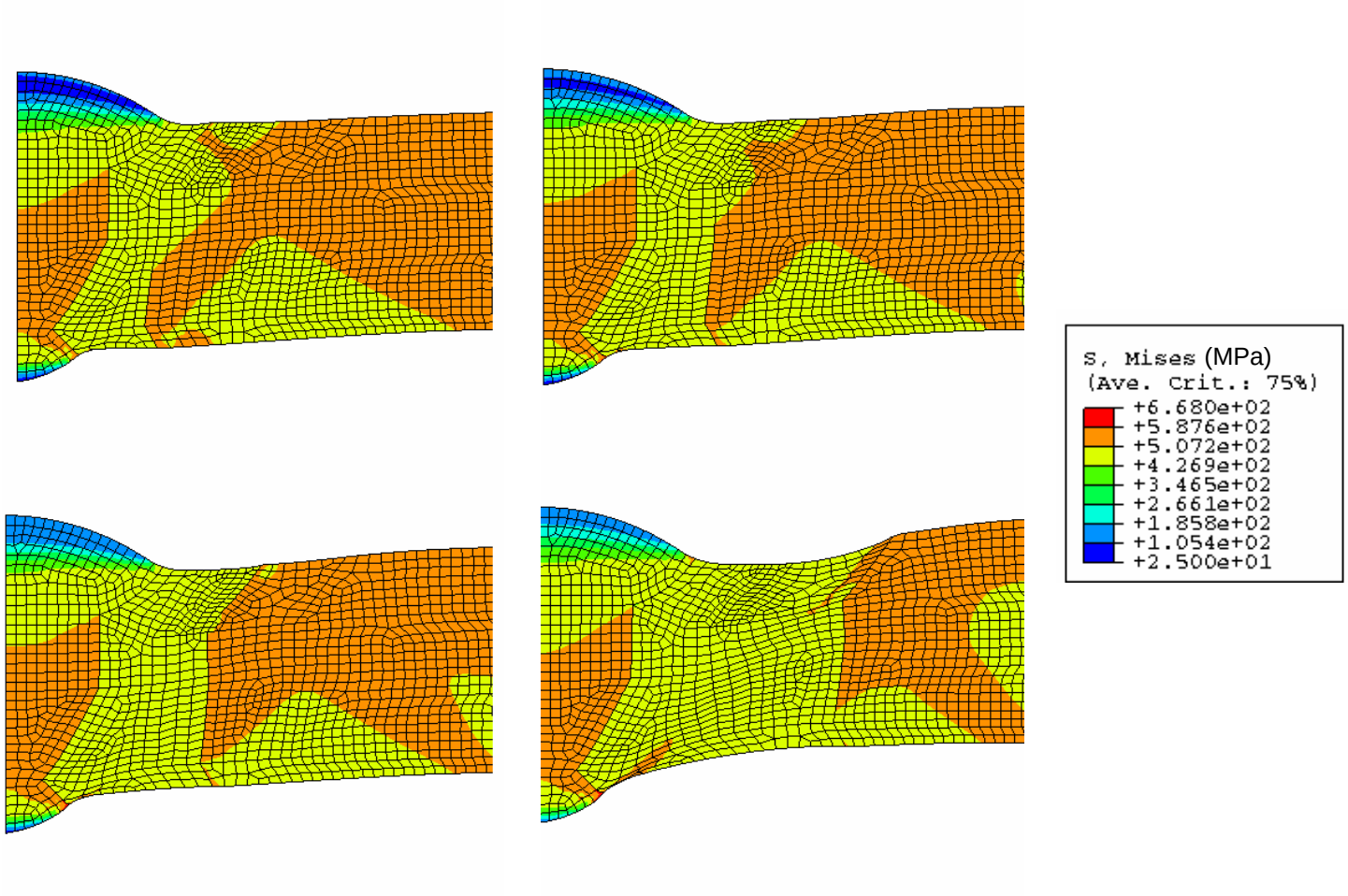

Figure 46. von Mises Stress for 4% Remote Axial Strain and 6.43-MPa (933-psi) Internal Pressure [Upper left HAZ ~2 mm (~0.08 in.), upper right HAZ ~3 mm (~0.12 in.), lower left HAZ ~4 mm (~0.16 in.), lower right HAZ ~7 mm (~0.28 in.)]

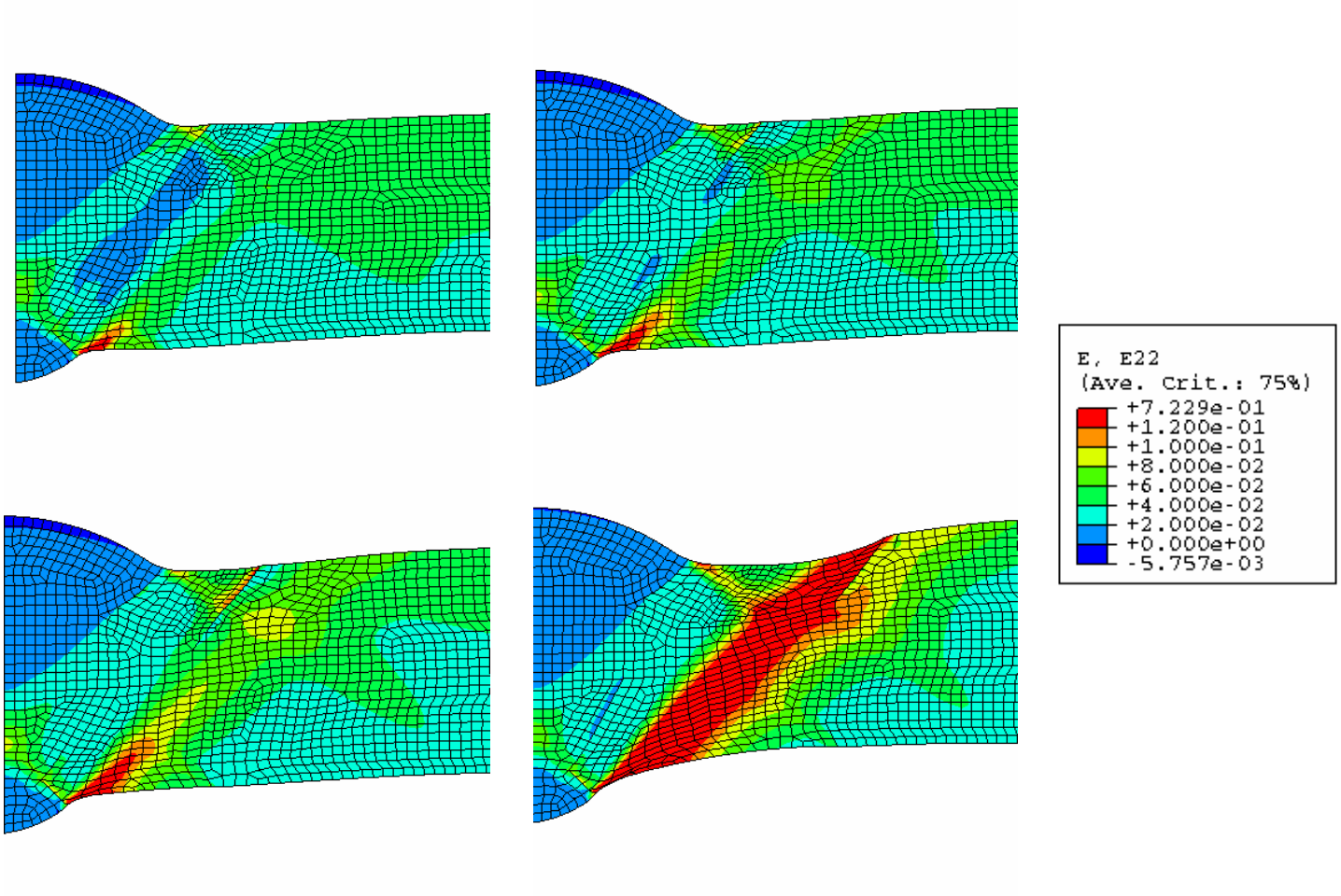

Figure 47. Axial Strain for 4% Remote Axial Strain and 6.43-MPa (933-psi) Internal Pressure [Upper left HAZ ~2 mm (~0.08 in.), upper right HAZ ~3 mm (~0.12 in.), lower left HAZ ~4 mm (~0.16 in.), lower right HAZ ~7 mm (~0.28 in.)]

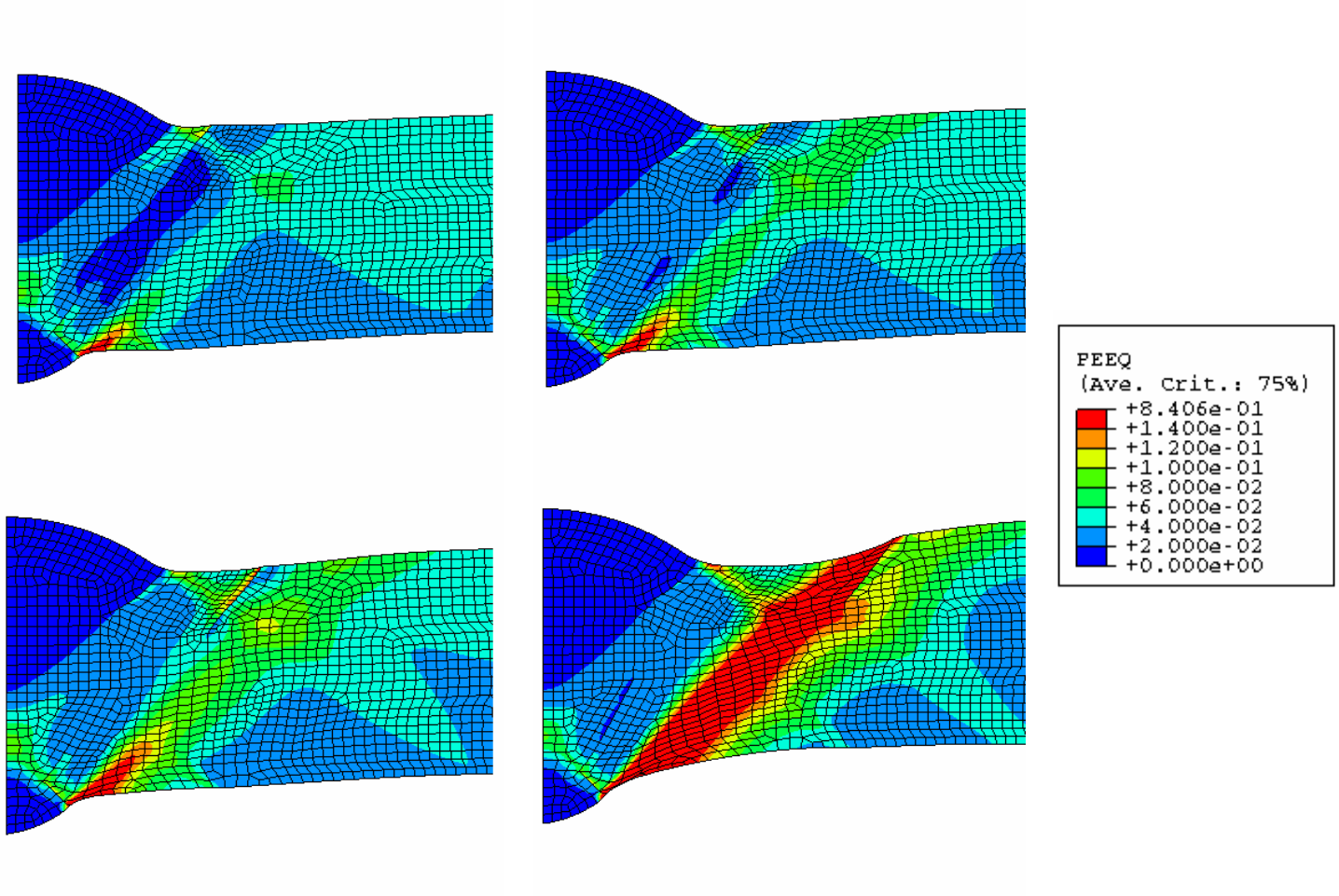

Figure 48. **Equivalent Plastic Strain for 4% Axial Remote Strain and 6.43-MPa (933-psi) Internal Pressure** [Upper left HAZ ~2 mm (~0.08 in.), upper right HAZ ~3 mm (~0.12 in.), lower left HAZ ~4 mm (~0.16 in.), lower right HAZ ~7 mm (~0.28 in.)]

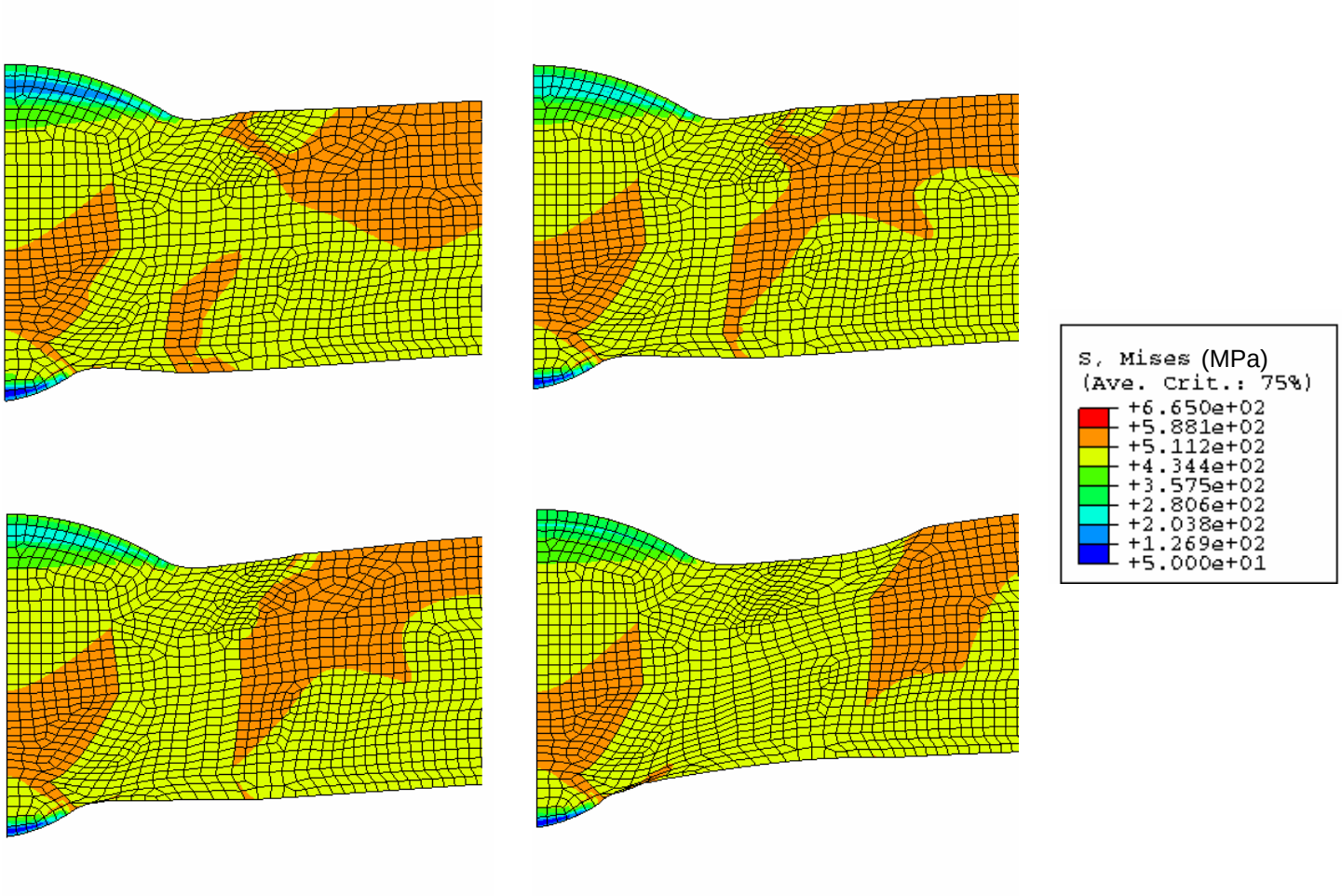

Figure 49. **von Mises Stress for 4% Axial Strain and 6.43-MPa (933-psi) Internal Pressure, Weaker Weld Metal** [Upper left HAZ ~2 mm (~0.08 in.), upper right HAZ ~3 mm (0.12 in.), lower left HAZ ~4 mm (~0.16 in.), lower right HAZ ~7 mm (~0.28 in.)]

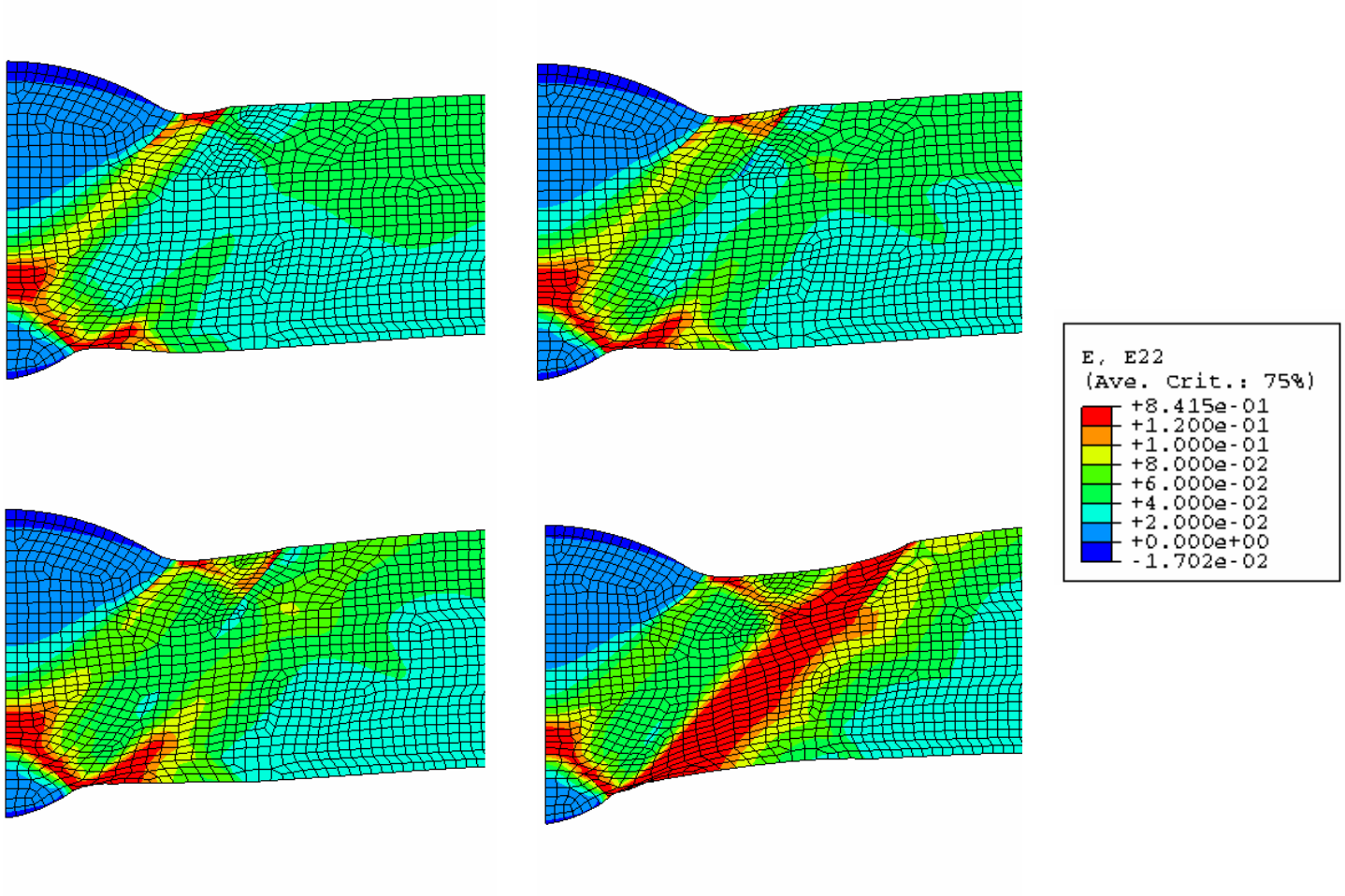

Figure 50. **Axial Strain for 4% Remote Strain and 6.43-MPa (933-psi) Internal Pressure, Weaker Weld Metal** [Upper left HAZ ~2 mm (~0.08 in.), upper right HAZ ~3 mm (~0.12 in.), lower left HAZ ~4 mm (0.16 in.), lower right HAZ ~7 mm (~0.28 in.)]

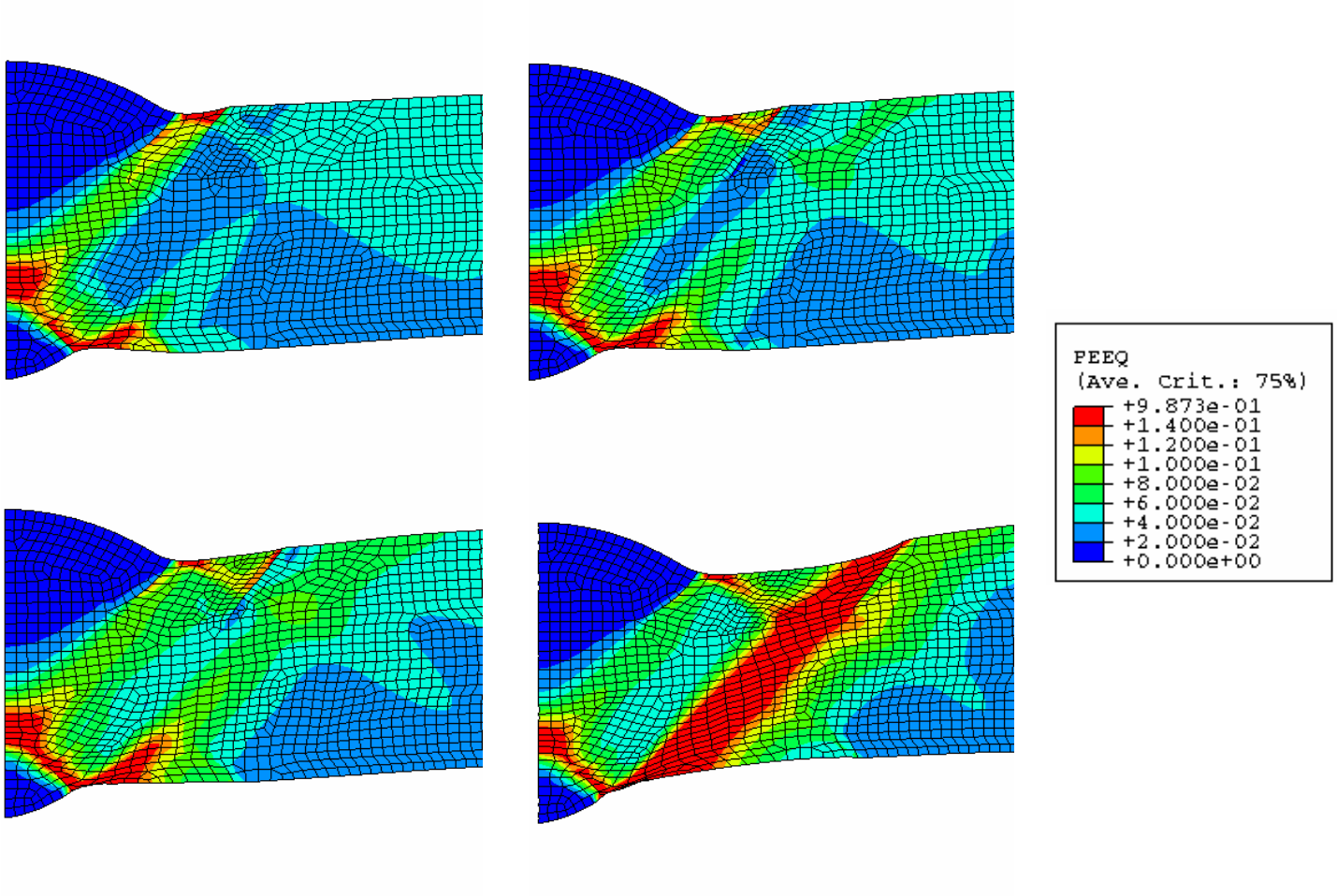

Figure 51. Plastic Equivalent Strain for 4% Remote Strain and 6.43-MPa (933-psi) Internal Pressure, Weaker Weld Metal
[Upper left HAZ ~2 mm (~0.08 in.), upper right HAZ ~3 mm (~0.12 in.), lower left HAZ ~4 mm (~0.16 in.), lower right HAZ ~7 mm (~0.28 in.)]

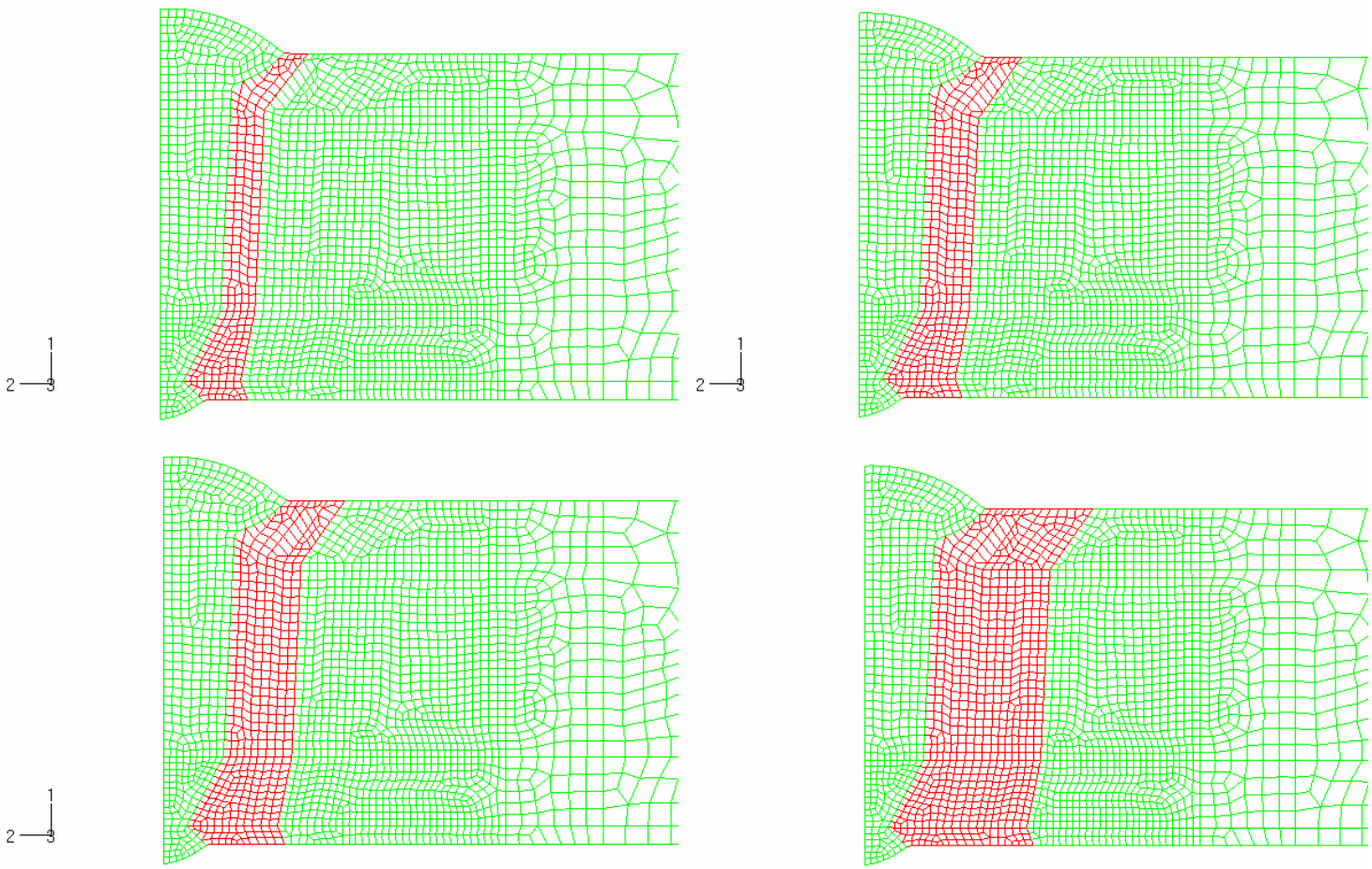

Figure 52. HAZ Models for 20-mm (0.79 in.)-Thick Pipe [Upper left HAZ ~2 mm (~0.08 in.), upper right HAZ ~3 mm (~0.12 in.), lower left HAZ ~4 mm (~0.16 in.), lower right HAZ ~7 mm (~0.28 in.)]

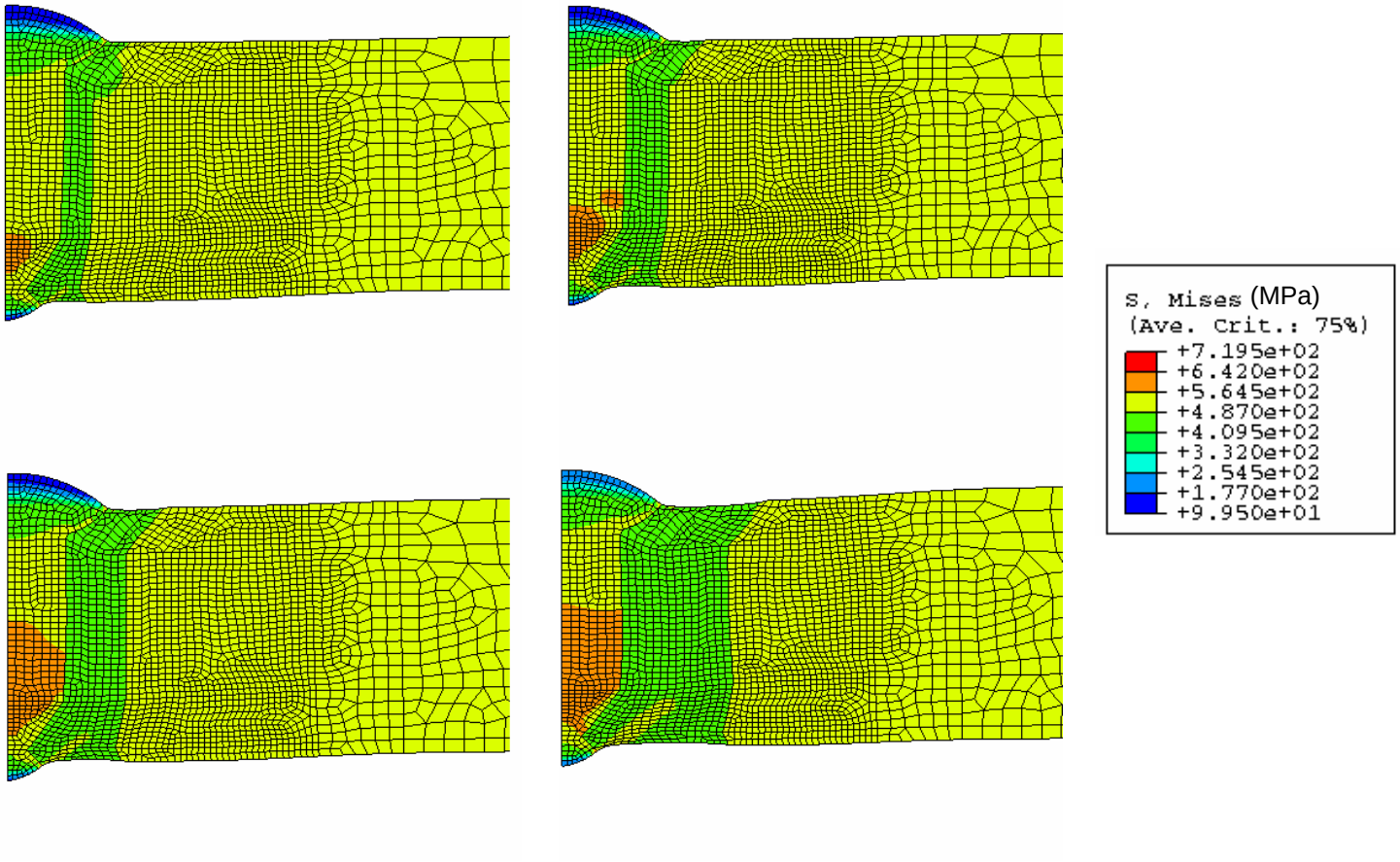

Figure 53. von Mises Stresses for 4% Remote Strain and 12.86-MPa (1866-psi) Internal Pressure, 20-mm (0.79-in.) Pipe
[Upper left HAZ ~2 mm (~0.08 in.), upper right HAZ ~3 mm (~0.12 in.), lower left HAZ ~4 mm (~0.16 in.), lower right HAZ ~7 mm (~0.28 in.)]

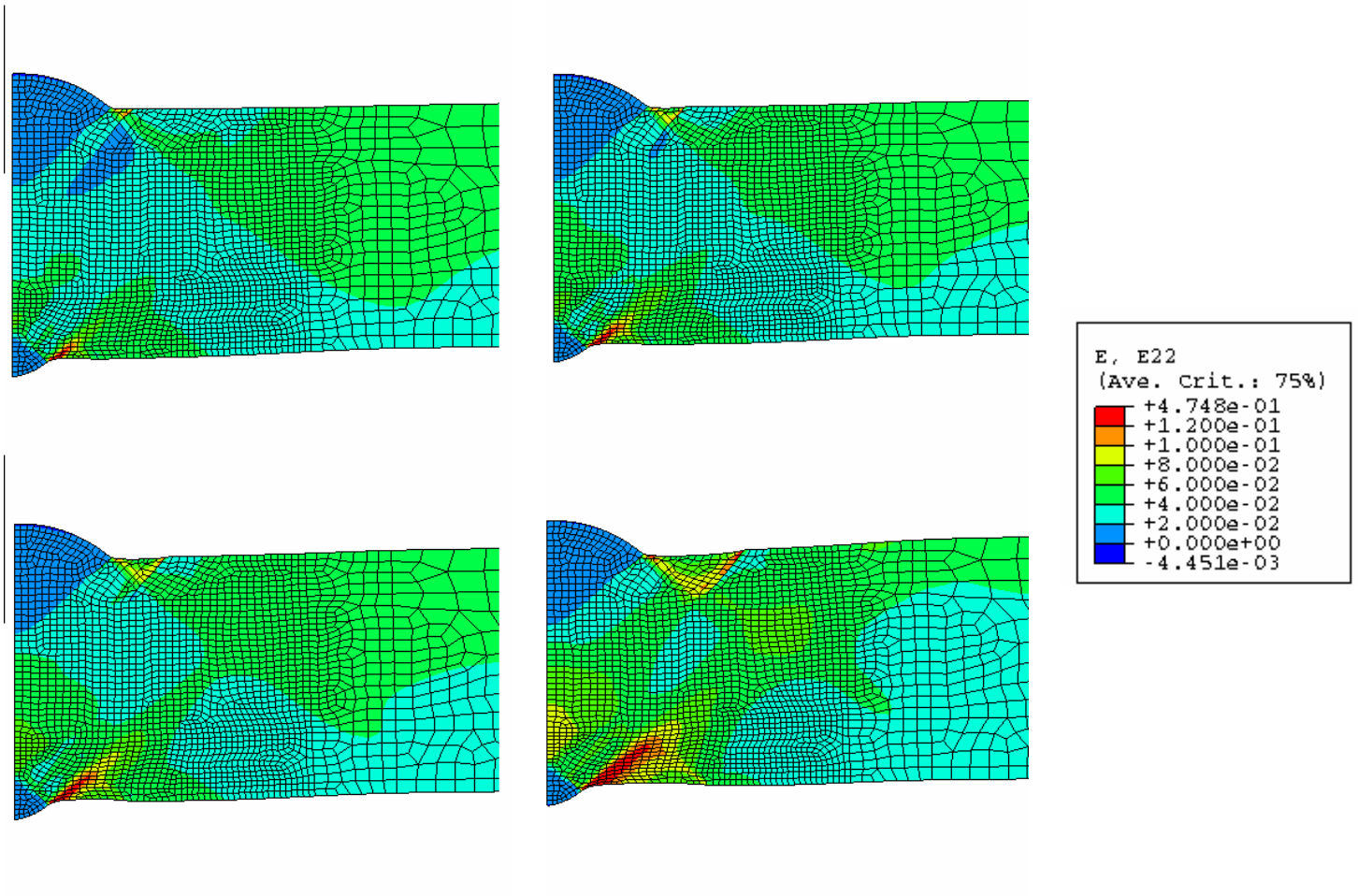

Figure 54. **Axial Strains for 4% Remote Strain and 12.86-MPa (1866-psi) Internal Pressure, 20-mm (0.79-in.) Pipe** [Upper left HAZ ~2 mm (~0.08 in.), upper right HAZ ~3 mm (~0.12 in.), lower left HAZ ~4 mm (~0.16 in.), lower right HAZ ~7 mm (~0.28 in.)]

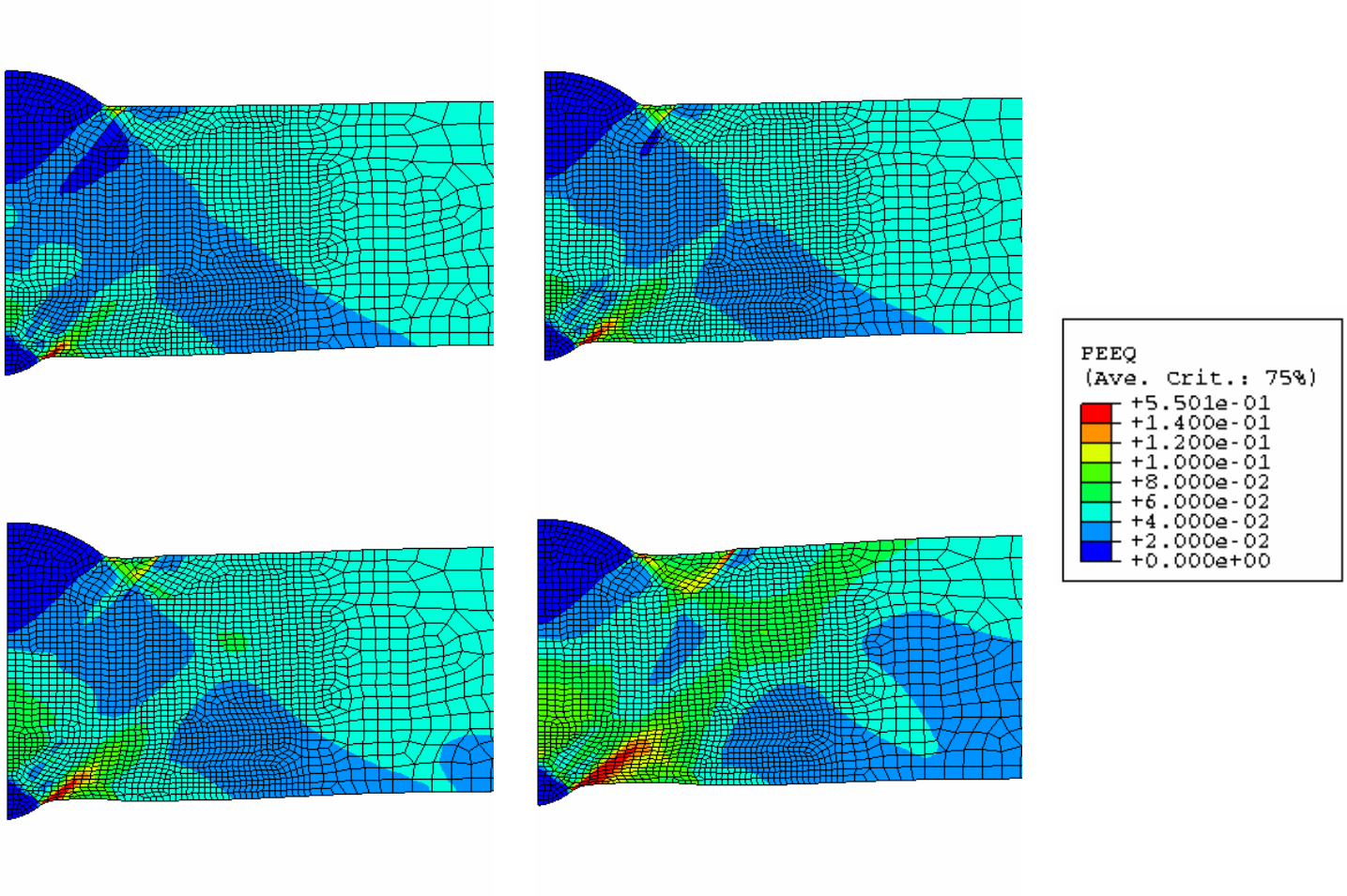

Figure 55. Equivalent Plastic Strains for 4% Remote Strain and 12.86-MPa (1866-psi) Internal Pressure, 20-mm (0.79-in.) Pipe [Upper left HAZ ~2 mm (~0.08 in.), upper right HAZ ~3 mm (~0.12 in.), lower left HAZ ~4 mm (~0.16 in.), lower right HAZ ~7 mm (~0.28 in.)]

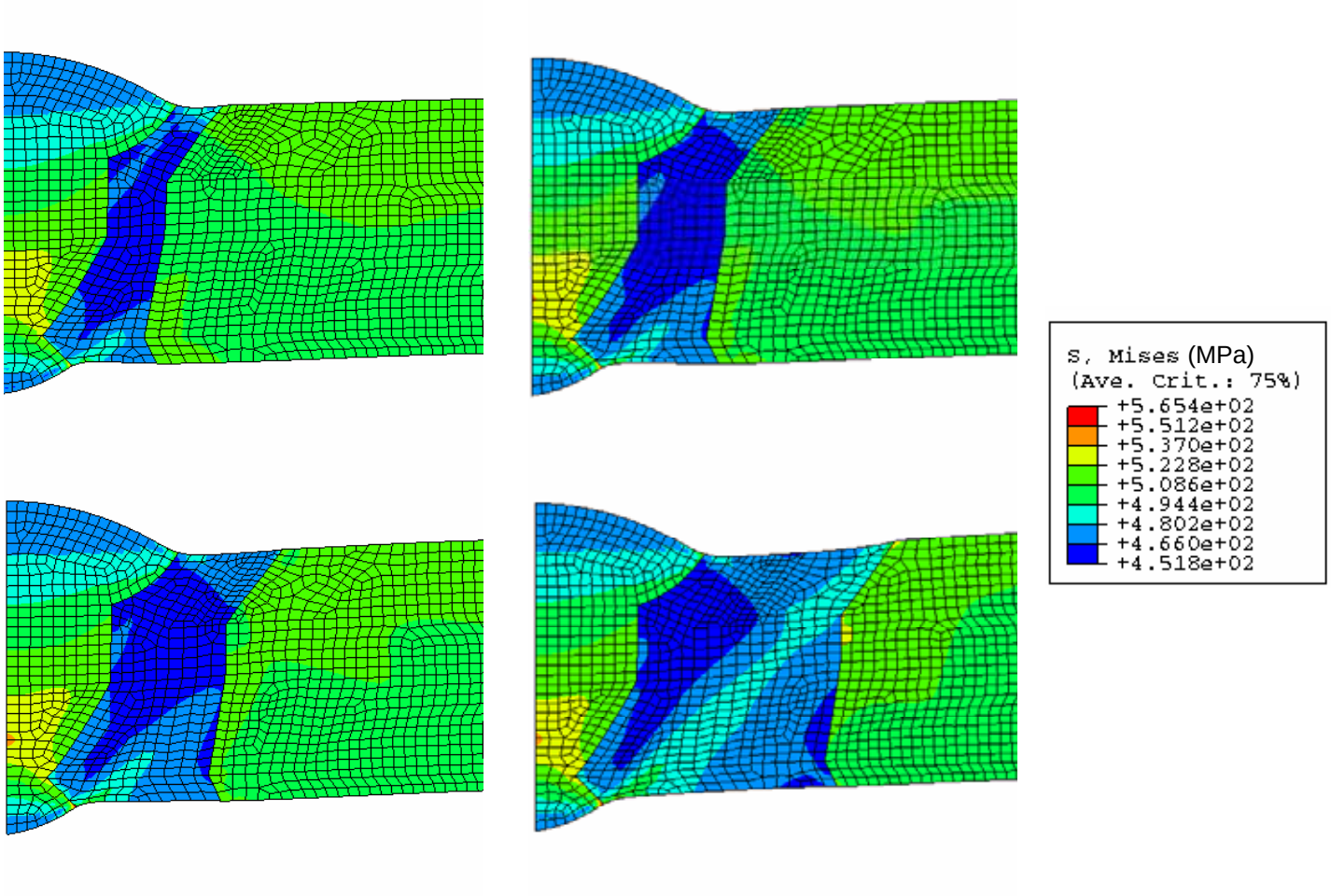

Figure 56. von Mises Stresses for 4% Remote Strain and 3.125-MPa (453-psi) Internal Pressure, 10-mm (0.39-in) Pipe
[Upper left HAZ ~2 mm (~0.08 in.), upper right HAZ ~3 mm (~0.12 in.), lower left HAZ ~4 mm (~0.16 in.), lower right HAZ ~7 mm (~0.28 in.)]

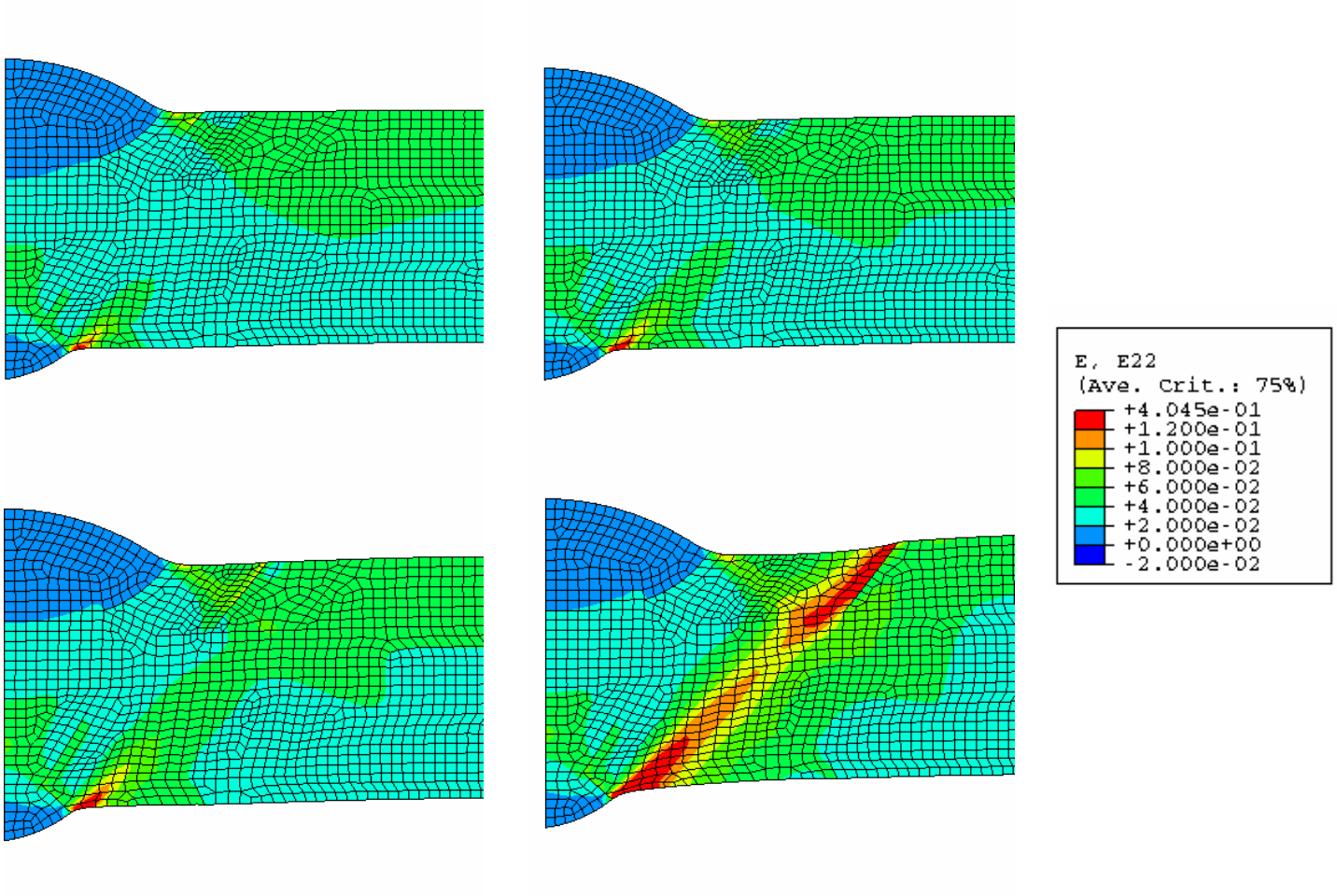

Figure 57. Axial Strains for 4% Remote Strain and 3.125-MPa (453-psi) Internal Pressure, 10-mm (0.39-in.) Pipe [Upper left HAZ ~2 mm (~0.08 in.), upper right HAZ ~3 mm (~0.12 in.), lower left HAZ ~4 mm (~0.16 in.), lower right HAZ ~7 mm (~0.28 in.)]

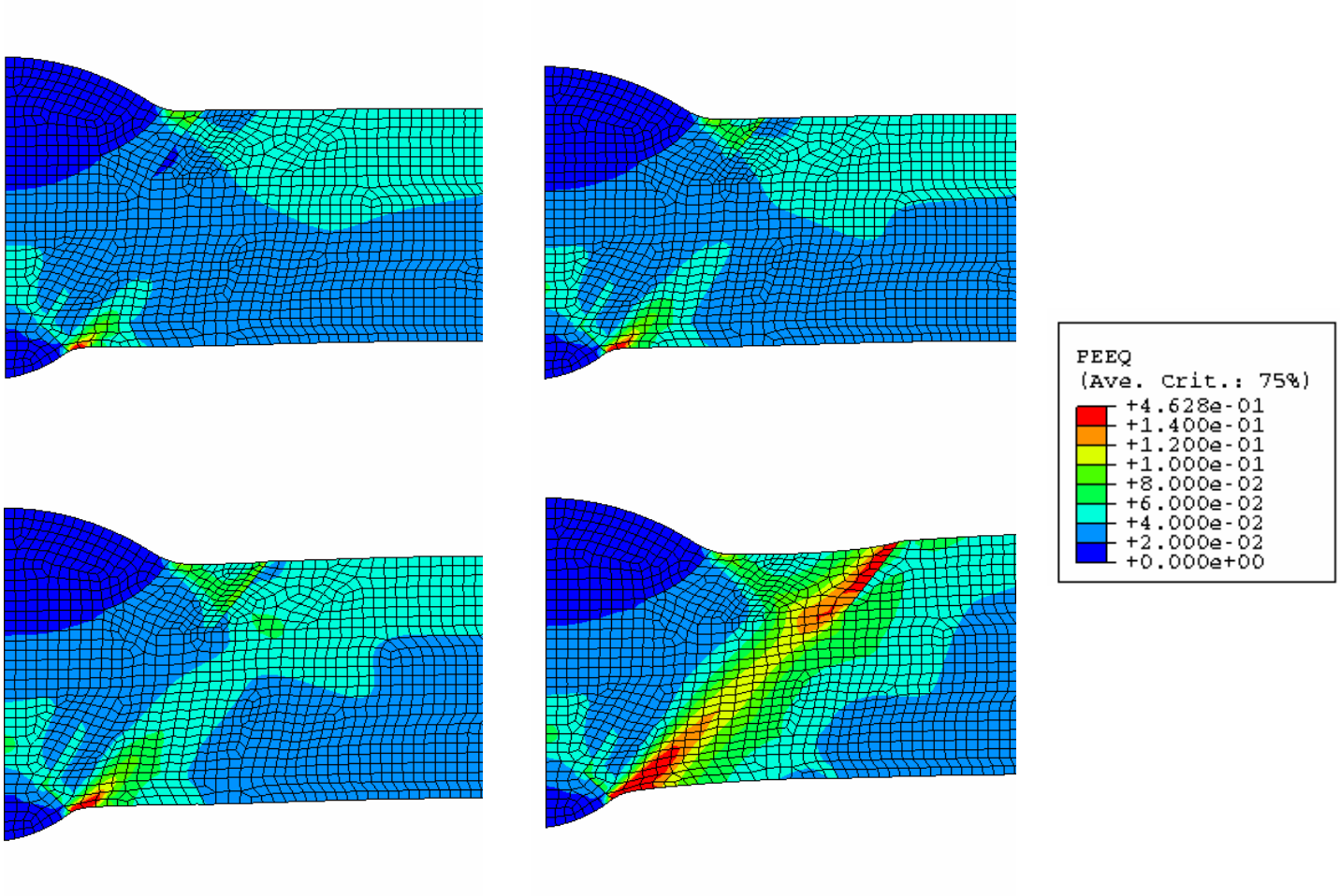

Figure 58. Equivalent Plastic Strains for 4% Remote Strain and 3.125-MPa (453-psi) Internal Pressure, 10-mm (0.39-in.) Pipe [Upper left HAZ ~2 mm (~0.08 in.), upper right HAZ ~3 mm (~0.12 in.), lower left HAZ ~4 mm (~0.16 in.), lower right HAZ ~7 mm (~0.28 in.)]

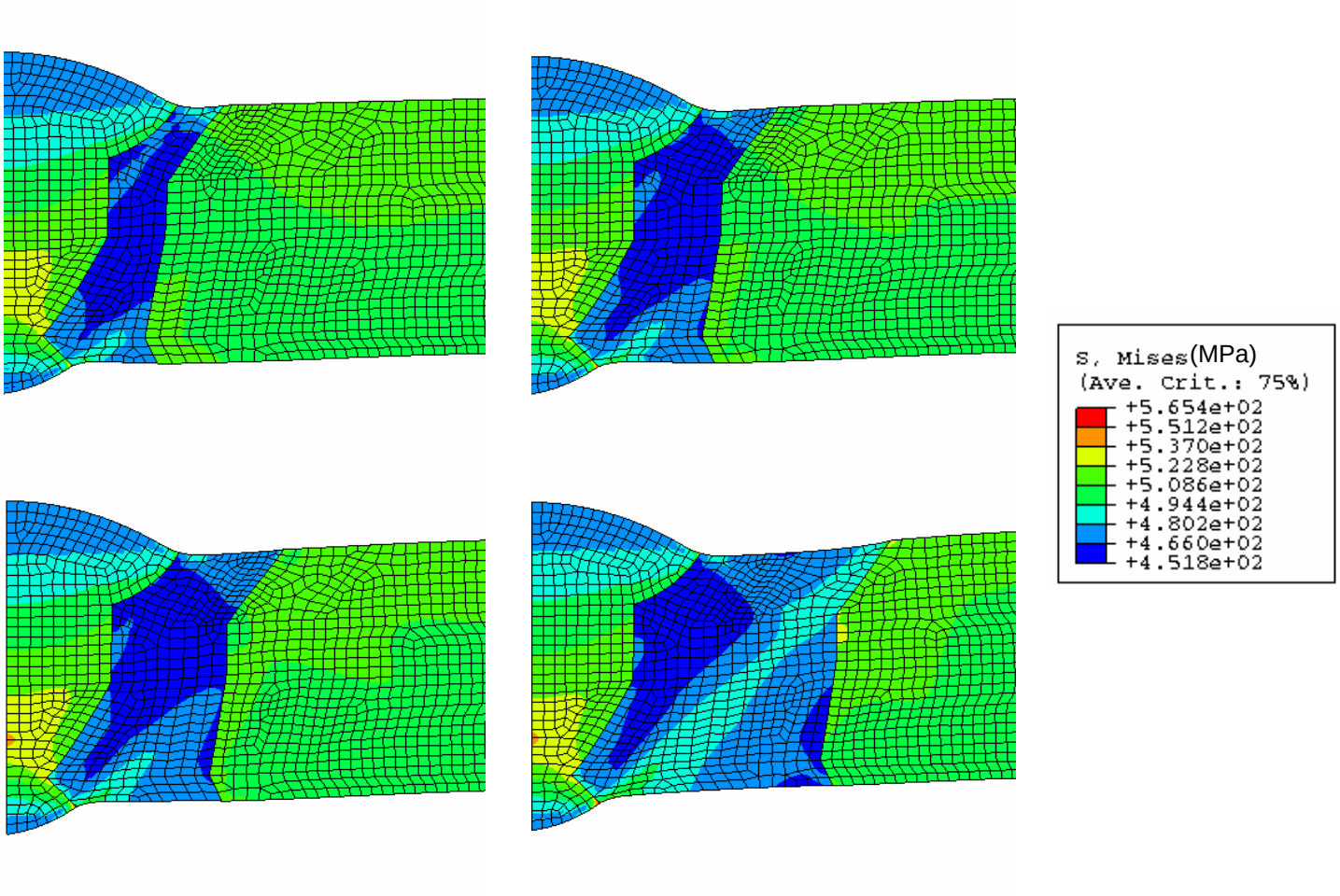

Figure 59. von Mises Stresses for 4% Remote Strain and 3.125-MPa (453-psi) Internal Pressure, Weaker Weld Metal
[Upper left HAZ ~2 mm (~0.08 in.), upper right HAZ ~3 mm (~0.12 in.), lower left HAZ ~4 mm (~0.16 in.), lower right HAZ ~7 mm (~0.28 in.)]

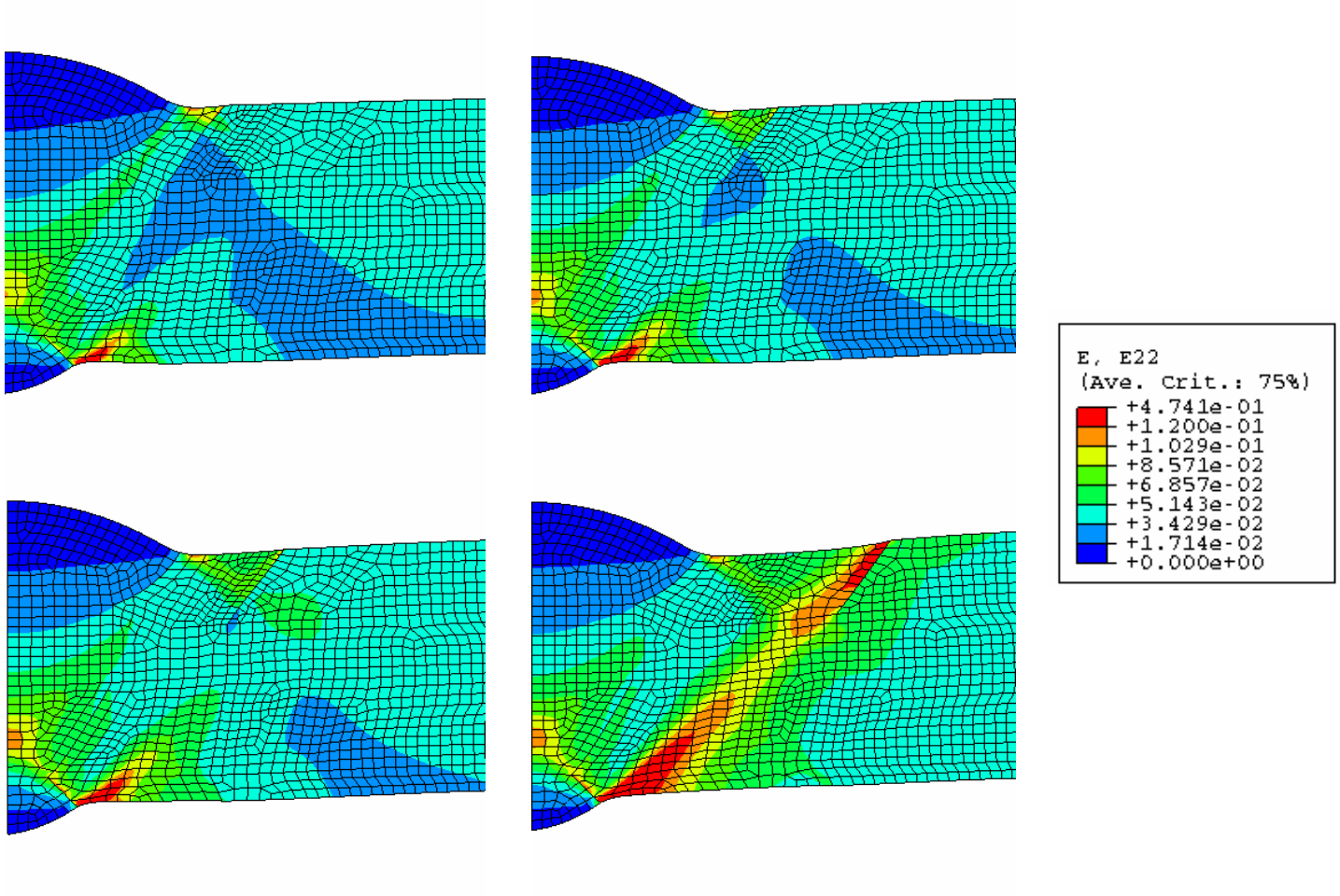

Figure 60. **Axial Strains for 4% Remote Strain and 3.125-MPa (453-psi) Internal Pressure, Weaker Weld Metal** [Upper left HAZ ~2 mm (~0.08 in.), upper right HAZ ~3 mm (~0.12 in.), lower left HAZ ~4 mm (~0.16 in.), lower right HAZ ~7 mm (~0.28 in.)]

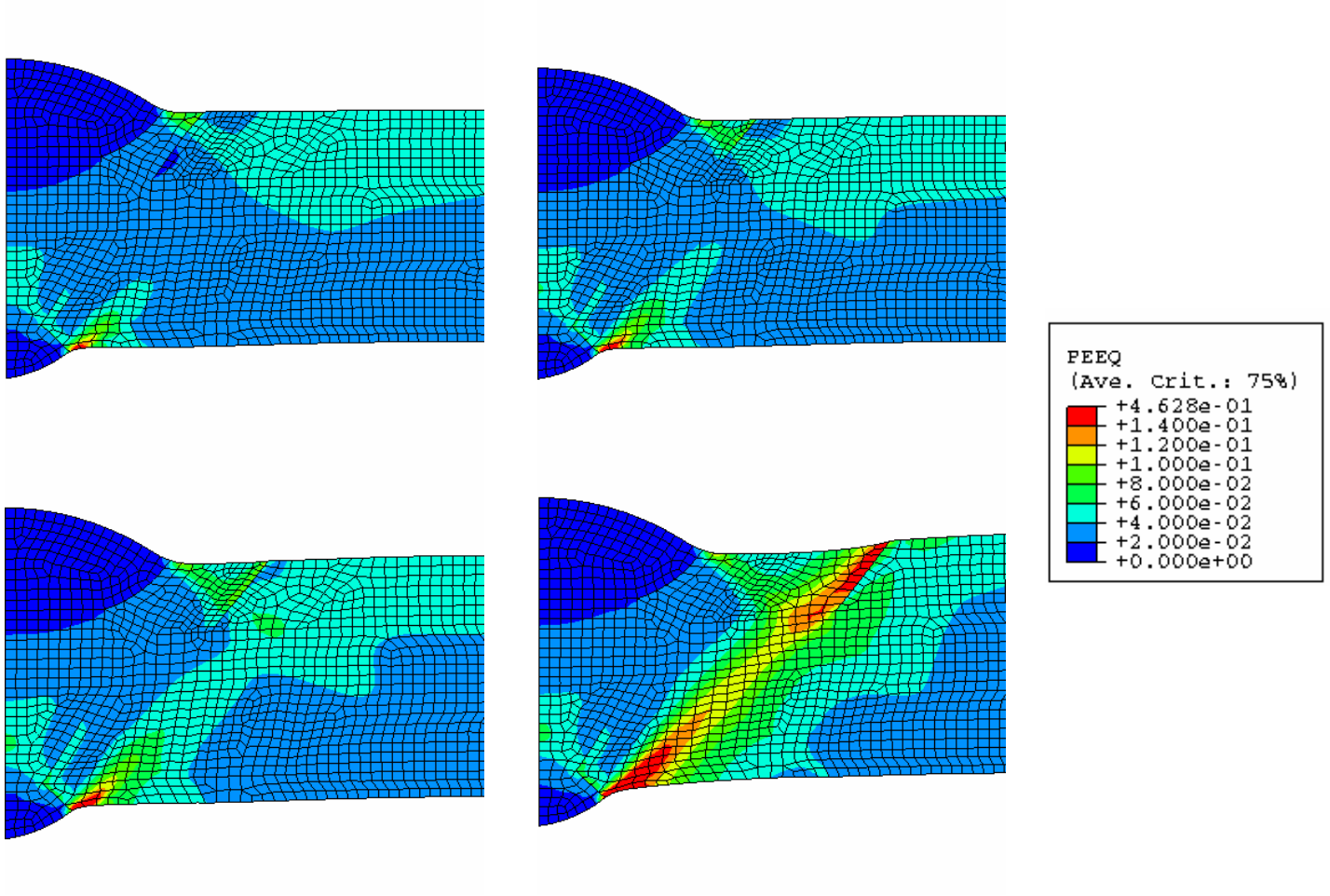

Figure 61. Equivalent Plastic Strains for 4% Remote Strain and 3.125-MPa (453-psi) Internal Pressure, Weaker Weld Metal
[Upper left HAZ ~2 mm (~0.08 in.), upper right HAZ ~3 mm (~0.12 in.), lower left HAZ ~4 mm (0.16 in.), lower right HAZ ~7 mm (~0.28 in.)]

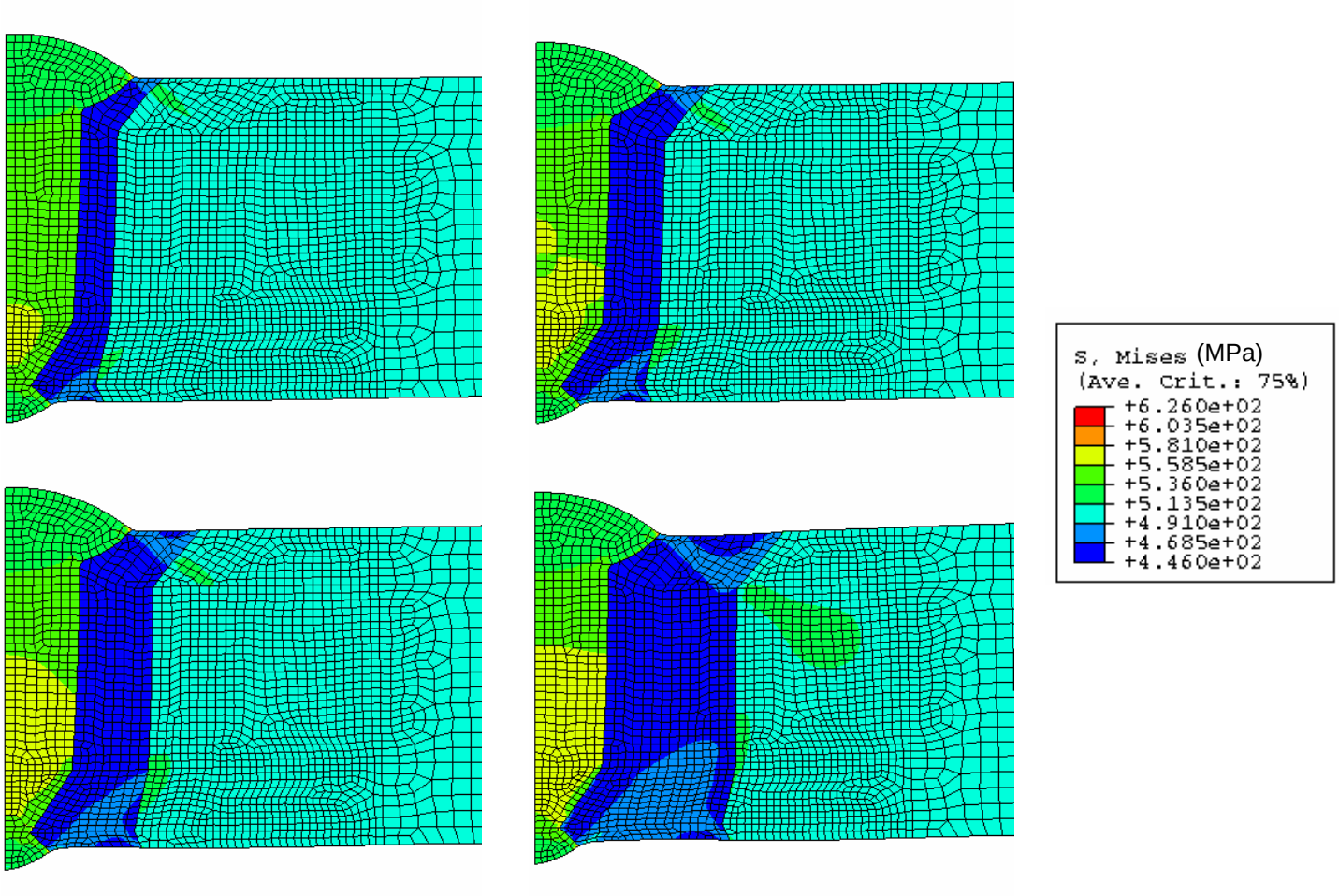

Figure 62. von Mises Stress for 4% Axial Strain and 6.43-MPa (933-psi) Internal Pressure, 20-mm (0.79-in.) Pipe [Upper left HAZ ~2 mm (~0.08 in.), upper right HAZ ~3 mm (~0.12 in.), lower left HAZ ~4 mm (~0.16 in.), lower right HAZ ~7 mm (~0.28 in.)]

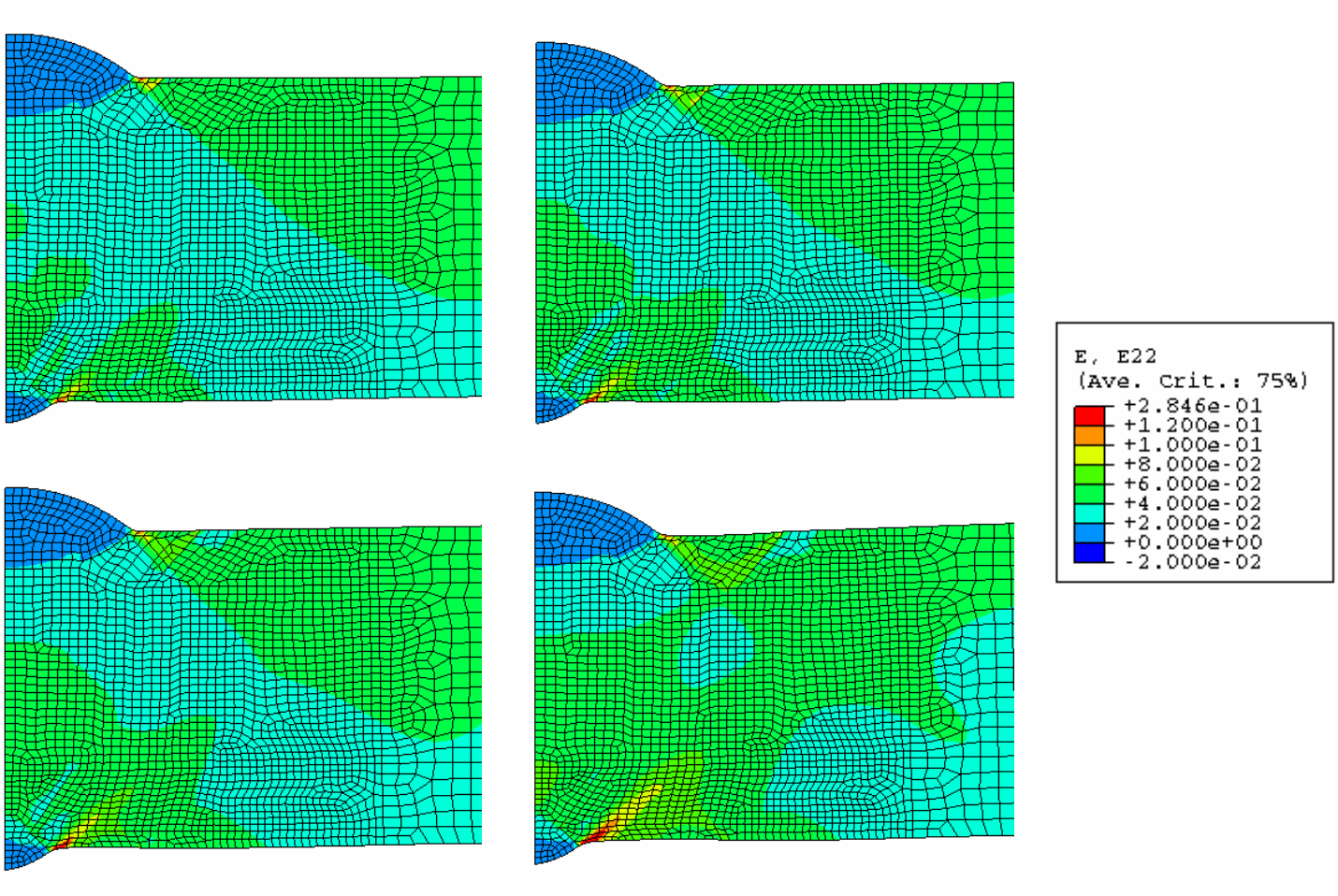

Figure 63. **Axial Strain for 4% Remote Strain and 6.43-MPa (933-psi) Internal Pressure, 20-mm (0.79-in.) Pipe** [Upper left HAZ ~2 mm (~0.08 in.), upper right HAZ ~3 mm (~0.12 in.), lower left HAZ ~4 mm (~0.16 in.), lower right HAZ ~7 mm (~0.28 in.)]

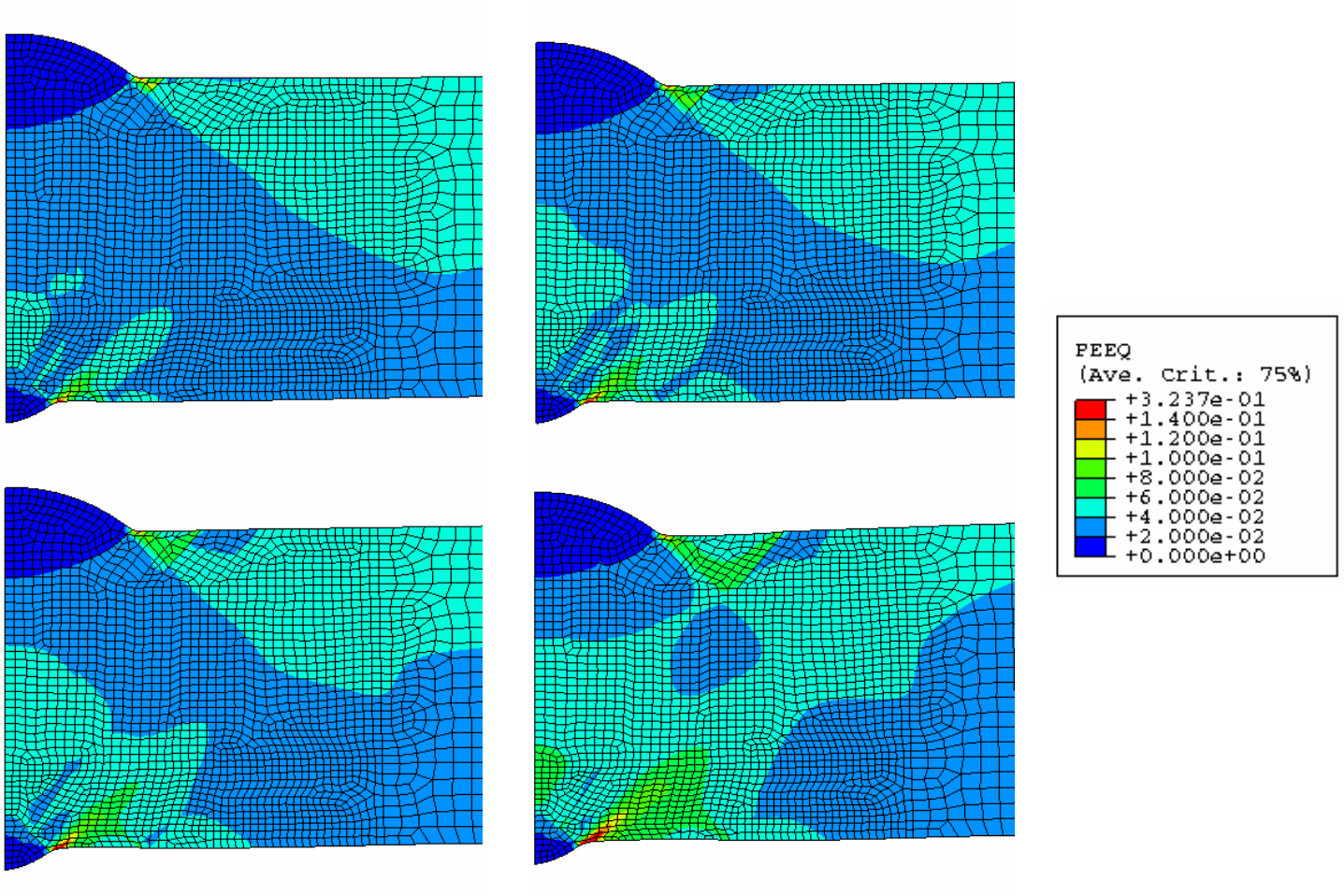

Figure 64. Equivalent Plastic Strain for 4% Remote Strain and 6.43-MPa (933-psi) Internal Pressure, 20-mm (0.79-in.) Pipe
[Upper left HAZ ~2 mm (~0.08 in.), upper right HAZ ~3 mm (~0.12 in.), lower left HAZ ~4 mm (~0.16 in.), lower right HAZ ~7 mm (~0.28 in.)]

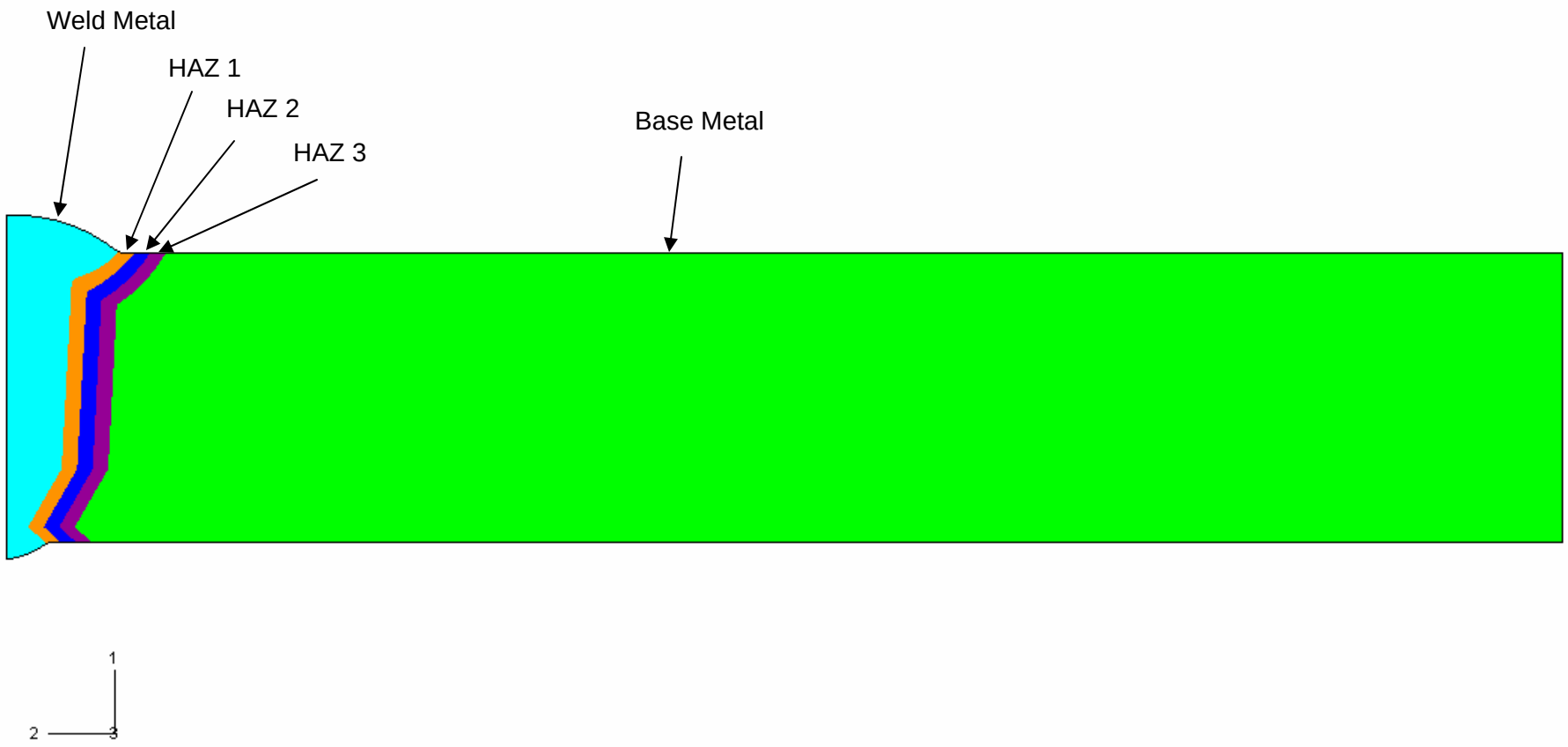

Figure 65. Material Regions in the Pipe Model Used With the Finer-Grained Material Model

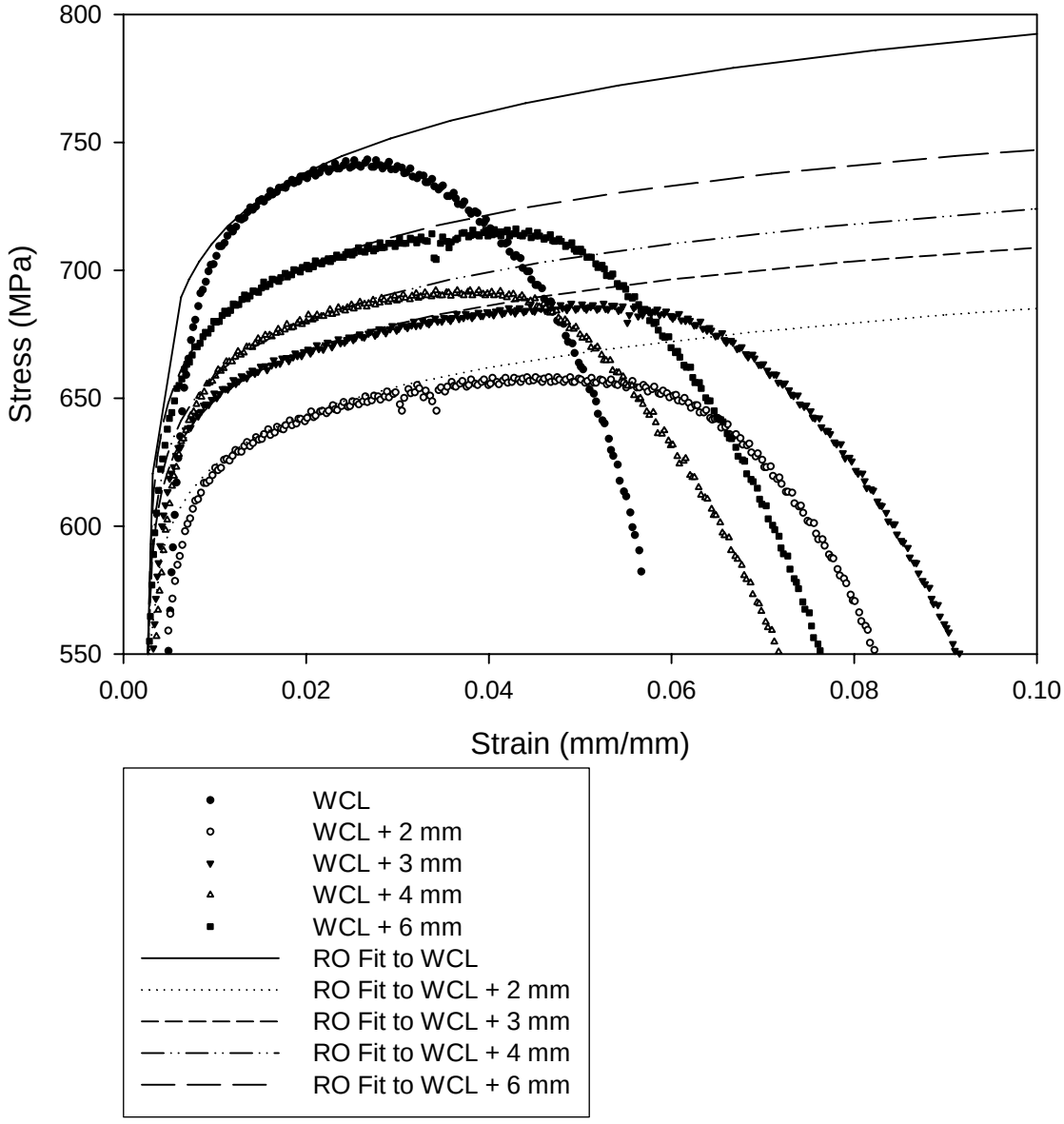

Figure 66. Ramberg-Osgood Stress-Strain Curves Fitted to Microtensile Data from Weld W1

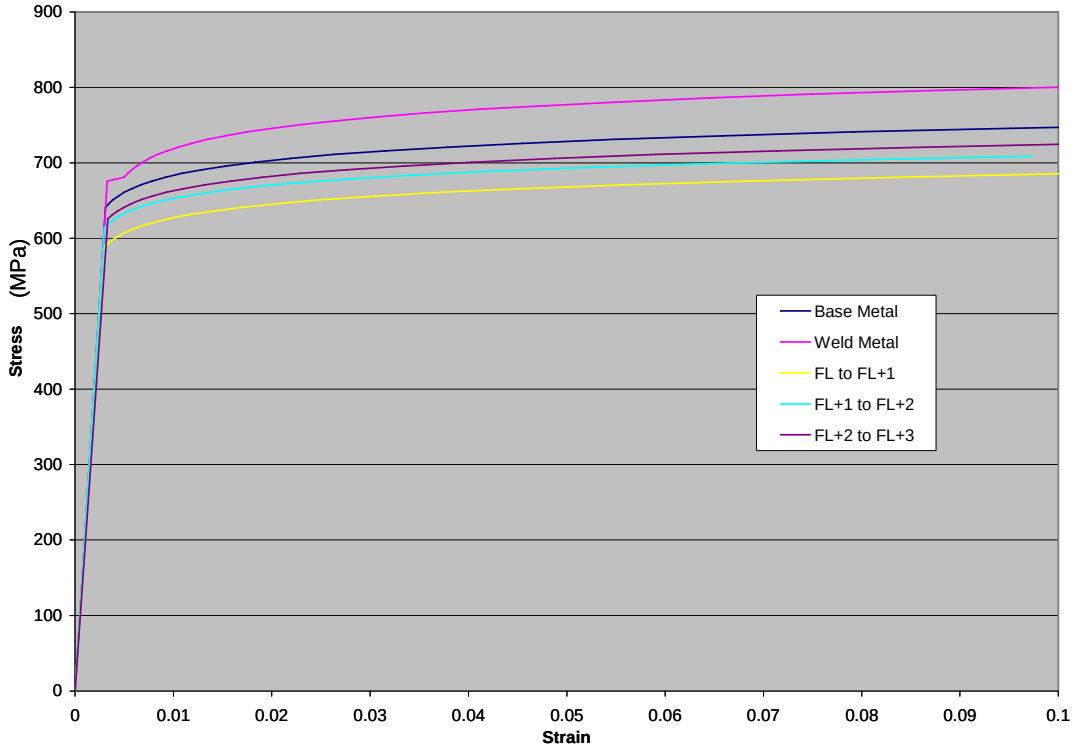

Figure 67. Stress-Strain Curves Used for Finer-Grained Model

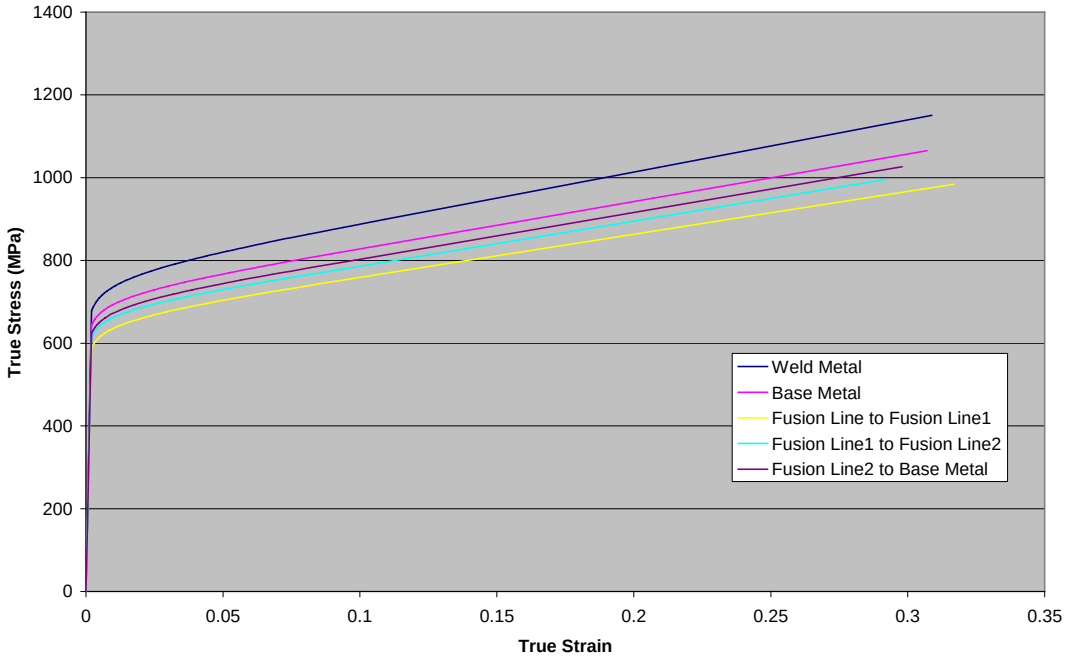

Figure 68. True-Stress/True-Strain Curves for the Materials in X-100 Model

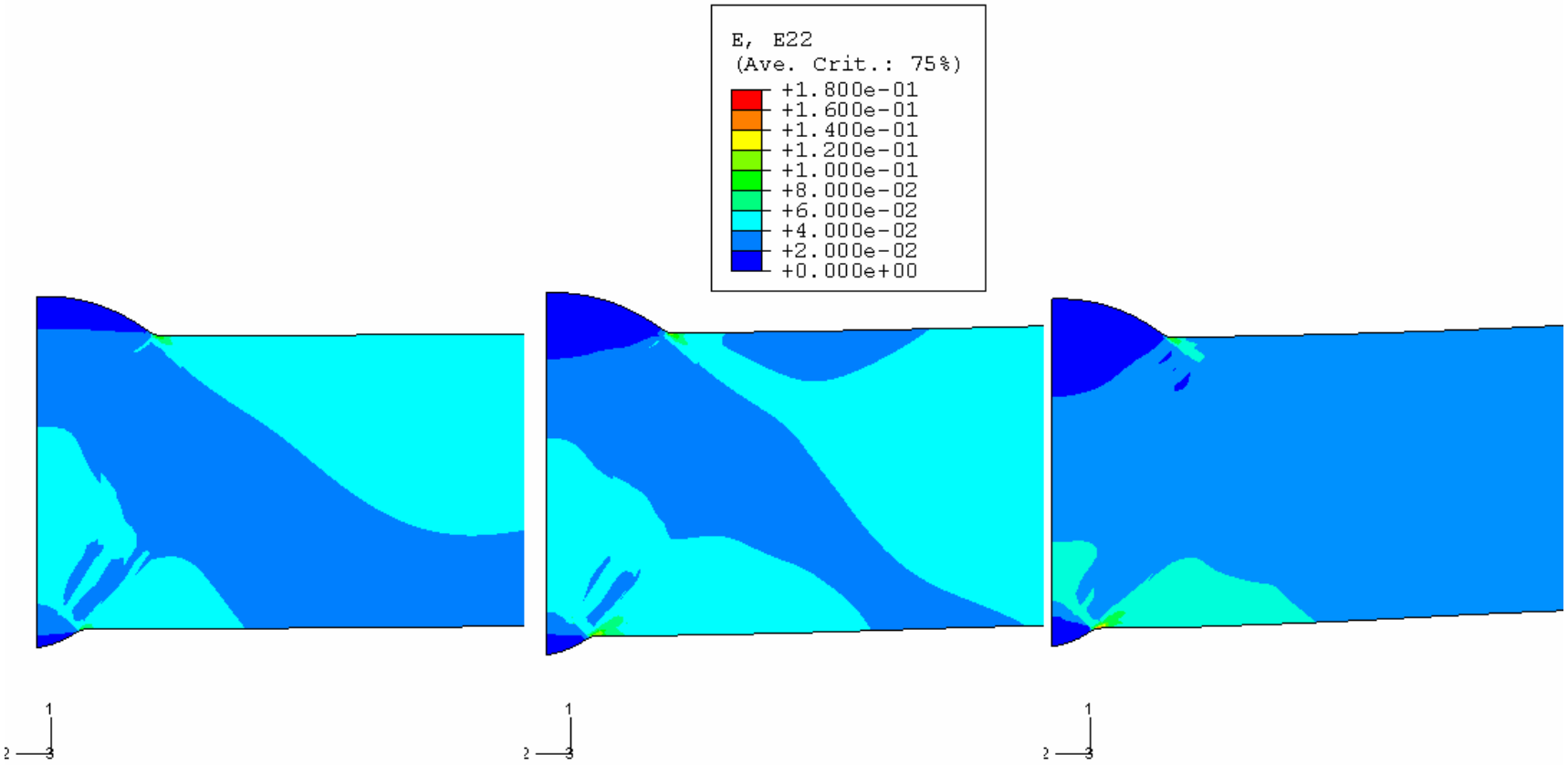

Figure 69. **Axial Strain for Isotropic Case with 4% Remote Strain** [Left – no pressure, center – 9.59-MPa (1390-psi) pressure, right – 19.18-MPa (2780-psi) pressure]

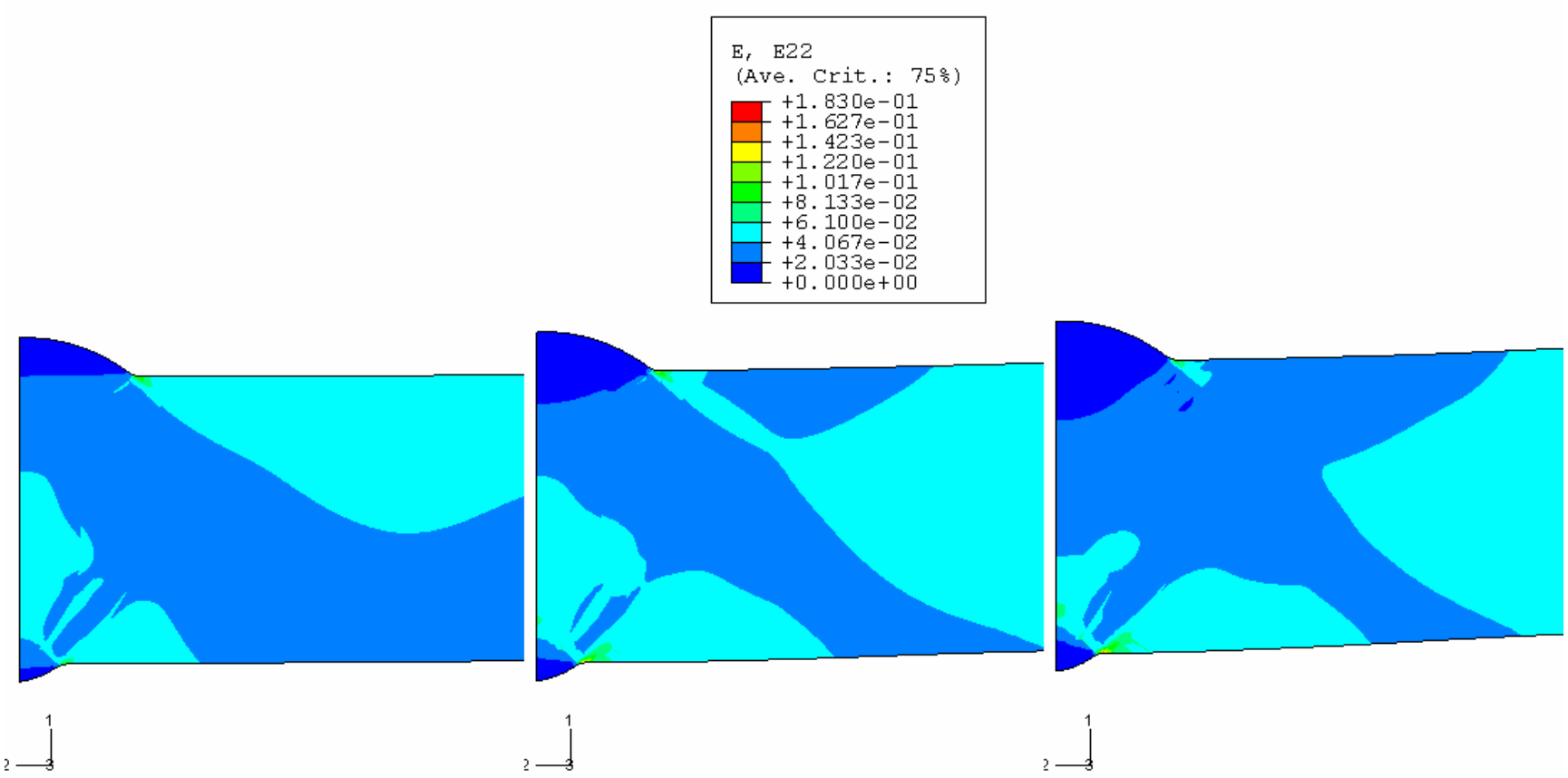

Figure 70. Axial Strain for Orthotropic Case with 4% Remote Strain [Left – no pressure, center – 9.59-MPa (1390-psi) pressure, right – 19.18-MPa (2780-psi) pressure]

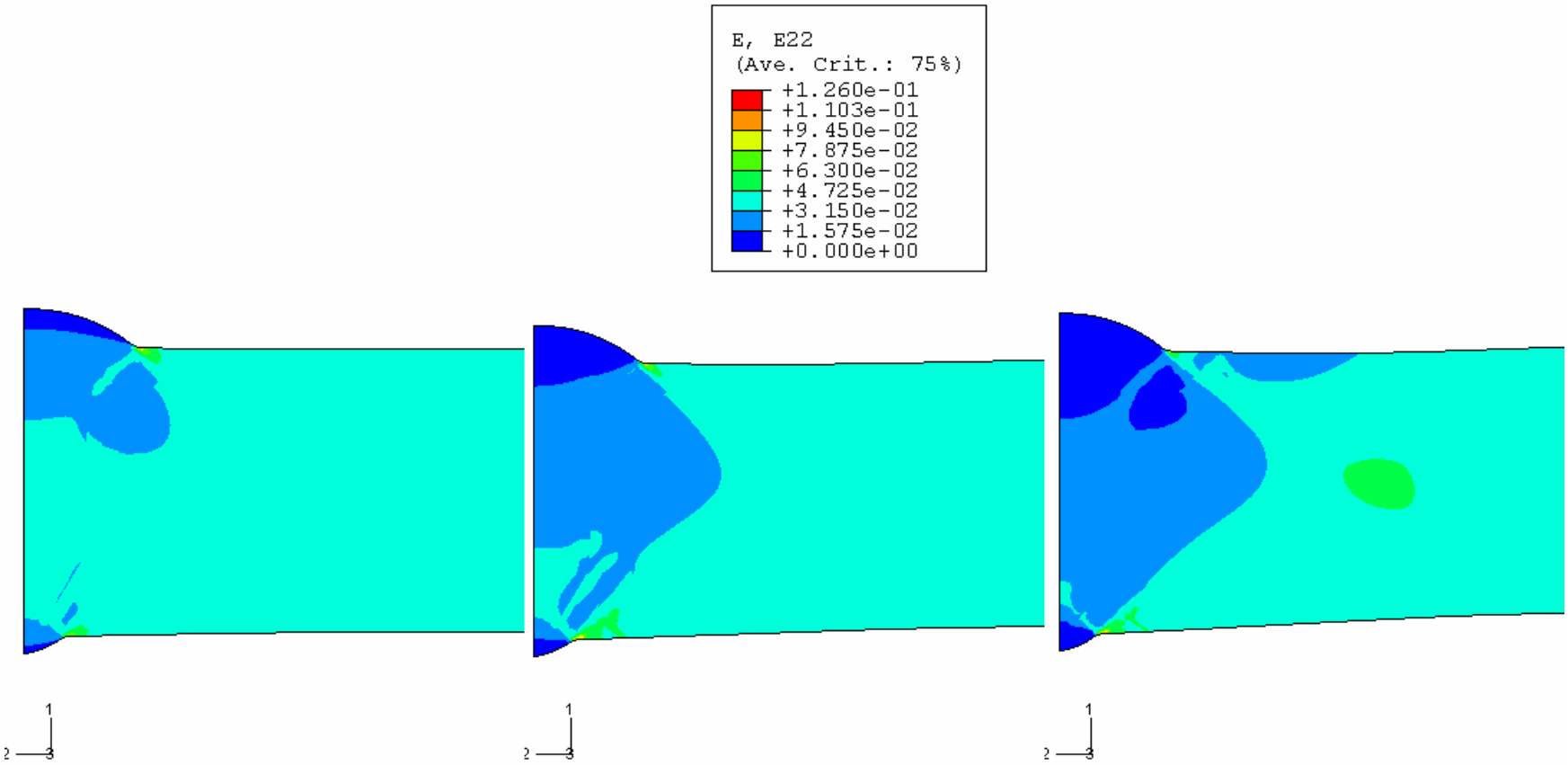

Figure 71. Axial Strain for Base Metal Orthotropic Case with 4% Remote Strain [Left – no pressure, center – 9.59-MPa (1390-psi) pressure, right – 19.18-MPa (2780-psi) pressure]

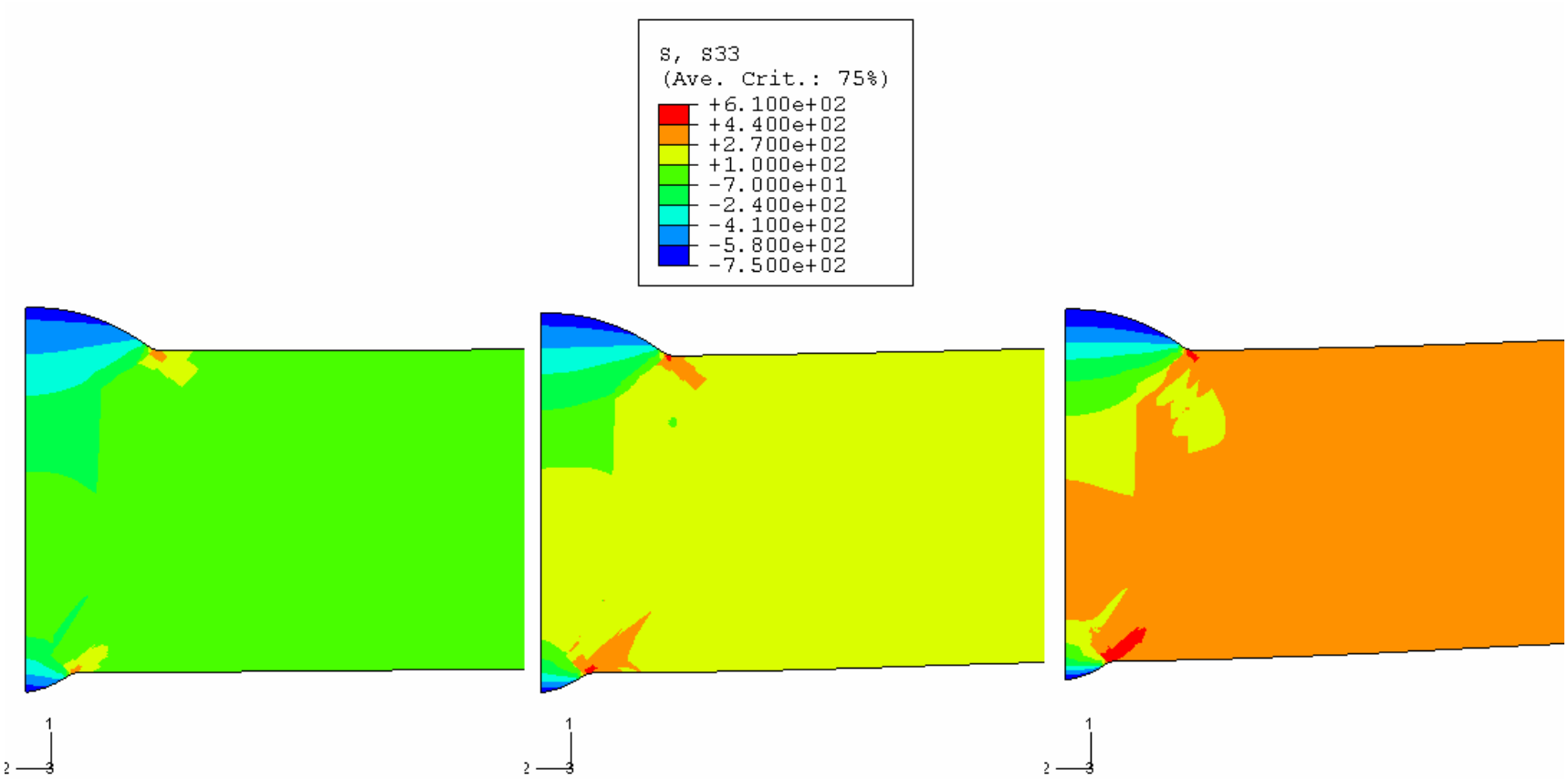

Figure 72. **Hoop Stress in MPa for Isotropic Case with 4% Remote Strain** [Left – no pressure, center 9.59-MPa (1390-psi) pressure, right – 19.18-MPa (2780-psi) pressure]

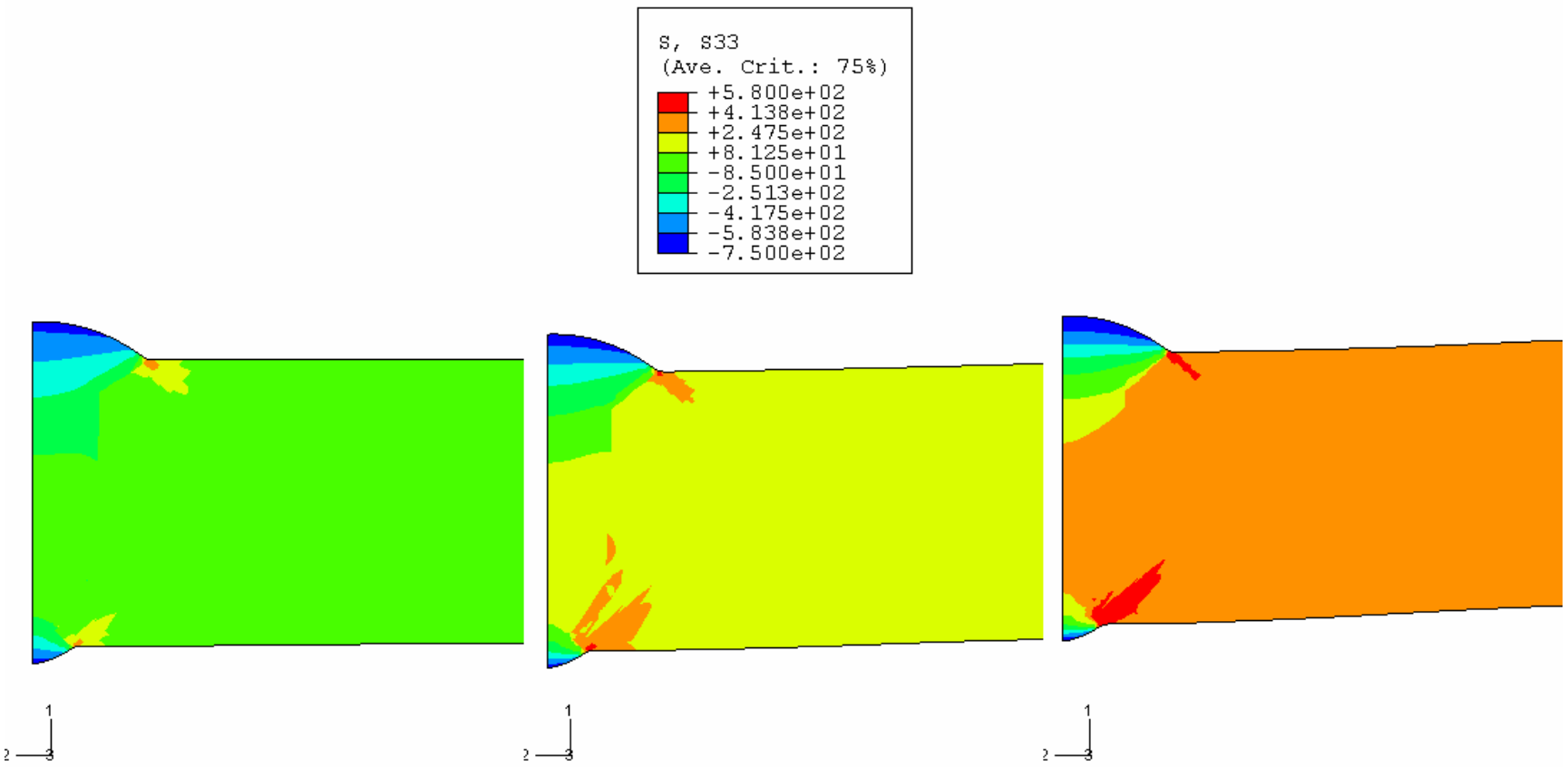

Figure 73. **Hoop Stress in MPa for Orthotropic Case with 4% Remote Strain** [Left – no pressure, center – 9.59-MPa (1390-psi) pressure, right – 19.18-MPa (2780-psi) pressure]

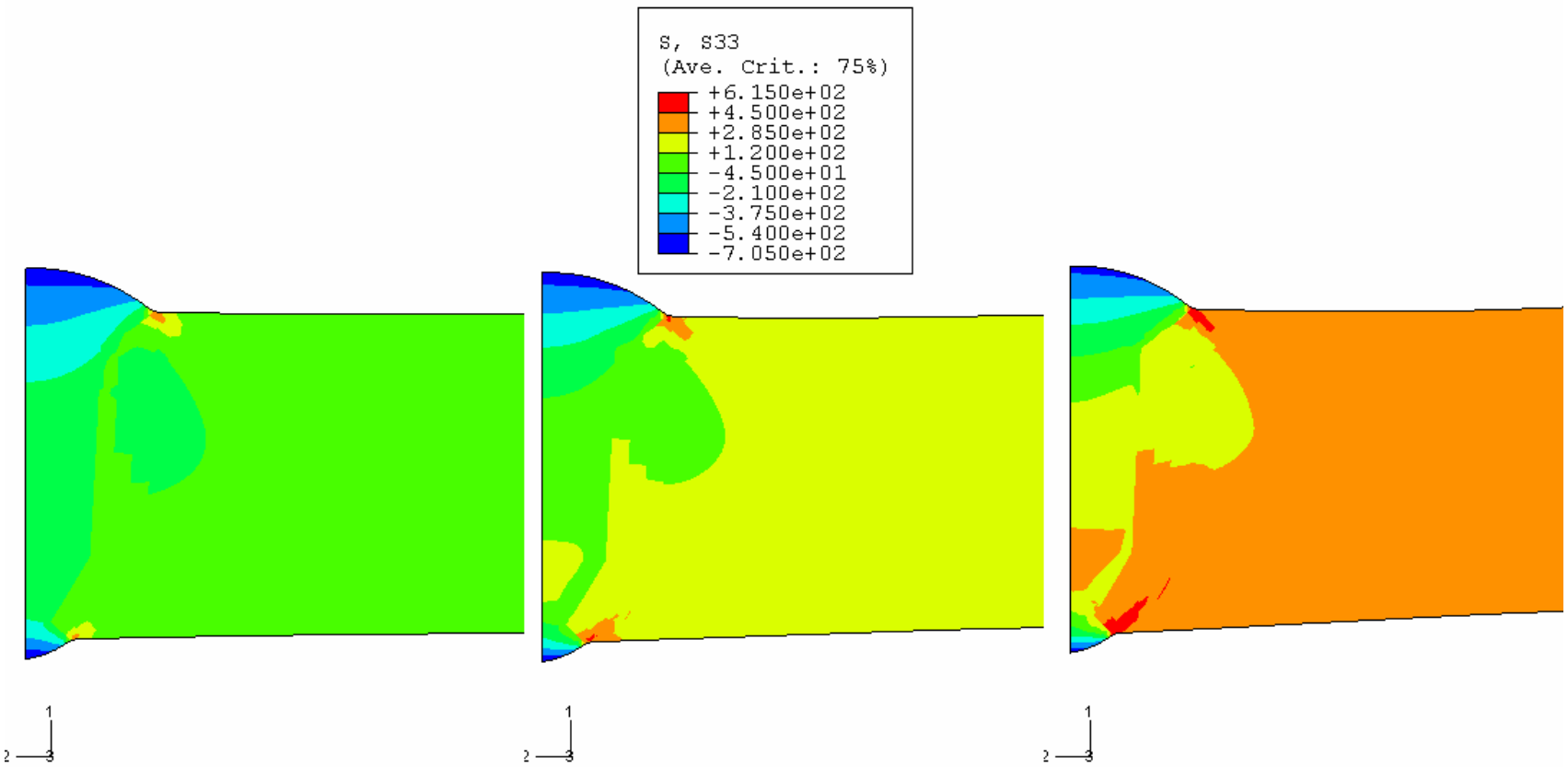

Figure 74. Hoop Stress in MPa for Base Metal Orthotropic Case with 4% Remote Strain [Left – no pressure, center – 9.59-MPa (1390-psi) pressure, right – 19.18-MPa (2780-psi) pressure]

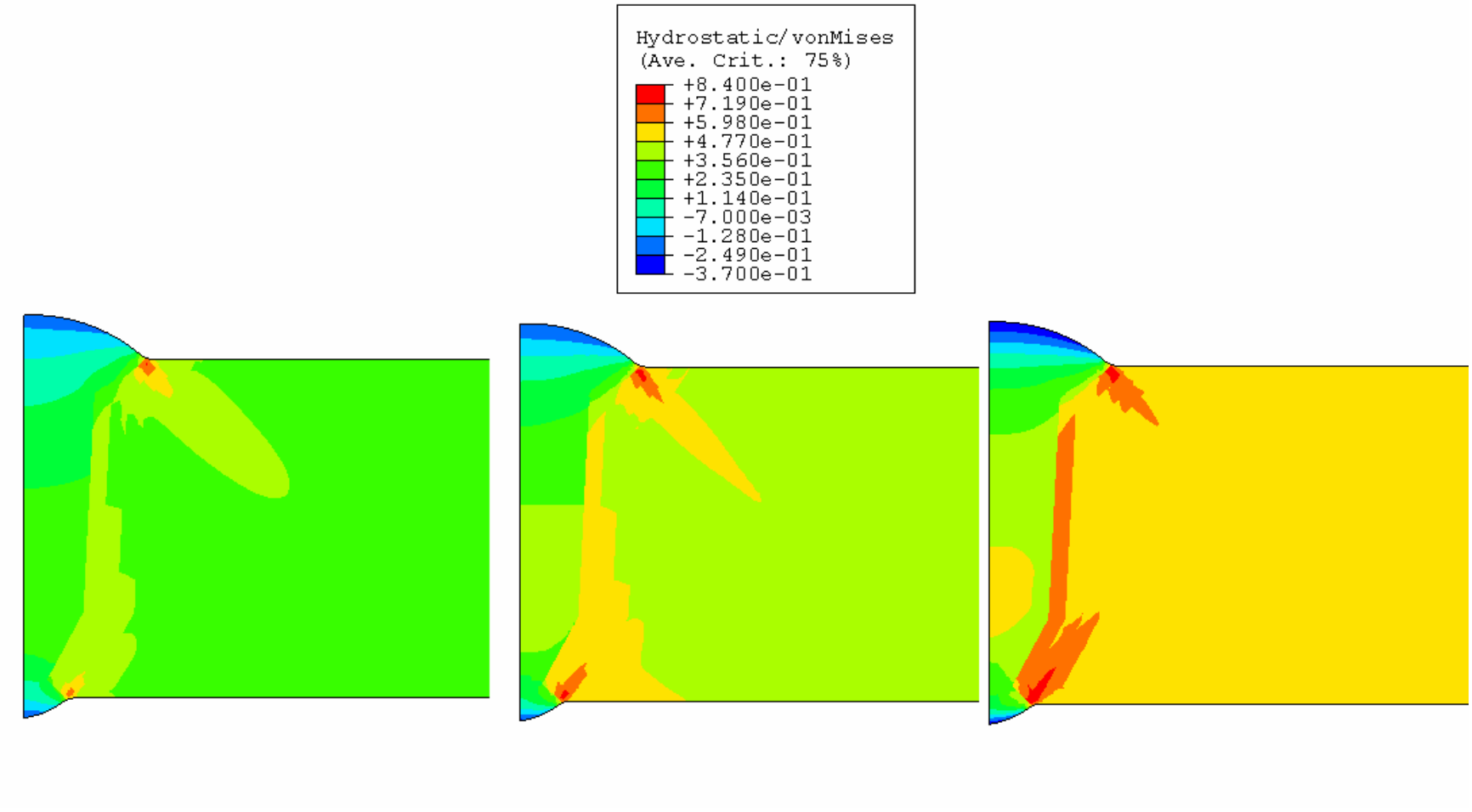

Figure 75. Stress Triaxiality Map for Isotropic Case with 4% Remote Strain [Left – no pressure, center – 9.59-MPa (1390-psi) pressure, right – 19.18-MPa (2880-psi) pressure]

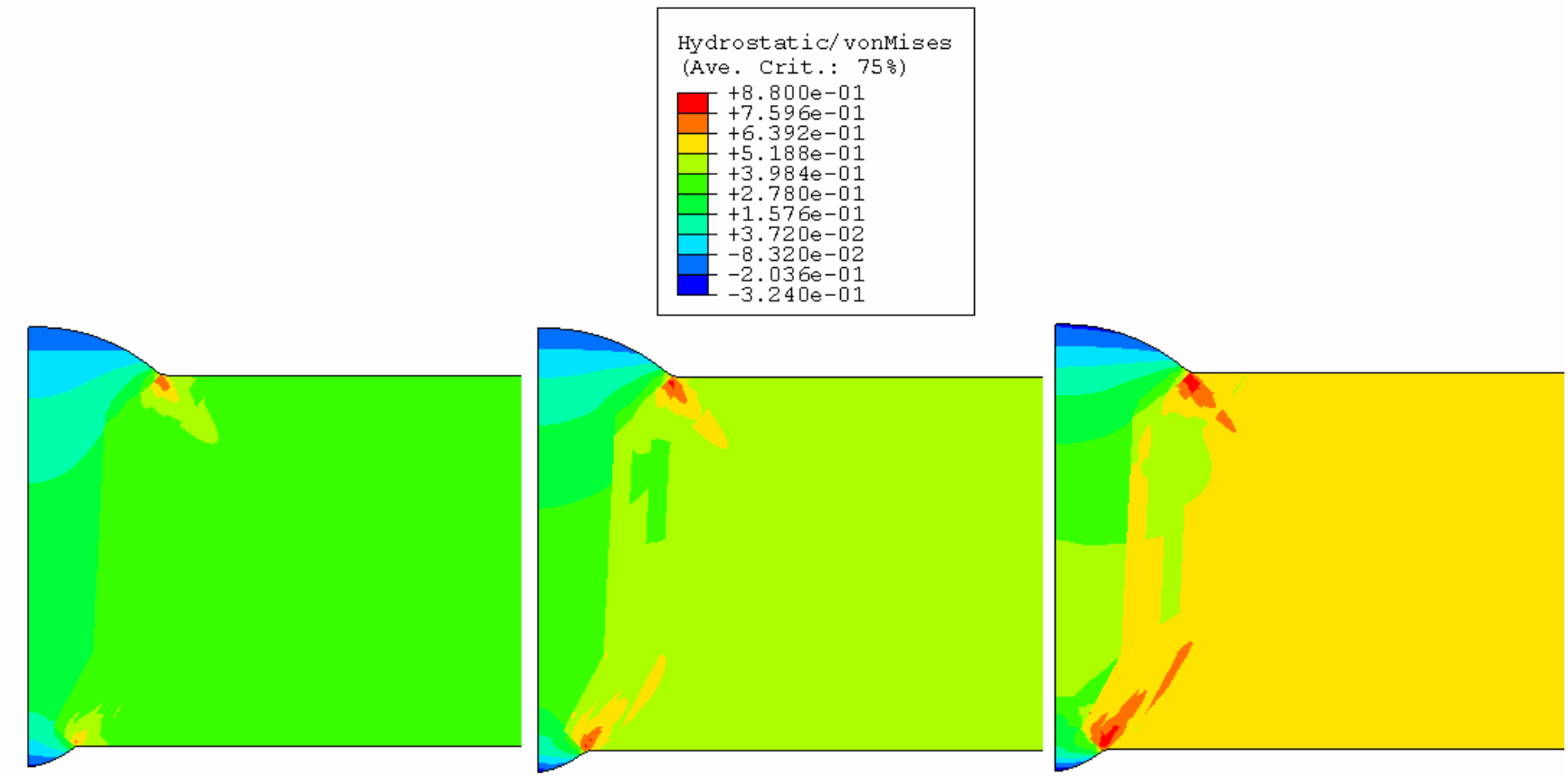

Figure 76. Stress Triaxiality Map for Base Metal Orthotropic Case with 4% Remote Strain [Left – no pressure, center – 9.59-MPa (1390-psi) pressure, right – 19.18-MPa (2780-psi) pressure]

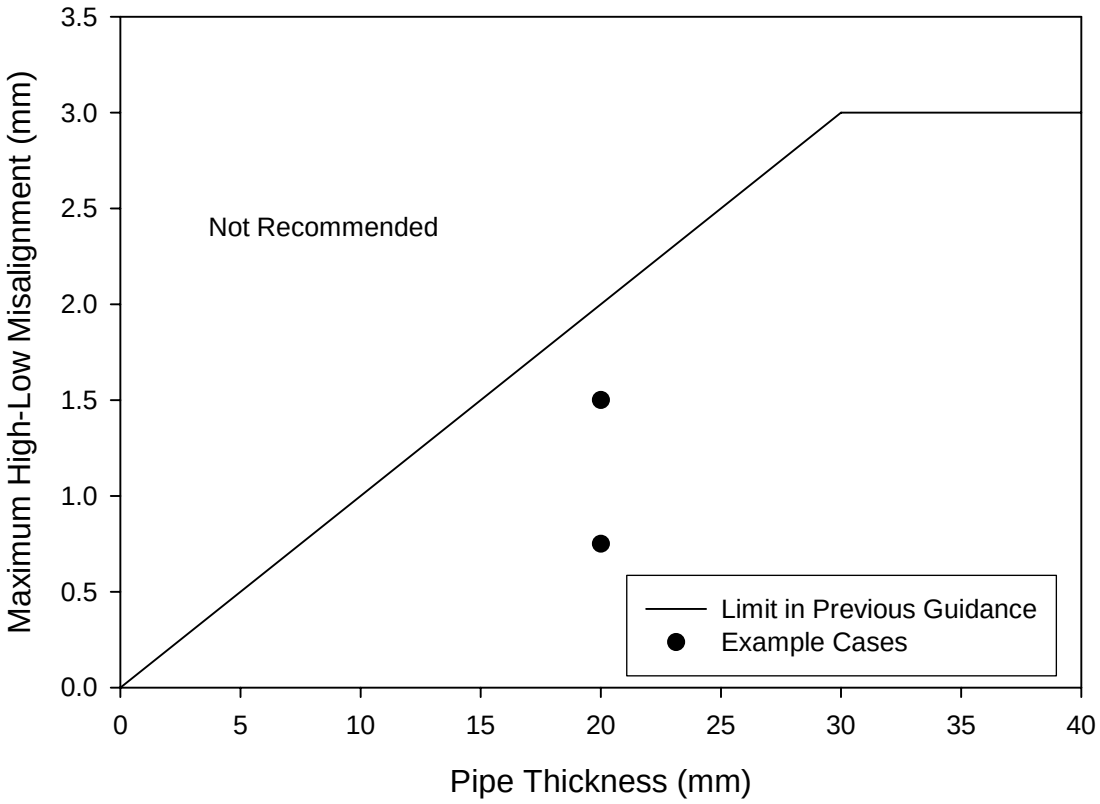

Figure 77. Levels of High-Low Misalignment Modeled in this Project

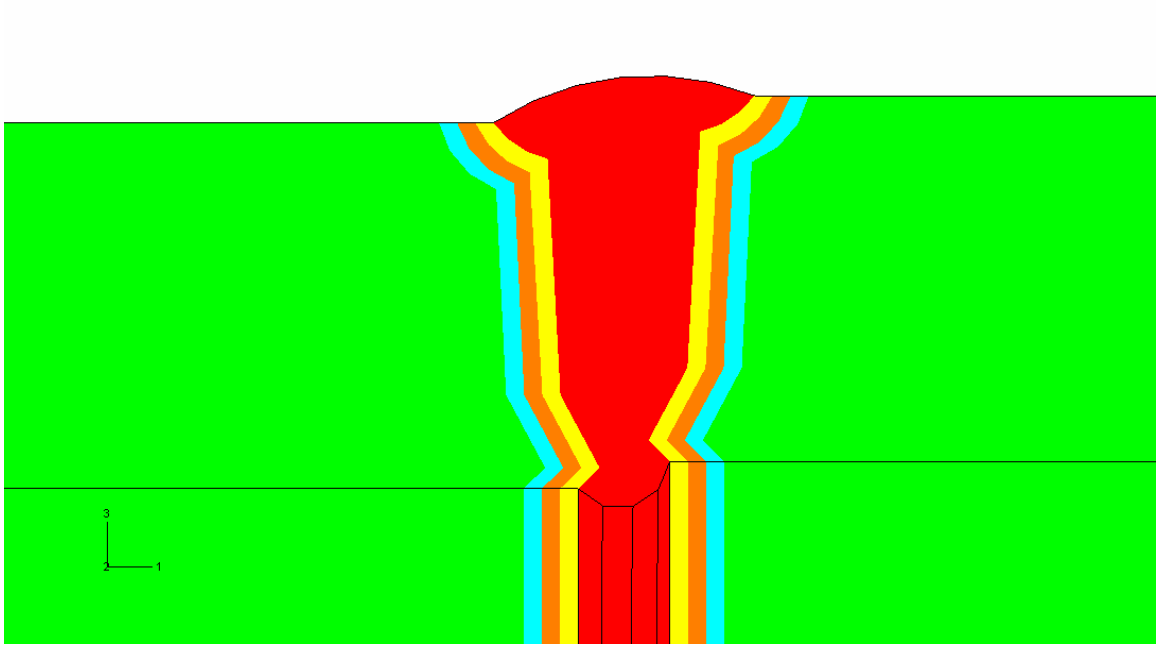

Figure 78. Model Configuration for Examination of High-Low at 1.5-mm (0.06-in.) Maximum High-Low

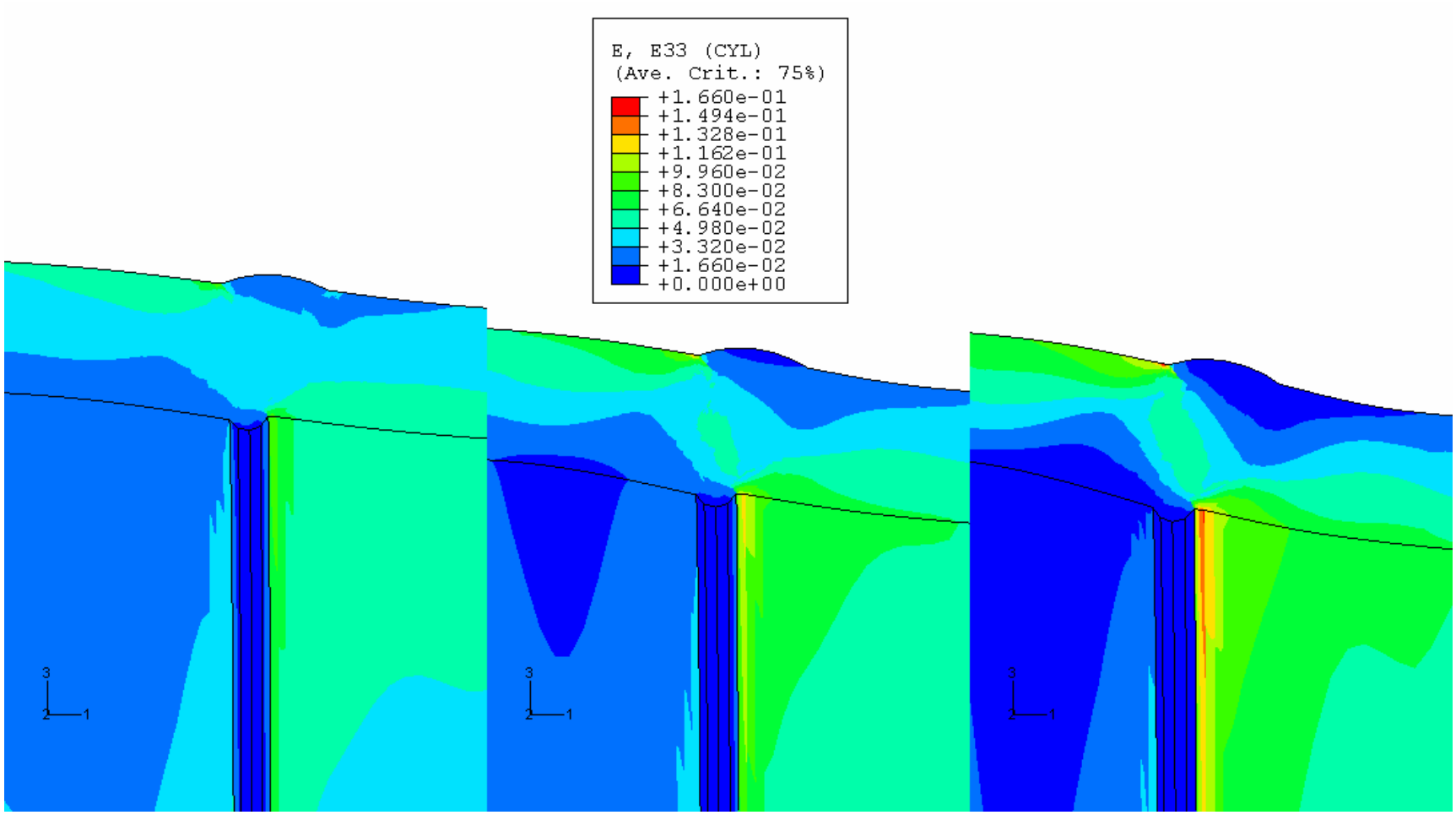

Figure 79. Axial Strain Around Girth Weld at 1.5-mm (0.06-in.) Maximum High-Low (Base Metal Orthotropic Case) [Left – no pressure, center – 9.59-MPa (1390-psi) pressure, right – 19.18-MPa (2780-psi) pressure]

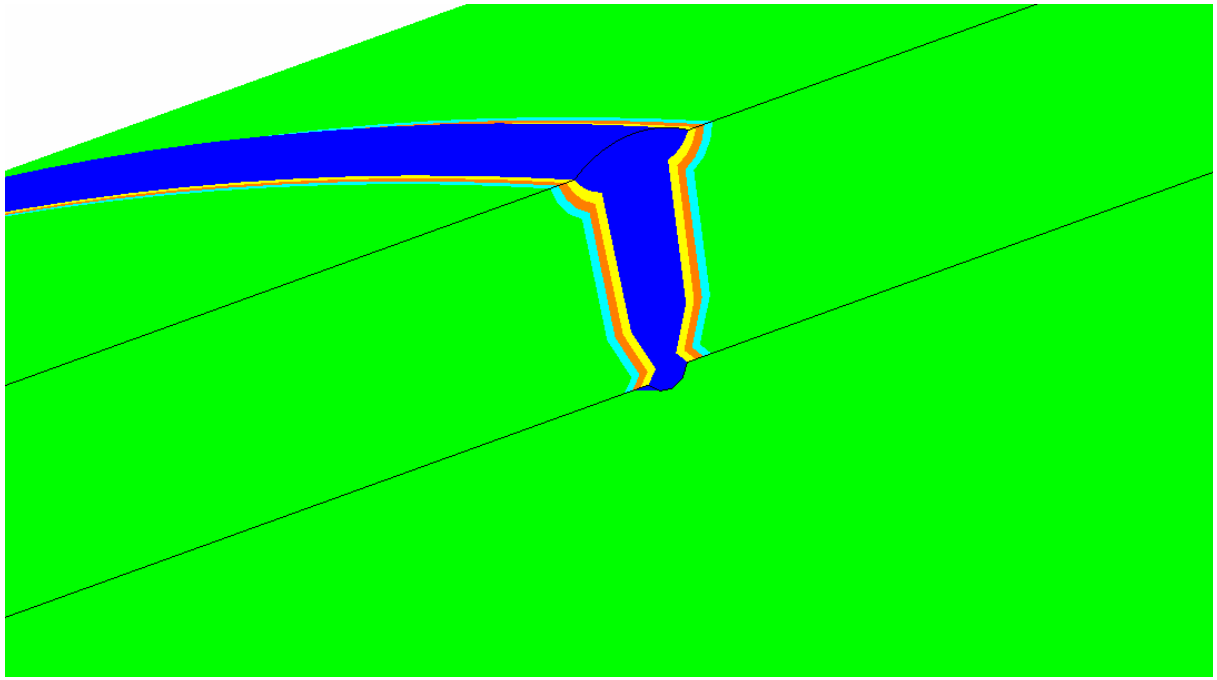

Figure 80. Model Configuration for Examination of High-Low at 0.75-mm (0.03-in.) Maximum High-Low

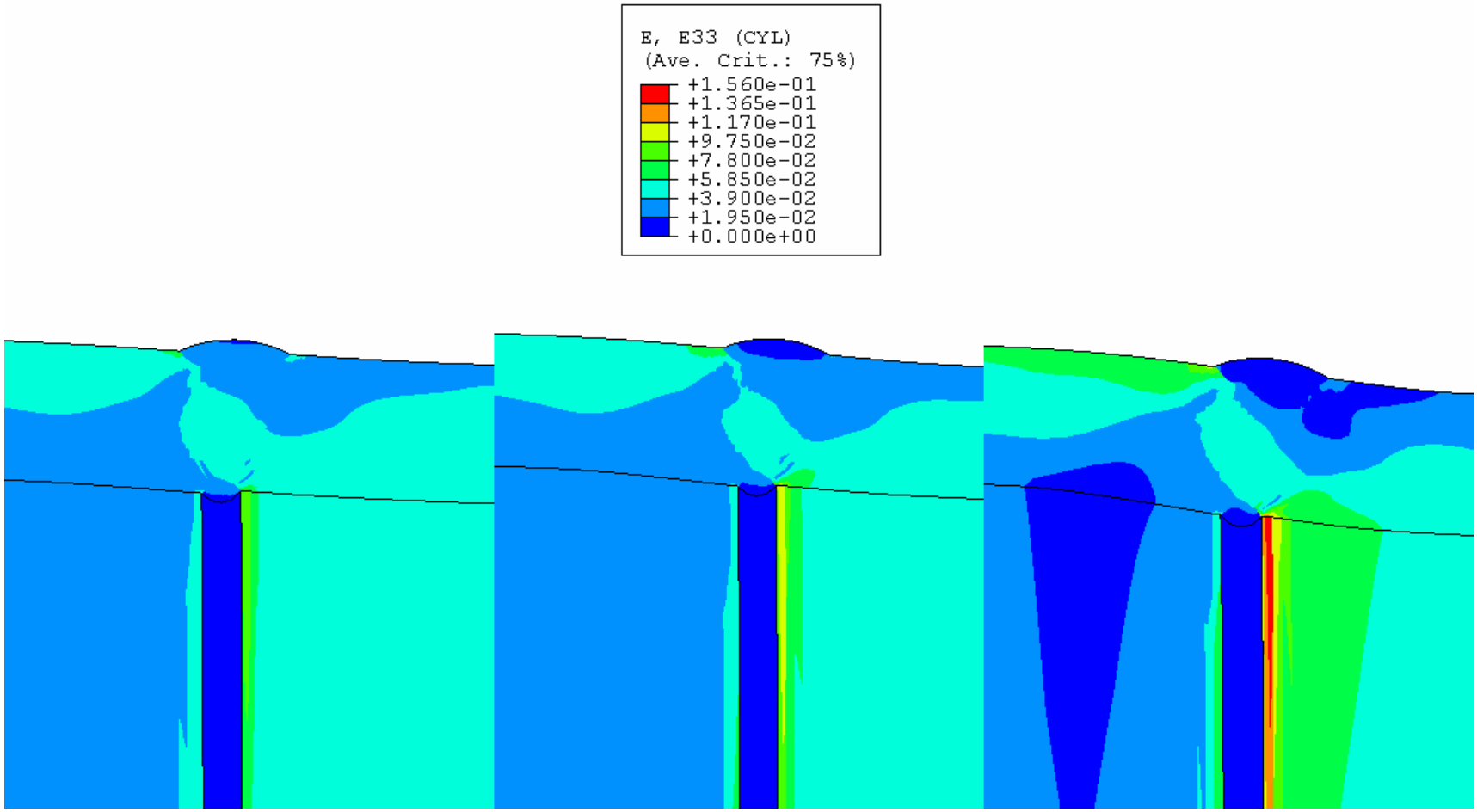

Figure 81. Axial Strain Around Girth Weld at 0.75-mm (0.03-in.) Maximum High-Low for X-100 (Base Metal Orthotropic Case) [Left – no pressure, center – 9.59-MPa (1390-psi) pressure, right – 19.18-MPa (2780-psi) pressure]

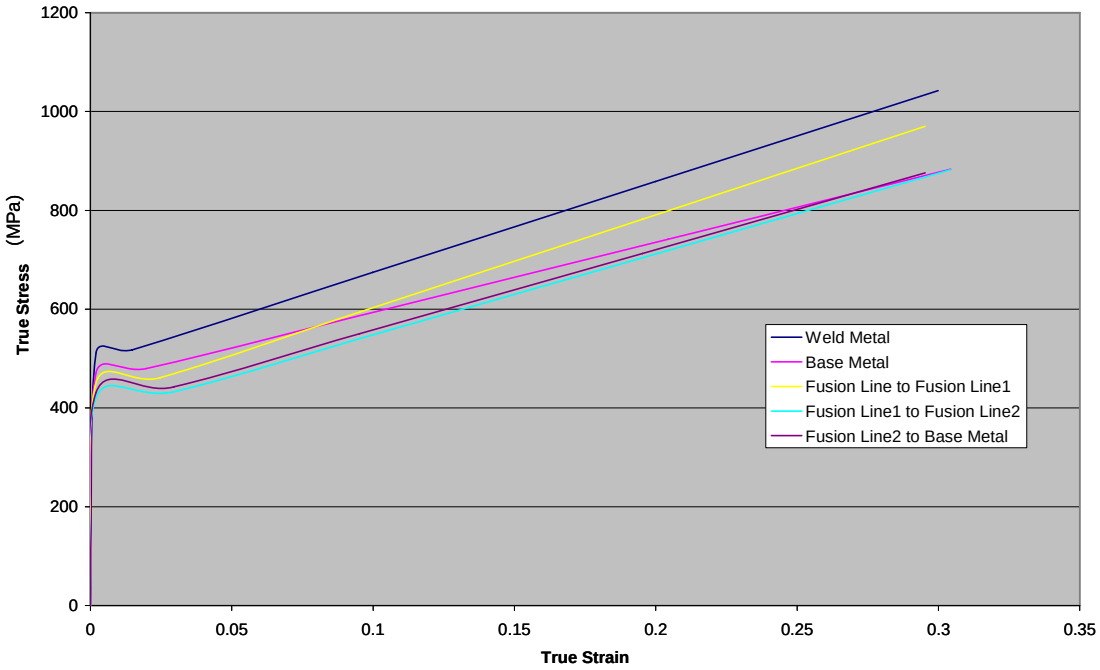

Figure 82. Stress-Strain Curves for X-65 Material Derived from Kim et al.[8] Microtensile Tests

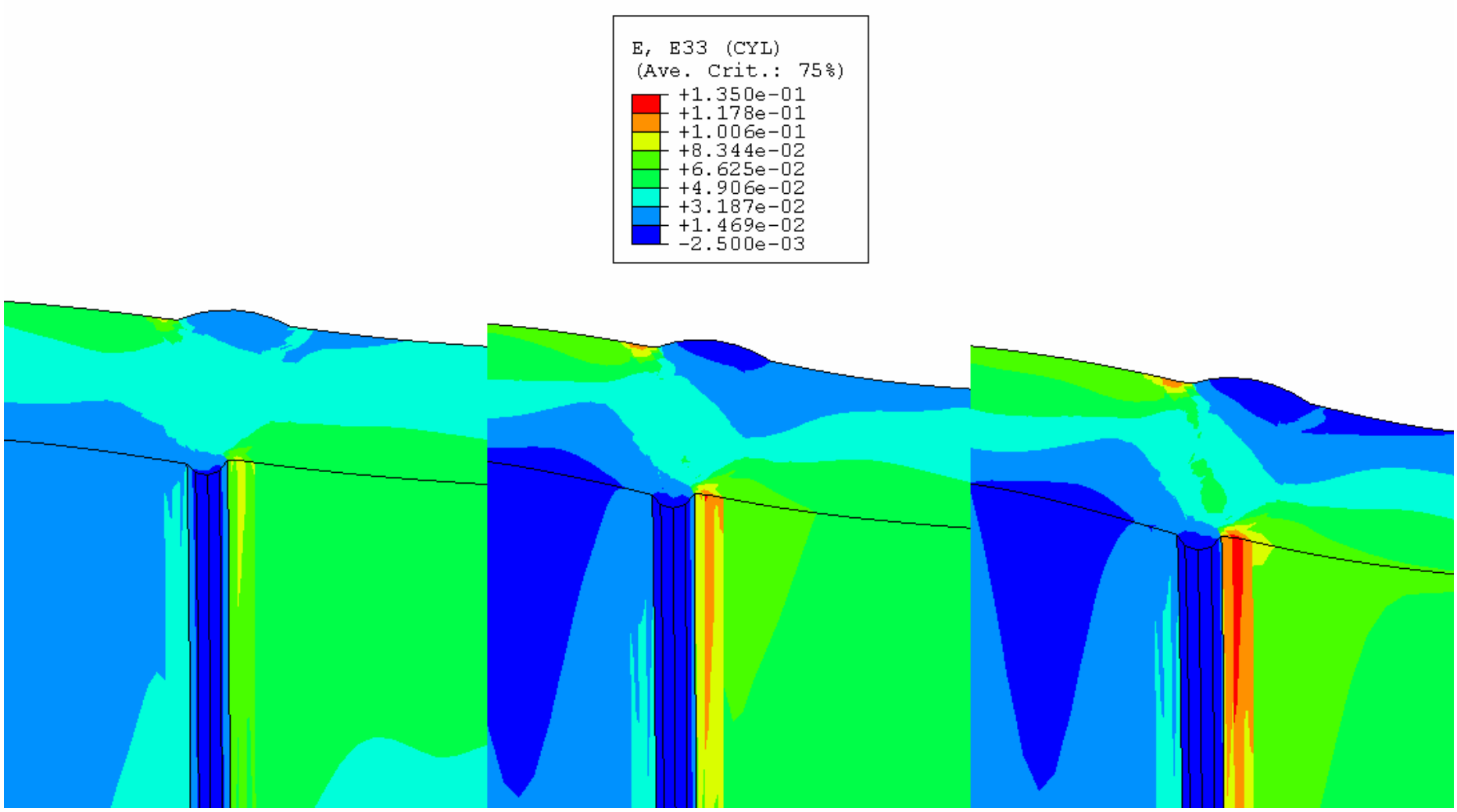

Figure 83. Axial Strain Around Area of Peak Misalignment of 1.5 mm (0.06 in.) in X-65 Girth Weld Region [Left – no pressure, center – 6.23-MPa (904-psi) pressure, right – 12.47-MPa (1809-psi) pressure]

Figure 84. Model Configuration for Models of X-65 Pipes

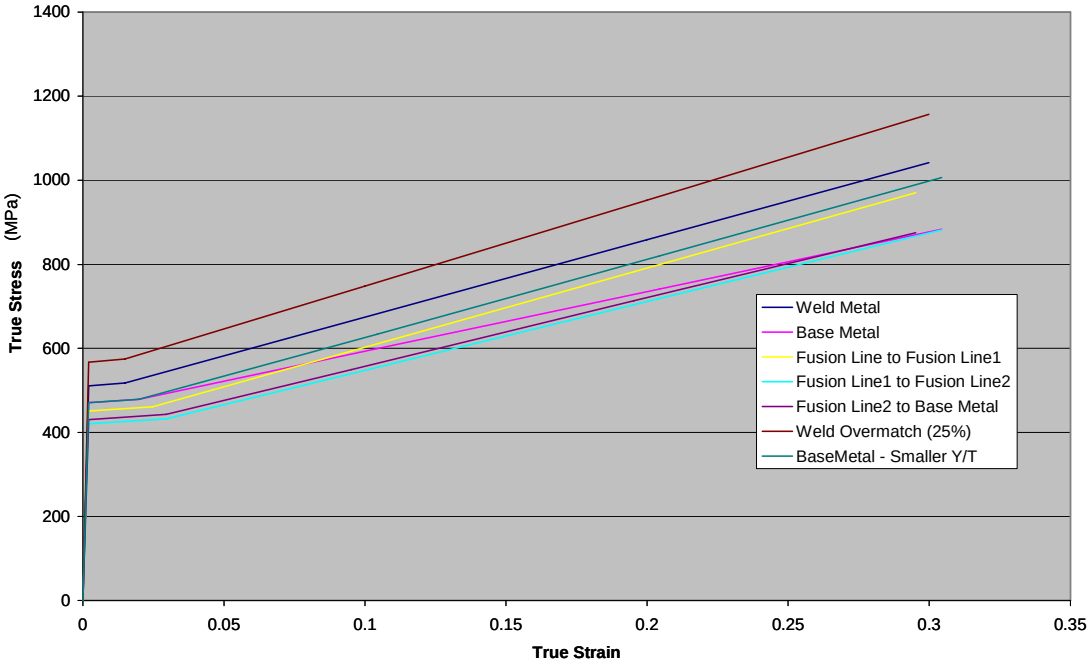

Figure 85. True-Stress/True-Strain Curves for X-65 Pipe Materials and Welds Areas

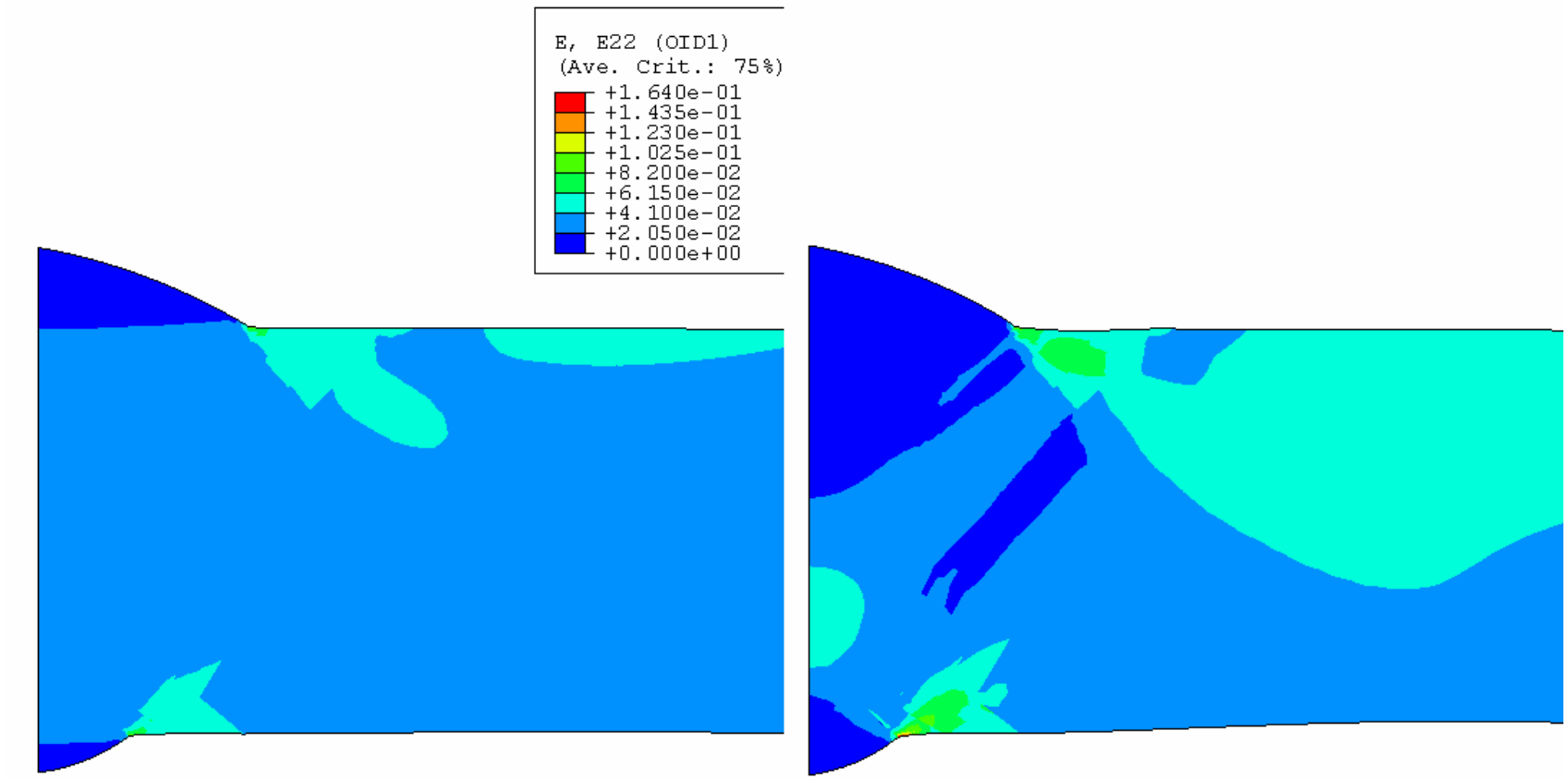

Figure 86. Axial Strain Distributions for Girth Welds in X-65 [Left – no pressure, right – 29.19-MPa (4234-psi) pressure]

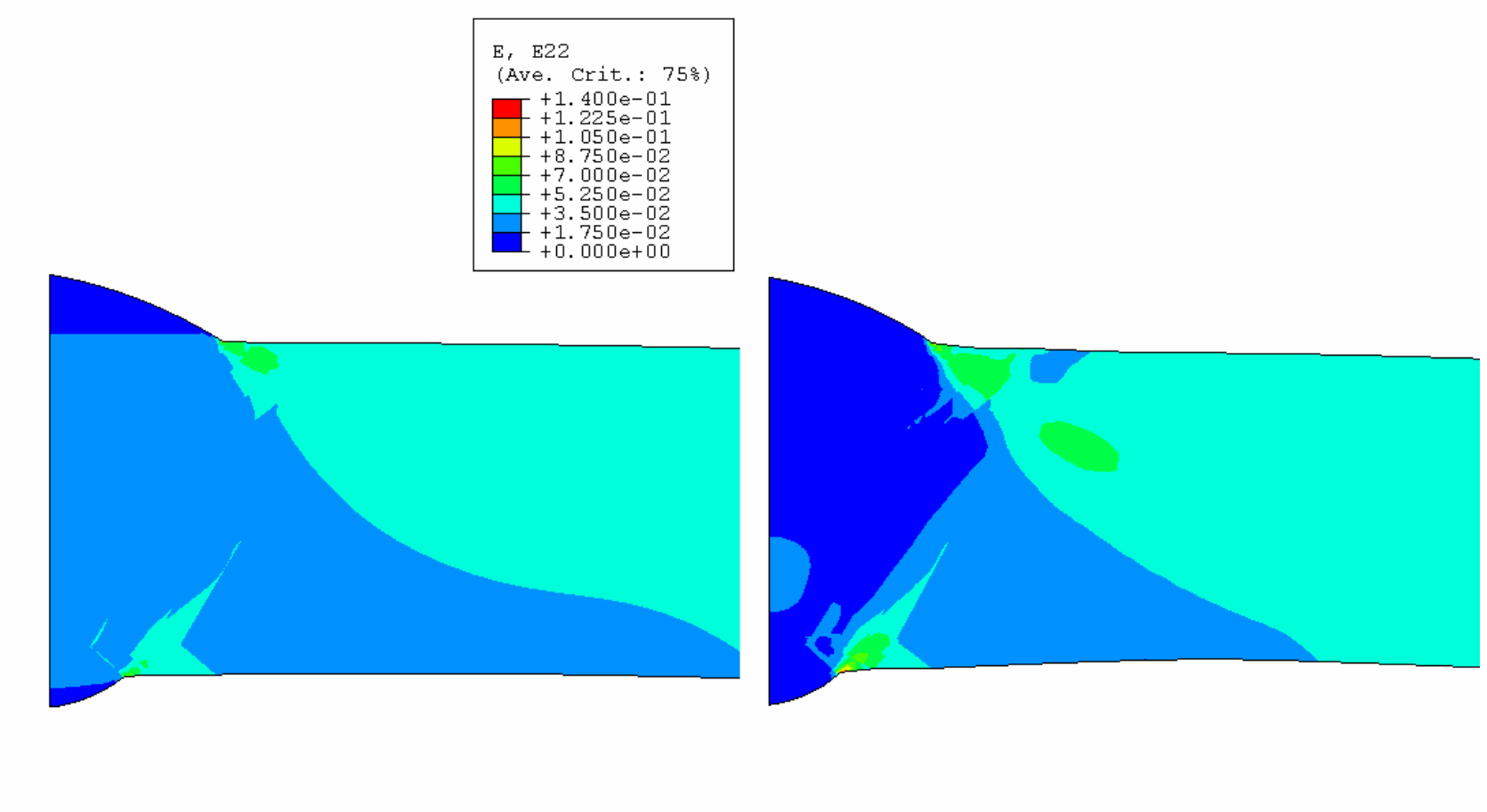

Figure 87. Axial Strain Distributions for Overmatched Welds in X-65 Pipes [Left – no pressure, right – 29.19-MPa (4234-psi) pressure]

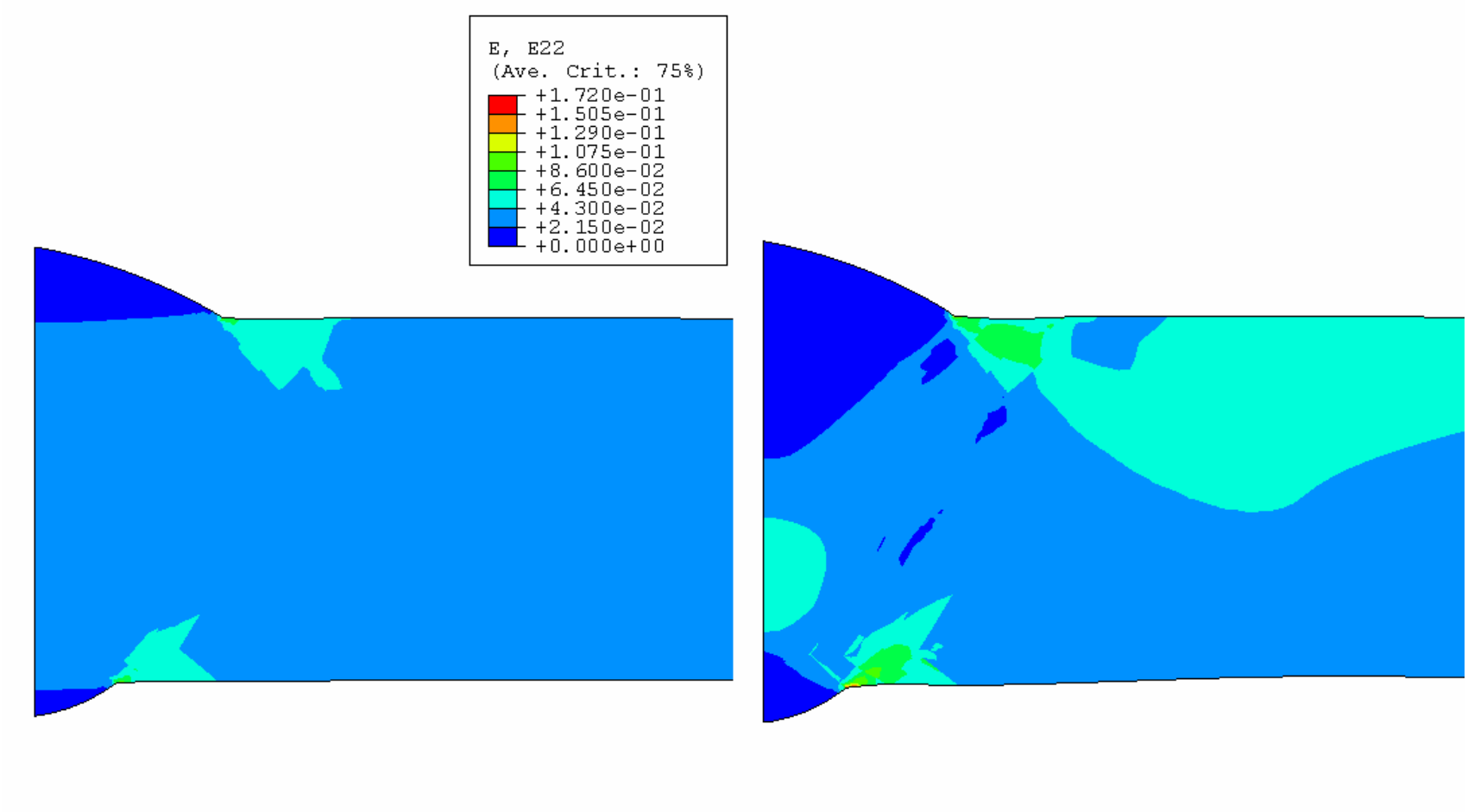

Figure 88. Axial Strain Distributions for X-65 Pipes with Lower Yield-to-Tensile [Left – no pressure, right – 29.19-MPa (4234-psi) pressure]

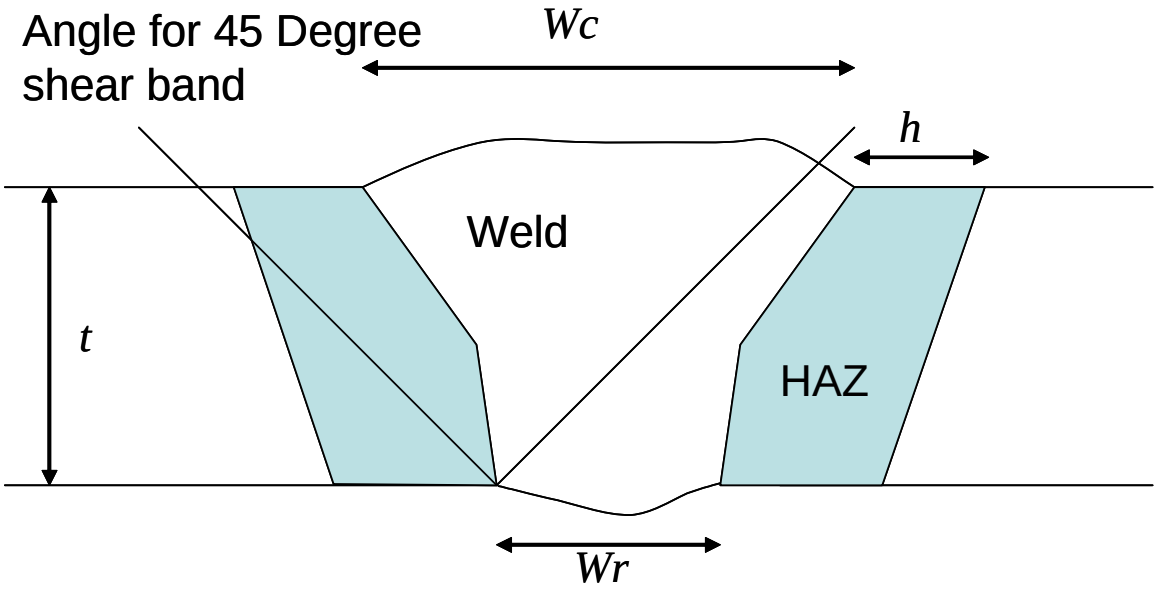

Figure 89. Schematic of Weld Showing 45-Degree Shear Band Positions

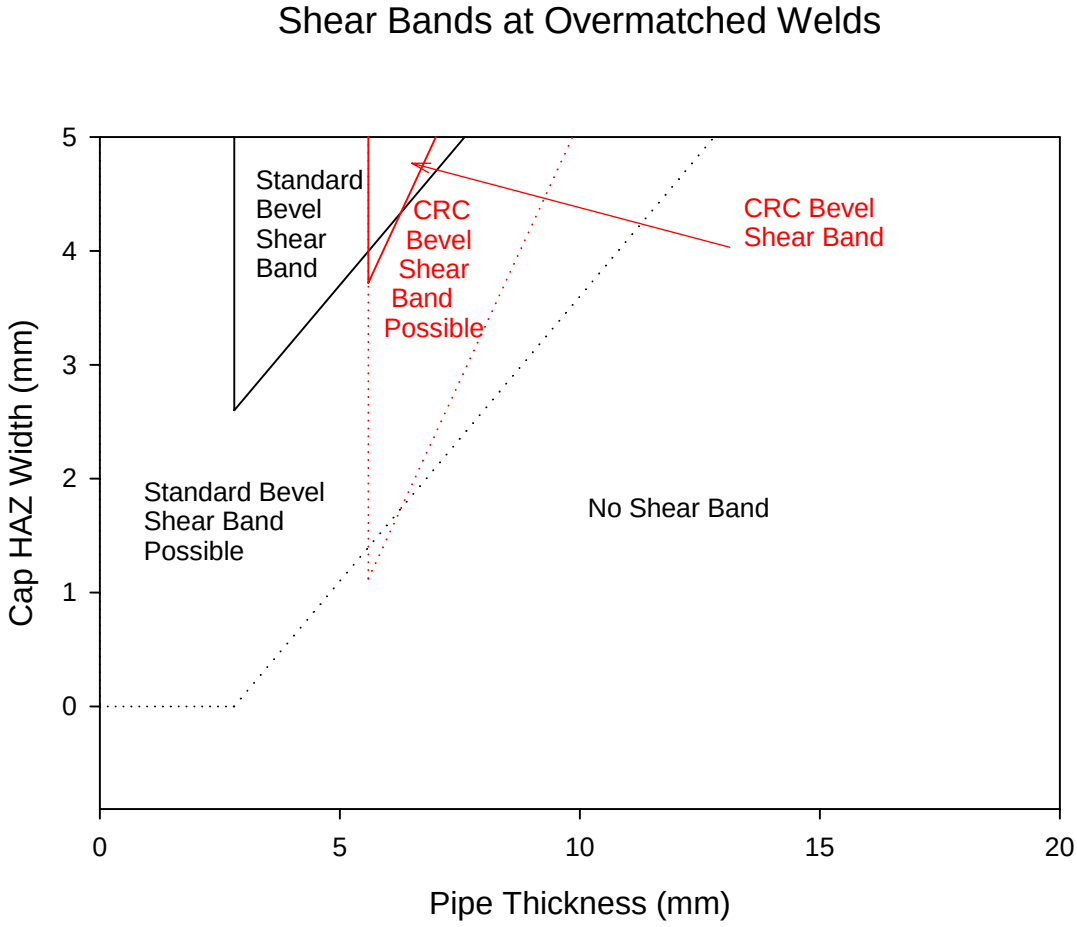

Figure 90. Diagram of Cases Where Full-Thickness Shear Bands in HAZ can be Expected

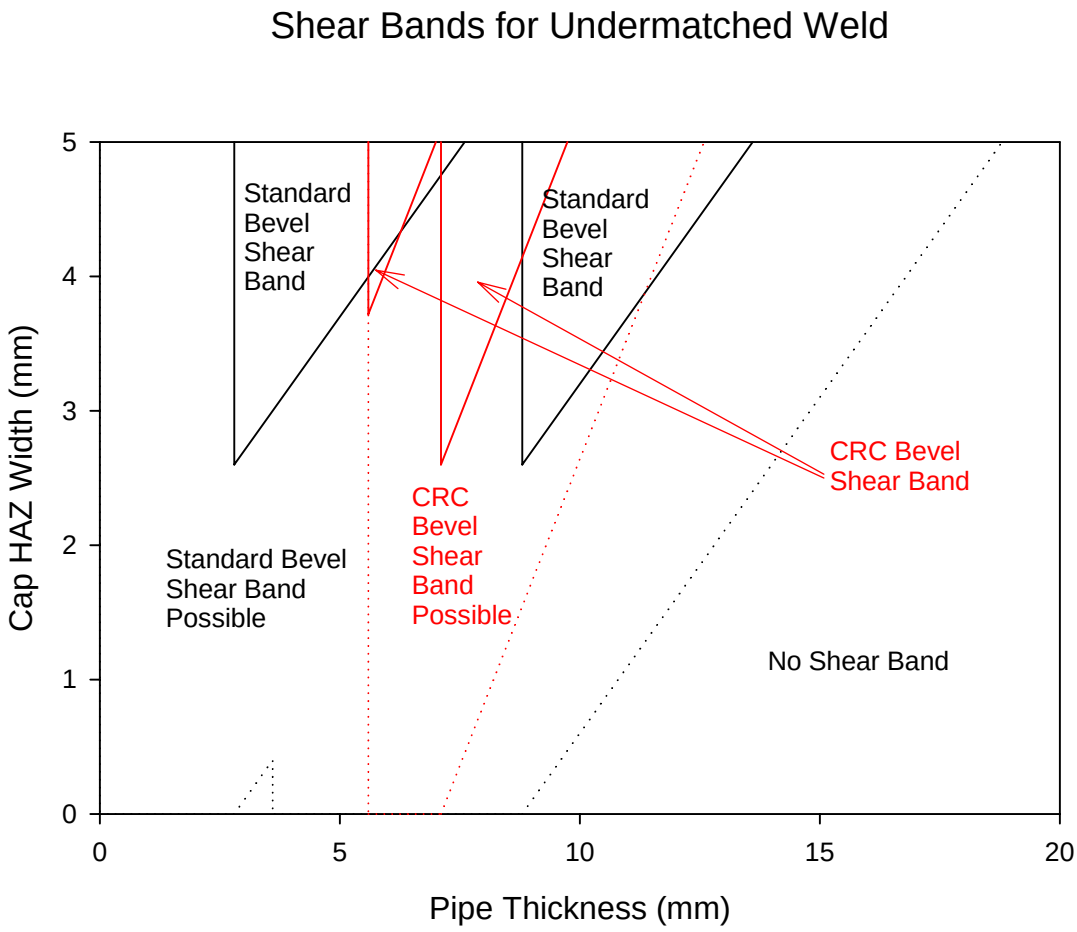

Figure 91. Diagram of Cases Where Full Thickness Shear Bands in Weak Material can be Expected at Undermatched Girth Welds

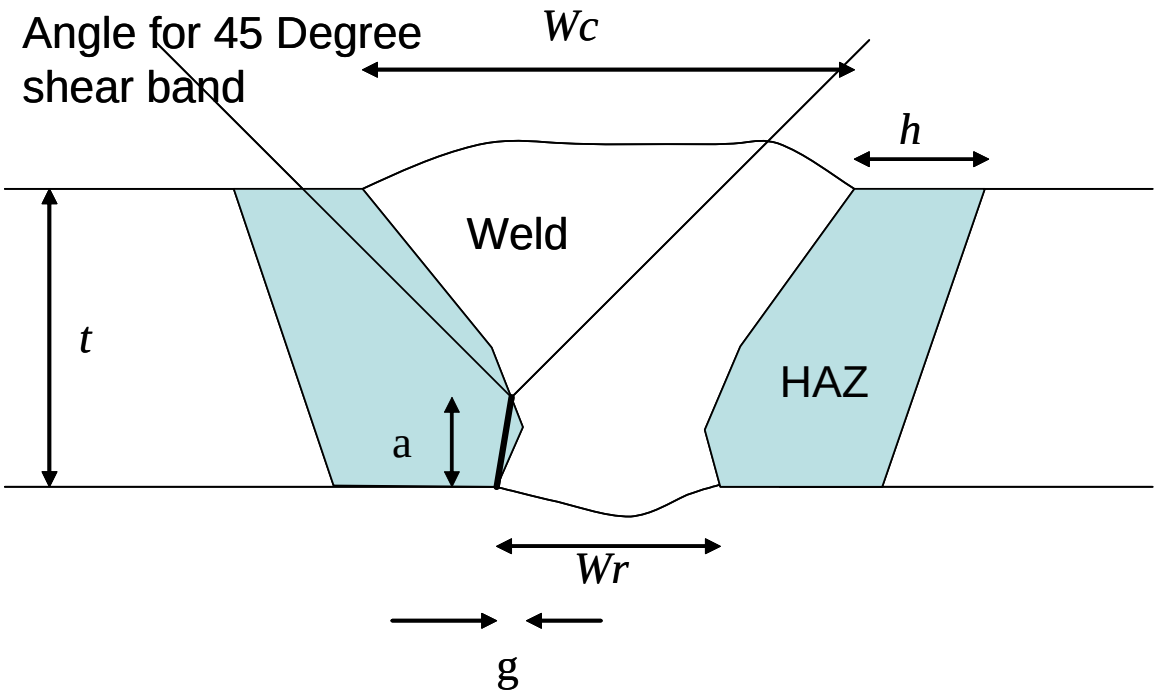

Figure 92. Schematic of Weld with Root Flaw Showing Shear Band Positions

Note: A planar flaw through the HAZ is not an expected configuration, but this drawing shows the relative position of the flaw tip and the mouth of the flaw at the root toe for this demonstration case.

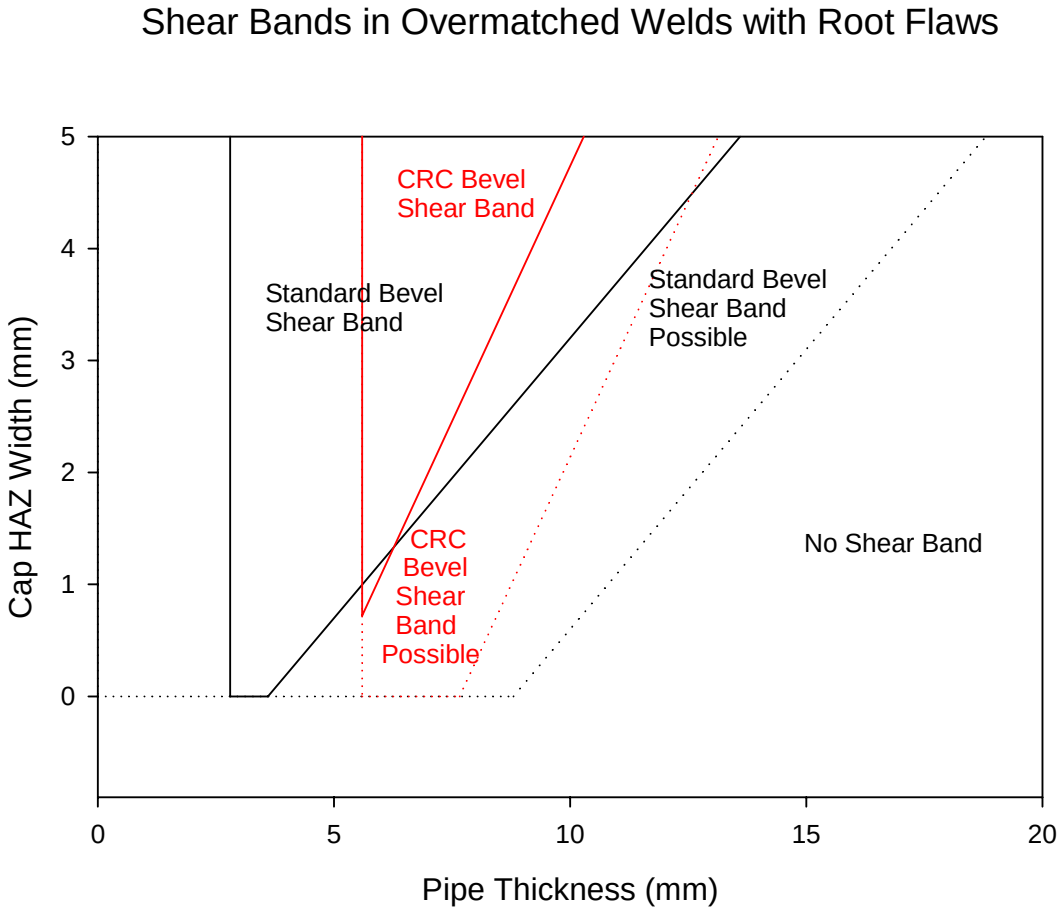

Figure 93. Diagram of Cases where Shear Bands from a 3-mm (0.12-in.)-Deep Root Flaw can be Expected

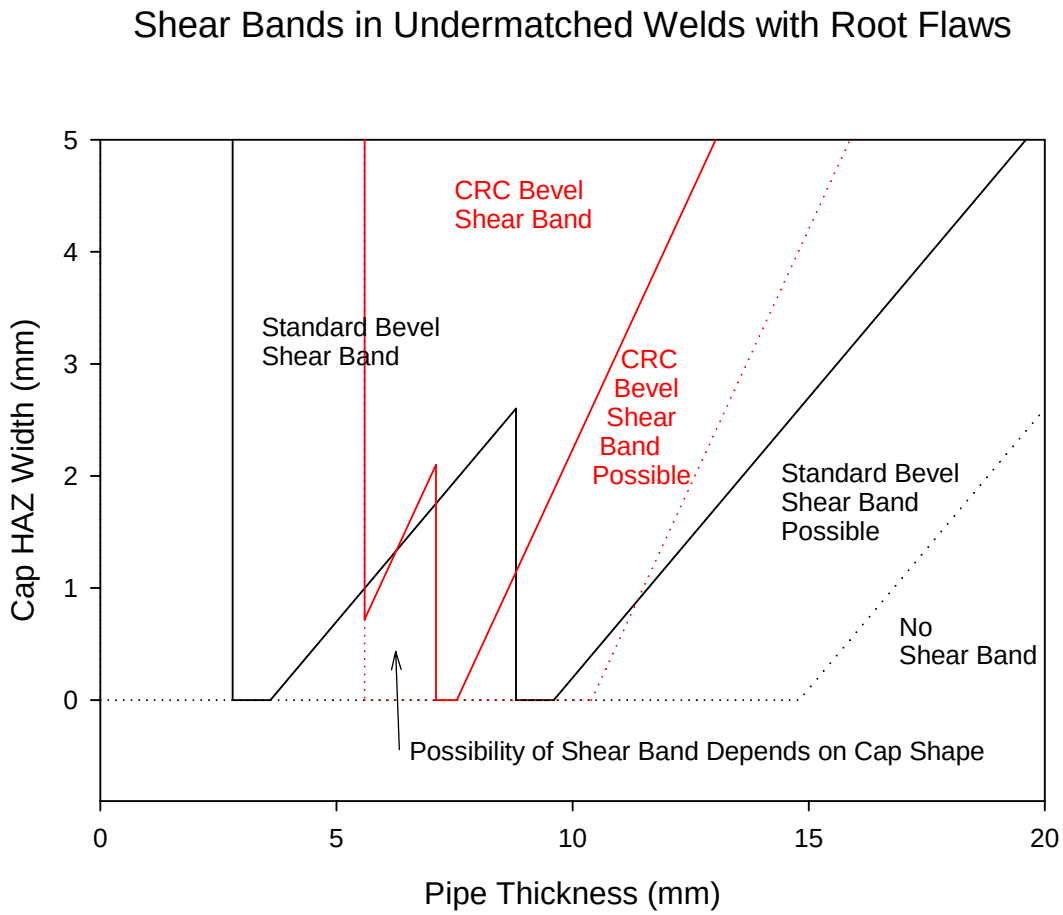

Figure 94. Diagram of Cases where Shear Bands in Weak Material can be Expected from a 3-mm (0.12-in.)-Deep Root Flaw in an Undermatched Weld

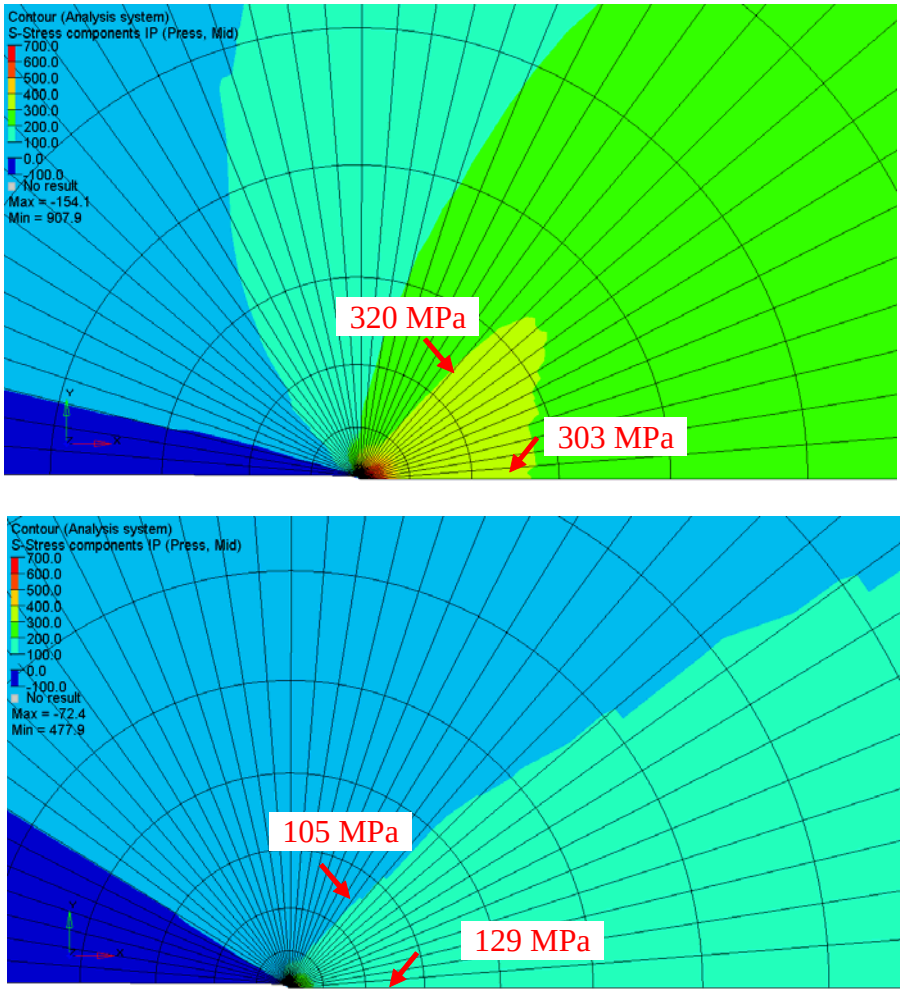

Figure 95. Hydrostatic Stress Distribution Around Crack Tip with Specific Values (Top – plane strain, bottom – plane stress)

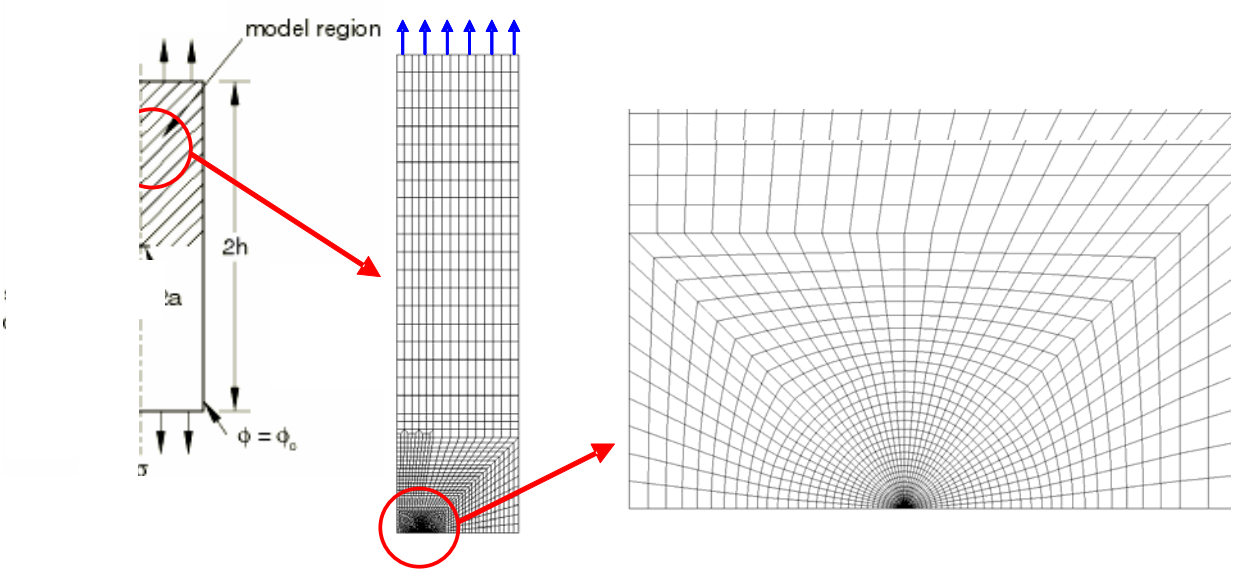

Figure 96. Geometry for Model of Cracked Cylinder

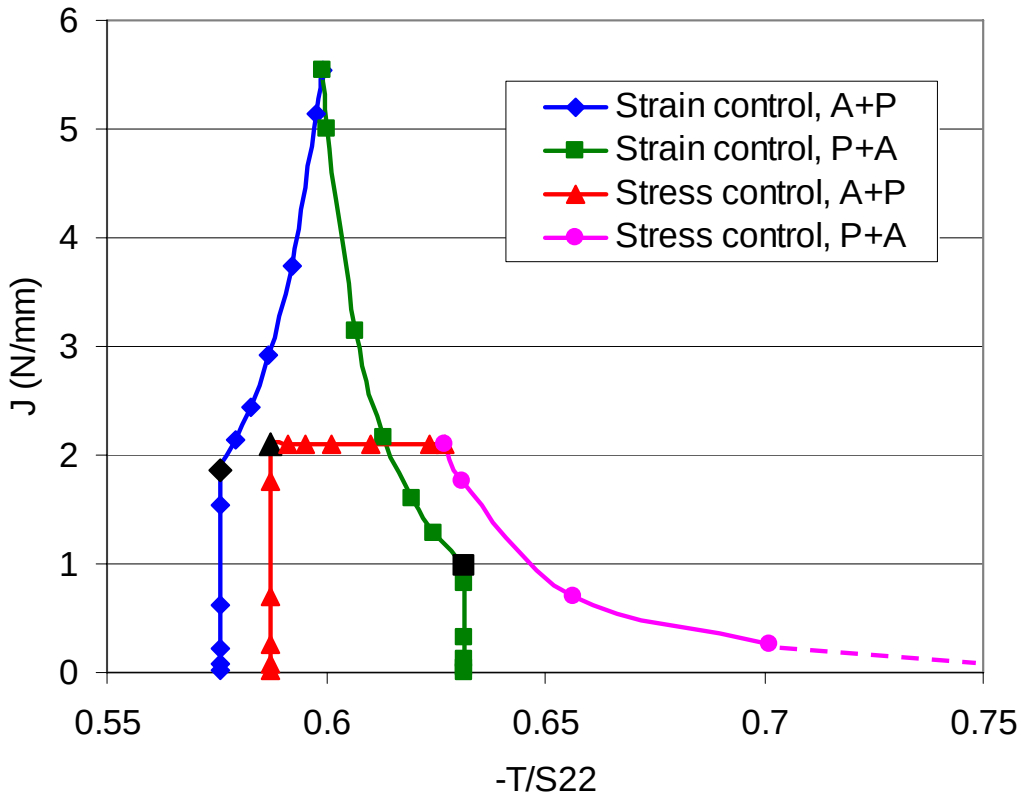

Figure 97. Elastic Results for J vs. Normalized T-Stress

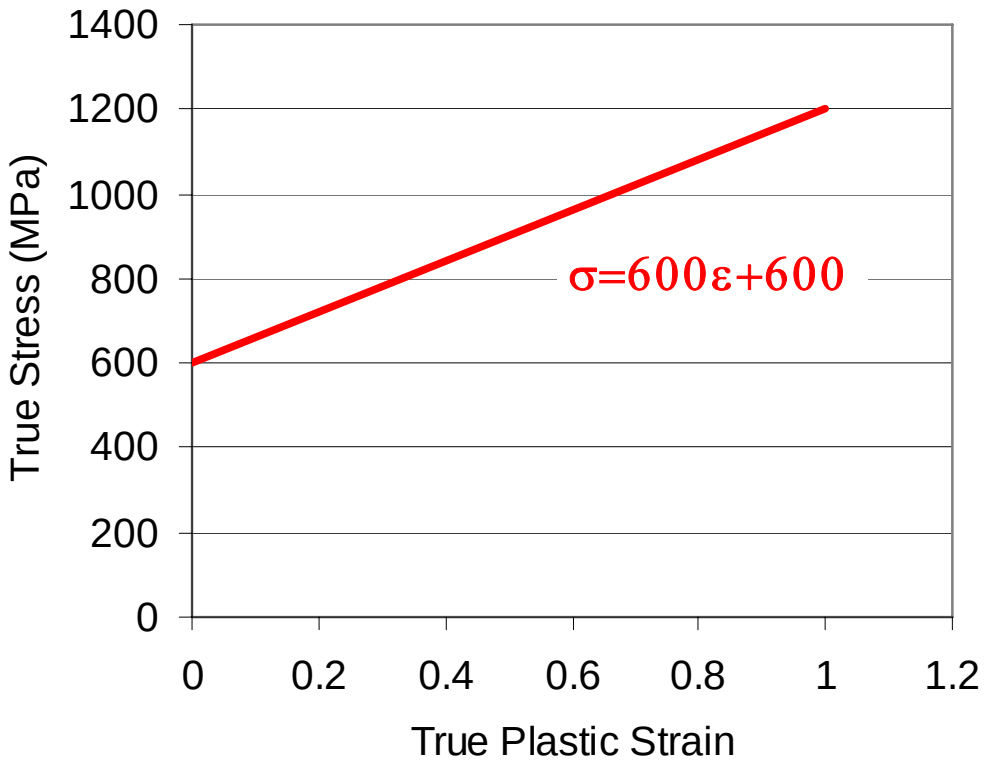

Figure 98. Stress Strain Curve for Plastic Constraint Models (E = 200000 MPa)

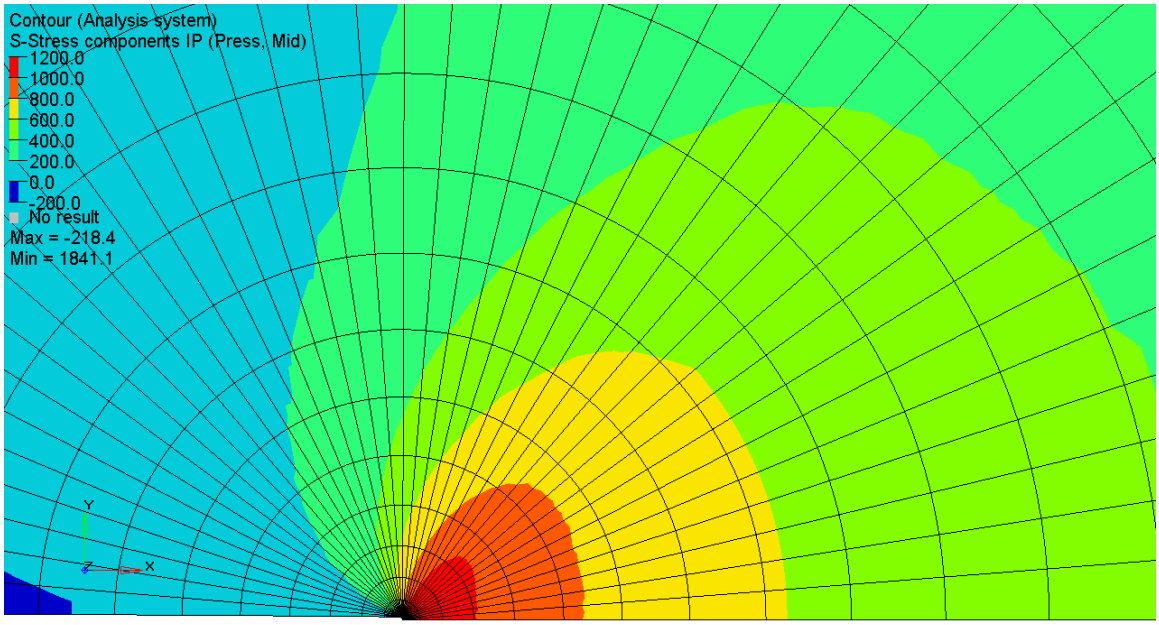

Figure 99. Hydrostatic Stress in MPa Around Crack Tip for Axial Strain of 0.1%

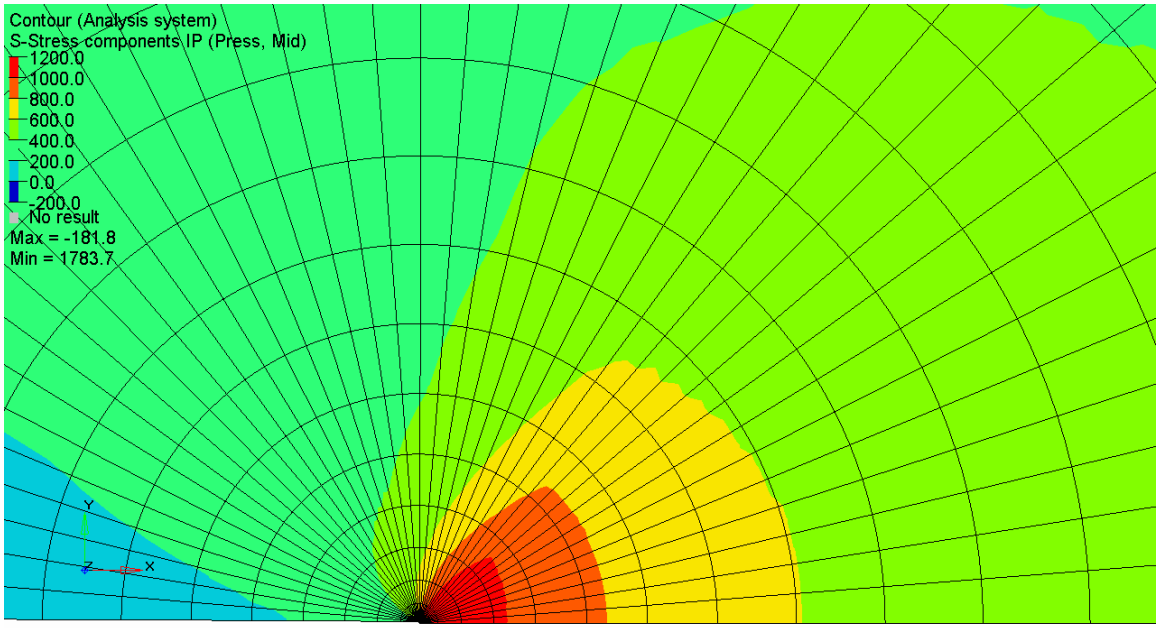

Figure 100. Hydrostatic Stress in MPa Around Crack Tip for Pressure with Ends Held Fixed

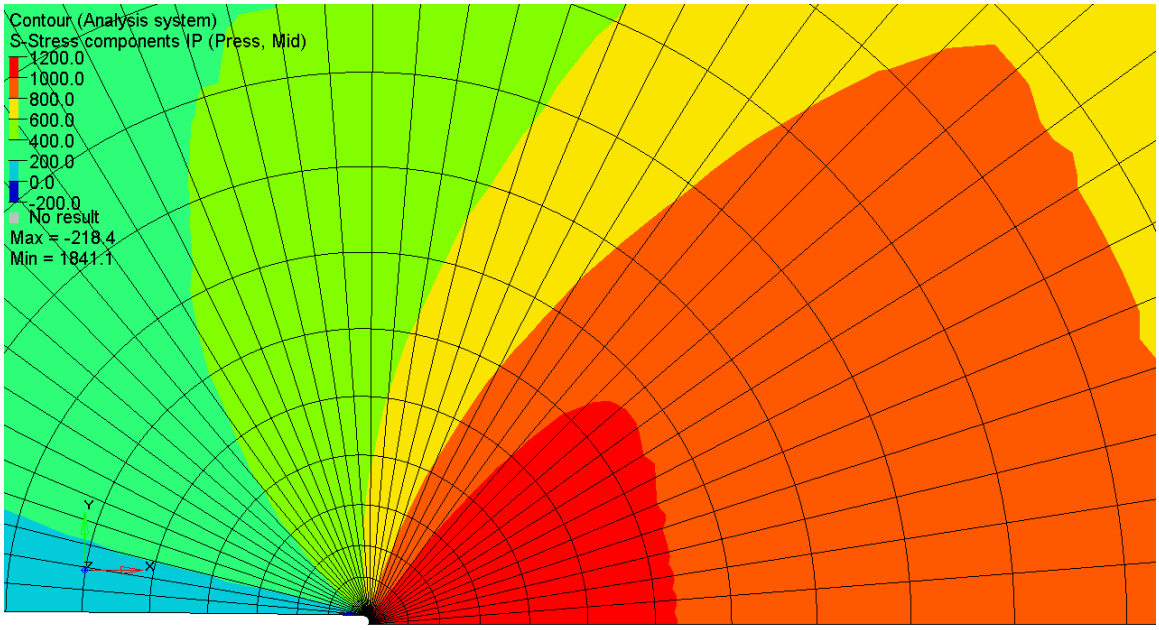

Figure 101. Hydrostatic Stress in MPa Around Crack Tip for Axial Strain Followed by Pressure

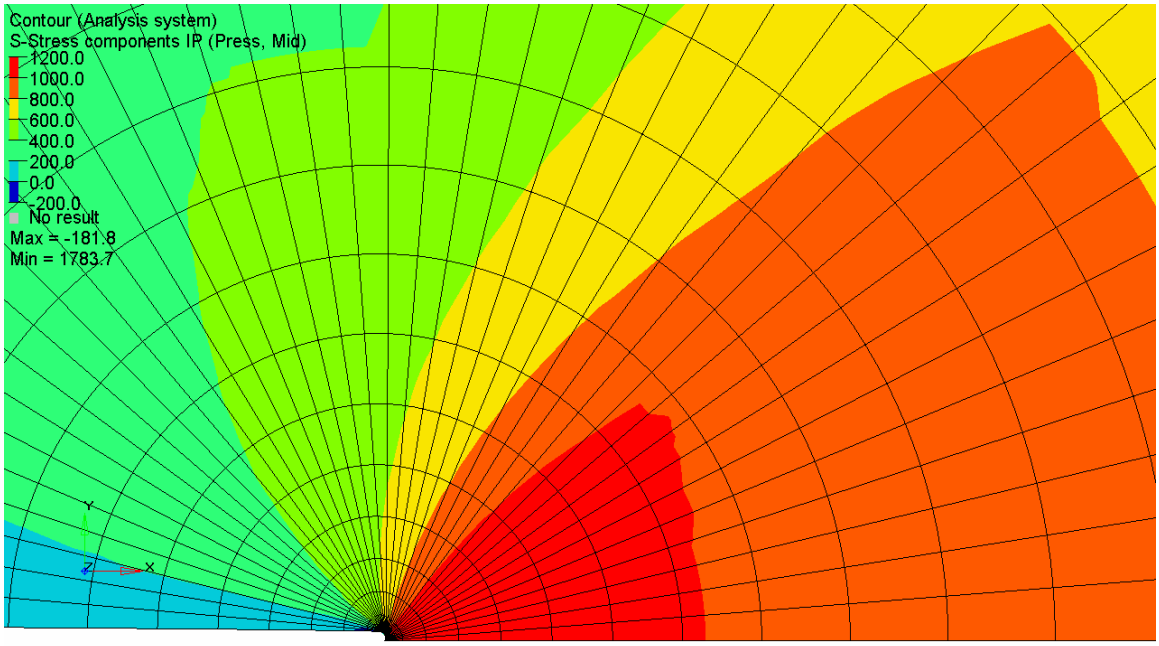

Figure 102. Hydrostatic Stress in MPa Around Crack Tip for Pressure Followed by Axial Strain

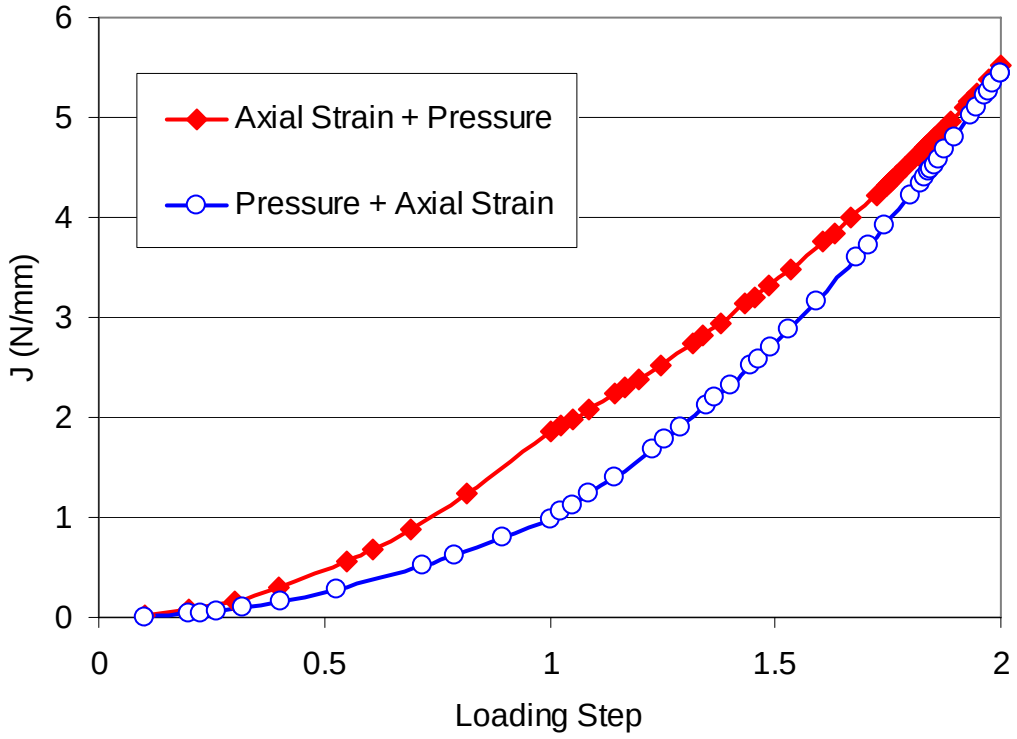

Figure 103. J Progression as Either Internal Pressure of 0.1% Remote Strain is Applied First Followed by the Other

Note: J in N/mm is calculated in several sub-steps as first one loading is applied and then the second loading is applied while the first is maintained at its maximum value. At loading Step 1, the first loading has been applied. At loading Step 2, both loadings have been applied.

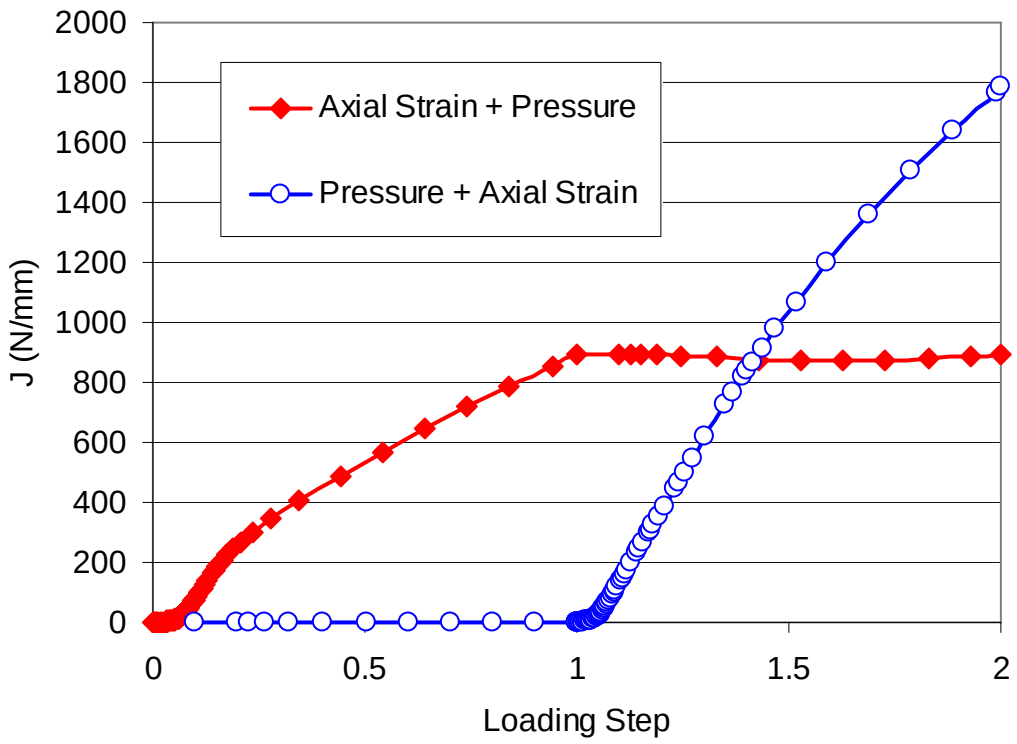

Figure 104. J Progression as Either Internal Pressure or 4% Remote Strain is Applied First Followed by the Other

Note: J in N/mm is calculated in several sub-steps as first one loading is applied and then the second loading is applied while the first is maintained at its maximum value. At loading Step 1, the first loading has been applied. At loading Step 2, both loadings have been applied.

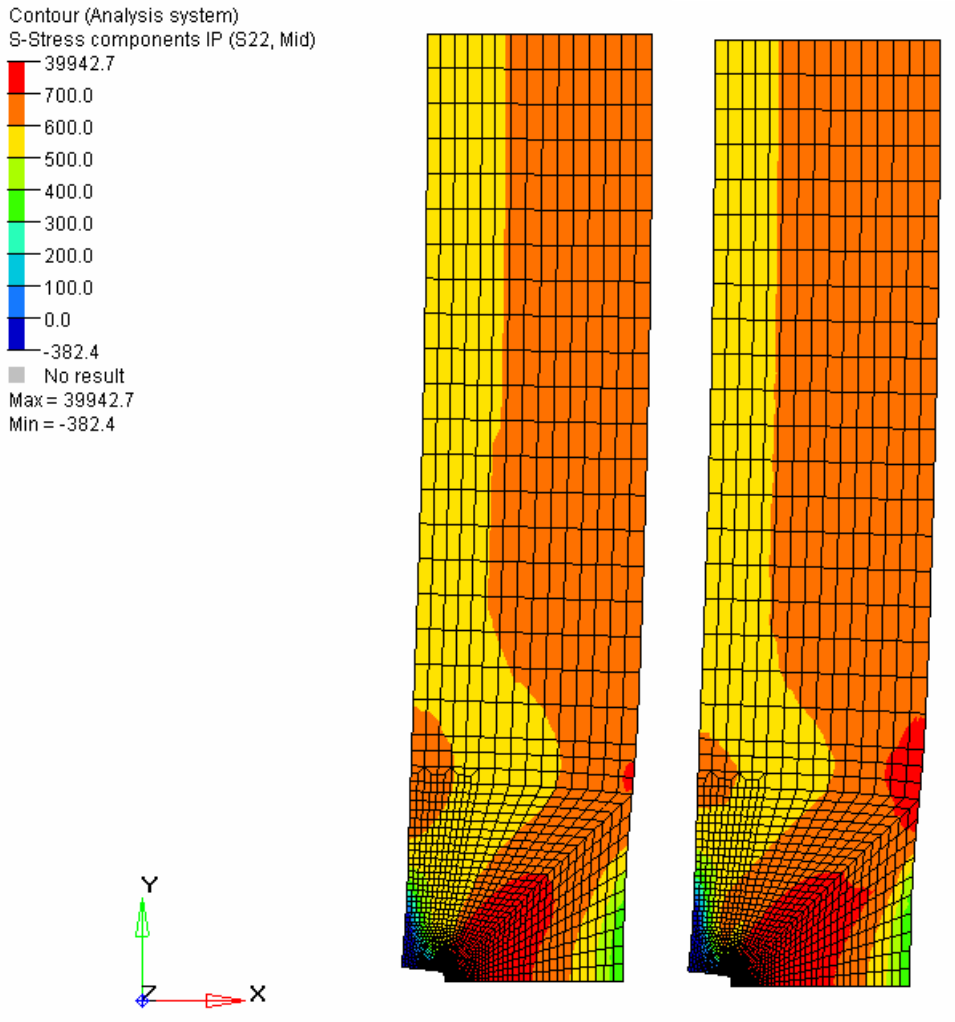

Figure 105. Axial Stress in MPa for Axial Strain to 4% (Left – no pressure, right – pressure after axial strain)

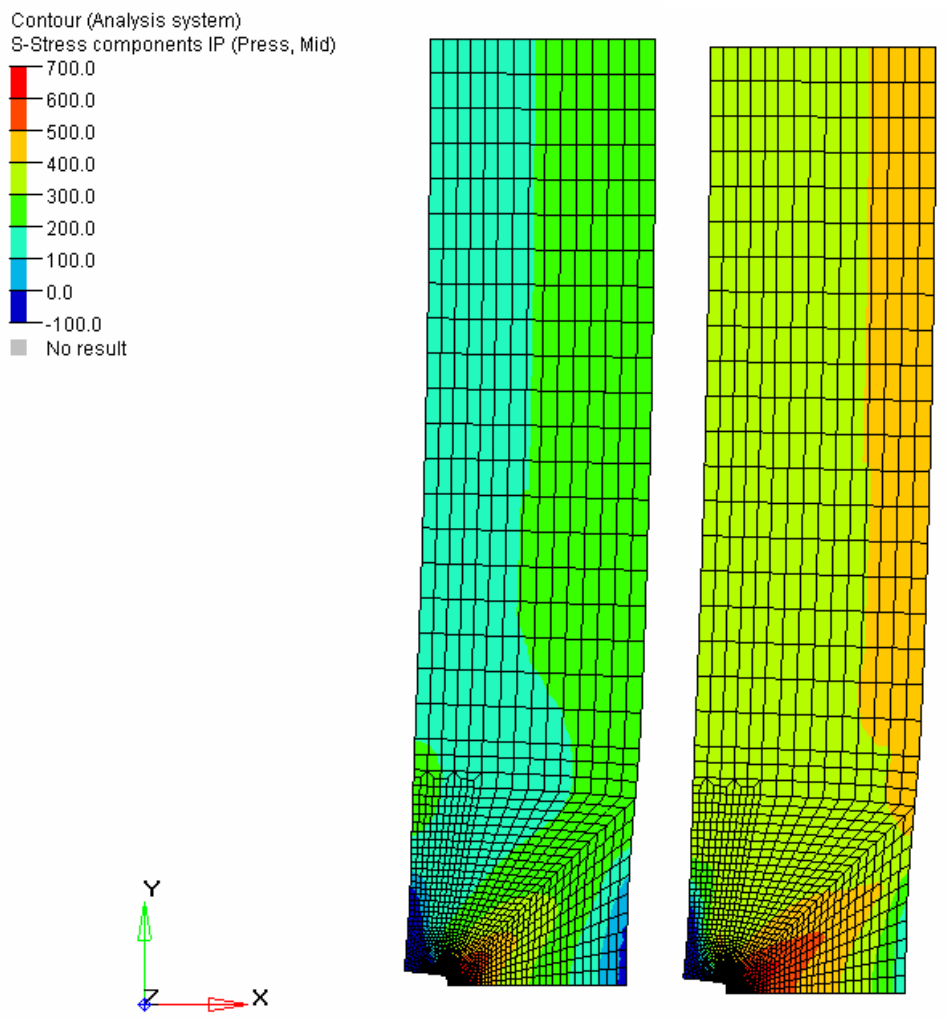

Figure 106. Hydrostatic Stress in MPa for Axial Strain to 4% (Left – no pressure, right – pressure after axial strain)

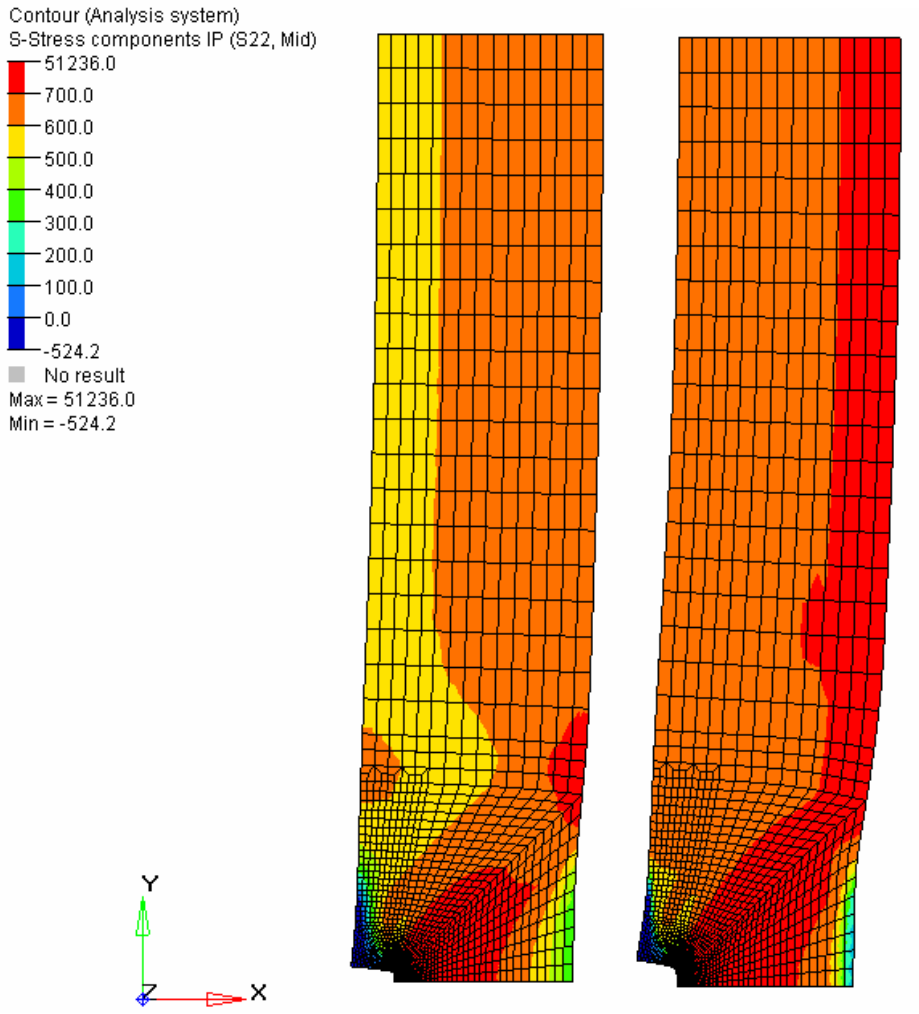

Figure 107. Axial Stress in MPa for Pressure and 4% Axial Strain (Left – strain first, right – pressure first)

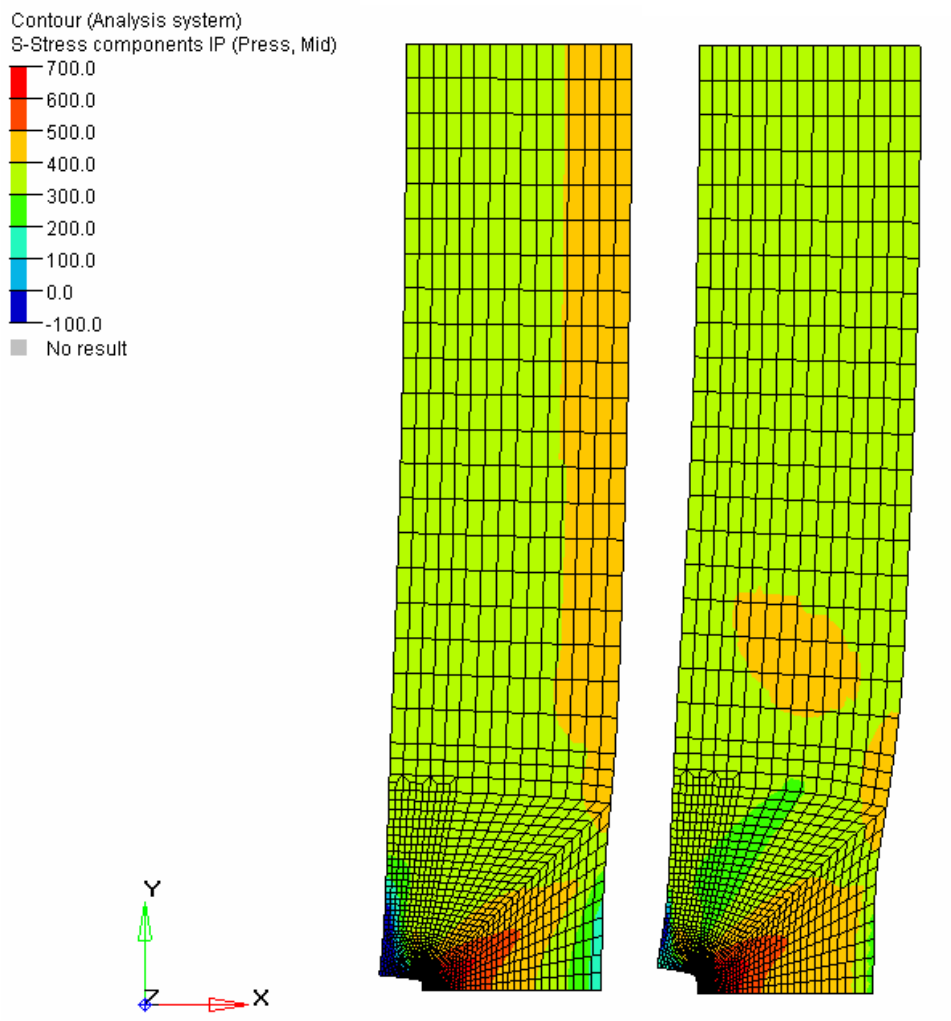

Figure 108. Hydrostatic Stress in MPa for Pressure and Axial Strain (Left – axial first, right – pressure first)

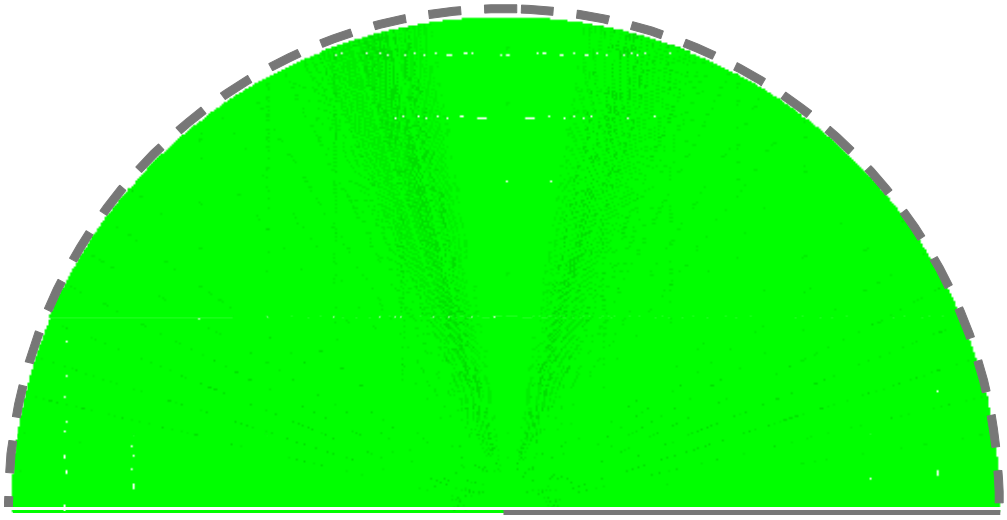

Figure 109. Finite-Element Model of Crack Tip in Infinite Body for Q Calculation

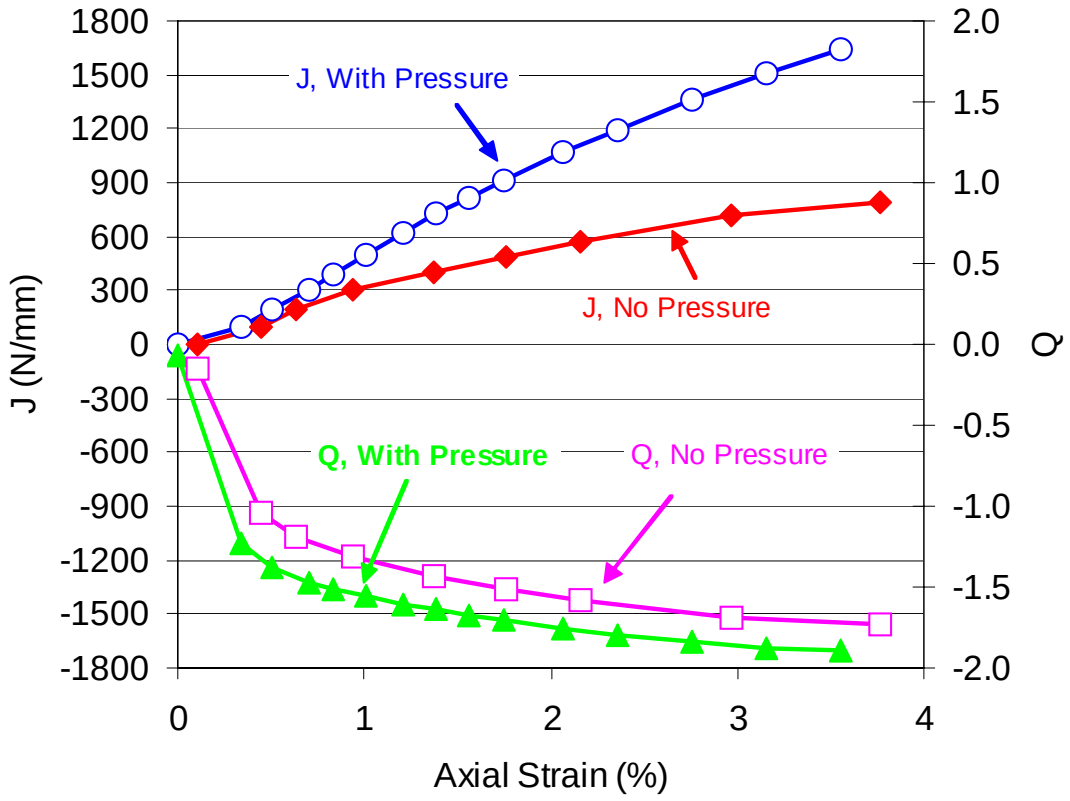

Figure 110. J and Q as a Function of Applied Strain for Pressure and No Pressure Cases

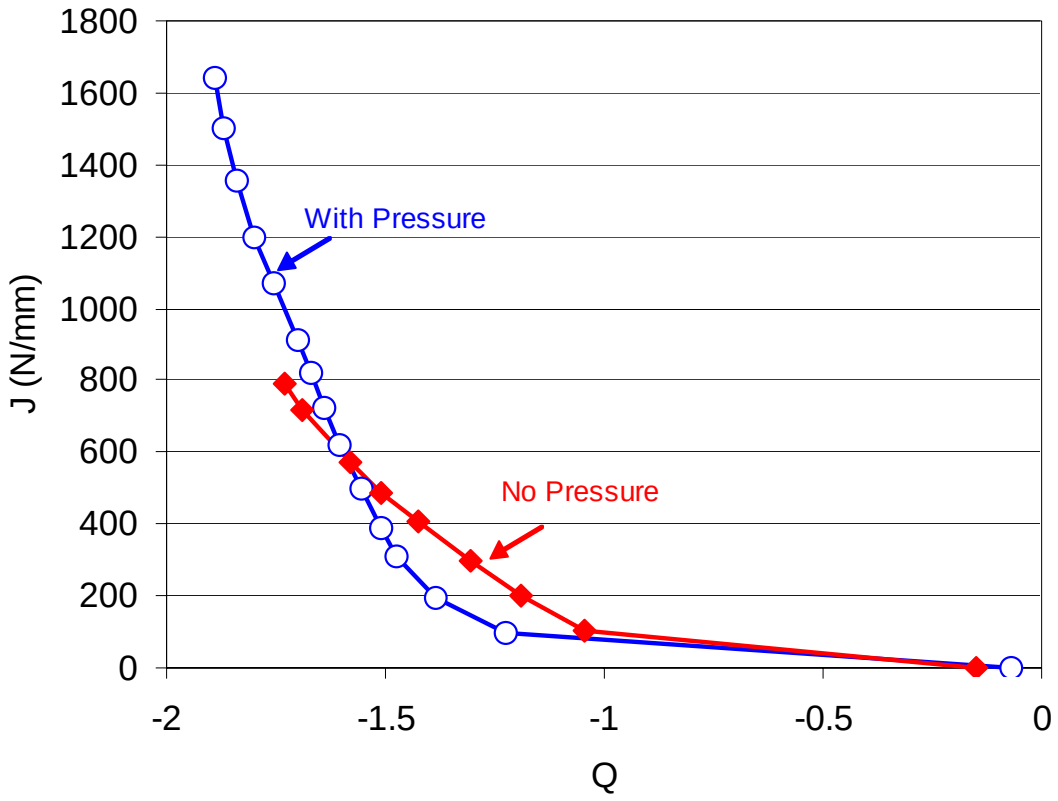

Figure 111. Q as a Function of J for Pressure and No Pressure Cases

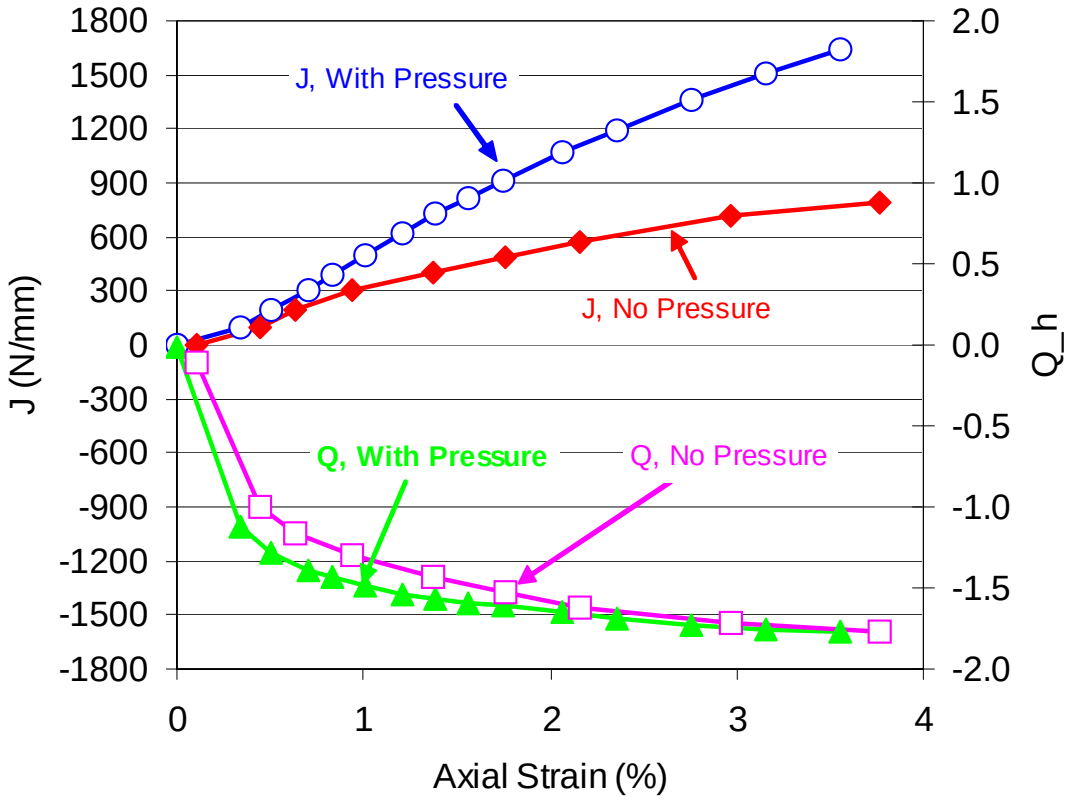

Figure 112. J and Q_h as a Function of Applied Strain for Pressure and No Pressure Cases

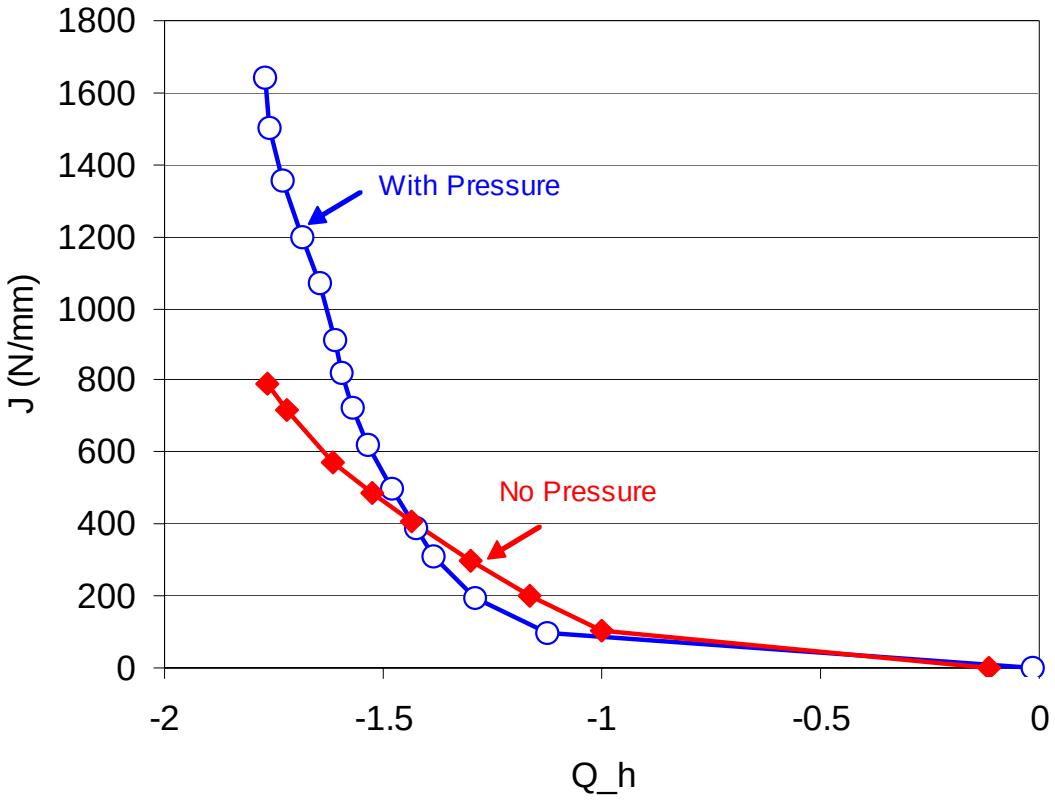

Figure 113. Q_h as a Function of J for Pressure and No Pressure Cases

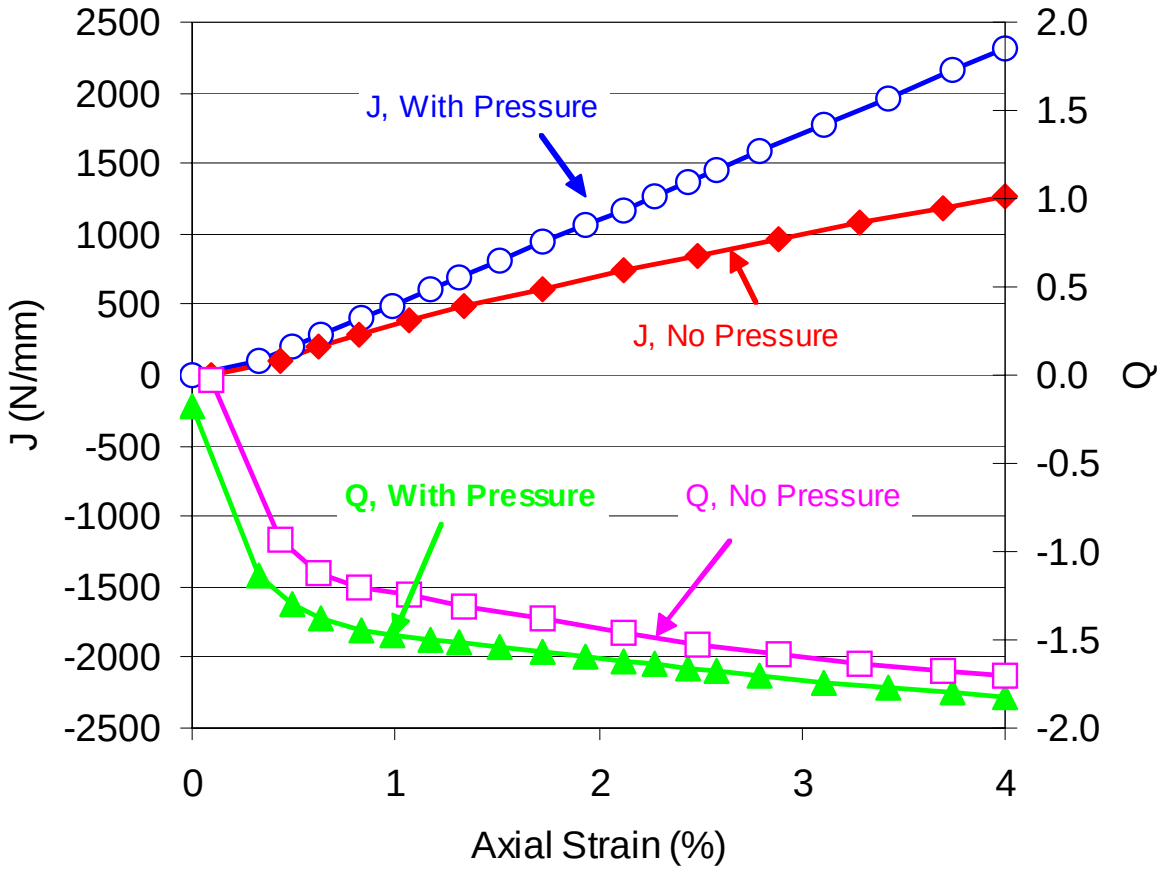

Figure 114. J and Q for Double Size Model

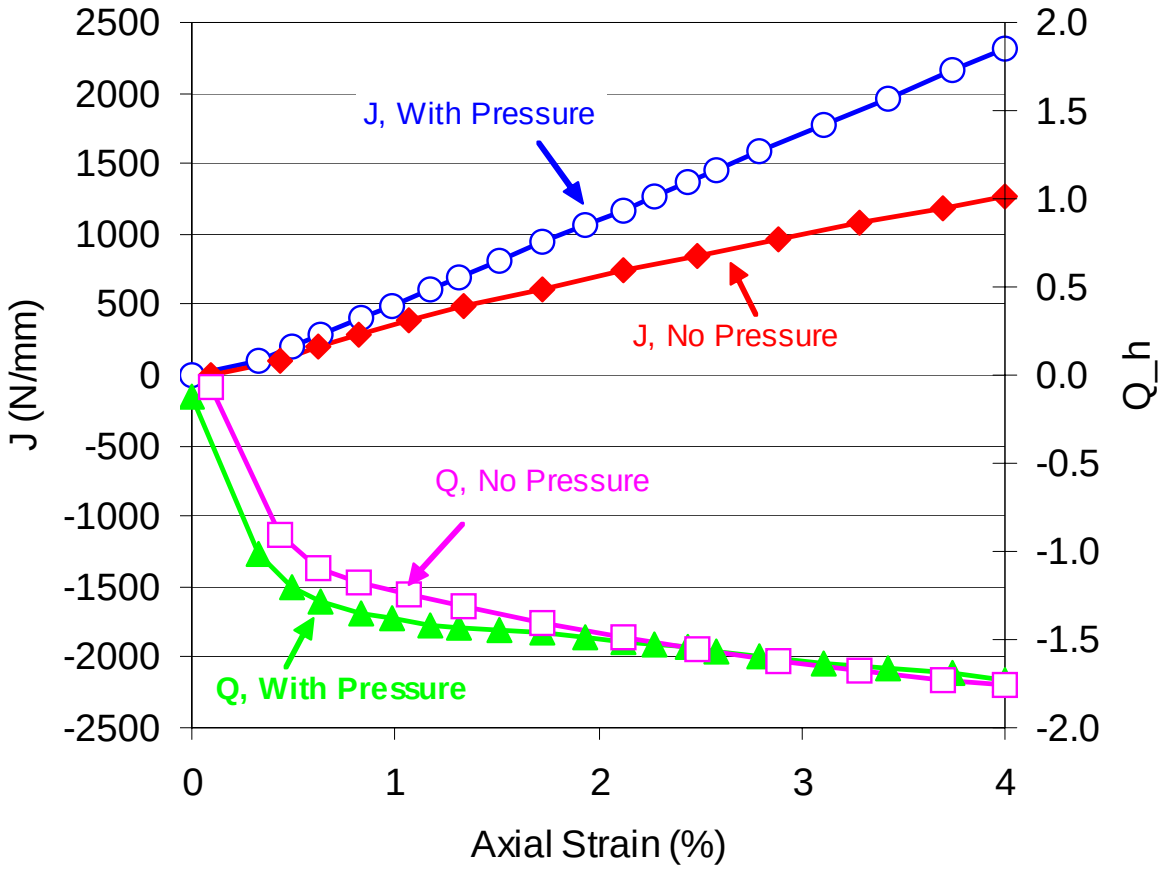

Figure 115. J and Q_h for Double Size Model